EFFECT OF CHLORIDE ON ENVIRONMENTALLY ASSISTED CRACKING OF LOW ALLOY STEELS IN OXYGENATED HIGH TEMPERATURE WATER

MATTHIAS G. J. HERBST

A thesis submitted in partial fulfilment of the
requirements of Liverpool John Moores University
for the degree of Doctor of Philosophy

This research program was carried out in collaboration
with Georg-Simon-Ohm University Nuremberg and AREVA GmbH

November 2013

ABSTRACT

The aim of this thesis was to derive a better understanding with regard to the effects of chloride on the general corrosion behaviour of low-alloy steels (LAS) in oxygenated high-temperature water (HTW) and to investigate the underlying mechanisms for crack initiation and propagation due to chloride assisted environmentally assisted cracking (EAC). Therefore, systematic investigations on the effect of chloride on the EAC behaviour of LAS were performed to understand and elucidate the underlying mechanisms.

The overall thesis is divided into three parts focussing on the effect of chloride on:

i) general corrosion
ii) crack initiation, and
iii) crack growth

of low-alloy steels in oxygenated high-temperature water.

Studies on the effect of chloride on the general corrosion behaviour were performed by immersion tests that were evaluated using electrochemical monitoring techniques and different post-test investigation methods like SEM, ToF-SIMS, and others. From the performed investigations it is concluded that the presence of small amounts of chloride in oxygenated HTW causes an incorporation of chloride into the oxide layer, a thinning of the oxide layer thickness, and pronounced pitting.

The crack initiation susceptibility of LAS was investigated using CERT tests. These tests showed an increased number of crack initiation locations and a decrease of the elongation at fracture with increasing chloride concentrations.

Crack growth rate tests clearly demonstrated that not the increase in the chloride concentration per se, but the conjoint occurrence of an active or dormant crack and increased chloride concentration causes an increase in the observed crack growth rates.

For practical applications of LAS in oxygenated HTW this means that short term transients seem to be not harmful regarding component integrity, but long term increased chloride concentrations should be prohibited since they cause increased general corrosion of LAS. Taking crack initiation and crack growth into consideration, the conjoint occurrence of increased chloride concentrations and mechanical straining at stress levels above the yield strength should be avoided.

PUBLICATIONS IN PEER REVIEWED JOURNALS AND CONFERENCE PROCEEDINGS

Some of the work described in this thesis has been previously published in the frame of different peer reviewed conference and journal papers (Herbst and Roth, 2013, Herbst et al., 2011, Herbst et al., 2012, Herbst et al., 2013).

M. Herbst, et al. (2011)

Effect of Chloride on Environmentally Assisted Cracking of Low Alloy Steels in Oxygenated High-Temperature Water – General Corrosion, 15th International Conference on Environmental Degradation of Materials in Nuclear Power Systems – Water Reactors, August 2011, Colorado Springs, Colorado.

M. Herbst, et al. (2012).

The Effect of Chloride on General Corrosion and Crack Initiation of Low-Alloy Steels in Oxygenated High-Temperature Water, 38th MPA Seminar, October 1 and 2, 2012, Stuttgart.

M. Herbst, A. Roth, (2013)

Investigations on the Effect of Chloride on the General Corrosion Behaviour of Low-Alloy Steels in Oxygenated High-Temperature Water. Materials and Corrosion, 2013. 63 (8), p. 691-699.

M. Herbst, et al. (2013).

Effects of Chloride on the EAC-Behaviour of Low-Alloy Steels in Oxygenated High-Temperature Water. 16th International Conference on Environmental Degradation of Materials in Nuclear Power Systems – Water Reactors, August 2013, Asheville, North Carolina.

CONTENT

ABBREVIATIONS AND SYMBOLS

AE	Auxiliary Electrode (~ Counter Electrode)
AES	Auger Electron Spectroscopy
ASME	American Society of Mechanical Engineers
ASTM	American Society for Testing Materials
BWR	Boiling Water Reactor
CASTOC	Crack Growth Behaviour of Low Alloy Steels for Pressure Boundary Components under Transient Light Water Operating Conditions
CE	Counter Electrode
CERT	Constant Extension Rate Tensile test (also designated as SSRT test)
CF	Corrosion Fatigue
CGR	Crack Growth Rate
CMOD	Crack Mouth Opening Displacement
CT	Compact Tension (design of test specimens)
DCPD	Direct Current Potential Drop (measurement technique)
DO	Dissolved Oxygen Concentration
DSA	Dynamic Strain Aging
EAC	Environmentally Assisted Cracking
EC	Electrical Conductivity
ECN	Electrochemical Current Noise
ECP	Electrochemical Corrosion Potential
EIS	Electrochemical Impedance Spectroscopy
EMF	Electro Motoric Force
EN	Electrochemical Noise
EPN	Electrochemical Potential Noise
EPRI	Electric Power Research Institute

FFT	Fast Fourier Transform
FIB	Focused Ion Beam
HAZ	Heat Affected Zone
HPDP	High Pressure Dosing Pump
HTBE	High-Temperature Reference Electrode
HTW	High-Temperature Water
K	Stress Intensity Factor
KWU	KraftWerkUnion (a former Siemens branch)
LAS	Low-Alloy Steel
LWR	Light Water Reactor
MPA	Materialprüfanstalt (Materials Testing Institute)
PPU	Periodical Partial Unloading (testing technique used in CGR-tests)
PSD	Power Spectral Density
PSI	Paul Scherrer Institute (Villingen, Switzerland)
PWR	Pressurized Water Reactor
R	Ratio between minimum and maximum load or elongation
RE	Reference Electrode
RPV	Reactor Pressure Vessel
SCC	Stress Corrosion Cracking
SEM	Scanning Electron Microscope
SICC	Strain Induced Corrosion Cracking
SIMS	Secondary Ion Mass Spectroscopy
SSRT	Slow Strain Rate Tensile
ToF-SIMS	Time of Flight – Secondary Ion Mass Spectroscopy
WE	Working Electrode

LIST OF TABLES

LIST OF FIGURES

1. INTRODUCTION

1.1 Background

The operating experience and performance of Low-Alloy Steel (LAS) primary pressure-boundary components in BWR (Boiling Water Reactor) and PWR (Pressurised Water Reactor) Light Water Reactors (LWRs) is very good worldwide. LAS used for pressure boundary components, e.g. the reactor pressure vessel, are usually not directly in contact with the primary coolant, since they are protected against erosion and corrosion using an austenitic stainless steel overlay cladding. However, depending on the plant design, unclad pipes made of LAS may be in direct contact with the primary coolant, e.g. in feedwater piping of some BWR designs. Furthermore, cladding discontinuities of the reactor pressure vessel surface, causing a direct contact of LAS and primary coolant, are postulated for conservative safety analyses. Therefore, for pro-active safety assessments it is assumed that cooling water can be in direct contact to the LAS materials of the pressure boundary. The behaviour of these components regarding Environmentally Assisted Cracking (EAC) has been the topic of scientific research and assessment during the last decades (Seifert, 2002, Hickling et al., 2005, Scott et al., 2005, Seifert and Ritter, 2005a, Seifert and Ritter, 2005b, Ford, 2006, Ford and Scott, 2008).

After some worrying crack growth rate data published in the late 1980´s (Speidel and Magdowski, 1988) further investigative projects have shown that LAS is not susceptible to Stress Corrosion Cracking (SCC) under nominal operating conditions of LWRs, in particular under BWR conditions, based on the existing data base (Kussmaul et al., 1997, Scott and Tice, 1990, Tenckhoff et al., 1990, Ford, 1992). More recently, the cessation of active fatigue crack growth under steady state (constant loading) conditions could be experimentally confirmed in the frame of a European cooperative project. Thereby the occurrence of SCC can be ruled out for steady state operation conditions (Ernestova et al., 2004, Föhl et al., 2004, Ehrnsten et al., 2003).

So far, no cracking incidents with a major contribution of SCC to the total crack advance in properly manufactured and heat treated LAS primary pressure-boundary components have occurred in service (Roth, 2005, Seifert and Ritter, 2005a, Seifert and Ritter, 2005b).

However, recent laboratory investigations of the Paul Scherrer Institute (Switzerland) have shown an effect of dissolved chloride on the crack growth rate of pre-cracked CT-specimen tested with the periodic partial unloading (PPU) technique under simulated BWR water chemistry (see Figure 1).

In these studies, three hours after the addition of 50 ppb chloride[1] to oxygenated high-temperature water (temperature 288 °C; dissolved oxygen (DO) 8 ppm; electrochemical corrosion potential (ECP) 110 mV_{SHE}) an onset of fast environmentally assisted crack growth occured during a constant load phase between two periodic partial unloadings due to the increased chloride concentration (Ritter and Seifert, 2004b, Roth et al., 2005). Up to today, the reason for this observed behaviour is not fully understood.

In addition to these studies, further research activities focused on the effect of chloride on crack growth in the transition region of dissimilar welds between nickel base alloys (e.g. alloy 182) and low-alloy steels. These investigations revealed sustained crack growth across the fusion line into the LAS for increased chloride concentrations, whereas without chloride no crack growth crossing the fusion line and propagating into the LAS has been observed in any tests (Kumagai et al., 2009, Peng et al., 2005, Ritter and Seifert, 2009, Seifert et al., 2008, Seifert et al., 2013).

Due to a lack of additional experimental data, the test results mentioned above and the fact that temporary chloride transients may occur during plant operation, for example, during plant start up or shut down and also during steady state operating conditions, further investigations on the influence of chloride on the passivity and crack growth behaviour of LAS in high-temperature water (HTW) are considered necessary by the international expert community in this field.

[1] For clarification it has to be noted that whenever it is referred to a chloride concentration in this work, this concentration always indicates the chlorine ion concentrations in the electrolyte throughout the whole thesis.

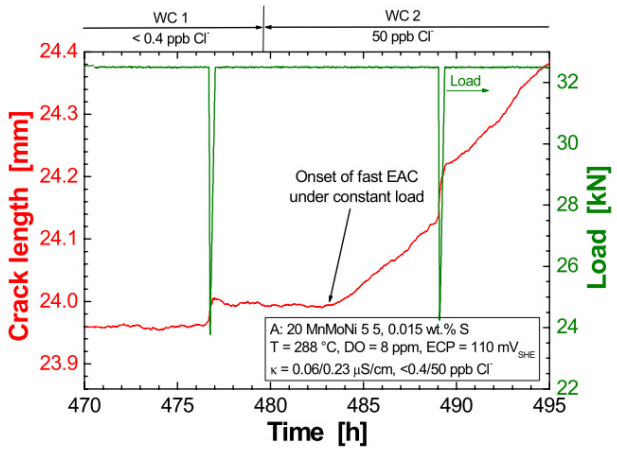

Figure 1: **Onset of SCC during a constant load phase three hours after the addition of 50 ppb chloride to oxygenated HTW (Ritter and Seifert, 2004b).**

It is therefore the aim of this thesis to derive a better understanding with regard to the phenomenology and mechanism behind chloride effects on the general corrosion behaviour of LAS in oxygenated HTW as well as its effects on crack initiation and propagation due to EAC.

1.2 Outline of the Work

In order to systematically investigate the effect of chloride on the EAC behaviour of LAS and to elucidate the underlying mechanisms, the following tasks have been performed in the frame of the experimental work and investigative studies of this thesis:

- development of a test rig and a specimen arrangement to enable in-situ testing at different chloride concentrations in oxygenated HTW
- electrochemical investigations during testing to study chloride induced effects on the corrosion behaviour on-line during exposure to HTW-conditions
- metallographic investigations after HTW-tests
- verification of the applicability of electrochemical methods to detect an influence of chloride on the quasi-passive behaviour of LAS in HTW
- investigations on the effect of different chloride concentrations on crack initiation
- development of a testing device to perform crack-tip micro sampling during crack growth rate testing under HTW-conditions
- studies on the effect of chloride on the crack growth rate and in particular on the composition of the crack-tip electrolyte

The **literature review** summarizes the current state of the art regarding EAC of LAS in HTW and, in particular, the corrosion behaviour of LAS and former investigations on the effect of chloride on EAC of LAS. Accordingly, the **testing methods** and the **experimental procedure** are described in two consecutive chapters. The experimental part of the thesis is divided into three main parts, each focusing on one particular question, as briefly described below.

Part 1: General Corrosion Behaviour

As already mentioned above, so far no complete understanding and no detailed model regarding the effect of chloride on the general corrosion behaviour of LAS in HTW exists. Therefore, the effect of chlorides on the electrochemical characteristics of different types of specimens was investigated in autoclaves containing oxygenated HTW. In these tests, unstressed coupon specimens were used to study the general corrosion behaviour of LAS. In order to study the

electrochemical behaviour under strained/stressed surface conditions, pre-strained C-ring specimens were used in addition to the coupon specimens in all exposure tests.

For this purpose a test rig and an auxiliary device for the specimens have been developed. The test facilities allow testing under simulated BWR conditions at different deliberately increased chloride concentrations with full environmental control. During testing, among others, the corrosion potential, electrochemical impedance behaviour and electrochemical noise characteristics of the tested specimens were recorded and evaluated, especially with respect to the effect of different chloride concentrations and chloride transients. After exposure to HTW, a number of different post-test investigations were performed including Scanning Electron Microscopy (SEM), Auger-Electron Spectroscopy (AES) and Time of Flight - Secondary Ion Mass Spectroscopy (TOF-SIMS) to study the effect of chloride on the oxide layer after testing.

Part 2: Crack Initiation

This part includes investigations on the effect of different amounts of deliberately added chloride concentrations on the crack initiation susceptibility of tensile specimens to which a continuously increasing strain was applied. Therefore, SSRT (Slow Strain Rate Tensile) also designated as CERT (Constant Extension Rate Tensile) tests were performed at different constant chloride concentrations and following chloride transients in once through refreshing autoclaves under simulated BWR conditions.

Derived from these test results and those of the electrochemical investigations, an improved understanding about the effect of chlorides on crack initiation were gained.

Part 3: Crack Growth Rate Testing

Based on the results of the electrochemical investigations and the crack initiation studies the final part of the experimental work of this thesis focuses on crack growth rate tests using 1 T-CT (CT 25) specimens (Compact Tension). In these tests special emphasis was laid on monitoring the effect of chloride transients and mechanical transients on crack initiation and crack growth rates. In particular, the dependence of crack growth rates on different chloride concentrations and mechanical loads is considered in discussions on the mechanistic aspects of CGR in LAS. In order to improve the understanding of chloride induced effects at the crack tip, a

device allowing so-called crack tip micro sampling was developed. By means of this technique it was possible to investigate the actual composition of the crack tip electrolyte, which is of importance to improve the understanding regarding the effects of chloride at the crack tip.

Finally, the results from all three phases are **summarized and discussed** with regard to potential effects of both temporary and long term increased chloride contamination levels on the general corrosion, crack initiation and environmentally assisted crack growth behaviour of LAS in oxygenated HTW. Special emphasis is laid on evaluating and assessing the effect of continuously increased chloride contamination levels and chloride transients in combination with mechanical load transients on crack initiation and propagation as a basis for improved assessment of component behaviour in power plant applications.

2. BACKGROUND AND LITERATURE REVIEW

This chapter summarizes the current state of the art and the research activities on the field of EAC of LAS in HTW during the last decades. Beginning with some general remarks on the nomenclature of SCC and EAC in the following paragraphs the focus is laid on the development of the current state of the art and mechanistic aspects regarding EAC of LAS. Finally, an overview on the corrosion and passivity of LAS is given, before the current state of the art regarding the effect of anionic impurities on the corrosion of LAS is summarized.

2.1 Environmentally-Assisted Cracking of Low-Alloy Steels

At temperatures above 100 to 150 °C a compact oxide film develops on the surface of LAS which prevents the surface from further general corrosion and is thereby acting as a protective layer for LAS that are in contact with HTW. At these temperatures the protective oxide layer develops by reaction with dissolved oxygen in oxygenated conditions (BWR conditions) and by direct oxidation of the LAS in conditions without dissolved oxygen in the HTW (PWR conditions). The developed oxide scale causes resistance of the material against both, general and localized corrosion in pure HTW, while the actual structure and characteristics of the oxide layer are depending on the given environmental conditions. The development and structure of these oxide films will be discussed in more detail in the following chapters. The conditions of concern in this work are oxygenated HTW conditions at a maximum temperature of about 288 °C and dissolved oxygen concentrations up to approx. 400 ppb.

The mechanism of corrosion assisted cracking of low-alloy steel in high-temperature water is often simply described as SCC (Stress Corrosion Cracking) or more general as EAC (Environmentally Assisted Cracking). Environmentally assisted cracking is depending on the conjoint occurrence of three different parameters:

- Material
- Environment
- Stress (Strain, Mechanical Load)

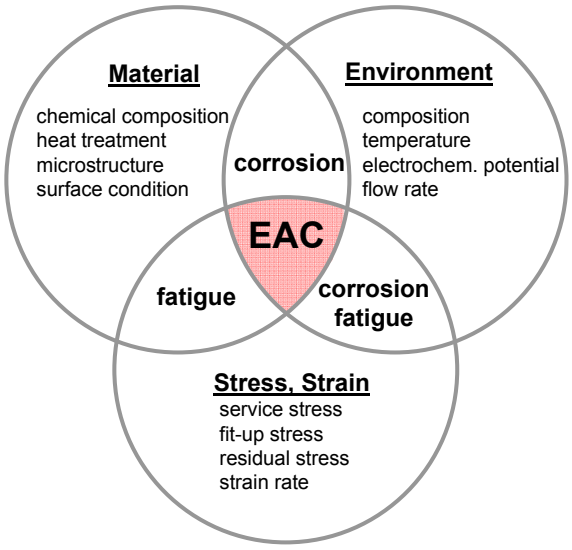

Figure 2: Conjoint conditions for material, environment, and stress as requirement for SCC as proposed by SPEIDEL (Speidel, 1984).

The correlation of the factors influencing the occurrence of SCC are probably best described as proposed by SPEIDEL et al. (Speidel, 1984) (see Figure 2).

Only if the values of all these parameters meet critical levels, EAC may occur. Therefore, EAC will only occur at a conjoint appearance of a critical environment (e.g. temperature, ECP, level of anionic impurities), a susceptible material condition (e.g. microstructure, heat treatment), and tensile stress (e.g. internal pressure, mismatch between pipes).

During the last decades, the EAC, and in particular the SCC crack growth behaviour of LAS in HTW was the topic of extensive research activities[2]. Therefore, the SCC behaviour of low-alloy steels can be designated to be comparatively well understood today. However, due to the large number of factors that influence environmentally assisted cracking, there are still some areas which remain the topic of on-going research activities.

[2] It has to be noted that the critical conditions for EAC in terms of general corrosion, SCC crack initiation and crack growth may be different for different corrosion systems and therefore always depend on a critical, conjoint occurrence of the three parameters shown in Figure 2 for a given corrosion system.

Also EAC is commonly used to refer to all types of SCC, this term does not necessarily describe the mechanism in enough detail in every case. For a detailed description of the observed cracking mode different nomenclatures have been proposed in the past. For LAS, the determination of the cracking mechanism is performed according to the type of mechanical loading (stress, strain conditions). It is distinguished between Stress Corrosion Cracking (SCC), Strain Induced Corrosion Cracking (SICC) and Corrosion Fatigue (CF).

As proposed by Staatliche Materialprüfanstalt (MPA) Stuttgart (Kussmaul et al., 1997) a differentiation may be performed by the local plastic deformation of the material, or component, respectively. Hence, the local strain rate at the surface of the component, respectively at the crack tip, is the major criterion for the description of the cracking mode (see Table 1). The local strain rate at the crack tip may not be directly observed by measurement at components in most cases. Therefore, this differentiation is difficult to handle for practical assessment.

Table 1: Overview on the arbitrarily defined cracking modes for low-alloy steels at the crack tip according to MPA Stuttgart (Kussmaul et al., 1997).

Designation	Type of mechanical load
Stress Corrosion Cracking (SCC)	Static Load $(d\varepsilon/dt)_{CT} = 0$ (until crack initiation)
Strain Induced Corrosion Cracking (SICC)	Static Load $(d\varepsilon/dt)_{CT} > 0$ (temporarily limited)
	Static Load or monotonically increasing $(d\varepsilon/dt)_{CT} > 0$ (permanently)
Corrosion Fatigue (CF)	Cyclic with high/low frequency $(d\varepsilon/dt)_{CT} > 0$

A slightly alternative differentiation that has been suggested by AREVA GmbH (former Siemens KWU) (Tenckhoff et al., 1990) and the PSI (Paul Scherrer Institute) is to differentiate the types of mechanical load that are applied to the component or the specimen in laboratory testing, respectively (see Table 2). Hence, this differentiation can be applied for description of cracking modes that are observed on components during plant operation. With this suggestion the transient free operation of components with predominantly constant load can be described as the condition under which SCC may be observed. On the other hand, for cyclic loading, the term Corrosion Fatigue is used for both, high- and low cyclic loading. Between CF and SCC, SICC involves conditions with slow, monotonically rising load, causing localized plastic deformation as it may occur during plant start-up and shut-down (Seifert et al., 2003, Seifert, 2002).

Table 2: Basic types of Environmentally Assisted Cracking of low-alloy steels according to PSI (Seifert et al., 2003, Seifert, 2002) .

Mechanism	Environmentally Assisted Cracking		
	SCC	SICC	CF
Type of loading	constant (static)	slow monotonically rising or very low-cycle	cyclic: low-cycle, high-cycle
LWR operation condition	transient-free, steady state power operation	start-up/shut-down, thermal stratification	thermal fatigue, thermal stratification
Characterization of crack growth	BWRVIP-60 lines	?	ASME XI Code Case N-643 (PWR)
Characterization of crack initiation	? $\sigma > YS$	susceptibility conditions: ECP_{crit}, $d\varepsilon/dt_{crit}$, ε_{crit}	ASME III KTA 3201.2 F_{en}-approach (acc. to Reg.-Guide 1.207)

2.2 Development of the Current Knowledge on EAC of LAS in HTW

LAS that are used in BWR and PWR primary circuits are usually not in direct contact to the reactor coolant. They are protected against erosion and corrosion using an austenitic stainless steel cladding. However, depending on the plant design, LAS in BWR´s can be in direct contact to the reactor cooling water. Especially feedwater pipes of some BWR´s are manufactured from unclad LAS (e.g. type 20MnMoNi55, 22NiMoCr 3 7, and 16Mo3). In addition, a local degradation of the austenitic cladding, leading to direct contact of LAS and primary coolant, is postulated e.g. for safety assessment of the RPV and other structural components.

2.2.1 Field Experience with Low-Alloy Steels in High-Temperature Water

During the last decades, some cracking incidents have occurred in operating components manufactured from LAS, like pressure vessels, steam generators, steam and feedwater pipings, condensate systems of BWR´s, feedwater nozzles of BWR RPV´s, deaerators, and steam turbine discs as reported by e.g. (Hickling and Blind, 1986, Kussmaul et al., 1986, Scott and Tice, 1990, Tenckhoff et al., 1990, Ford, 1992, Seifert et al., 2003, Seifert and Ritter, 2005a, Carter, 2003).

Most of those cases have occurred on carbon or LAS types SA333Gr6, SA106, SA304, A533Gr.B, A508 or their national equivalents (Ford, 1992). The cracking occurred in base metal, as well as weld filler metal and heat affected zones. The cracking mode was observed to be mainly transgranular in nature. In addition, particularly in Germany, SICC was observed in the high strength fine grained structural steels WB35 and WB36 (15 NiCuMoNb 5) that were widely used for construction of e.g. piping in BWR´s as well as feedwater tanks and heat exchangers in PWR´s (Hickling and Blind, 1986, Kussmaul et al., 1986).

Despite these reported failures, it can be summarized that no cracking incidents with a major contribution of SCC to the total crack advance in properly manufactured and heat treated LAS primary pressure-boundary components have occurred in operating plants so far, as reported by e.g. (Roth, 2005, Seifert and Ritter, 2005a, Seifert and Ritter, 2005b).

As reviewed by different authors, (Scott, 1985, Ford, 1992, Seifert and Ritter, 2005a, Hickling et al., 2005) cracking incidents in LAS have always been associated with various combinations of the following aspects:

- **Severe dynamic straining**
  e.g. cyclic loading due to thermal fluctuations during plant start-up/shut-down

- **High residual stress**
  e.g. due to localized post weld heat treatment, fit up deformation causing local stress raisers, SCC of austenitic or nickel-based cladding or weldments resulting in a significant stress intensity at interface between LAS and cladding

- **Highly oxidizing environment**
  e.g. due to Cu^{2+} cations or other anionic impurities like Cl^- or SO_4^{2-} or due to dissolution of MnS inclusions from the material

2.2.2 Current Knowledge of SCC-Crack Growth Rates of LAS in HTW

Despite the very good operating experience with LAS in HTW, some worrying crack growth rate data were published in the late 1980´s by SPEIDEL (Speidel and Magdowski, 1988). These data showed a spreading of crack growth rates for LAS reactor pressure vessel (RPV) materials over five orders of magnitude which caused controversial international discussions. Similar crack growth rate data were also reported by FORD (Ford, 1992, Ford et al., 1991) who summarised the data base on crack growth rates that were available in 1990. Taking the data reported by FORD and SPEIDEL et al. into account it seemed that under nominal operating conditions crack growth rates with up to 10^{-7} m/s (approx. 300 mm/yr) were possible (see Figure 3).

Due to the mismatch between the very good worldwide operating experience and the possible crack growth rates reported by SPEIDEL et al. further experiments and assessments of the data base that was available at that time were performed in the beginning of the 1990´s.

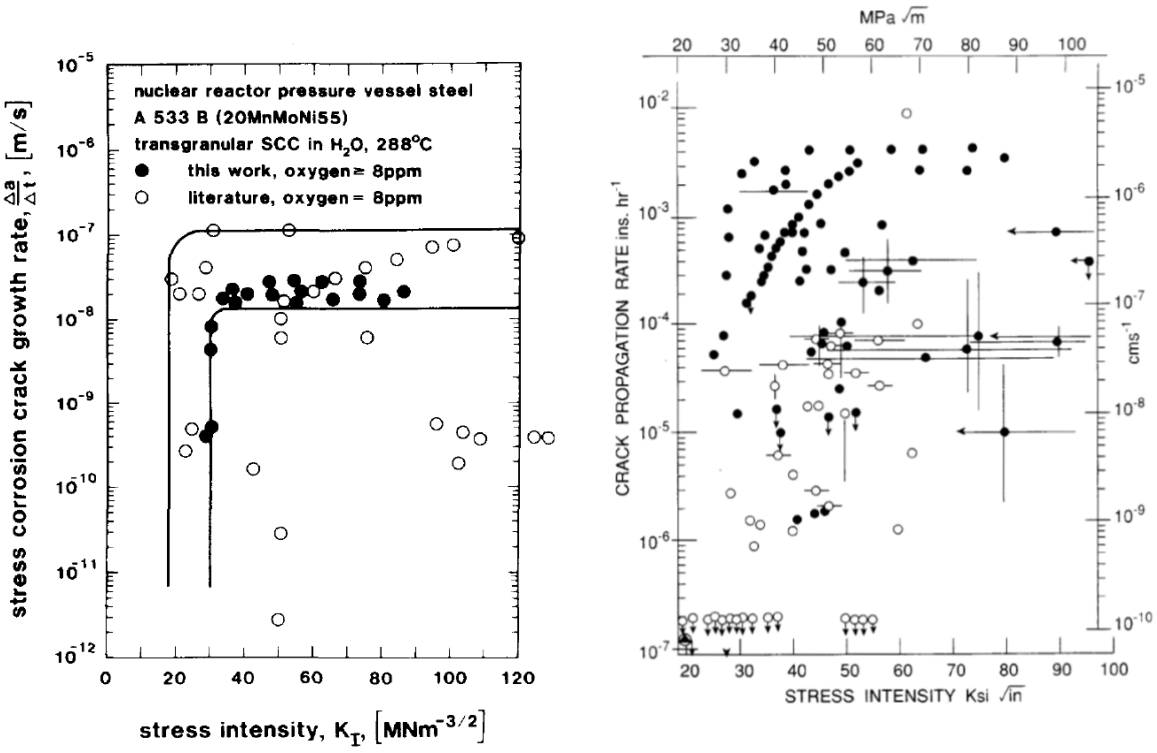

Figure 3: **Dependence of crack growth rate on the stress intensity factor K_I for low-alloy steel reactor pressure vessel material.**
(a) Crack growth rate data of low-alloy steel RPV material (A533 B) in oxygenated HTW, reported from SPEIDEL et al. (Speidel and Magdowski, 1988) for 288 °C and 8 ppm oxygen. (b) Summary of the available crack growth rate database in 1990 by FORD et al. (Ford et al., 1991). The crack growth rates were obtained using different types of low-alloy steels in oxygenated water at 288 °C. Full symbols were obtained at 8 ppm dissolved oxygen, open symbols at 200 ppb dissolved oxygen.

The assessment of crack growth rate data was performed by filtering data that did not meet the requirements for crack growth rate tests under testing conditions representative for BWR operating conditions. Especially results from tests that were not performed under constant load and without or with no sufficient monitoring of the environmental conditions during testing were filtered out and removed from the database. This procedure reduced the obtained crack growth rates both quantitatively and qualitatively. The remaining crack growth rates were all in the range below 3 mm/yr (~ $1{,}0 \cdot 10^{-10}$ m/s), see Figure 4 (Hickling, 1994, Roth, 2005).

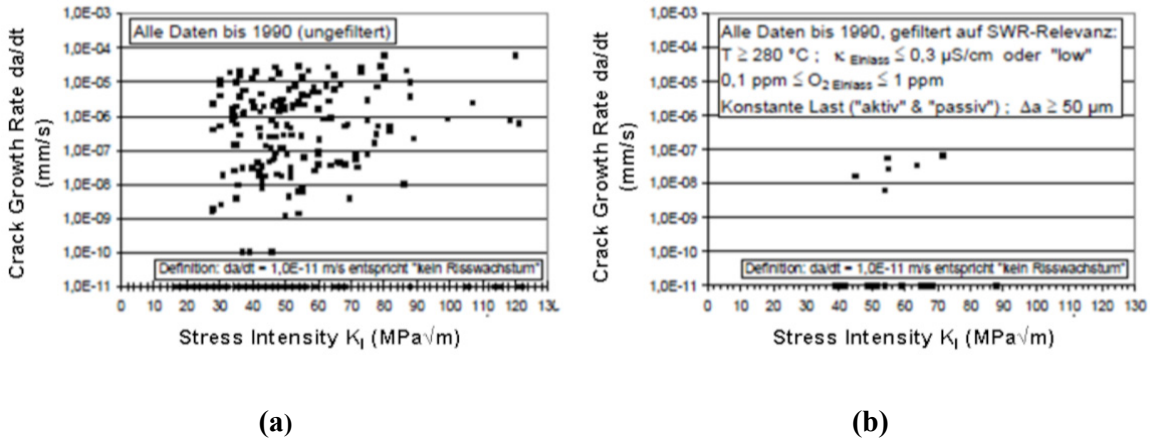

(a) **(b)**

Figure 4: **(a) Unfiltered results of the crack growth rate testing database by 1990. (b) Remaining crack growth rate testing data points after application of filtering of the testing results regarding BWR-relevant environmental conditions under constant load (Roth, 2005, Hickling, 1994).**

With regard to the topic of this thesis, it is important to mention here that one of the origins of the high crack growth rates reported by SPEIDEL may be attributed to the presence of halides, more precisely chlorides during testing. The chloride contamination may originate from the use of chloride containing reference electrodes during testing. Since the water chemistry was often not sufficiently or not at all monitored during some of the early crack growth rate tests, the presence of chloride during these tests cannot be ruled out. Therefore, based on recent research results (see Chapter 2.2.3) some of the reported, very high crack growth rates may also be explained by the presence of chloride contaminations during testing.

The results of the crack growth rate assessment described above is in good agreement with results that were reported by VAN DER SLUYS (Van der Sluys and Pathania, 1991) who investigated the crack growth rates of LAS in HTW with 200 ppb and 8 ppm dissolved oxygen, respectively. In their experiments they used the DCPD (Direct Current Potential Drop) technique to obtain the crack growth rate of LAS. The tested material showed no sustained crack growth rates above $1.0 \cdot 10^{-11}$ m/s. Crack growth rates above $1.0 \cdot 10^{-11}$ m/s were only observed in oxygenated (8 ppm) HTW at high K_I-values above 44 MPa√m. They furthermore found that the crack growth was intermittent and starting and stopping with no apparent reason. Therefore, they conclude, that continued crack growth may only be obtained when a critical crack tip elec-

trolyte is maintained by dissolution of MnS inclusions from the LAS at the advancing crack tip. If the equilibrium between the strain-rate at the advancing crack and dissolution of MnS is disturbed no further crack growth will be observed.

In addition to these tests, extensive crack growth tests were performed at the MPA Stuttgart in the 1990´s (Kussmaul et al., 1997, Läpple, 1996, Läpple and Deimel, 1994). These experiments were performed using Compact Tension (CT) 50 specimens manufactured from the two LAS 22 NiMoCr 3 7 and 20 MnMoNi 5 5 that are both used as RPV materials. The tests were performed under quasi stagnant HTW conditions at a temperature of 240 °C and electrical conductivities between 0.25 to 0.7 µS/cm. The tests were performed at high (8 ppm) and low (200 ppb) dissolved oxygen concentrations. During testing, the crack growth rate was determined using the crack mouth opening displacement (CMOD) technique. The crack growth rate obtained by CMOD during testing was corrected by the actual crack length that was obtained by fractography after the end of the crack growth rate testing.

For stress intensity factor (K_I) levels of $K_I < 60$ MPa√m the tests revealed no effect of K_I, steel sulphur content, and dissolved oxygen concentration on the crack growth rate of the investigated LAS. Furthermore, they observed a virtual decrease of the crack growth rate with increasing testing time under constant load. After the onset of cracking due to the increasing loading at the beginning of the test, a decrease in the crack growth rate and finally crack arrest (no further crack growth) was observed. Hence, this clearly indicated that crack growth is only limited to straining conditions during start-up of testing.

For K_I-levels 60 MPa√m < K_I< 75 MPa√m increasing, continuous crack growth was observed. The observed crack growth rate strongly depended on the stress intensity factor in this K_I-range, whereas, the observed change in the crack growth rate was independent of the oxygen concentration in the HTW and the steel sulphur content. At these K_I-levels the crack propagates during the whole testing period. However, as observed by the on-line CMOD measurement, the crack growth rate decreased with increasing testing time as a function of time but did not cease to zero.

For the highest investigated K_I-levels $K_I > 75$ MPa√m very high crack growth rates in the range of up to 10^{-7} m/s were observed (see Figure 5).

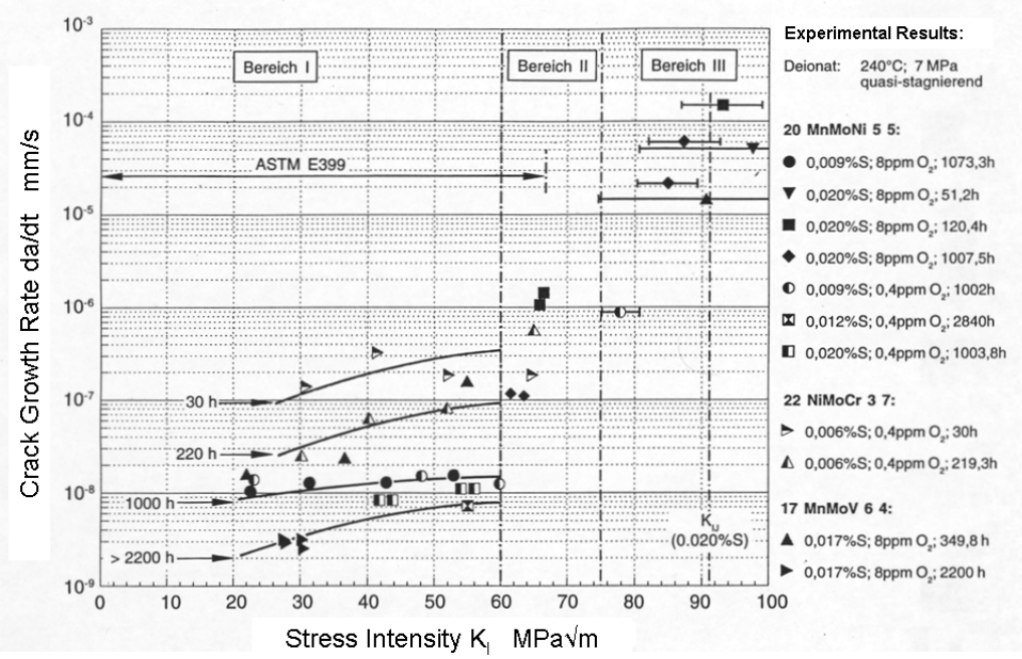

Figure 5: Crack growth rates of different low-alloy steels in oxygenated high-temperature water versus stress intensity factor (Läpple and Deimel, 1994).

Due to the still large scatter in crack growth rate data for LAS in the late 1990´s an international Round-Robin test was launched by a number of testing laboratories including MPA Stuttgart, Siemens KWU (now AREVA GmbH), PSI Villigen, and VTT Espoo (Blind et al., 1999). In the frame of this Round-Robin, crack growth rate tests were performed using the low-alloy fine grained structural steel 20 MnMoNi 5 5 (~ SA508 Cl.3) under identical, well defined and continuously controlled testing conditions in all participating testing laboratories (Temperature 288 °C, electrical conductivity at inlet 0.06 to 0.08 µS/cm, electrical conductivity at outlet 0.11 to 0.27 µS/cm, dissolved oxygen concentration at inlet 400 ppb).

During the experiments, the crack growth was measured on-line using the reversed direct current potential drop (DCPD) technique. Hence, crack growth during the experiments could be directly attributed to each testing phase. However, this was not possible in practice, since no crack growth was observed during the experiments by the DCPD signal. The slight crack growth that was observed after the end of the tests by fractography (e.g. about 20 µm for K_I = 25 MPa√m) most probably occurred during the initial straining of the specimen when in-

creased straining at the crack tip was implied during start-up. For the calculation of the crack growth rate, this crack advance was divided by the overall testing time, which still resulted in the low crack growth rates reported in Figure 6. For all testing laboratories the measured crack growth rates were below $1.0 \cdot 10^{-11}$ m/s up to a maximum stress intensity factor of $K_I = 70$ MPa√m. The authors therefore summarised that their testing results indicated that the large range in published crack growth rate data seems to be caused by the different experimental conditions in these crack growth rate tests (Blind et al., 1999).

In addition to this Round-Robin, extensive investigations on the crack growth behaviour of LAS were performed in Switzerland at the PSI in co-operation with the Eidgenössische Technische Hochschule (ETH) Zürich. MAGDOWSKY and SPEIDEL performed extensive testing regarding the factors influencing EAC of LAS and the resulting crack growth rates (Magdowski et al., 1994, Magdowski et al., 1995, Speidel and Magdowski, 1995). In their experiments they used actively loaded (constant load) 1 T-CT specimens and passively loaded (constant displacement) double cantilever beam (DCB) specimens. The experiments showed results similar to those reported by the MPA Stuttgart i.e. at stress intensity factors below $K_I = 60$ MPa√m they observed low crack growth rates (below $2.0 \cdot 10^{-8}$ m/s) indifferent of oxygen concentration and specimen size.

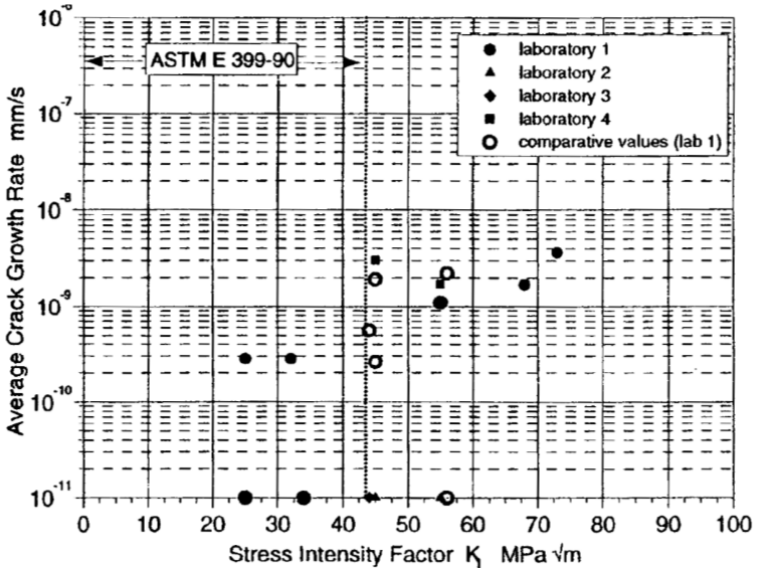

Figure 6: Results of an European Round-Robin investigating the crack growth rate of low-alloy steel 20 MnMoNi 5 5 under identical, well defined and continuously monitored environmental testing conditions in different laboratories (Blind et al., 1999).

These research activities were continued at the PSI mainly by SEIFERT and RITTER. In their investigations, using CT-specimens, stable crack growth was only observed for distinct, very aggressive combinations of electrical conductivity and oxygen concentration. In oxygenated HTW (DO = 200 to 8000 ppb, ECP = -50 to + 150 mV_{SHE}) almost instantaneous crack arrest was observed after switching to constant load at $K_I < 30$ MPa√m. For stress intensities between $K_I = 30$ MPa√m and $K_I = 60$ MPa√m only very localised cracking was observed, if cracking occurred at all. Sustained crack growth was only observed at $K_I > 60$ MPa√m but with still decreasing crack growth rates at longer testing times after switching to constant load. Even addition of up to 320 ppb sulphate (as Na_2SO_4 or H_2SO_4) did not remarkably accelerate the crack growth under both, PPU (Periodical Partial Unloading) and CL (Constant Load) conditions up to stress intensities of 60 MPa√m. In contrast to these results already very low concentrations of chloride in the range of 5 to 15 ppb chloride resulted in fast SCC crack growth down to stress intensity factors of 20 MPa√m in tests with PPU (Seifert and Ritter, 2008b). The effect of chloride on SCC crack growth rates is discussed in more detail later in this chapter.

As depicted in Figure 7, the test results of the PSI were also in good agreement with the Disposition Lines that were published in the frame of the US BWR-VIP Project for transient-free stationary power operation (Ford et al., 1999) (Seifert et al., 2004) (Hickling et al., 2005).

The research activities on the EAC of low-alloy steel e.g. focussing on the effect of anionic impurities and cyclic loading (e.g. ripple loading and environmentally assisted fatigue – EAF) were continued at the PSI up to today, as described in more detail later (e.g. (Ritter and Seifert, 2008b, Seifert and Ritter, 2008a, Ritter and Seifert, 2003, Ritter and Seifert, 2004b, Seifert et al., 2004)).

Since the discussion regarding the quality of crack growth rates obtained in laboratory tests and especially their practical relevance still went on during the late 1990´s, a research program named CASTOC (Crack Growth Behaviour of Low Alloy Steels for Pressure Boundary Components under Transient Light Water Reactor Operating Conditions) was launched that was sponsored by the European commission and in which several European research laboratories participated (Ehrnsten et al., 2003, Ernestova et al., 2004, Roth et al., 2005, Föhl et al., 2004).

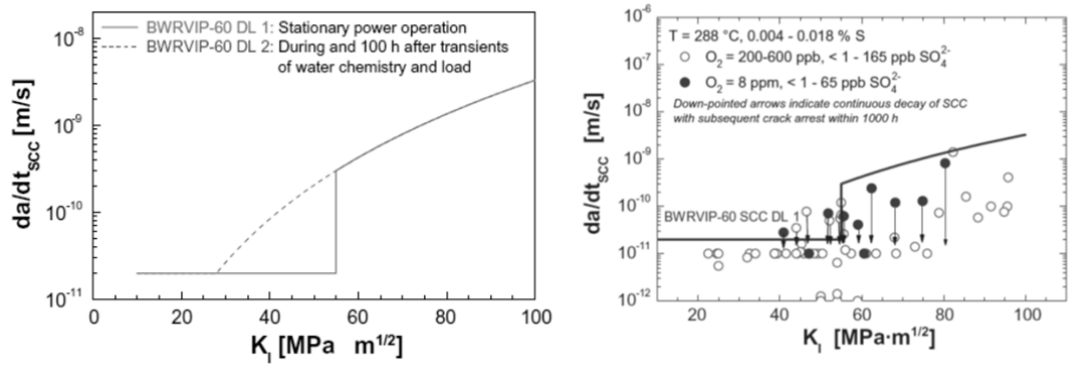

(a) **(b)**

Figure 7: **(a) BWRVIP-60 disposition lines for crack growth rates of low-alloy steels in oxygenated high-temperature water (Ford et al., 1999).**
(b) Confirmation of the conservative character of the BWRVIP-60 disposition line for stationary, transient free power operation (constant load testing in high-purity oxygenated high-temperature water (Seifert and Ritter, 2008b).

In this project, the procedure of the crack growth tests was changed to meet the often raised criticism regarding the practical relevance of laboratory crack growth rate tests. In former tests, CT-specimens were fatigue pre-cracked in air, assembled into the autoclave and CGR-testing was started after adjustment of the environmental conditions without further "activation" of the crack growth in HTW.

The criticism to this technique was that it might be possible that the crack initiation time exceeds the actual testing time and the observed crack advance would therefore only occur during the initial straining of the specimens.

Therefore, in the experiments of this testing program, an actively growing SCC-crack under HTW conditions was established at the beginning of the test. Thus, the following testing procedure was applied in all CGR-test:

Prior to testing in HTW the CT-specimens were fatigue pre-cracked in air. Unlike to prior crack growth rate tests, within this research project the crack growth rate testing in the HTW started with cyclic loading of the investigated specimens. The loading of the specimens was switched to constant load only after the crack had started to grow as revealed by measurement

of the crack extension using the DCPD-technique. This procedure ensured the existence of an actively growing crack and thereby the development of a critical crack tip environment. During all experiments in oxygenated HTW (temperature 288 °C, dissolved oxygen concentration at inlet 400 ppb, electrical conductivity at inlet < 0,08 µS/cm) of this program the crack growth almost immediately ceased after switching to constant loading conditions at stress intensity factors between K_I = 30 MPa√m and K_I = 58 MPa√m (Ehrnsten et al., 2003, Ernestova et al., 2004, Föhl et al., 2004), see Figure 8.

Therefore, from these investigations it can be concluded that even for actively growing cracks, crack arrest is immediately observed after switching to constant loading conditions up to high stress intensity factors (up to K_I ~ 60 MPa√m).

Another topic of world-wide research activities during the last years was the so-called dynamic strain aging (DSA) of LAS. First indications of the DSA phenomena were observed by ATKINSON and YU (Atkinson and Yu, 1997). More detailed investigations on DSA-effects were performed by HÄNNINEN et al. (Hänninen et al., 2001), ROTH et al. (Roth et al., 2003), DEVRIENT (Devrient, 2007, Devrient et al., 2007), and SEIFERT et al. (Seifert and Ritter, 2005a) in the last decade.

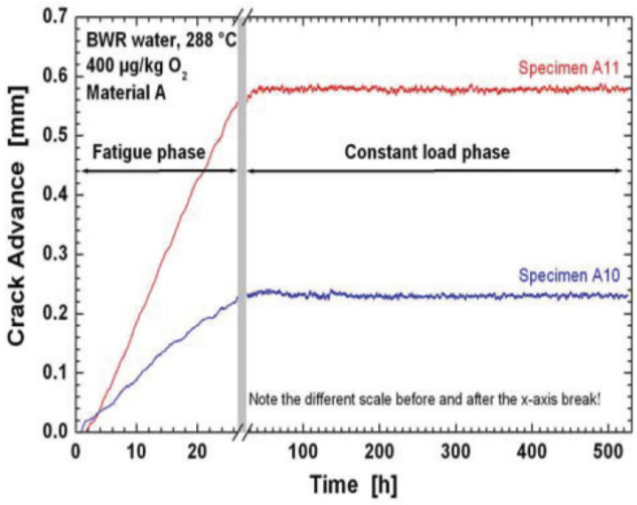

Figure 8: Crack advance according to DCPD signal versus time, showing the cessation of crack growth after switching from cyclic to static loading in oxygenated high-temperature water (Roth et al., 2005).

The first experimental results that showed a correlation between DSA and SCC cracking of LAS were published by SEIFERT et al. (Seifert et al., 2003). They reported laboratory results showing that DSA is an important factor influencing the EAC of low-alloy steels in the temperature range between 150 °C to 300 °C, see Figure 9.

The main material parameter affecting the DSA of low-alloy steels is discussed to be the content of free interstitials, mainly nitrogen. The DSA susceptibility was shown to depend on a critical combination of temperature and strain-rate, whereas the observed SCC susceptibility seems to mainly result from the reduced plasticity of DSA-susceptible materials. As proposed by RITTER et al. (Ritter and Seifert, 2004a) DSA may result in higher crack-tip strain and an inhomogeneous localisation of deformation and thereby an increased dislocation density. This in terms may result in a reduction of the local fracture toughness.

The effect of DSA on EAC of LAS was investigated in detail by DEVRIENT et al. (Devrient, 2007, Devrient et al., 2007). These investigations revealed that DSA significantly affects the EAC behaviour of DSA-susceptible materials. The results of DEVRIENT showed that the reduction of the macroscopic plasticity originates from localized plastic deformation, since the number of active slip bands is reduced by the interstitial nitrogen. This causes a localized, severe rupture of the oxide layer at active slip bands with larger slip steps, thus resulting in increased crack initiation and crack growth at active slip bands due to the pronounced, localized rupture of the protective oxide layer. For LAS with a high susceptibility to DSA it has been observed, that crack advance under constant loading conditions may be strongly influenced by localized plastic deformation. Experiments performed by DEVRIENT et al. revealed that crack advance enhanced due to significant cumulative strain in small material volumes at the crack tip region. Hence, local film rupture at the crack tip is significantly facilitated by DSA (Devrient et al., 2009).

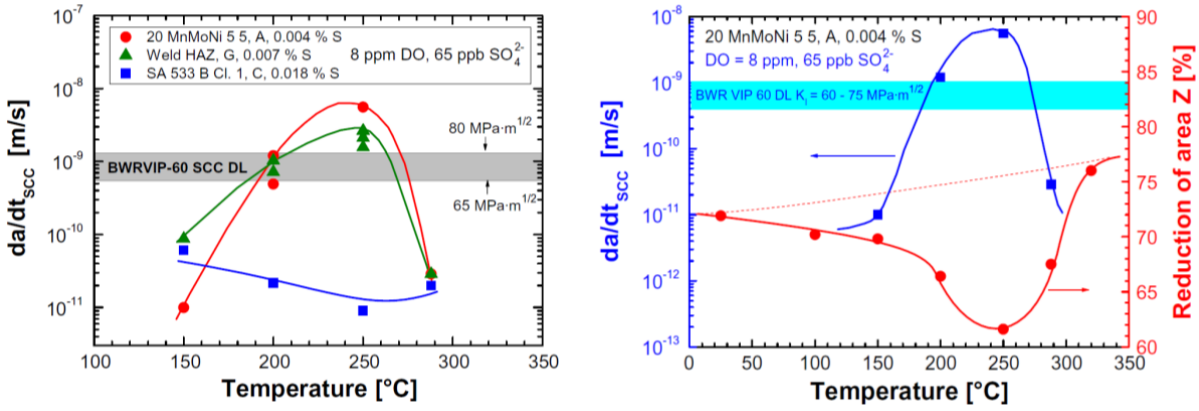

(a) **(b)**

Figure 9: **(a) Effect of temperature on the crack growth rates of different low-alloy steels (Seifert et al., 2008).**
(b) Coincidence between maximum SCC CGR and DSA susceptibility as revealed by the reduction of area Z depending on testing temperature (Seifert et al., 2003).

2.2.3 Effect of Anionic Impurities on the SCC Behaviour of Low-Alloy Steels

Another, very recent topic of international research activities is the effect of anionic impurities, in particular sulphate and chloride on the crack growth rate of LAS in HTW. The effect of increased chloride levels on EAC of LAS was not investigated in detail in the past, because it was thought not to be of major importance compared to the effect of sulphate.

Also, nearly 30 years ago, first indications on detrimental effects of small amounts of chloride impurities (in the ppm range) on the crack SCC susceptibility of LAS were observed in oxygenated HTW (Choi et al., 1983), the main focus regarding the effect of contaminations was laid on the sulphur concentration, resulting from the dissolution of MnS in the material and also from the environment in the past. This was for example considered by the definition of the so-called low- and high-sulphur lines that are used for calculation of the theoretical crack propagation in low-alloy steels according to the FORD-ANDRESEN Model (Ford, 1992).

In the 1990´s crack growth experiments were performed at different levels of anionic impurities in the frame of the CASTOC project. Within these experiments the effect of both, increased sulphur and increased chloride concentration was investigated using CT-specimens (Roth et al., 2005).

In experiments with increased sulphate concentrations, no enhanced crack growth was observed although the sulphate concentrations were increased up to an electrical conductivity of the test environment of 1400 µS/cm.

The effect of increased chloride concentrations was investigated in a CGR test with 8000 ppb oxygen using the PPU-technique. After increasing the chloride concentration to 50 ppb chloride the crack growth rate increased after an incubation period of approx. 3 hours ($R^3 = 0.7$, $K_{I,max} = 67$ MPa√m) during a constant load phase between two partial unloadings (see Figure 10 a). After switching back to high-purity water conditions the crack growth rate decreased to the same levels as observed before the chloride transient within approx. 24 hours. This result

[3] R is the ratio between minimum and maximum load that is applied to the specimen during testing.

indicated that there seemed to be no drastic memory effect of the temporarily increased chloride concentration.

Based on these first results within the CASTOC project the effect of chloride on the crack growth rate of LAS was investigated in more detail at the PSI (Ritter and Seifert, 2004b, Seifert and Ritter, 2008b). A test at a chloride concentration of 20 ppb (T = 288 °C, DO = 8 ppm) under pure constant load showed no accelerating effect of the increased chloride concentration under purely constant load (up to 241 hours with 20 ppb chloride). After a single partial un- and re-loading (R = 0.7) onset of crack growth was observed in the specimens (see Figure 10 b). After returning to high-purity water conditions, the crack growth rate slowed down again depending on the investigated material. The observed crack growth rate in a high-sulphur material did not return to the same levels as before the transient, whereas the crack growth rate of a low-sulphur specimen slowed down again within approx. 35 h after the end of the transient.

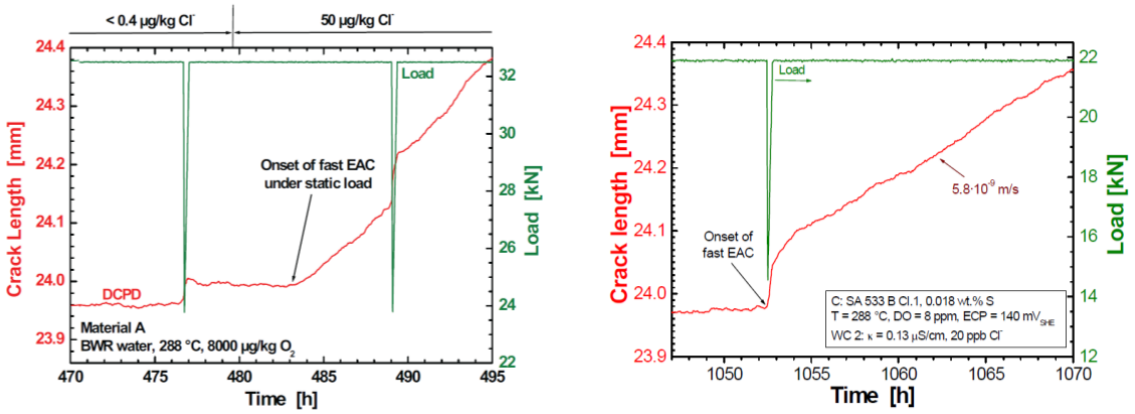

(a) **(b)**

Figure 10: **(a) Initiation of fast crack growth in a C(T)25 specimen during a phase of constant, static load between two PPU unloadings during a 50 ppb chloride transient (T = 288 °C, DO = 8000 ppb) (Ritter and Seifert, 2004b, Roth et al., 2005).**
(b) Crack length versus time for a crack growth rate experiment with a chloride concentration of 20 ppb chloride indicating that crack growth starts after a single unloading (R = 0.7) 241 hours after the chloride concentration was increased to 20 ppb (Ritter and Seifert, 2004b).

In addition to the 20 ppb chloride experiment another CGR-test was conducted at a chloride contamination level of 10 ppb (T = 288 °C, DO = 400 ppb). In this experiment no crack growth was observed during the first 24 hours after increasing the chloride concentration to 10 ppb at constant load. Therefore, like in the 20 ppb chloride test, a single unloading and reloading was performed (R = 0.5). This single unloading and reloading resulted in an increase of the measured crack growth rate (see Figure 11 a). After the end of the transient the crack growth rate slowed down to similar values as before the transient. It has to be noted that the crack growth rate remained one order of magnitude above the rate obtained prior to the chloride transient even 300 hours after the end of the 10 ppb chloride transient.

Finally, the correlation between chloride concentration and the ECP was investigated. In these experiments the environmental conditions were changed from oxygenated conditions (approx. 400 ppb oxygen) to hydrogenated conditions (150 ppb hydrogen), causing a decrease of the ECP from approx. 100 mV_{SHE} to approx. - 550 mV_{SHE}. These experiments revealed that the critical chloride concentration for the onset of SCC clearly increased with decreasing ECP (Ritter and Seifert, 2009). Soon after the reduction of the corrosion potential from approx. 100 mV_{SHE} to about -550 mV_{SHE} the crack growth rates clearly slowed down (see Figure 12).

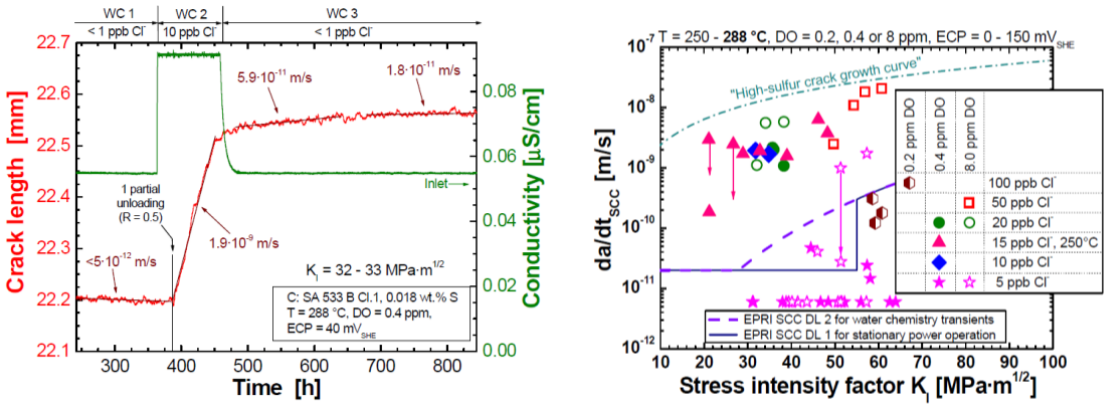

(a) **(b)**

Figure 11: (a) Crack growth rate before, during and after a 10 ppb chloride transient. (b) Comparison of SCC crack growth rates during chloride transients under BWR NWC conditions with EPRI SCC disposition lines (Ritter and Seifert, 2009).

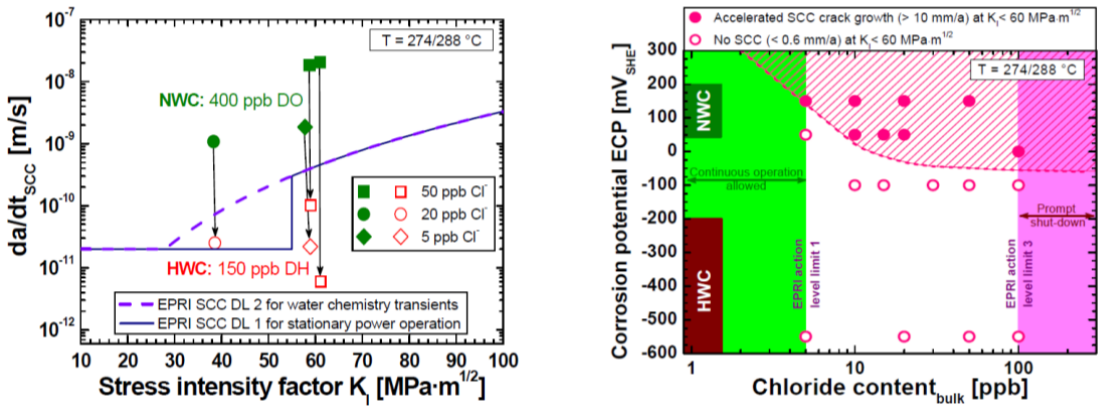

(a) **(b)**

Figure 12: **(a) Effect of ECP on the crack growth rate during chloride transients (Note: The ECP was decreased by changing from oxygenated (400 ppb DO) to hydrogenated (150 ppb DH) water chemistry conditions. This decreased the ECP from about 100 mV_{SHE} (oxygenated conditions) to – 550 mV_{SHE} (hydrogenated conditions) (Ritter and Seifert, 2009).**
(b) Susceptibility area for onset of chloride induced SCC of low-alloy steels depending on chloride concentration and corrosion potential (Ritter and Seifert, 2009).

The effect of increased chloride concentrations on the crack growth behavior in the transition region between alloy 182 weld material and LAS was investigated by PENG et al. in the frame of a co-operation between the PSI and the Tohoku University (Peng et al., 2005, Seifert et al., 2008). The experiments were performed at 288 °C at different oxygen concentrations using CT-specimens. The crack tip of the CT-specimens was initially positioned in the alloy 182 material in front of the transition line between alloy 182 and LAS. Prior to the deliberate increase of the level of anionic impurities, the inlet conductivity was below 0.07 µS/cm. During all experiments in high-purity water, and even with sulfate levels up to 30 ppb sulfate, the cracks stopped at the fusion line between alloy 182 and the LAS. In contrary to these results, prolonged crack growth across the fusion line and into the LAS was experienced at chloride concentrations of 50 ppb chloride under both, PPU and constant loading of the specimen.

These results were also confirmed by experiments of KUMAGAI et al. (Kumagai et al., 2009). They performed crack growth rate tests using CT-specimens taken from the transition region between alloy 182 and LAS with the crack tip positioned in the alloy 182 adjacent to the transition line with the LAS. They also found no crack growth into the LAS for stress intensity fac-

tors up to 50 MPa√m and a sulphate concentration up to 30 ppb. For a chloride level of 5 ppb and a stress intensity of K_I = 30 MPa√m their experiments revealed that the crack continued to grow across the transition line into the LAS. From these results, they proposed disposition lines regarding the conjoint effect of stress intensity and the level of anionic impurities on the crack growth in the transition region between alloy 182 and LAS (see Figure 13 a). The latest results regarding the effect of chloride on crack growth behavior in the transition region between alloy 182 and LAS have been published by SEIFERT et al. (Seifert et al., 2013). They confirmed that cracks do not cross the fusion line under high-purity water conditions up to very high K_I values (up to approx. 60 MPa√m). For chloride containing HTW, they showed that crack growth crossing the fusion line extending into the LAS seems to be possible down to very low K_I values of approx. 20 MPa√m and low chloride concentrations of down to 10 ppb chloride. Under BWR/HWC and PWR conditions, the tolerance to increased chloride concentrations is obviously much higher, since no effect of chloride with respect to SCC was observed up to K_I values of 60 MPa√m and chloride concentrations up to 100 ppb. Derived from these results they modified the disposition lines for the correlation of K_I and chloride concentrations proposed by KUMAGAI et al. as shown in Figure 13 b.

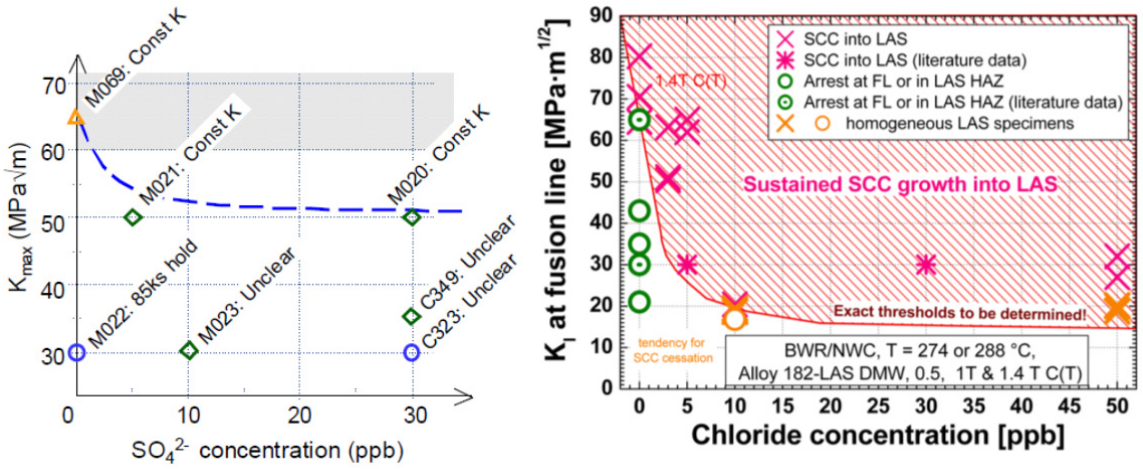

(a) **(b)**

Figure 13: Suggested disposition lines for crack growth into low-alloy steel depending on the stress intensity factor at different (a) sulphate (Kumagai et al., 2009) and (b) chloride injected environments (Seifert et al., 2013).

The observed behavior is in good agreement to the field experience, where SCC cracking also stops at the transition line between alloy 182 and LAS under static loading conditions in chloride free environments (Seifert et al., 2013). For increased chloride contaminations and high stress intensity factors, however, crack growth crossing the fusion line and sustained crack growth into the LAS cannot be fully ruled out (Ritter and Seifert, 2012, Seifert et al., 2013).

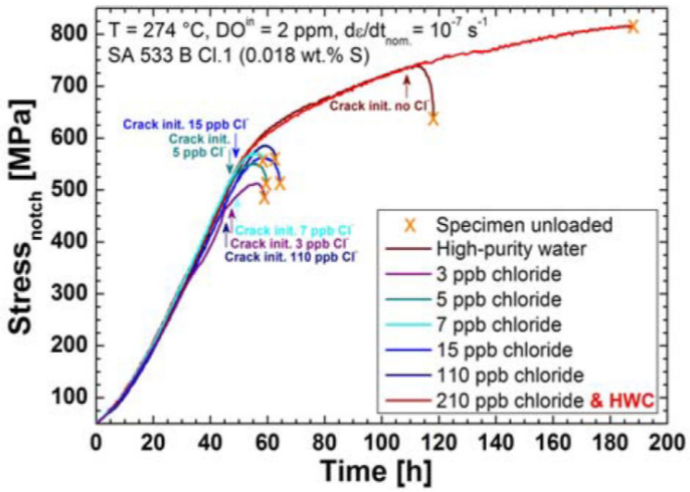

Figure 14: Effect of chloride on the crack initiation in oxygenated HTW (Ritter and Seifert, 2011).

Investigations on the effect of chloride on the crack initiation susceptibility of LAS in oxygenated HTW revealed that down to a concentration of 3 ppb, EAC initiation occurred at lower strains compared to tests performed in high purity water (see Figure 14). The initiation strains for chloride concentrations of 3, 5, 7, and 15 ppb were rather similar, indifferent of the chosen chloride concentration, and only slightly higher in a test with 110 ppb chloride (Ritter and Seifert, 2011).

In contrast to earlier published data by RITTER and SEIFERT, crack growth rate tests performed by HERTER et al. showed that chloride transients did not cause crack initiation by SCC under constant loading with up to 50 ppb chloride and K_I up to 50 MPa√m (Herter et al., 2013). If load transients were performed in chloride containing environments, significant, SCC-

induced crack growth was induced in their experiments, indicating that the conjoint occurrence of mechanical loading and increased chloride concentrations is needed to initiate SCC crack growth in oxygenated HTW. A memory effect with regard to preceding chloride transients was not observed in their experiments (Herter et al., 2012, Herter et al., 2013).

Based on the first published laboratory test results, the question arose, how such chloride contaminated environments might affect the EAC-behavior of plant components. Therefore, it is the aim of this thesis to systematically study the effect of increased chloride concentrations on the general corrosion and the SCC behavior of LAS in oxygenated HTW.

2.3 Mechanistic aspects of EAC of LAS

The preceding chapter described the current field experience and some recent fields of investigative research activities with regard to EAC of LAS. The following chapters will focus on the proposed crack growth mechanism and the most important factors that are influencing the crack growth of LAS in HTW.

2.3.1 Factors influencing EAC of LAS

As it has already been described in the preceding chapter, EAC, in particular SCC, is governed by a complex interaction of material, environment and loading conditions. The most important influencing factors for EAC of LAS will be briefly described in this chapter.

- **Material parameters**

The sulphur content of the steel, the type (chemical composition), size, morphology and spatial distribution of the MnS inclusions are material parameters that have the most important effect on SCC or SICC susceptibility of LAS in HTW (Atkinson and Forrest, 1985, Atkinson et al., 1996, Combrade et al., 1989, Bulloch and Atkinson, 1992).

Different results have shown that both, EAC initiation and also EAC growth are affected by the presence of MnS inclusions (Hänninen et al., 1987, Scott and Tice, 1990, Shoji et al., 1988, Van der Sluys, 1993, Rippstein and Kaesche, 1989). The effect of the steel´s sulphur content is synergistic with different environmental parameters like the sulphur anion concentration in the bulk environment, the electrochemical corrosion potential (in terms of dissolved oxygen concentration), the flow rate, temperature, and pH (Congleton et al., 1985, Choi et al., 1982, Lenz et al., 1988).

On smooth specimens, it has been shown that pitting often occurs at MnS inclusions which intersect the steel surface (Ford and Scott, 2008, Choi et al., 1982, Congleton et al., 1985). In addition to the effect of MnS inclusions, different experiments revealed that pitting is strongly favoured under highly oxidizing conditions, at low temperatures and low flow. Hence, crack initiation may take place at pits and not at MnS inclusions and the role of MnS inclusions is therefore less pronounced under these conditions (Rippstein and Kaesche, 1989, Weinstein, 1982). From a mechanical point of view it seems that the development of a multiaxial stress

state caused by local surface flaws is acting as a driving force for crack initiation in addition to any environmentally assisted effects.

Since MnS is preferably dissolved under HTW conditions, the dissolution of MnS strongly affects the electrolyte at the crack tip of actively growing cracks. Due to the dissolution of MnS and the according generation of e.g. sulfates this dissolution, among other factors, plays a vital role in the creation of an aggressive crack tip electrolyte (Hänninen et al., 1988, Van der Sluys and Pathania, 1991, Ford and Andresen, 1989b).

Special focus on the effect of sulphur on the crack growth rate and the composition of the crack tip electrolyte has been laid in different investigations which focused on the composition of the crack tip electrolyte. These investigations are described in more detail in chapter 7 which is focusing on the effect of chloride on crack growth, and in particular on the composition of the crack tip electrolyte (Andresen and Young, 1995b, Andresen and Young, 1995a, Lee and Shoji, 1999, Young and Andresen, 1995).

Different laboratory investigations in oxygenated HTW at 288°C showed no effect of the steel sulphur content on the SCC crack growth rate up to K_I values of approx. 60 MPa√m. Furthermore it was revealed that increased sulphur concentrations in the bulk medium have no detrimental effect on the crack growth rate of high sulphur materials under high mechanical loading conditions (Seifert and Ritter, 2008b, Seifert and Ritter, 2003).

Another material related topic that has been recently investigated in detail is the dynamic strain aging (DSA). The main material parameter DSA of LAS is discussed to be the content of free interstitials, mainly nitrogen and the thereby caused reduced plasticity of DSA-susceptible materials (Devrient, 2007, Devrient et al., 2007, Devrient et al., 2009). Details regarding the occurrence and effects of DSA are summarized in chapter 2.2.2.

In addition to this, the yield strength and hardness of the material also have to be considered. Little or even no effect of the yield strength and hardness of the material have been reported for hardness values below approx. 300 HV5 and yield strength values below approx. 700 MPa (Seifert and Ritter, 2008b).

Contrary to that, crack growth rates exceeding the BWRVIP-60 line are possible if critical hardness and yield strength values are surpassed. These critical levels are in the range of 350 HV5 and 800 MPa. For hardness values above 450 HV5 even the "high-sulfur" line can be exceeded (Seifert and Ritter, 2008a, Seifert and Ritter, 2008b).

- **Loading conditions**

As described in chapter 2.1 (Table 1 and Table 2), three different types of EAC have to be considered regarding the effect of loading conditions on the EAC behavior of LAS:

These three types are Stress Corrosion Cracking (SCC), Strain Induced Corrosion Cracking (SICC), and Corrosion Fatigue (CF). For initiation of both, SCC and SICC a slow, positive strain rate in the plastic strain region is generally necessary. In general it can be summarized that the SICC susceptibility is increasing with decreasing strain rates at a given environment and material combination. The susceptibility region for SCC crack initiation lies at strain rates between 10^{-4} and 10^{-7} s^{-1} furthermore depending on different environmental parameters. The maximum susceptibility to SCC crack initiation in HTW has been observed at a strain rate of 10^{-6} s^{-1} (Lenz and Wieling, 1986b, Lenz and Wieling, 1986a). At higher strain rates (above approx. 10^{-4} s^{-1}), pure mechanical ductile crack growth is dominating and corrosion assisted crack growth is less important. If a strain rate threshold below 10^{-7} s^{-1} exists is not fully clear at the moment since so far only little experimental work has been performed under these extremely low strain rates (Seifert, 2002). Experiments performed by GLADEN indicate a decrease of the SCC/SICC susceptibility at strain rates below 10^{-7} s^{-1} (Gladen and Kaesche, 1994). A very comprehensive description of the correlation between critical parameters of oxygen concentration, temperature, and strain rate was compiled by LENZ et al. (Lenz and Wieling, 1986b) (see Figure 15).

The critical strains for crack initiation typically lie in the range of 1 % to 5 % depending on strain rate, electrochemical corrosion potential, temperature, steel sulphur content, surface condition, and concentration of ionic impurities in the bulk medium (Congleton et al., 1985, Shoji et al., 1988, Lenz and Wieling, 1986b). As revealed by RIPPSTEIN, crack initiation only occurs beyond approx. 95 % of the ultimate tensile strength (UTS) (Gladen and Kaesche, 1994, Rippstein and Kaesche, 1989). Tests with pre-loaded, smooth tensile specimens revealed no crack initiation at specimens loaded below the high-temperature yield strength, if the speci-

mens were exposed to high-temperature water before cessation of low-temperature creep. Pre-cracked specimens that were exposed to high-temperature water after cessation of low-temperature creep showed no further crack advance, which again visualizes the importance of a slow rising load as a precursor for SCC crack initiation (Kussmaul et al., 1997). KUNIYA et al. furthermore revealed that LAS was only susceptible to SCC when the applied stress level was above 2 Sm[4]. In their tests using uniaxial constant load (UCL) specimens, SCC did not initiate at stress levels below 2 Sm. Furthermore, their experiments showed that SCC initiated at corrosion pits, and a correlation between SCC susceptibility and the number of pits has been observed (Kuniya et al., 1985).

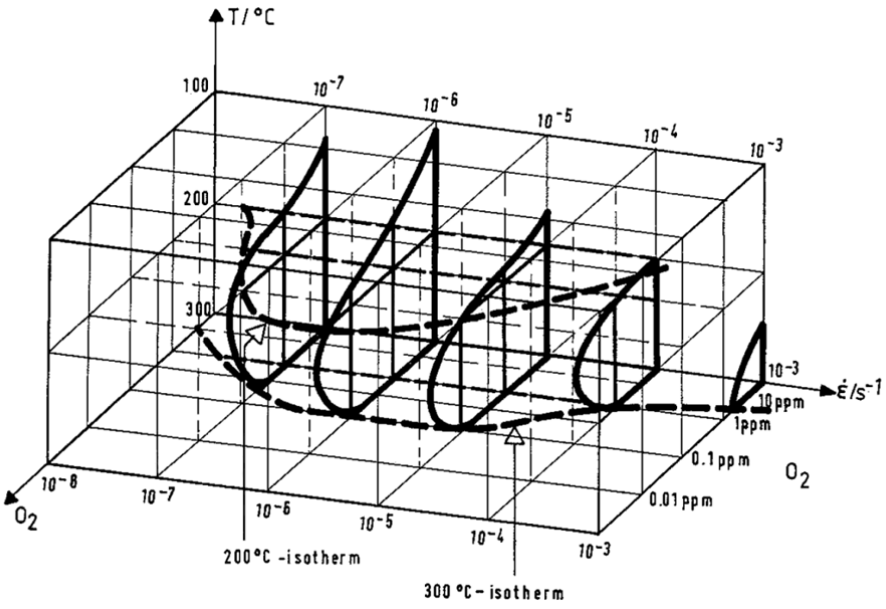

Figure 15: Range of susceptibility to SICC of low-alloy steels versus temperature, dissolved oxygen concentration, and strain rate according to LENZ (Lenz and Wieling, 1986b).

As reported by e.g. RIPPSTEIN, crack initiation typically occurs at loads close to the ultimate tensile strength of the material, even if a monotonically increasing strain is applied (Rippstein

[4] Sm is defined as design stress intensity in the nuclear codes and can be calculated depending on the used code and material type. For the investigated low-alloy steel the Sm can be calculated to be 184 MPa at 288 °C.

and Kaesche, 1989). These results are also confirmed by CERT-tests performed by RITTER and SEIFERT. They monitored the crack initiation by application of EN-monitoring. These tests also revealed crack initiation close to the tensile strength at the given testing temperature (Ritter and Seifert, 2011).

- **Environmental conditions**

The most important environmental conditions regarding EAC in HTW are temperature, dissolved oxygen concentration, pH, flow rate, and the amount of anionic impurities. Those parameters influence the corrosion potential of the material exposed to HTW. Regarding the system LAS in oxygenated HTW, the oxygen concentration and the temperature are particularly important because these parameters are the main parameters influencing the corrosion potential of LAS.

An overview of the corrosion potentials at different temperatures and oxygen concentrations is given in Figure 16 (Läpple, 1996). This figure reveals a shift of the corrosion potential to more positive values with increasing oxygen concentrations at a given temperature. Furthermore, a steep transition from low to high potentials is observed between approx. 10 and 100 ppb oxygen. For oxygen concentrations above approx. 200 ppb the corrosion potential of LAS reaches a plateau which lies between -100 and 100 mV_{SHE}, furthermore depending on temperature and flow conditions (Läpple, 1996).

Apart from temperature and corrosion potential, an important role regarding the corrosion behaviour of LAS is also being played by anionic impurities as e.g. sulphur or chloride. These ionic impurities may influence the electrical conductivity or the pH or alter the corrosion processes of the oxide layer and therefore play a significant role regarding the stability of the protective oxide layer formed on the surface of the LAS (Congleton et al., 1985).

Special emphasis on the effect of the environmental conditions on the corrosion behaviour of LAS in HTW water will be laid in chapter 2.4.2.

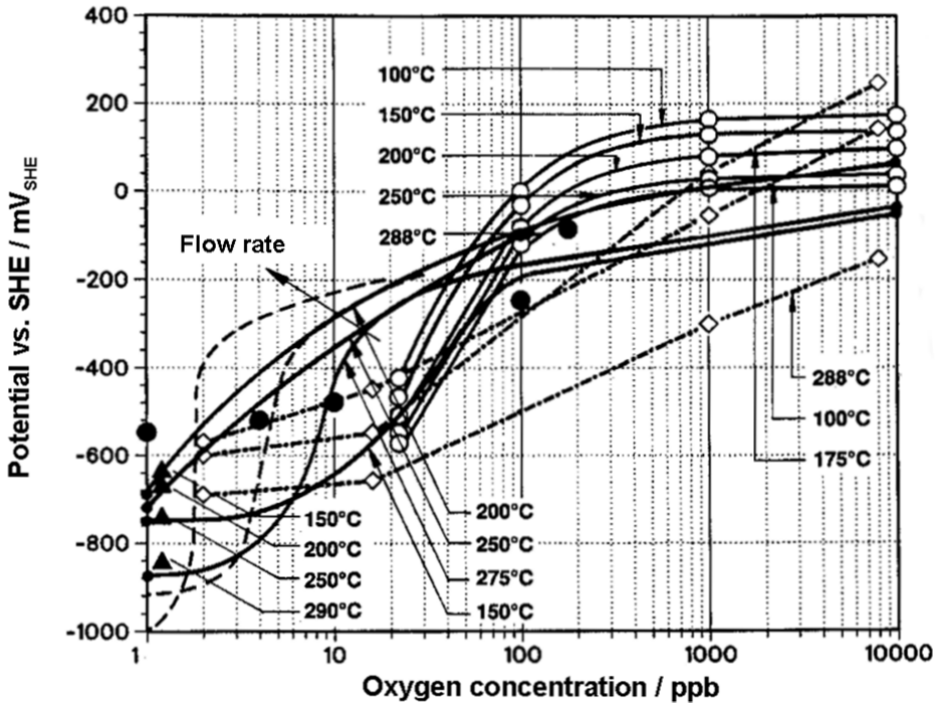

Figure 16: Correlation between oxygen concentration and the corrosion potential of low-alloy steels at different temperatures (Läpple, 1996).

2.3.2 Crack Growth Mechanisms

In this chapter, the most popular and accepted crack growth mechanisms for LAS in HTW will briefly be described. Before going into details of the crack growth mechanisms that have been proposed in the literature, the vital pre-cursor for SCC has to be discussed. The first criterion for SCC to occur is that the material has to be protected against general corrosion by a protective layer, e.g. a passive layer that may form at room temperature or a high-temperature oxide layer. If a crack initiates, the crack flanks have to be protected by a protective layer leading to an active crack tip (Engell and Speidel, 1968, Engell, 1971). Otherwise, if the crack flanks are not covered by a protective layer, so-called crack blunting may occur leading rather to localized general corrosion than the maintenance of a sharp crack tip and hence cessation of crack growth.

There have been a number of crack growth mechanisms that have been proposed in the past, which has also been the topic of different review papers, e.g. (Tirbonod, 2000, Turnbull, 1993, Gutman, 2007, Hall Jr, 2009b, Hall Jr, 2009a) . The cracking mechanisms that have been mainly discussed with regard to the system LAS / HTW in the literature are:

- Film rupture / anodic dissolution (FRAD) model (Ford, 1992, Ford, 1989, Ford and Andresen, 1990, Ford and Andresen, 1989a, Ford, 1993) and
- Hydrogen-assisted environmentally assisted cracking (HAEAC) model (Hänninen et al., 1985, Hänninen et al., 1983).

Both, film rupture anodic dissolution and hydrogen assisted cracking are thermodynamically and kinetically possible under light water reactor (LWR) operating conditions. In practice, it is difficult to experimentally distinguish between these two mechanisms since the same rate limiting steps (oxide film rupture frequency, re-passivation kinetics, crack tip electrolyte, etc.) are acting. It is most likely, that at temperatures above 150 °C the HAEAC plays no significant role due to the increasing mobility of hydrogen with increasing temperature and the FRAD-mechanism is becoming more important. However, even at high temperatures hydrogen effects may still play some role especially with increasing yield strength and in the coarse grain zone of weld HAZ´s (Seifert, 2002).

2.3.2.1 Hydrogen-assisted environmentally assisted cracking (HAEAC)

Since hydrogen is always present under LWR operating conditions,[5] its role on corrosion of LAS has widely been discussed. Hydrogen embrittlement is usually associated with high strength alloys. However, HÄNNINEN et al. suggested that a hydrogen embrittlement mechanism also occurs in relatively ductile low-alloy pressure vessel steels in HTW (Hänninen et al., 1983). This is explained by the brittle crack features (brittle striations, striationless cleavage-like fracture) that are observed in the fracture morphology of low-alloy steels in HTW. It has been observed that the brittle fracture morphology was associated with MnS-inclusions and that brittle cracks often spread like a fan from inclusions. These quasi-brittle features are similar to those generated in H_2 gaseous atmospheres at lower temperatures (Törrönen and Kempainen, 1984).

The most relevant model for hydrogen assisted EAC of LAS in HTW has been developed by HÄNNINEN et al (Hänninen et al., 1985, Hänninen et al., 1983, Törrönen and Kempainen, 1984). The series of steps occurring according to this model are shown in Figure 17 and can be described as follows:

(1) Enhanced oxidation (anodic dissolution and oxide reformation) at the strained crack tip after oxide film rupture
(2) Hydrolysis of the metal cations and generation of H^+ accompanied by an acidification of the crack-tip electrolyte
(3) Liquid phase transport
(4) Dissolution of MnS-inclusions in the crack tip area causing creation of H_2S and HS^- and incorporation of sulphur into the reformed oxide layer
    Creation of adsorbed hydrogen atoms due to the local hydrogen ion reduction reaction followed by hydrogen adsorption
(5) Hydrogen adsorption kinetics into the metal lattice are enhanced by the presence of adsorbed HS^- and the bare metal surface at the crack tip

[5] Hydrogen is either deliberately added to the coolant, as it is done in PWR primary coolant conditions, or may be present in the HTW due to general corrosion processes that always occur under HTW conditions.

(6) Hydrogen transport in the lattice

(7) Hydrogen trapping on MnS-inclusion

(8) Hydrogen-induced cracking

(9) Linkage of micro-cracks to main fracture causing a discontinuous crack advance.

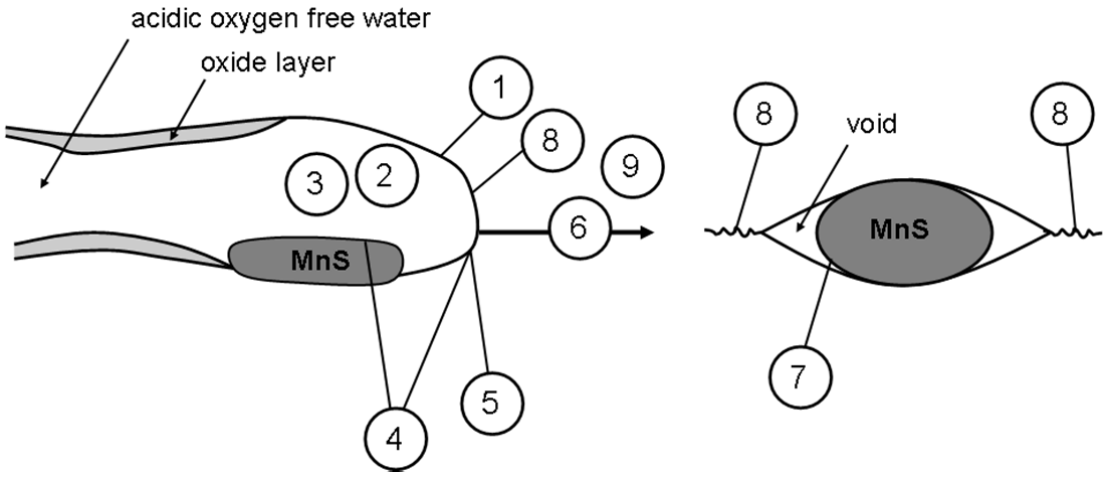

Figure 17: Schematic illustration of the corrosion reactions and hydrogen-induced crack growth model proposed for corrosion fatigue crack growth of low-alloy pressure vessel steel in high-temperature water according to HÄNNINEN et al. (Hänninen et al., 1987, Hänninen et al., 1983)

2.3.2.2 Film rupture anodic dissolution model (FRAD)

This model for EAC of LAS in HTW has been mainly proposed and developed by FORD and ANDRESEN. The basic concept behind this model is as follows:

In HTW, a protective oxide layer is formed on the surface of LAS. This oxide layer is delaying or suppressing further corrosion of the LAS. If this rather brittle oxide layer is fractured by plastic straining of the low-alloy steel, this causes local exposure of bare metal to the HTW. Consequently, localized anodic dissolution takes place at the freshly exposed crack tip area and the crack advances until repassivation of the active spot occurs.

Therefore, according to this model, the correlation between the frequency of the oxide fracture and the repassivation rate are defining the crack growth rate. The oxide fracture rate depends

on the applied mechanical loading and localized plastic deformation processes (e.g. at crack tips). The repassivation velocity at the crack tip is depending on the chemical composition of the crack tip electrolyte which is related to the bulk water chemistry, the dissolution of MnS from the material and other parameters (Ford, 1992, Läpple, 1996, Ford, 2006).

The above described dependencies and processes are schematically depicted in Figure 18. According to FORD, the crack propagation rate can be described as follows (Equation 1):

Equation 1

$$v_{crack} = \frac{M}{z \cdot \rho \cdot F} \cdot \frac{Q_f}{\varepsilon_f} \cdot \dot{\varepsilon}_{ct}$$

M, ρ	atomic weight and density of the metal
F	Faraday´s constant
z	number of electrons involved in the overall oxidation of a metal atom
Q_f	oxidation charge density between film rupture events
ε_f	fracture strain of the oxide
$\dot{\varepsilon}_{ct}$	strain rate at the crack tip

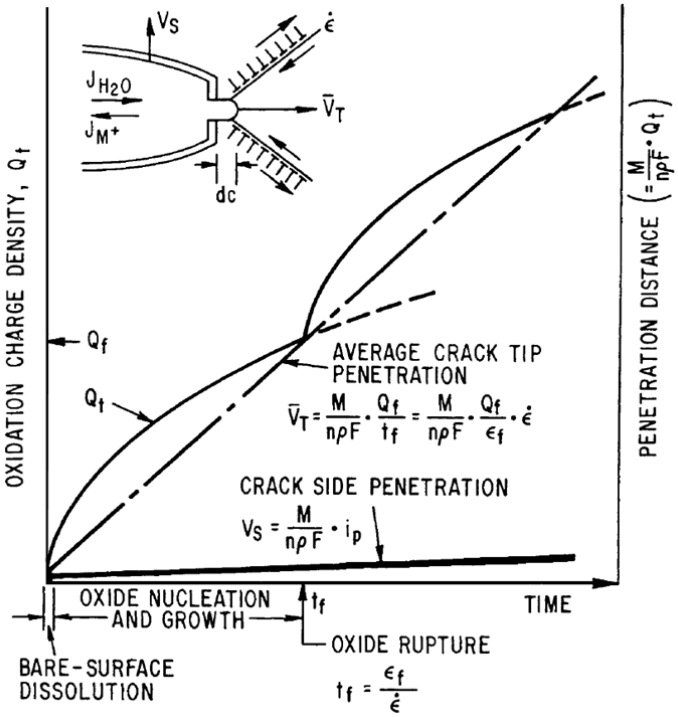

Figure 18: Schematic illustration of the relationship between oxidation charge density and time for a strained crack tip and unstrained crack sides, according to FORD (Ford, 1992).

According to this model, the film rupture frequency is an important parameter for crack growth. Film rupture occurs, as the crack tip strain exceeds the fracture strain of the oxide. Different investigations on the oxide film rupture strain deliver values ranging between 0.01 % to 0.5 % (Ford, 1982b, Field et al., 1963, Harrison, 1967, Diegle and Vermiliyea, 1976, Ford and Combrade, 1985, Deimel and Läpple, 1991).

It has been observed that the transgranular crack growth rates that are sometimes observed in LAS exposed to HTW are above the oxidation rate that was calculated by pure oxidation from Equation 1. In addition, the so-called cleavage-like crystallography of the fracture surface cannot be explained by pure anodic dissolution. Therefore, an additional brittle fracture mechanism has to be considered (Ford, 1989, Ford, 1992).

Hence, it has been suggested that the crack front initially moves forward by an oxidation process controlled by the parameters described above. When film rupture occurs, the crack in the oxide film has enough energy to additionally penetrate a small amount into the underlying material. This additional crack growth is accounted by introduction of an additional term a* into Equation 1, resulting in Equation 2 (see e.g. (Ford, 1992)). A schematic illustration of this crack propagation theory is shown in Figure 19.

Equation 2

$$v_{crack} = \left[\frac{M}{z \cdot \rho \cdot F} \cdot Q_f + a^* \right] \frac{\dot{\varepsilon}_{ct}}{\varepsilon_f}$$

The oxidation rates after fracture of the oxide layer have been measured by COMBRADE (Combrade, 1985) and FORD et al. (Ford et al., 1987). Their investigations revealed oxidation rates of about 0.5 – 3 A/cm² (i_0) directly after oxide fracture events. Those rates are maintained for about 10^{-2} – 10^{-1} s (t_0) and decrease following a power law function during the re-formation of the oxide layer (see Equation 3) (Ford, 1989).

Equation 3

$$i_t = i_0 \left(\frac{t}{t_0} \right)^{-n}$$

i_t	Current density at time t
i_0	Current density after fracture of the oxide layer
n	Parameter depending on the crack tip anion concentration (see Figure 21 b)
t_0	Time during which i_0 is maintained after fracture of the oxide

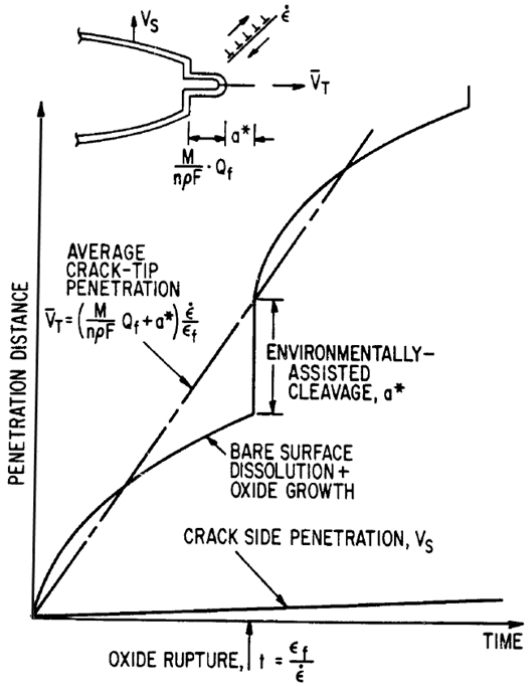

Figure 19: Schematic illustration of the elements of the film-induced cleavage mechanism of crack propagation according to FORD (Ford, 1992).

In systems with reasonable passivation rates and constant load the crack propagation rate can be described using the parameter Q_f from Equation 2. This parameter depends on the frequency of the oxide rupture $\varepsilon_f / \dot{\varepsilon}_{ct}$ and the oxidation current density (see Figure 20).

Accordingly, the summation of the bare surface oxidation charge density (directly after fracture of the oxide layer) and the time dependent oxidation charge density during repassivation from Equation 3 results in Equation 4:

Equation 4

$$Q_f = i_0 t_0 + \int_{t_0}^{\varepsilon_f / \dot{\varepsilon}_{ct}} i_0 \left(\frac{t}{t_0}\right)^{-n} dt = i_0 t_0 + \frac{i_0 t_0}{1-n}\left(\left(\frac{\varepsilon_f}{\dot{\varepsilon}_{ct}}\right)^{1-n} - t_0^{1-n}\right)$$

For very low crack tip strain rates (e.g. constant loading conditions) where $\varepsilon_f / \dot{\varepsilon}_{ct} >> t_0$ Equation 4 simplifies to Equation 5:

Equation 5

$$Q_f = \frac{i_0 t_0}{1-n}\left(\frac{\varepsilon_f}{\dot{\varepsilon}_{ct}}\right)^{1-n}$$

By introducing Equation 5 into Equation 1 the crack propagation rate may be described as:

Equation 6

$$v_{crack} = \frac{M}{z \cdot \rho \cdot F} \cdot \frac{{i_0 t_0}^n}{(1-n)\varepsilon_f{}^n} \quad \dot{\varepsilon}_{ct}{}^n$$

The bare surface dissolution rate of LAS at corrosion potentials relevant for those occurring at the crack tip markedly depends on the sulphur crack tip anion activity, whereas the precise dependency furthermore is a function of the concentration of other anions in the solution[6] (Ford, 1992, Ford and Scott, 2008).

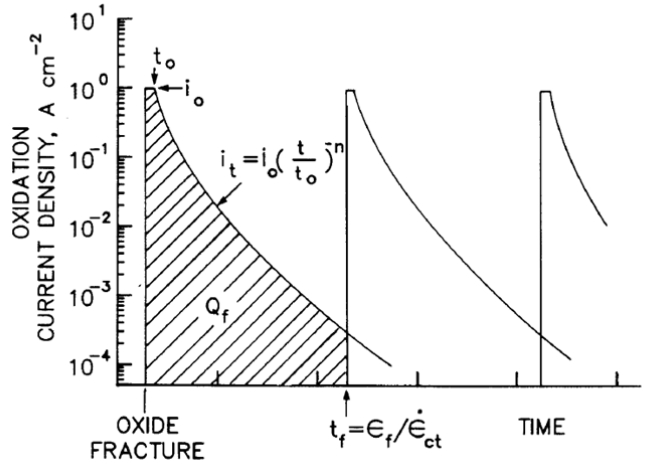

Figure 20: Schematic illustration of the oxidation current density/time transients on a strained surface (Ford, 1992).

[6] With regard to the topic of this thesis it is important to highlight that the presence of chloride in the solution plays a significant role on the oxidation current density and therefore on the crack growth rate (see also Figure 21).

Different authors proposed various hypotheses regarding the effect of sulphur anions on the repassivation behavior. According to COMBRADE et al. (Combrade et al., 1987, Combrade, 1985) and MARCUS et al. (Marcus et al., 1984), the sulphur anions will be adsorbed on the bare metal surface and thereby hinder the solid state formation of the passivating oxide. ANDRESEN (Andresen, 1987) proposed that the bare surface dissolution is limited by the diffusion of solvating water molecules in the solution immediately adjacent to the crack tip surface, and that this diffusion process is governed by the interrelationship between anionic activity, local solution pH, and oxide solubility.

Taking the above considerations into account, it may be summarized that the crack propagation rate depends on the crack tip strain rate and the anionic activity at the crack tip. According to FORD the crack propagation rate is therefore bounded by two limiting algorithms which are depending on the crack tip strain rate and the crack tip sulphur anion activity. These algorithms are (Ford, 1992):

- the "Low Sulphur Line" for "low sulphur" activities (< 2 x 10^{-4} ppm S^{2-}),

Equation 7 $$v_{crack} = 10^{-2}\,\dot{\varepsilon}_{ct}\; cm/\sec$$

- and the "High Sulphur Line" for "high sulphur" activities (> 2 ppm S^{2-})

Equation 8 $$v_{crack} = 2.25x10^{-4}\,\dot{\varepsilon}_{ct}^{\;0.35}\; cm/\sec$$

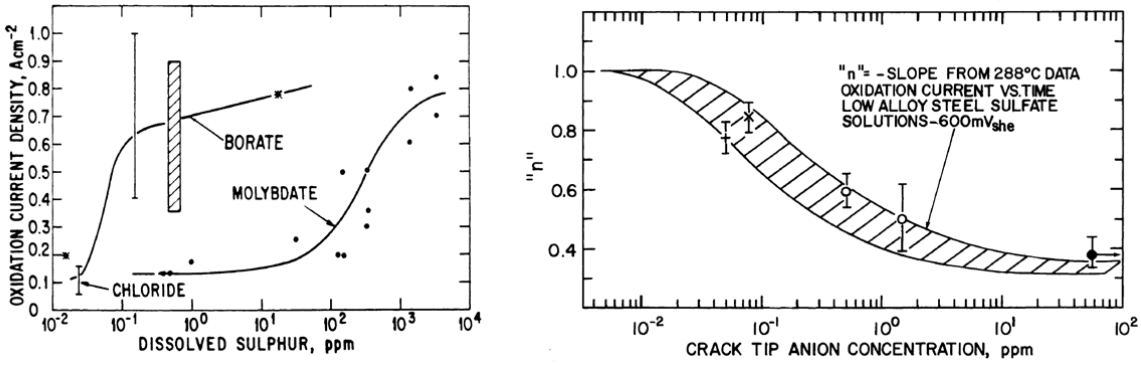

(a) **(b)**

Figure 21: (a) Variation of oxidation current density (10^{-2} sec after oxide fracture – exposure of bare metal surface) with dissolved sulphur concentration for molybdate, borate and chloride containing solutions.
(b) Slope of the parameter "n" on the concentration of dissolved sulphur at the crack tip. According to (Ford, 1992, Ford, 1989).

2.4 The Corrosion and Passivity of Low-Alloy Steels in Different Environments

Before discussing corrosion and passivity of LAS the term "passivity" should be properly defined as a baseline for further discussions on this topic.

According to WAGNER (Wagner, 1965), passivity of metal is the state in which the rate of anodic dissolution of materials in a given electrolyte is much less than the rate at a less noble potential or at some lower driving force for the corrosion reaction and can therefore be neglected for practical applications of this material.

The passivity of metals and alloy was extensively reviewed in the past by UHLIG (Uhlig, 1979). As proposed by UHLIG and REVIE (Uhlig and Revie, 1985) two different definitions for passivity can be used:

Type 1: A metal active in the emf (electro motoric force) series is passive when its electrochemical behaviour becomes that of a metal noble in the emf series (low corrosion rate, noble potential)

Type 2: A metal is passive while still at an active potential when it exhibits a low corrosion rate (low corrosion rate, active potential)

A very comprehensive definition of passivity was proposed by SCHULTZE and HASSEL (Schultze and Hassel, 2003):

> *"A passive system consists of a thermodynamically unstable material, which is covered by a passive film separating the material from a corroding liquid (or gaseous) phase. This film prohibits the active attack of the bare metal. It is formed from the metal itself and components of the environment (oxygen, water or other liquids).*
> *Formation is typically an electroless process in water or in air, or is an anodic process in water. The anodic current density may be supplied from an exterior circuit or compensated by cathodic currents, for example, hydrogen evolution or oxygen reduction at open circuit conditions."*

Taking this definition into account, LAS immersed to HTW can be designated to be passive, since the corrosion rate of the steel is drastically reduced due to the growth of a protective oxide layer. Once the oxide layer is developed, it prohibits the further uniform dissolution of the LAS. The nature of different passive films and techniques for determination film thickness, microstructure and other properties of passive films have been recently reviewed by SCHULTZE and LORENGEL (Schultze and Lohrengel, 2000).

2.4.1 Corrosion and Passivity of Iron at Low Temperatures

The corrosion of iron in different electrolytes has been extensively studied by different authors, e.g. (Feser, 2003, Heusler, 1982, Bockris et al., 1961).

If iron is immersed to acids, the corrosion rate of iron is generally very high and decreases with time due to the formation of surface films at the iron surface. A good example for the development of such surface layers is iron immersed to nitric acid. Iron that is immersed into 75 % HNO_3 immediately reacts with the solution, as it can be seen by the evolution of gaseous nitrous oxides. After a short time, the reaction stops almost immediately, and afterwards the material remains bright and uncorroded. The material is “passivated” regarding the thermodynamically strongly favoured corrosion reaction, thus showing “similar to noble metal behaviour” (Kaesche, 2003).

The explanation for this behaviour is that the HNO_3 is sufficiently oxidizing to produce a thin, nonporous oxide film on the surface of iron that dissolves into the solution only at negligible rates. Since the thickness of this oxide film is far below the wavelength of the visible light, the oxide film is transparent, and the surface of the metal remains bright.

In contrast to this behaviour, the corrosion rate of LAS in e.g. sulphuric acid is too high, to use this material in contact with H_2SO_4. If, however, iron is e.g. immersed in H_2SO_4, passivation of iron by external anodic polarization is possible. This observation can be described as follows (see also Figure 22):

If a LAS, that is immersed to an acid solution, is polarized away from the free corrosion potential ε_r, the current density of the metal increases very fast with increasing potential. If only

charge-transfer was the rate-controlling step, the increase would be proportional to $\exp(\alpha n_e F\varepsilon/RT)$ until the passivation potential ε_p would be reached.

For low-pH acid corrosion the observed curve would be distorted to line AC from Figure 22 by an ohmic component. Since the current density of the metal dissolution is limited to lower values, a layer of e.g. ferrous sulphate is precipitated at the surface of the metal causing the current-potential curve to follow line AH until a plateau is reached. The current corresponding to this plateau is called the critical passivating current density I_{crit}. The material is only in the passive state after this critical passivation current density is exceeded. This limiting current density increases with increasing exchange rate of the solution at the metal/electrolyte interface. Further factors influencing the critical passivating current density are the chromium concentration and the pH of the electrolyte. The critical passivating current density decreases with increasing chromium concentration of the material and with increasing pH.

After exceeding the passivation potential ε_{p1} the current density drops drastically until ε_{p2}, called the activation or the so-called “Flade” potential is reached.

Beyond the Flade potential, the metal is in the so-called passive state and the corresponding current density is the passive current density i_{pass}. This passivity current density is constant until the point E is reached. This point corresponds to the oxygen evolution ($2\ H_2O \leftrightarrow O_2 + 4\ H^+ + 4\ e^-$). From this point on, the current density increases exponentially with increasing potential. Accordingly, also the rate of iron dissolution is strongly increasing after reaching this point. This process is called transpassivity of the metal.

Taking the formation of the surface, or passive layer on the material surface into account the following processes have to be considered. Beginning with the deposition of a salt layer, the passivation of the metal is initiated after reaching the critical passivating current density. Beyond the so-called Flade potential the developed, semiconducting oxide film has to be nonporous, since otherwise active pore bottoms in contact with the electrolyte would act as anodes causing active metal dissolution and thereby activation of the corrosion system (Vetter, 1953, Weil and Bonhoeffer, 1955).

The properties of this nonporous passive layer are strongly different from those of the initially developed salt layer which was formed by metal dissolution and following oxide deposition.

Since the deposition of the oxide film is not possible, as long as the acid is not saturated with iron oxides and iron hydroxides, this process is not possible as the growth mechanism of the nonporous, protective oxide film. Therefore, the mechanism of film formation has to be similar to the growth of oxide films in HTW, giving the opportunity to study the growth of such oxide films at low temperatures (Kaesche, 2003).

In comparison to acid solution some different observations are made in neutral and alkaline electrolytes[7]. In neutral electrolytes noticeable oxidation of iron only occurs if an oxidizing agent, like dissolved oxygen, is present. Hence, the diffusion of the reduction agent, in this case O_2 ($O_2 + 2\ H_2O + 4\ e^- \leftrightarrow 4OH^-$), is the rate determining step and there is a correlation between the oxygen concentration and the oxidation rate of iron in such solutions (Feser, 2003).

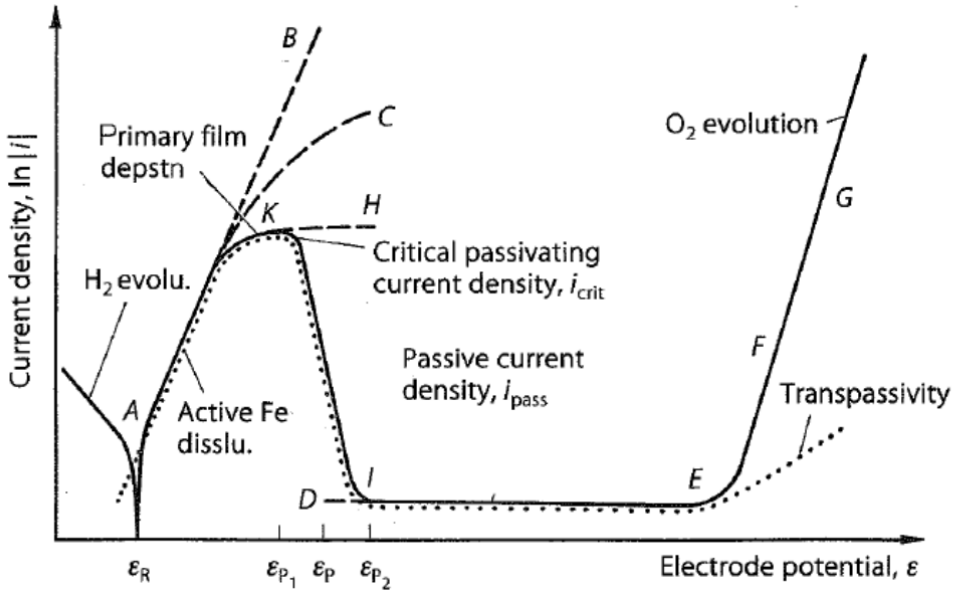

Figure 22: Schematic current-potential curve for an electrode undergoing open-circuit acid corrosion. The electrode is passivated by a semiconducting oxide film that is formed at the passivation potential ε_p also showing the anodic oxygen evolution beyond the equilibrium potential EO_2 accompanied by the transpassive increase in the metal dissolution rate. Solid curve: Total current-potential curve. Dotted curve: Partial current-potential curve for the metal dissulotion (Kaesche, 2003).

[7] For the corrosion of iron the following corrosion mechanisms have to be considered according to the actual pH: For pH < 4 acid corrosion, for 4 < pH < 9 oxygen corrosion, and for pH > 9 alkaline corrosion.

For iron in neutral and slightly alkaline solutions it can be summarized, that i_{pass} decreases with increasing pH. At pH-levels above approx. 11.5, spontaneous passivation of the metal is observed (Kaesche, 2003). In contrast to acid solutions the precipitation of a salt layer on the metal surface is no longer the rate limiting step. In these solutions, the critical current density is governed by the adsorption of OH^- ions to the surface and accordingly the growth of nonporous oxide films (Hoare, 1970, Evans, 1971). Hence, the overall corrosion reaction in this case is transport controlled.

It can be summarized, that the development of a protective, nonporous oxide film on the surface of iron is the essential step for corrosion protection of iron under these environmental conditions. Hence, the possibility to use iron in different environments strongly depends on the formation and stability of different oxide films that develop according to the environmental conditions, like type and composition of the electrolyte, the corrosion potential, pH, etc.

This correlation is summarized in so-called potential/pH or also named POURBAIX diagrams. These diagrams describe thermodynamic stability regions for different compounds that can be calculated for different materials under certain environmental conditions. Such potential/pH diagrams for the system Fe/H_2O at 25 °C and 100 °C are shown in Figure 25. In these diagrams it is of importance to understand the two main parameters that are (Chen et al., 1983b, Chen et al., 1983a):

- Electrochemical Potential:

  The electrochemical potential describes the equilibrium of metals in water, more precisely it decides which state e.g. Fe_3O_4 as an oxide, Fe^{2+} as an ion or Fe as the base metal is stable at this potential. The electrochemical potential in different solutions and at different temperatures can be calculated using the NERNST equation:

Equation 9

$$E = E^0 + \frac{R\,T}{z_e\,F} \ln \frac{a_{ox}}{a_{red}}$$

E	Electrode Potential
E^0	Standard Electrode Potential
R	Universal gas constant in J K^{-1} mol^{-1}
T	Temperature
a	Activity of the relevant species, either reductant or oxidant
F	Faraday constant (96485 C mol^{-1})
z	valency number of the ions

- pH:

  The pH describes the properties of the solution, either acid (pH below 7), neutral pH 7, or alkaline (pH above 7). It should be noted that at increasing temperature the pH decreases, thus the pH for neutral water is also decreasing.

Equation 10 $$pH = -\log_{10}(a_{H^+})$$

pH pH value
a_{H^+} hydrogen activity in a solution

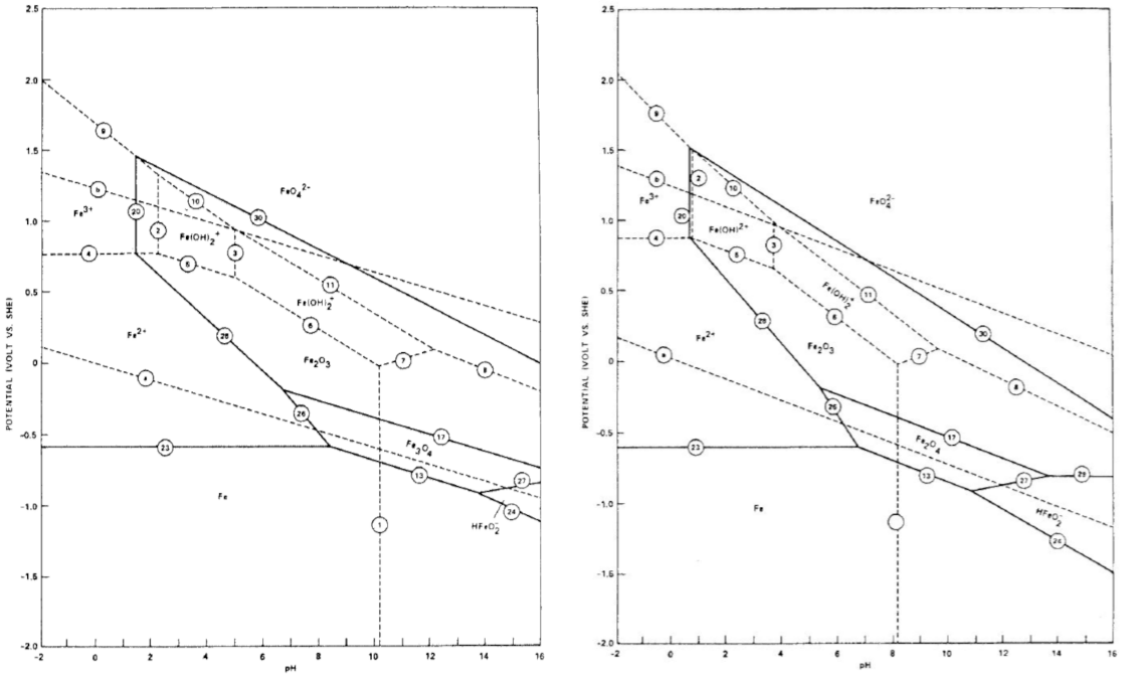

(a) 25 °C **(b) 100 °C**

Figure 23: Potential/pH diagram for the system Fe-H_2O at (a) 25 °C and (b)100 °C. Taken from (Chen et al., 1983b).

In such areas of the POURBAIX diagram, where the material is not immune to corrosion in the given environment, FARADAYs law applies. Knowing the current density of the material under the actual operating conditions, the material loss can be calculated using FARADAYs law. This is of practical importance, since the applicability of materials is often defined by the material loss during a specified time period in the literature.

Equation 10

$$m = \frac{M \cdot Q}{z \cdot F} = \frac{M \cdot I \cdot t}{z \cdot F}$$

m	Material loss
M	Molar Mass
Q	Total electric charge
F	Faraday constant (96485 C mol^{-1})
I	Current
t	time
z	valency number of the ions

2.4.2 Corrosion of Carbon Steel and Low-Alloy Steels in High-Temperature Water

This chapter summarizes the most important corrosion reactions of Carbon Steel (CS) and Low-Alloy Steel (LAS) in HTW. Before going into details of the concerned corrosion processes, it has to be mentioned that most of the discussed experimental work on the development and structure of oxide layers has been performed using CS. However, for practical assessment and due to the similarity of the occurring corrosion processes, these experiments may also be transferred to LAS.

The development of oxide layers on LAS initiates from some local spots by adsorption of hydroxide or water ions (Field et al., 1963). Since the adsorption process is a kind of physisorption, it needs no activation energy and this process occurs very fast (Läpple, 1996). Once the local adsorption process is initiated, iron ions are also going into solution and accumulate in the vicinity of the surface. If the local solubility limit of the surrounding solution is exceeded, iron hydroxides, mostly $Fe(OH)_2$, are deposited on the iron surface, whereas the type of iron hydroxides strongly depend on pH and corrosion potential (see Equation 11 and Figure 24).

Equation 11 $$Fe^{2+} + 2\,H_2O \rightarrow Fe(OH)_2 + 2\,H^+$$

Since iron hydroxide is not stable in water, it further reacts to hematite according to the SCHIKORR reaction (see Equation 12) (Gadiyar and Elayathu, 1980, Bornak, 1988, Bohnsack, 1971).

Equation 12 $$3\,Fe(OH)_2 \rightarrow Fe_3O_4 + H_2 + 2\,H_2O$$

This reaction is very slow at ambient temperatures and up to about 100 to 150 °C. At temperatures above approx. 150°C the SCHIKORR reaction occurs very fast and a protective oxide film develops on the surface of LAS that are in contact with HTW. At these temperatures the protective oxide layer develops with and also without dissolved oxygen in the HTW and the growth velocity of the oxide layer follows a parabolic growth law (Mabuchi et al., 1991).

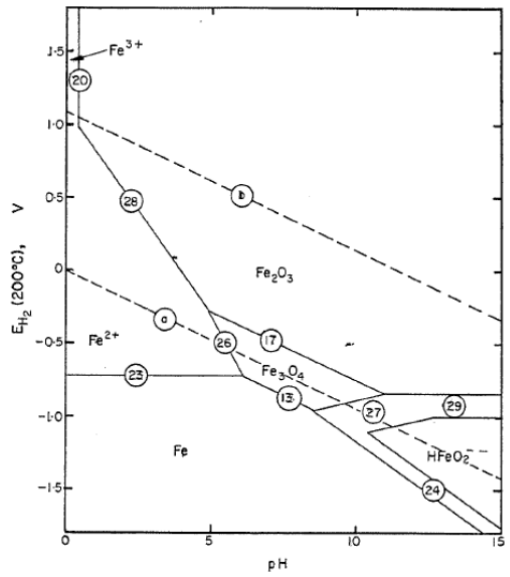

Figure 24: **Potential/pH Diagram for the system iron in high-temperature water at 200 °C. The dashed line (a) corresponds to the H_2/H^+ equilibrium and line (b) to the O_2/H_2O equilibrium. The pH-values under BWR-conditions are approx. from pH 5 to 7. (Diagram taken from (Townsend, 1970)).**

For LAS in contact to approximately neutral deoxygenated water, the main reduction process is that of hydrogen cations or water, whose equilibrium potential/pH characteristics can be shown using POURBAIX diagrams (see dashed line (a) in Figure 24). Accordingly, the counteracting oxidation process is the direct formation of magnetite[8] (Townsend, 1970, Beverskog and Puigdomenech, 1996).

Equation 13 $$3\,Fe + 4\,H_2O \rightarrow Fe_3O_4 + 8\,H^+ + 8\,e^-$$

Under oxygen free conditions the typical corrosion potential is approximately in the range of - 600 mV_{SHE} to - 800 mV_{SHE}. Therefore, under these conditions very low corrosion rates are expected, if no very acidic or alkaline conditions occur (Ford and Scott, 2008).

[8] Note that this reaction is a simplified version of the overall reaction, where different intermediate species may exist.

In deoxygenated (dissolved oxygen concentration below approx. 30 ppb) HTW the oxide layer that develops on the low-alloy steel surface consists of two Fe_3O_4 layers, an inner topotactic layer and an outer epitactic layer (Effertz, 1972). The interface between these two layers corresponds more or less to the former metal surface (see Figure 25).

Both oxide layer types are growing simultaneously from the former material surface. The inner, topotactic magnetite layer is growing into the LAS, the outer epitactic layer into the opposite direction. This growth behaviour also explains their different morphology (Potter and Mann, 1963).

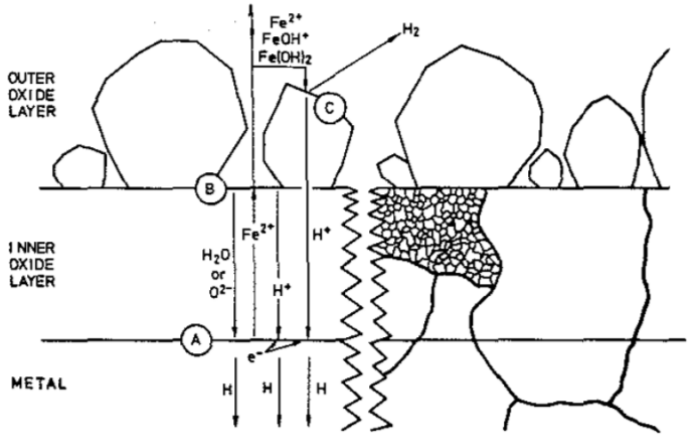

Figure 25: Model of the corrosion of low-alloy steel by high-temperature water at pH<11. Diffusing species are shown on the left side, the grain structure is shown within one ghost ferrite grain (Tomlinson, 1981). (A) corresponds to the interface between metal and inner (topotactic) oxide layer, (B) to the interface between topotactic and epitactic oxide layer, and (C) corresponds to the interface between HTW and epitactic oxide layer.

The microporic topotactic layer consists of small magnetite grains which are chemically bound to the low-alloy steel. Therefore, this layer is protective since it reduces the further dissolution of iron by strongly reducing both, the outward diffusion rate of iron and the inward diffusion rate of oxygen to the metal through the developed oxide layer (Effertz, 1972).

The composition of the outer epitactic oxide layer strongly depends on the environmental conditions, especially oxygen concentration, temperature and flow rate (Effertz, 1972, Gadiyar and Elayathu, 1980). The epitactic layer consists of rather loose individual, adherent magnetite crystals that grow from the former material surface into the solution.

According to EFFERTZ (Effertz, 1972) half of the iron that undergoes corrosion diffuses outwards from the metal to the inner oxide/water interface and goes into solution as Fe^{2+}. The outer layer is therefore formed by deposition of magnetite from ferrous ions from the solution (Tomlinson, 1981).

The growth of the protective oxide layer involves two principal steps:

1. Surface reactions at the metal/oxide interface, and

2. Transport of different elements through the oxide to the material/oxide interface.

The growth rate of the oxide layer and thereby also the protectiveness of the oxide layer is determined by the slower of these two steps (Bornak, 1988). In the system iron/magnetite in high-temperature water, the transport of material is the rate controlling step. This includes in particular the diffusion of H_2O or O^{2-} along grain boundaries, dislocations, and other short circuit paths through the inner oxide layer to the metal/oxide interface and the outward diffusion of iron through the topotactic oxide layer to the oxide/solution interface along similar routes as depicted in Figure 25 (Tomlinson, 1981, Mabuchi et al., 1991).

For the development of a protective oxide layer the access of oxygen to the oxide/metal interface is essential. The details of this process are still under discussion, possibly being diffusion of H_2O or OH^- or also the diffusion of oxygen O^{2-} (Tomlinson, 1981, Mabuchi et al., 1991).

The presence of oxygen in HTW introduces a new reduction reaction which markedly increases the potential/pH region where corrosion may occur.

Equation 14 $$O_2 + 2\,H_2O + 4e^- \rightarrow 4\,OH^-$$

Equation 15 $$O_2 + 4\,H^+ + 4e^- \rightarrow 2\,H_2O$$

The corrosion potential of LAS in high-purity water is a function of oxygen concentration and temperature (Mizuno et al., 1983b). At increased oxygen concentrations, the corrosion potential of the LAS moves to more positive values depending on the dissolved oxygen concentration and temperature. A plateau level is reached at oxygen concentrations above approx. 400 to 1000 ppb (see Figure 16).

As already described above, a pure epitactic magnetite layer develops on the surface of the LAS in deoxygenated HTW. Whereas in oxygenated HTW water a mixed α-Fe_2O_3 or γ-Fe_2O_3 layer may develop due to the presence of oxygen and the higher corrosion potential (Gadiyar and Elayathu, 1980, Mabuchi et al., 1991).

Equation 16 $$2Fe^{2+} + 6\,H_2O \rightarrow 2Fe(OH)_3 + 2e^- + 6H^+$$

Equation 17 $$2Fe(OH)_3 \rightarrow Fe_2O_3 + 3H_2O$$

Extensive research has been performed on the type, structure and stability of the different types of oxide films developed on LAS at different combinations of temperature and oxygen concentration (Mizuno et al., 1983b, Vreeland et al., 1962, Pearl and Wozadlo, 1965, Bornak, 1988, Brush and Pearl, 1972).

Especially during start-up and shut-down of plants, different environmental conditions may occur with respect to temperature and oxygen concentration. MABUCHI et al. (Mabuchi et al., 1991) intensively investigated the structure and composition of oxide layers developed under different environmental conditions. The results of there studies are summarised in Figure 26.

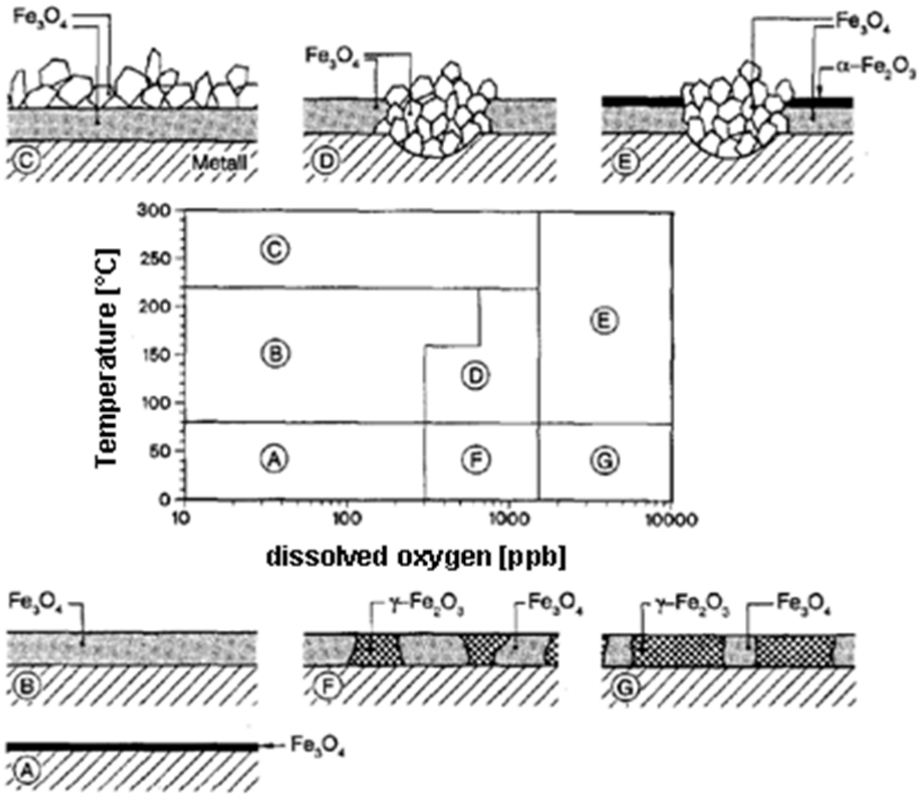

Figure 26: Composition and type of oxide layers that develop on low-alloy steels under different environmental conditions with respect to temperature and dissolved oxygen concentration of the high-temperature water (according to (Mabuchi et al., 1991, Läpple, 1996)).At intermediate oxygen concentrations (200 ppb to 2000 ppb) and low temperatures a magnetite (Fe_3O_4) layer with islands of hematite (γ-Fe_2O_3) crystals is developed (area F). At higher oxygen concentrations above approx. 2000 ppb the diameter of the yellow-brownish appearing γ-Fe_2O_3 crystals increases (area G).

The results of MABUCHI (Mabuchi et al., 1991) showed that at low temperatures and low oxygen concentrations very thin, non-protective oxide layers are developed (area A). At increasing temperatures without oxygen, a ticker magnetite layer with a thickness of up to 5 µm is developed (area B). Above temperatures of approx. 200 °C magnetite crystals with a diameter between 2 µm and 30 µm are deposited on the surface of the inner, protective magnetite layer (area C). This oxide layer causes the typical greyish-black appearance of LAS that are used under these conditions.

The growth of a magnetite layer is observed at intermediate temperatures (80 °C to 200 °C) and oxygen concentrations between approx. 200 ppb and 2000 ppb (area D). This magnetite layer

contains islands of large magnetite crystals. The diameter of these islands is in the range of 0.1 mm up to 1.0 mm. These crystals cause local corrosion at the surface of the oxide layer. This behaviour also explains the occurrence of pitting at LAS that are used under such environmental conditions as it was observed in different laboratory tests and operating plants in the past even in the absence of chloride. Such observations have also been reported by VIDEM and HICKLING (Hickling and Blind, 1986, Videm, 1975) who summarised the effect of temperature and oxygen concentration on the occurrence of pitting and the SCC susceptibility of LAS at different combinations of temperature and oxygen concentration (see Figure 27).

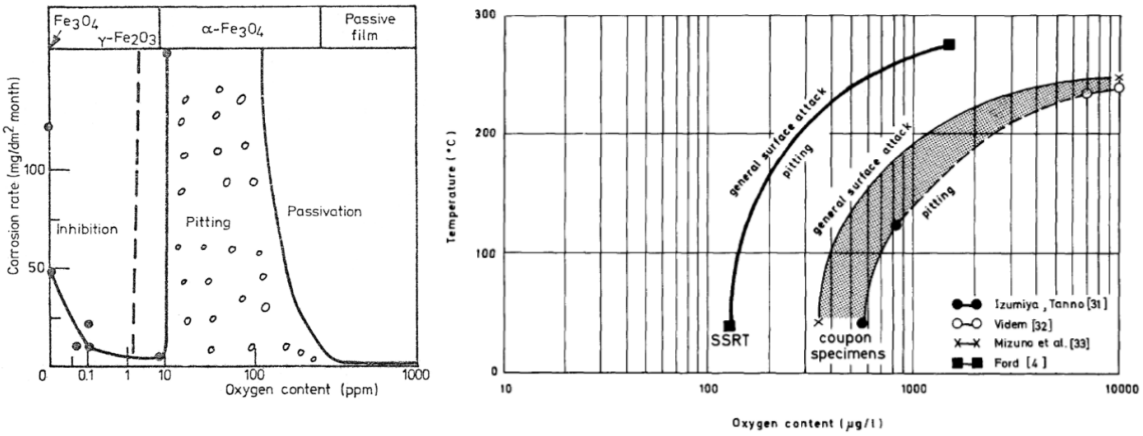

(a) **(b)**

Figure 27: (a) Effect of oxygen concentration in the water on the corrosion rate of low-alloy steel after 1 month exposure at temperatures between 240°C to 315 °C (Videm, 1975). (b) Effect of oxygen concentration and temperature on pitting of low-alloy steel in stagnating high-temperature water, according to (Hickling and Blind, 1986) (with data from (Videm, 1975, Mizuno et al., 1983a, Ford, 1982a) and Izumiya and Tanno cited in (Indig, 1982).

Finally, at high oxygen concentrations (above 2000 ppb) and temperatures above approx. 80°C a Fe_3O_4, α-Fe_2O_3 double layer with islands of γ-Fe_2O_3 crystals develops on low-alloy steel (area E). The α-Fe_2O_3 layer on top of the oxide gives the surface a red-brownish appearance.

Under oxygenated HTW conditions with oxygen concentrations of about 400 ppb, as they are used in this work, the corrosion potential of the LAS is typically above the so-called critical

corrosion potential for stress corrosion cracking of LAS, which is about -200 mV_{SHE} (Shoji et al., 1988). As investigated by e.g. SHOJI et al. under these environmental conditions the occurrence of SCC on LAS cannot be fully ruled out and therefore is an important topic for component evaluation and assessment (see Figure 28). Since the corrosion potential of LAS in HTW without contaminants is only a function of oxygen concentration at constant temperatures, the oxygen concentration in the HTW is an essential parameter regarding the SCC behaviour of LAS, see Figure 16. Hence, it can be summarised that the SCC susceptibly of LAS increases with higher oxygen concentrations.

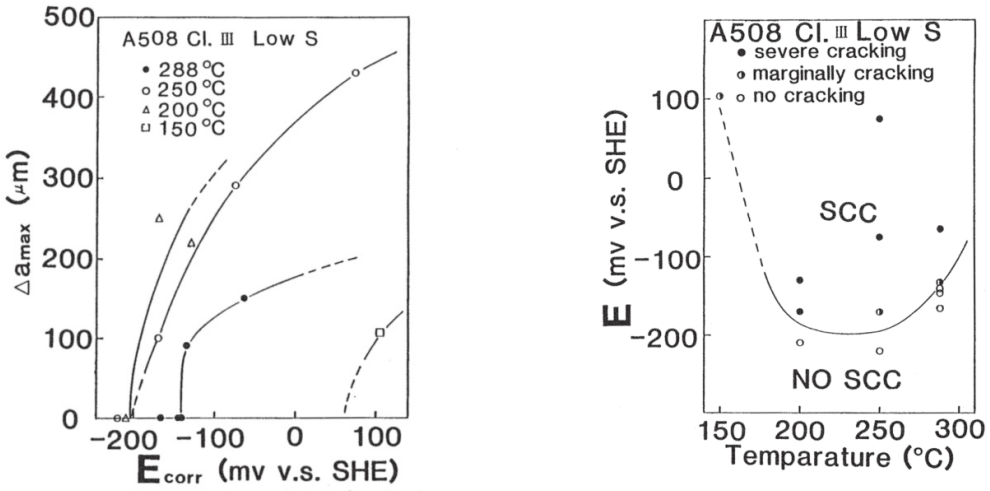

(a) **(b)**

Figure 28: Effect of temperature and corrosion potential on the critical SCC potential of low-alloy steels (Shoji et al., 1988).

2.5 Effect of Chloride on the Corrosion of LAS

An essential precursor for the occurrence of pitting is that the material has to be in the passive state, i.e. either a passive layer or a protective oxide layer on the surface has to be present (see Chapter 2.4).

For LAS in contact with either moist air or cold water general corrosion or shallow pitting is usually occurring, since no protective oxide layer is developed on the surface of the LAS under such conditions. In the case of LAS immersed to HTW we are still not dealing with a passive layer in the ideal sense, i.e. spontaneous passivation of the material by a very thin, transparent oxide film, but with a rather thick oxide double layer that is growing on the surface of the LAS and is thereby decreasing the further oxidation of the metal to such low rates that one can speak of passivation. Hence, the hereafter presented mechanisms may be also applied for LAS under HTW conditions.

Regarding the effect of chloride on the breakdown of passivity and pit nucleation three main mechanisms are being discussed (Bard et al., 2003, Kaesche, 2003). These three main mechanisms are:

- Penetration mechanism
- Film breaking mechanism
- Adsorption mechanism

These mechanisms are mainly discussed for austenitic stainless steel, where chloride causes local breakdown of the passive layer that develops at the material surface[9]. However, since, at high-temperatures of concern in this work, a protective oxide layer develops at the surface of the LAS, these mechanisms may also be applied for LAS under these conditions. In principle, it can be summarised that the local breakdown of passivity causes a high anodic current density since the surface of the anode is very small compared to the cathodic surface. This causes very high local corrosion rates of the material if no repassivation occurs.

[9] For clarification it has to be noted that chloride is not directly involved into the corrosion reactions, but is acting as a pre-cursor for the occurring processes.

Before a detailed description of these processes is given, it has to be noted, that the experiments, used to derive the mechanistical description of the ongoing processes have been performed at ambient or slightly increased temperatures often including polarisation of the specimens to receive a passive film on the specimen surface and not under HTW conditions.

The **penetration mechanism** (see Figure 29) involves the penetration of aggressive anions (e.g. chloride) from the electrolyte through the passive layer to the interface between metal and oxide layer. These anions destabilize the film and finally cause active dissolution. This process, which is strongly influenced by the electrical field at the oxide film, is not favoured by different laboratory results as described in more detail below (Strehblow, 2003, Strehblow, 1976).

Tests on specimens where aggressive anions were introduced into the test solution after the specimens were pre-passivated in a solution without any contaminations revealed increased chloride concentrations only in the outer part of the oxide film by applying Auger Electron Spectroscopy (AES) and Secondary Ion Mass Spectroscopy (SIMS). At most materials, including LAS, the oxide films have at least a bilayer structure, with an inner protective layer and an outer hydroxide film. As it could be shown for the hydroxide film on Ni, chloride is only incorporated into this outer hydroxide film if it is introduced to the test solution after prepassivation of the specimens (Yang et al., 1992, Mischler et al., 1991).

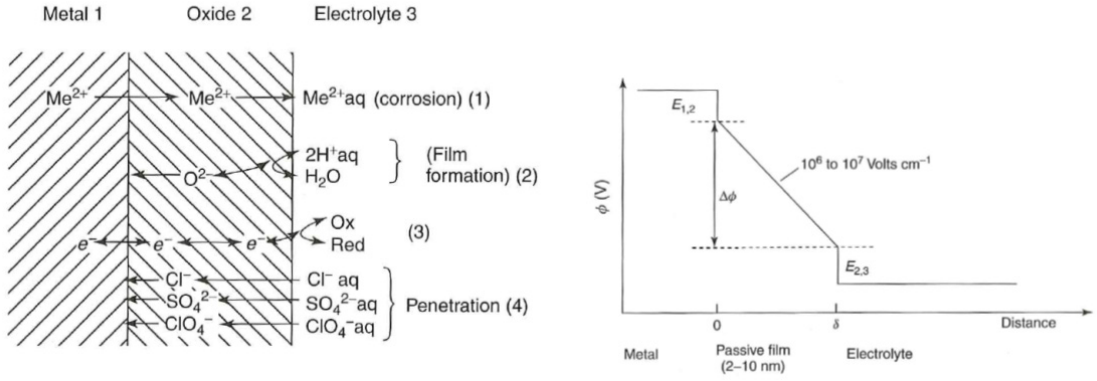

Figure 29: Schematic diagrams depicting (a) the penetration mechanism with migration of aggressive anions in the high electrical field of the passive layer as shown in (b) (Strehblow, 2003).

Chloride was only found to be incorporated in the inner part of the oxide layer after long exposure to chloride containing solutions. Under these conditions, the presence of chloride in the inner part of the passive layer was explained by continuous breakdown and repair events of the passive layer, which cause an incorporation of chloride into the newly growing oxide layer (Strehblow, 2003).

Furthermore, it has to be noted that if the penetration mechanism was the leading mechanism, the velocity of the diffusion of e.g. chloride through the passive film would be the rate determing step for pit initiation. Since pit initiation occurs much faster (within below 1 s to 1 µs) than the diffusion of anions through the oxide film, this contradicts the penetration mechanism as the leading initiation mechanism (Strehblow, 2003).

The basic idea of the **film breaking mechanism** (see Figure 30) is that small cracks in the oxide film cause the temporary exposure of small areas of bare metal surfaces. Since stresses between the oxide film and the metal are always present due to their different specific molar volume it has been proposed that these stresses cause local rupture processes. If no aggressive anion is present, these local film ruptures are repassivated immediately, whereas, in the presence of chloride this repassivation behaviour is declined and pitting may initiate (Kaesche, 2003, Strehblow, 2003, Strehblow, 1976).

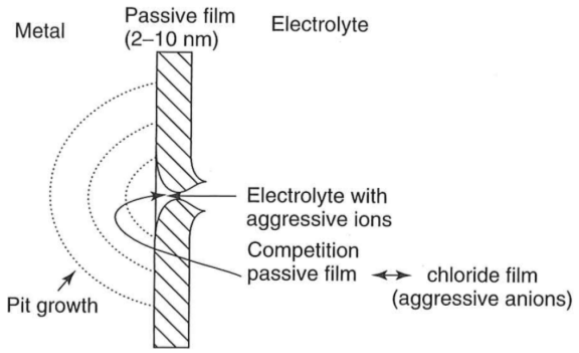

Figure 30: Schematic diagram depicting the film-breaking mechanism with the competing processes at defects in the passive layer (Strehblow, 2003).

The **adsorption mechanism** (see Figure 31) can be described by an increase of the transfer of cations from the passive film to the electrolyte due to the complexing properties of aggressive anions. This process causes a local thinning of the passive layer and finally local breakdown of the oxide layer and thereby exposure of bare metal to the electrolyte.

Experiments performed by HEUSLER and FISCHER clearly showed that the average thickness of the oxide layer decreases during the pit initiation period. In their experiment they detected increased dissolution rates of iron (Fe(III)) in chloride containing electrolytes. Since the overall current density stayed constant in these experiments, the enhancement of the passive current density of Fe(III) is compensated by an increase of the cathodic current density. This cathodic current density corresponds to the transfer of oxygen ions from the oxide to the solution (Heusler and Fischer, 1976c, Heusler and Fischer, 1976b).

This behavior has been experimentally detected in fluoride containing electrolytes for both, iron and nickel (Löchel et al., 1984, Khalil et al., 1985, Strehblow et al., 1979, Löchel and Strehblow, 1983) and of special interest for this work is for iron in contact with chloride containing electrolytes (Khalil et al., 1985). In their experiments they used high-purity iron samples that were pre-passivated for one hour in a phthalate buffer (pH 5.0) at a potential of 1.2 V_{SHE} that was externally applied to the specimens. After this pre-passivation procedure the iron samples were subject to another buffer containing different concentrations of halide ions. During this exposure the iron samples were polarised to 0.5 V_{SHE}. The results of this second exposure were evaluated with respect to the effect of different halides and halide concentrations on the film thickness and pit initiation.

The tests showed that the passive film is thinned by the catalytical action of halides (see Figure 31). The strong complexing properties of halides cause the formation of strong surface complexes with the cations at the oxide surface (Heusler and Fischer, 1976c, Heusler and Fischer, 1976b, Heusler and Fischer, 1976a).

Accordingly, the developed complexes are much more mobile and increased dissolution into the electrolyte is established. This causes a new stationary situation with a higher electric field strength and an increased (local) thinning of the oxide/passive film due to the increased dissolution rate (Strehblow, 2003).

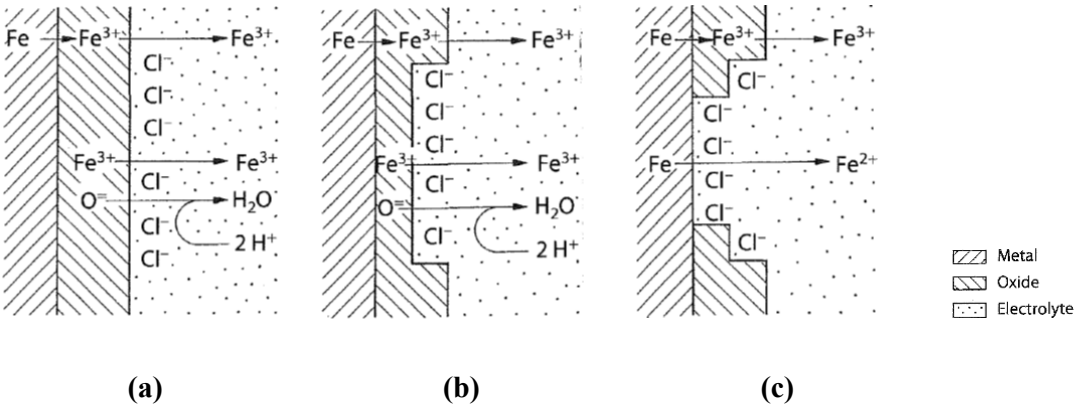

Figure 31: Schematic drawing of the adsorption mechanism:
(a) Chloride accumulation on the surface of the metal.
(a) Island adsorption of chloride causes local thinning of the oxide film.
(c) Localized thinning of the oxide film causes exposure of bare metal to the electrolyte.
According to HEUSLER quoted in (Kaesche, 2003)

A model regarding the breakdown of passivity with special emphasis on the oxide layer nanostructure and the role of inter-granular boundaries has been developed recently by MARCUS et al. (Marcus et al., 2008). Based on the proposed model, the metal-ion release in the passive state occurs faster at the inter-granular boundaries of the oxide film. They conclude that the surface will depassivate locally at the less resistant inter-granular boundaries due to local dissolution or rupture of the oxide layer. In the absence of chloride these local spots will re-passivate. If chloride is present, the chloride ions are competing with OH^- for adsorption at the oxide surface, including the inter-granular boundaries. The proposed model considers that the adsorption of chloride will lower the activation energy for the transfer of metal cations at the oxide grain boundary, thus leading to a faster local thinning of the oxide layer. Furthermore they propose that chloride can also penetrate into the oxide layer to the oxide metal interface via the inter-granular oxide boundaries. Hence, the reaction of chloride with cations causes the formation of chloride containing particles which causes stress-induced fracture of the passive film.

As summarized in this chapter, three mechanisms are discussed to be possible for pitting initiation. From these three mechanisms there are two main mechanisms that are most likely to be the leading mechanisms for pit initiation in LAS exposed to HTW. These are two mechanisms are the film breaking mechanism and the adsorption mechanism.

The film breaking mechanism describes initiation for non-stationary situations as they are applied e.g. during straining of tensile specimens or loading of CT-specimens. During non-stationary conditions, frequent breakdown and repair events of the passive film are observed in the absence of halides. If halides are present, repair of these defects does not occur at all or it is strongly declined and pits may initiate in much less than one second (Strehblow, 2003).

The adsorption mechanism is effective in describing initiation processes under stationary conditions and is therefore most likely to be the leading mechanism. The passive film is thinned due to the complex forming properties of halides which do not only cause pit initiation due to local breakdown of passivity, but are also responsible for the subsequent pit growth. The repassivation kinetics are declined, which is also respected in the formulation of the crack growth rate algorithms described in chapter 2.3.2.2 (see n-slope in Figure 21).

In addition to the effects on passivity breakdown, halides are also responsible in terms of stabilizing pit growth in the later stages, e.g. due to the formation of a salt film, potential drops and local acidification (Strehblow, 2003).

Finally, it has to be noted that there are also some other factors that play a decisive role regarding pit initiation and accordingly pit growth. From the material perspective, these are especially the chromium concentration of the alloy and also the type, amount and direction of inclusions. From the electrolyte side conductivity, temperature, oxygen concentration, etc. have to be considered.

For alloying elements, the effect of two different elements, namely Cr and Mo has to be pointed out here. Cr stabilizes the passive layer due to the extremely low dissolution kinetics of Cr-compounds. Hence, Cr accumulates within passive layers giving them a very good protection against further general and localised corrosion. The second alloying element playing an important role is Mo. Although its effect on passivity is still controversial discussed in the literature, it seems that the precipitation of insoluble halides like $MoCl_3$ or $MoCl_2$ is a good explanation for its protecting properties especially against localised corrosion (Strehblow, 2003).

3. TESTING METHODS

The aim of the electrochemical testing during this work was to study the general corrosion behaviour of LAS in oxygenated HTW, and, in particular, the effect of chloride on the general corrosion behaviour of LAS. One of the major requirements to the monitoring methods was that the investigated specimens should not be influenced by the applied testing methods e.g. by external perturbation of the corrosion system away from the equilibrium.

Therefore, two methods were used: firstly, the electrochemical noise analysis (EN), and secondly the electrochemical impedance spectroscopy (EIS). These electrochemical methods do not or just minimally influence the corrosion system of interest by external perturbation. The corrosion behaviour of the investigated specimens was absolutely not influenced by EN-analysis; in the case of EIS just a minimal external alteration of the system was imposed.

3.1 Electrochemical Noise Analysis

Electrochemical Noise (EN) is a known phenomenon for more than 40 years. First results of electrochemical noise measurements have been published in the late 1960´s by IVERSON (Iverson, 1968). Application of EN-measurements for corrosion experiments and for corrosion monitoring has only become possible during the last decades due to increased computer capacity and enhanced data analysis methods (Eden, 1998, Huet et al., 2001, Göllner, 2002, Dawson, 1994, Gabrielli and Keddam, 1992).

Electrochemical noise measurements require the measurement and analysis of spontaneous electrochemical transients occurring at materials in electrolytes due to the occurring electrochemical processes (e.g. due to dissolution of iron) (Hladky and Dawson, 1981, Hladky and Dawson, 1982). These transients in current and potential are referred to as the so-called “noise”.

EN analysis is a unique monitoring technique (Zhou et al., 2002), since

- It can be conducted under open circuit conditions.
- It needs no externally imposed perturbation of the system.
- The spontaneous fluctuations in current and voltage are sufficiently small that the constraint of linearity of the system is satisfied.

The electrochemical noise, in particular the intensity and frequency of potential and current fluctuations are depending on a variety of testing parameters, like material, material condition, testing temperature, testing environment (electrolyte) and others (Eden et al., 1991, Eden, 1998).

The amplitudes of electrochemical potential noise (EPN) and electrochemical current noise (ECN) signals are typically in the range of µV to mV for EPN and nA to µA for ECN. The frequencies of interest are typically in the range of 0,001 to 1 Hz (Bäßler et al., 2000).

Monitoring of the current noise is usually performed by coupling the test specimen with a similar electrode, which is in the ideal case manufactured from the same material heat and has the same size and shape. The potential fluctuations are monitored with respect to a reference electrode of suitable design, which may be a special high-temperature reference electrode or e.g. a platinum electrode acting as a so-called pseudo reference electrode. Correlation of simultaneous ECN and EPN measurements can provide information on the type of corrosion, initiation times and may be helpful to determine the rate of metal loss (Göllner and Burkert, 1998, Göllner et al., 1998, Hickling et al., 1998, Legat and Dolecek, 1995, Legat and Zevnik, 1993). Electrochemical noise can be used to investigate local corrosion processes like pitting, or crack initiation for mechanically loaded specimens (Göllner et al., 1998, Cottis and Gebril, 2005, Gabrielli and Keddam, 1992).

As reviewed by COTTIS (Cottis and Gebril, 2005), several studies on EN of stress corrosion cracking have been performed including slow strain-rate (Dorsch et al., 1998, Andresen et al., 1997, Ritter and Seifert, 2008a, Hickling et al., 1998), constant displacement, C-Ring, constant load, and U-bend tests (Eden, 1998, Eden et al., 1991).

EDEN (Eden, 1998) has described two principal system configurations for EN-measurements in a three-electrode arrangement (see Figure 32). These are firstly an arrangement for studies under potentiostatic / galvanostatic control and secondly an arrangement for studies without

polarisation control. These two principal arrangements may be further classified as proposed by GÖLLNER et al. (Göllner and Burkert, 1998) (see Figure 33).

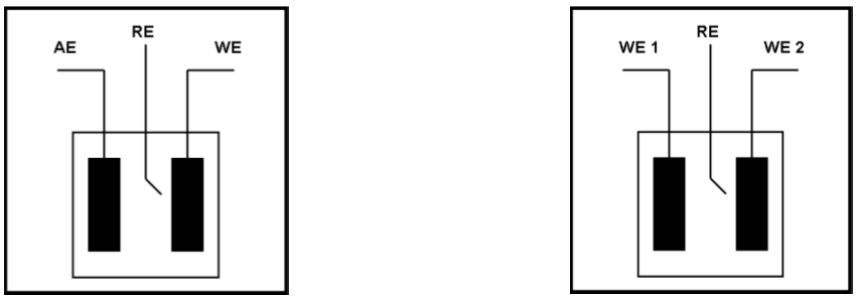

(a) **(b)**

Figure 32: Three electrode arrangement for
(a) electrochemical studies under potentiostatic / galvanostatic control, and
(b) electrochemical studies at free corrosion potential without polarisation control.
(Eden, 1998)

Experiments under potentiostatic / galvanostatic control are frequently used for laboratory studies, in particular for accelerated testing. If tests are performed under potentiostatic control, a potential is imposed to the WE with respect to the RE by polarising the working electrode via the auxiliary electrode (AE) (see Figure 32 a). For tests under galvanostatic control, the current between AE and WE is held at a constant level (Eden, 1998).

The electrode configuration for measurements at free corrosion potential is commonly used for studies on the evolution of naturally occurring corrosion processes and in particular for corrosion monitoring and surveillance applications (Figure 32 b). The advantage of this electrode configuration is that the naturally occurring ECN and EPN can be monitored simultaneously without any external perturbation of the system. This enables one to actually "listening to corrosion" as proposed by HUET et al. (Huet et al., 2001).

In this arrangement usually two similar specimens are used as working and counter electrode for electrochemical noise measurements. These electrodes are connected using zero resistance ammeter (ZRA). Hence, the current that is flowing between these specimens can be recorded. Since the two electrodes are electrically connected via the ZRA, they are at the same electro-

chemical potential. The fluctuations in the electrochemical potential can therefore be monitored using a reference electrode that is connected to the WE. The reference electrode may be a "real" reference electrode or a so-called "pseudo" reference electrode (e.g. platinum electrode). Especially for electrochemical noise measurements in HTW often a so-called pseudo reference electrode is used due to the very high noise and impedance of high-temperature reference electrodes. For the three-electrode arrangement a number of different electrode arrangements are possible without and also with additional external polarisation (see Figure 33). Within this work the arrangement b) in Figure 33 was used for the electrochemical noise measurements. The advantage of this arrangement is the possibility of simultaneous acquisition of both, EPN and ECN at open circuit conditions (Huet et al., 2001).

For data analysis of noise signals two different approaches are used: Firstly, the statistical approach, secondly transformation of the real time signals into the frequency domain and evaluation of the noise signals in the frequency domain.

Using the statistical approach, the standard deviation or the root-mean square of the noise signals are often used for data analysis and evaluation (Göllner, 2002, Eden, 1998, Pistorius, 1997).

For data evaluation in the frequency domain, the Power Spectral Density (PSD) is the commonly used method. This method gives the energy of the voltage and/or current noise signals for each given frequency.

According to RITTER, HUET and COTTIS (Ritter et al., 2010) the calculation of the PSD should be performed using the Fast Fourier Transform (FFT). The Fourier transform of the noise signal can be defined as (Brigham, 1995):

Equation 18

$$X_T(f) = \int_{-\infty}^{\infty} x(t)\, e^{-j2\pi f t}\, dt$$

$j^2 = -1$

$x(t)$ is the signal (u or i)

X_T Fourier transformed current or potential noise signal

f Frequency

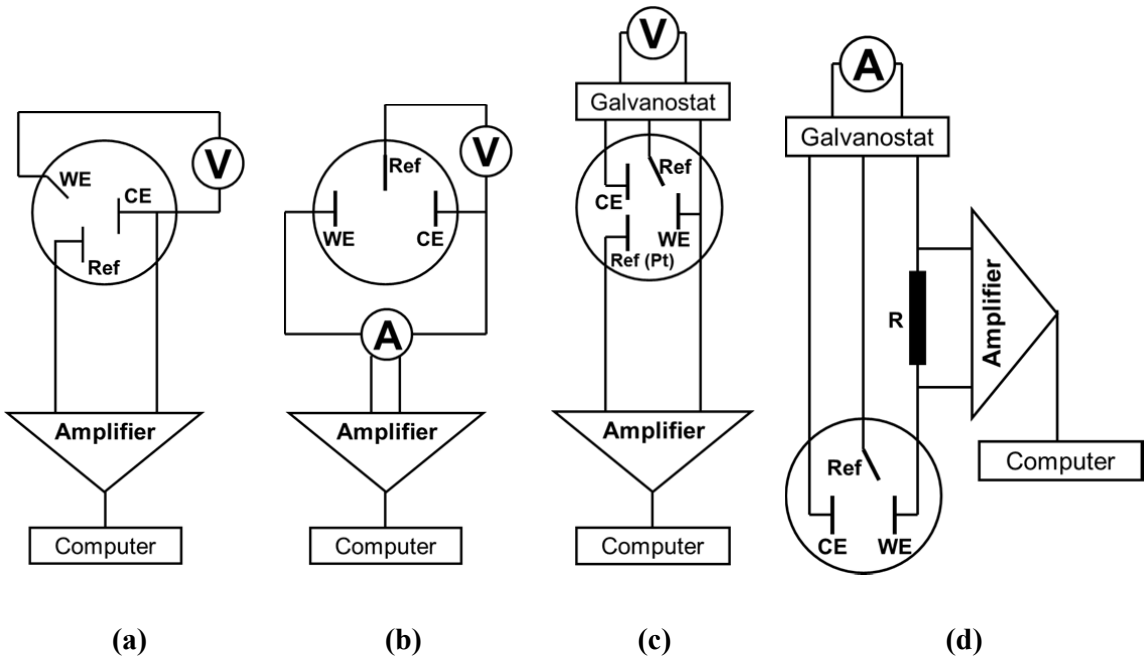

Figure 33: Measuring principles of electrochemical noise measurement arrangements of working electrode (WE), counter electrode (CE) and reference electrode (RE).
(a) Electrochemical potential noise (EPN) measurement without external polarisation.
(b) Electrochemical current noise (ECN) measurement without external polarisation (simultaneous measurement of ECN and EPN is possible).
(c) EPN under galvanostatic conditions.
(d) ECN under potentiostatic conditions (Göllner and Burkert, 1998).

Since the signal is only known for a specific time period between time 0 and time T, the Fast Fourier Transform(FFT) depends on T. The most commonly used definition for the FFT is defined as (Ritter et al., 2010).

Equation 19

$$X_{FFT}(f) = \int_0^T x(t) e^{-j2\pi f t} dt$$

Since the acquired noise signal practically consists of discrete data points the discrete, and not the continuous FFT should be used for calculations, which is defined for i = 0, 1,… , N-1 and n = 0, 1,… , N-1 as follows:

Equation 20

$$X_{FFT,n} = \sum_{i=0}^{N-1} x_i e^{-j2\pi n i / N}$$

The corresponding PSD is:

Equation 21

$$\psi_X(f) = \frac{2}{T}\left|X_{FFT}(f)\right|^2$$

Figure 34 exemplarily shows the potential noise signal obtained at Al 99 specimen in a borate puffer solution before and after increasing the chloride concentration in the solution and after introducing an inhibitor to the solution in the time domain. Furthermore, the potential PSDs that were obtained during these testing phases are depicted. These Figures reveal that the changes of the noise signal due to the change of the electrolyte (addition of chloride) can be visualized using both, the time domain and the frequency domain.

Derived from the PSD, the so-called spectral noise impedance can be calculated using the following equation (Bertocci et al., 1997a, Bertocci et al., 1997b, Bertocci and Huet):

Equation 22

$$R_{SN}(f) = \left(\frac{\Psi_V(f)}{\Psi_I(f)}\right)^{1/2}$$

R_{SN} Spectral Noise Impedance

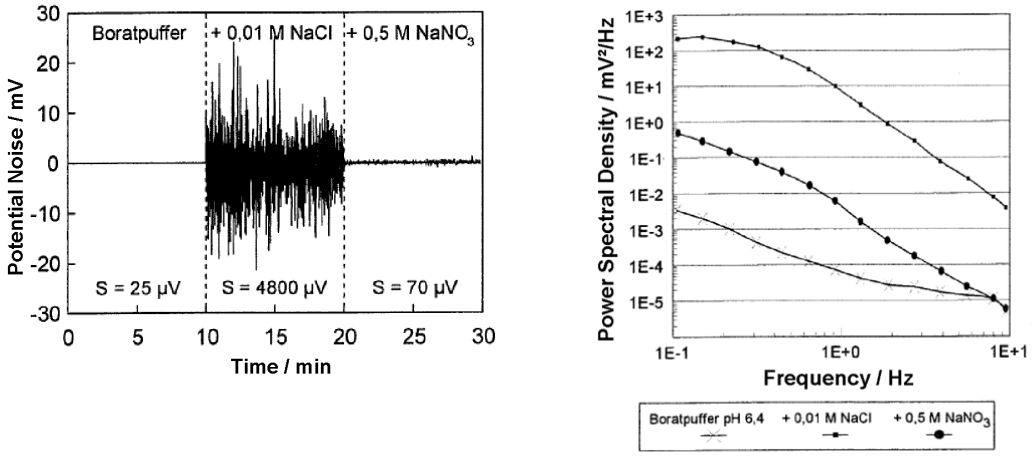

(a) Potential noise signal **(b) Potential PSD**

Figure 34: (a) Potential noise signal from an Al 99 specimen under different environmental conditions. The standard deviation of the potential noise is calculated for each environmental condition. (b) PSD of Al 99 calculated from the noise signal shown in (a). Taken from (Göllner, 2002).

3.2 Electrochemical Impedance Spectroscopy

The electrochemical impedance spectroscopy (EIS) is a very important, well established and powerful technique that is commonly used for investigating electrochemical and corrosion systems (Macdonald, 1990, Macdonald, 2006, Gabrielli and Keddam, 1992). Among many other applications EIS is used for investigating passive surfaces, oxides of materials (Park and Macdonald, 1983, Park and Macdonald, 1989) and also SCC in HTW (Macák et al., 2006, Bosch, 2005).

According to BARD (Bard and Faulkner, 2001) and MACDONALD (Macdonald, 2006) this technique accrues a number of advantages:

- It is a linear technique and therefore it provides the ability to treat the system response theoretically by linearized current-potential characteristics.
- It delivers experimental ability to perform high-precision measurements because the response may be indefinitely steady and can therefore be averaged over a long term.
- The experimental efficiency is very high since the amount of information transferred to the observer is very high compared to the amount of data produced by the experiment.
- Measurement over a wide time (frequency) range (10^{-4} to 10^{6} Hz) is possible.

Using EIS, an alternating perturbation with a small magnitude is applied to the investigated system. Accordingly, the system follows this perturbation at steady state and the electric response of the system to the external perturbation is monitored (e.g. for potentiostatic EIS a potential perturbation is impressed to the system and the current response is monitored). The investigated system should usually consist of two similar electrodes and a reference electrode, but other test assemblies are also often used due to special testing requirements. The principal test assembly used for impedance measurements is schematically shown in Figure 35.

In contrary to other techniques which usually drive electrodes to a condition far from the equilibrium, EIS is based on perturbation of the electrodes with a small magnitude at equilibrium. Therefore, the main advantage of this technique is that the response of the investigated system can be regarded as approximately linear (Bard and Stratmann, 2003).

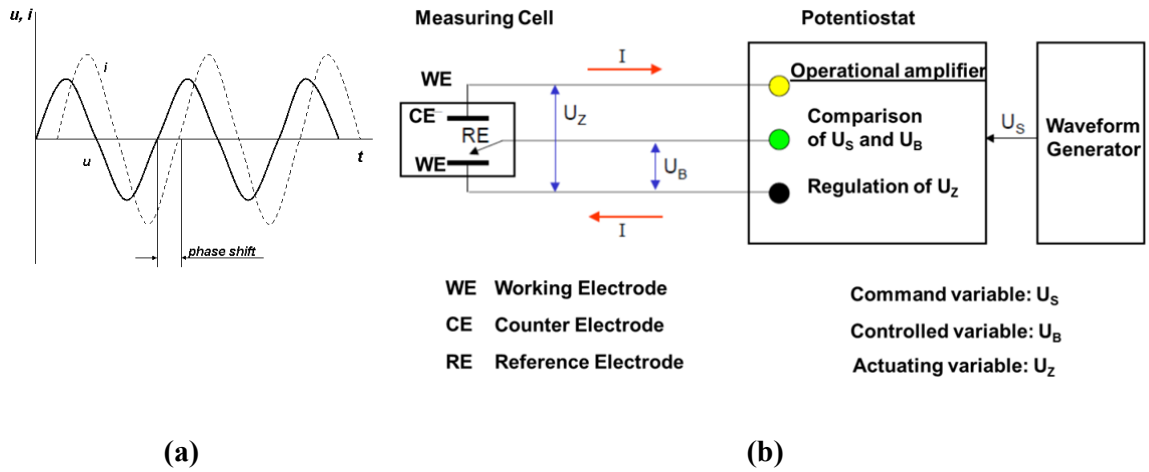

Figure 35: (a) Relationship between alternating potential excitation and current answer of the system. (b) Principal diagram of the potentiostatic data acquisition of EIS.

The perturbation applied to the investigated system is usually a sinusoidal potential excitation. Accordingly, the system response, in the case of a potential excitation the current aresponse, is measured and evaluated with respect to the amplitude and phase shift of the acquired signal (see Figure 35).

The current excitation of the system can be described as:

Equation 23 $$u(t) = V_0 \cos(\omega t)$$

The potential response of the system follows the equation:

Equation 24 $$i(t) = I_0 \cos(\omega t - \phi)$$

$u(t)$	impressed potential with respect to E_{corr}
$i(t)$	current response of the system
V_0	magnitude of the impressed potential
I_0	magnitude of the current response
ϕ	phase shift between potential excitation and current answer of the system
t	time
ω	angular frequency of the sinusoid in radians per second ($\omega = 2\pi f$)

Furthermore, the time dependent potential and current can be described as follows:

Equation 25 $$\vec{V} = V_0 e^{(j\omega t)}$$

Equation 26 $$\vec{I} = I_0 e^{(j\omega t - \phi)}$$

Where $j^2 = -1$ and and EULERs relation, which is defined as:

Equation 27 $$e^{jx} = \cos(x) + j\sin(x)$$

and where x is any real number it follows, that:

Equation 28 $$u(t) = \mathrm{Re}\left(\vec{V}\right)$$

Equation 29 $$i(t) = \mathrm{Re}\left(\vec{I}\right)$$

Where $\mathrm{Re}(z)$ denotes the real part of z and the relation between $u(t)$ and $i(t)$ may be described as the impedance of the electrode.

Equation 30 $$Z = \frac{\vec{V}}{\vec{I}} = \frac{V_0}{I_0} e^{j\phi}$$

For evaluation and visualisation of impedance analysis, usually the FOURIER domain impedance is used, which can be expressed as a complex number (Macdonald, 2006):

Equation 31 $$Z(j\omega) = Z' - jZ''$$

where Z' is the real component and Z'' is the imaginary component. Therefore, the impedance may also be expressed as:

Equation 32 $$Z(j\omega) = |Z| e^{j\phi(\omega)}$$

where $|Z|$ is the modulus of the impedance.

The expressions given in Equation 31 and Equation 32 form the basis of the two common ways to present impedance data.

Firstly, derived from Equation 31 the so-called NYQUIST diagram, where the imaginary component Z'' is plotted versus the real component Z' (see Figure 36 b). Secondly, derived from Equation 32, the BODE plot, where $\log|Z|$ is plotted versus $\log\omega$ (see Figure 36 c).

When one is investigating an electrochemical system using EIS, it is the goal of the data evaluation to define an electrical equivalent circuit to describe the electrochemical system. In such

equivalent circuits each element of the electrochemical system corresponds to the physical properties of its electrical counterpart. The most common elements of the electrochemical system that are of interest are:

- Solution Resistance
- Polarisation Resistance
- Charge Transfer Resistance
- Double Layer Capacitance
- Warburg Impedance, etc.

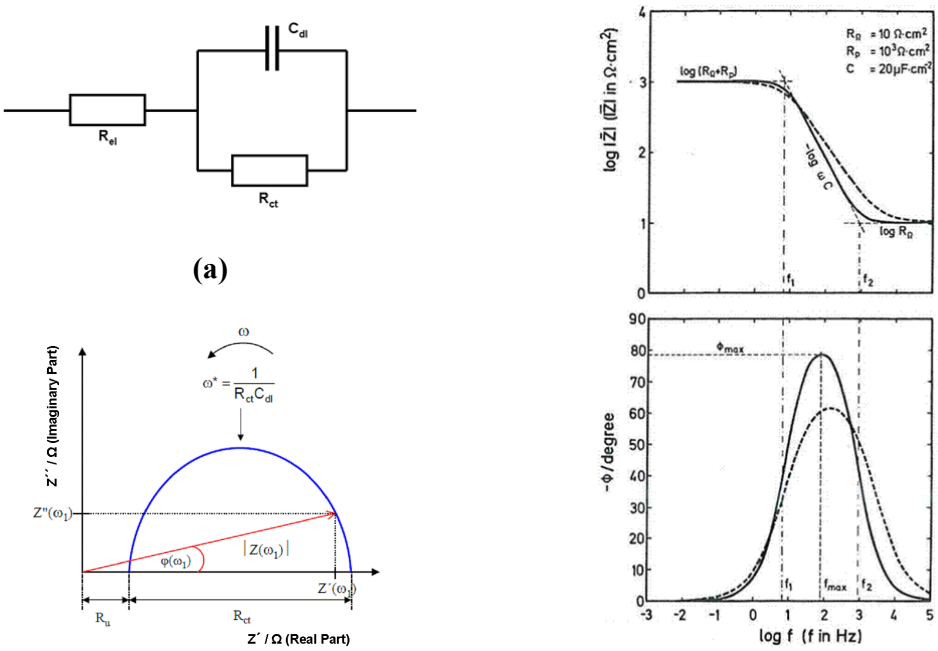

Figure 36: **(a) Equivalent circuit for a corrosion system (Randles Cell), where C_{dl} is the double layer capacity, R_{el} corresponds to the solution resistance, and R_{ct} corresponds to the charge transfer resistance.**
(b) Nyquist plot of the equivalent circuit shown in (a).
(c) Bode plot of the equivalent circuit shown in (a) (Jüttner et al., 1985).

The RANDLES cell (see Figure 36 a) is one of the most common models and is often used as a starting point for more complex models. Depending on the investigated system the equivalent circuit has to be adapted using more components to fit the equivalent circuit. In many cases this very simple equivalent circuit is a good starting point for further data assessment and evaluation. Based on this simple equivalent circuit a number of different electrochemical equivalents

can be included into the equivalent circuit to improve the fit of the model to the investigated electrochemical system.

As already mentioned above, each element in the equivalent circuit is related to physical properties of the cell. The most important elements of equivalent circuits will be discussed in the following section.

The **Solution or Electrolyte Resistance** is a significant factor in the impedance of electrochemical systems. Modern 3-elctrode potentiostats[10] compensate the solution resistance between the counter and reference electrode. However, any solution resistance between reference and working electrode has to be considered in modelling of an equivalent circuit (GAMRY, 2011). The solution resistance is defined as:

Equation 33
$$R_{el} = \rho \frac{l}{A}$$

where R_{el} is the electrolyte resistance, ρ is the solution resistivity, l is the distance between the electrodes, and A is the area carrying a uniform current. By introducing the electrical conductivity κ, which is the reciprocal of the solution resistivity, to Equation 33, the following equation is obtained for the electrolyte resistance:

Equation 34
$$R_{el} = \frac{l}{\kappa A}$$

The **Double Layer Capacitance** is used to describe the interface between the electrode and the surrounding electrolyte. The double layer is formed as ions from the solution are attached to the surface of the electrode and the charged electrode is separated from the charges of these ions. These charges, that are separated from the electrode by an insulator, form a capacitor, the so-called double layer capacity. The capacity of a bare metal immersed in an electrolyte is about 30 µF of capacitance for every cm² electrode area (GAMRY, 2011, Lowe, 2002). Furthermore, the value of the double layer capacitance depends on many variables like electrode potential,

[10] The potentiostat used within this work is a Gamry Type Reference 600 Potentiostat/Galvanostat. Therefore, in this work only the solution resistance between reference and working electrode has to be considered.

temperature, ionic concentrations, types of ions, oxide layers, electrode roughness, impurity adsorption, etc. (GAMRY, 2011).

The **Polarisation Resistance** may be described as follows: Whenever an electrode is polarised away from the open circuit potential this causes a current to flow via electrochemical reactions that occur on the electrode surface. In this reaction, the amount of current is essentially controlled by the kinetics of the reaction and the diffusion of the reactants towards and away from the electrode.

In electrochemical systems that undergo uniform corrosion, the open circuit potential is controlled by the equilibrium between two electrochemical reactions, on the one hand reactions generating cathodic current, on the other hand reactions generating anodic current. At the open circuit potential these two currents are equal. This potential is also referred to as the mixed potential and the value of either the anodic or cathodic current is the corrosion current (GAMRY, 2011). If only two simple, kinetically controlled reactions occur, the potential of the cell (E) is related to the current by the following equation (Hamann and Vielstich, 1998):

Equation 35

$$I = I_{corr}\left(e^{\frac{2.303(E-E_{oc})}{\beta_a}} - e^{\frac{-2.303(E-E_{oc})}{\beta c}}\right)$$

I	is the measured cell current (A)
I_{corr}	is the corrosion current (A)
E_{oc}	is the open circuit potential (V)
β_a	is the anodic Beta coefficient (V/decade)
β_c	is the cathodic Beta coefficient (V/decade)

If a small signal approximation is applied to Equation 35 the following equation (also called Stern-Geary Equation) is obtained (GAMRY, 2011):

Equation 36

$$I_{corr} = \frac{\beta_a \beta_c}{2.303(\beta_a + \beta_c)} \cdot \frac{1}{R_p}$$

This equation introduces the polarisation resistance R_p. As it can be derived from this equation, the polarisation resistance is representative for the rate of corrosion, if the other factors in this equation are constant. Therefore, it can be summarized, the larger R_p, the lower the rate of corrosion, and the smaller R_p, the higher the rate of corrosion (Lowe, 2002).

The **charge transfer resistance** is similar to the polarisation resistance, but unlike the polarisation resistance it is not formed by a mixed potential, but by a single kinetically-controlled electrochemical reaction. If a metal in an electrolyte is considered, as it is the case in the frame of this thesis, the according reaction is as follows:

Equation 37 $$Me \Leftrightarrow Me^{n+} + ne^{-}$$

In this equation, electrons enter the metal, and charge is being transferred into the solution by the diffusion of metal ions into the electrolyte. This charge transfer reaction has a certain speed which depends on various parameters, like the kind of reaction, the temperature, the potential, and the concentration of the reaction products.

The general relation between the potential and the current is given as (GAMRY, 2011, Hamann and Vielstich, 1998):

Equation 38 $$i = i_o((\frac{C_0}{C_0^*} \cdot e^{(\frac{\alpha n F \eta}{RT})}) - (\frac{C_R}{C_R^*} \cdot e^{(\frac{-(1-\alpha) n F \eta}{RT})}))$$

i_o	is the exchange current density
C_0	is the concentration of oxidant at the electrode surface
C_0*	is the concentration of oxidant in the bulk solution
C_R	is the concentration of reductant at the electrode surface
C_R*	is the concentration of reductant in the bulk solution
η	is the overpotential ($E_{applied}$-E_{oc})
F	is the FARADAY constant
T	is the temperature
R	is the gas constant
α	is the reaction order
n	is the number of electrons involved

If the concentration of oxidants and reductants at the electrode surface and in the bulk solution are the same, Equation 38 can be simplified to:

Equation 39 $$i = i_o(e^{(\frac{nF}{RT}\eta)} - e^{(-(1-\alpha)\frac{nF}{RT}\eta)})$$

This equation is also known as the BUTLER-VOLMER equation (Hamann and Vielstich, 1998, Kaesche, 2003). This equation can be applied, when the polarization depends only on the charge-transfer kinetics and not on diffusion of species from and to the electrode surface into the electrolyte.

When the overpotential η is very small and the electrochemical system is at equilibrium, the expression for the charge transfer resistance can be defined as:

Equation 40

$$R_{ct} = \frac{RT}{nFi_0}$$

Especially for investigations in high-purity water **transport controlled processes are** of importance. When diffusion of species from and to the surface is, at least partial, a rate limiting step, this process has to be considered by the introduction of the so-called WARBURG impedance. This impedance depends on frequency and potential perturbation of the system. At high frequencies the Warburg impedance is small, since the diffusing species do not have to move very far between metal and bulk solution. At lower frequencies, the diffusing species have to diffuse further, thereby increasing the Warburg impedance. For data evaluation it is important to know that on a Nyquist diagram the Warburg impedance appears as a diagonal line with a 45° slope. On a Bode plot, the Warburg impedance exhibits a phase shift of -45 °(see Figure 37) (GAMRY, 2011, Lowe, 2002).

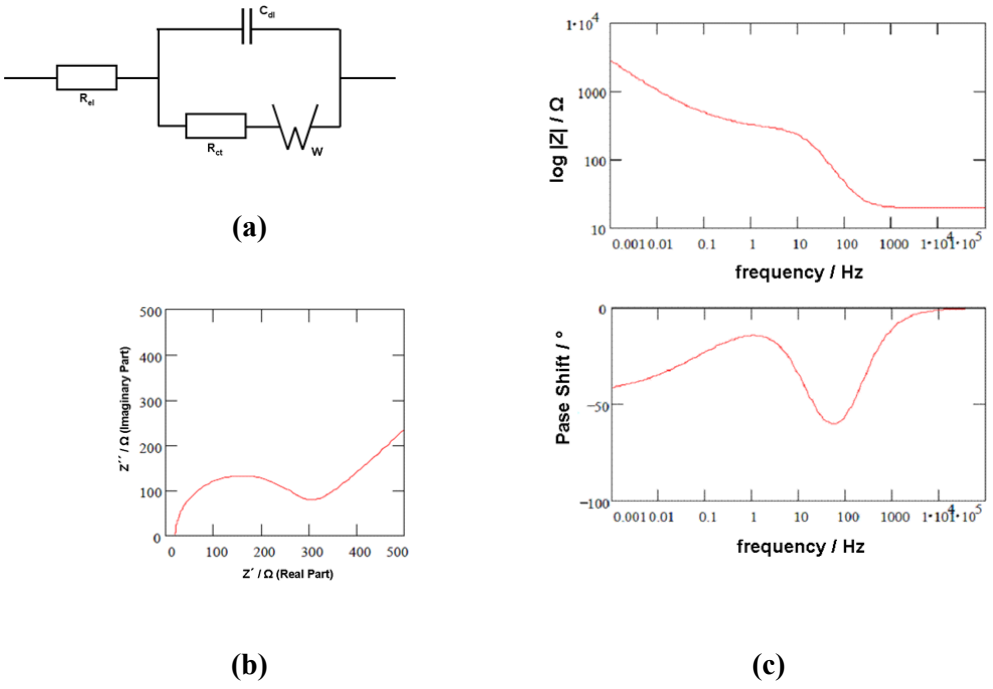

Figure 37: (a) Equivalent EIS circuit for mixed transport and diffusion control with following parameters: R_s=20 Ohm, R_{ct} = 250 Ohm, C_{dl} = 40µF, and Warburg coefficient σ = 150.
(b) Nyquist plot for equivalent circuit depicted in (a).
(c) Bode plot for the equivalent circuit depicted in (a) (GAMRY, 2011).

3.3 Testing Techniques for Specimen Analysis

Regarding the surface analysis of the investigated specimens a number of different techniques were applied. After the exposure tests the specimen appearance was documented using a stereomicroscope (type LEICA M165C). The Scanning Electron Microscope (SEM) investigations on the surface appearance after the exposure tests were performed using either a SEM type (CAMSCAN MAXIM 2500) or a SEM type (ZEISS NEON 40 EsB) which is a dual beam Focused Ion Beam (FIB) microscope.

For the measurement of the oxide layer thickness, this dual beam FIB microscope, a combination of a standard SEM with a gallium ion column was used. Using the FIB-technique, it was possible to cut the oxide layer using a gallium beam and directly measure the oxide layer thickness. For this purpose a platinum layer is deposited on the oxide to receive a better quality of the cut. Accordingly, the oxide layer is cut using a gallium beam. In front of the cut, a wedge shaped area of the specimen surface was removed by the gallium beam in order to allow direct measurement of the oxide layer thickness using SEM (see Figure 38).

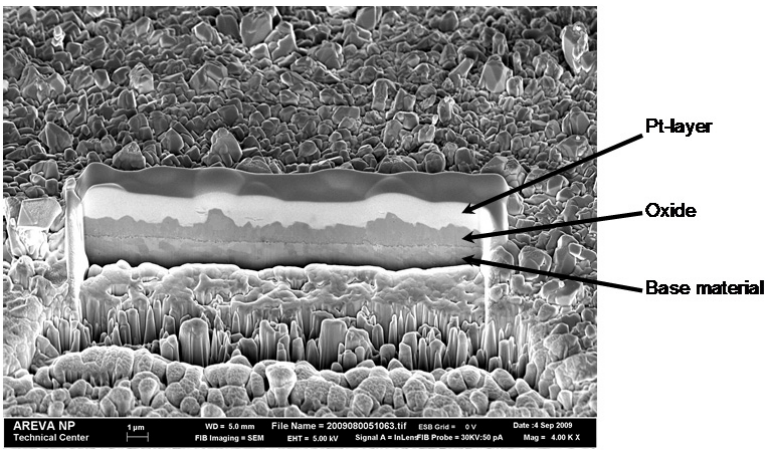

Figure 38: Side view on a FIB cut through the oxide layer developed on a coupon specimen exposed to oxygenated high-temperature water. The micrograph shows the platinum layer (white layer on the surface of the oxide layer) that is deposited to the surface of the oxide layer before cutting of the oxide layer. Beneath this platinum layer the oxide and the base metal are visible.

4. EXPERIMENTAL PROCEDURE

The aim of the experimental program was to systematically study the effect of different amounts of deliberately added chloride contaminations on the corrosion, crack initiation, and crack growth rate behaviour of LAS. Therefore, the experimental program was divided into three main phases, which were focusing on the effect of chloride on:

- General Corrosion,
- Crack Initiation, and
- Crack Growth.

All tests were performed in once-through refreshing autoclaves with full environmental control. The nominal test environment was oxygenated HTW relevant for BWR normal water chemistry operating conditions with a slightly increased oxygen concentration. The oxygen concentration during the tests was increased to achieve conservatism of the experiments with regard to pitting and crack initiation susceptibility. Hence, the following water chemistry parameters were adjusted at the inlet position of the test rig:

- Electrical Conductivity (EC_{in}) ≤ 0.1 µS/cm
- Dissolved Oxygen (DO) 400 ppb
- Temperature (T) 288 °C
- Pressure (p) 100 bar

During all tests, all relevant water chemistry parameters were continuously monitored online and controlled to maintain the specified water chemistry conditions.

The material is a typical low-alloy steel RPV material 22 NiMoCr 3 7 (~ SA 508 Cl.2). The chemical composition of the material is summarized in Table 3.

Table 3: Chemical composition (in weight-%) of the investigated low-alloy RPV steel.

Alloy	C	Si	Mn	P	S	Cr	Mo	Ni	Cu
22 NiMoCr 3 7 (~ SA 508 Cl. 2)	0.22	0.20	0.91	0.008	0.007	0.42	0.53	0.88	0.04

The chloride concentrations that were adjusted during the tests were chosen in accordance with the Action Levels of the VGB water chemistry guideline VGB-R 401 J (VGBPowerTech, 2006). A summary of the Action Levels and the corresponding monitoring parameters according to this VGB guideline is shown in Table 4. This guideline recommends that if one of the so-called monitoring parameters exceeds the defined Action Levels, different actions regarding the plant operation have to be performed. For example, if a monitoring parameter exceeds action level 2, and the parameter may not be reduced within a certain time period, the plant has to be shut down to temperatures below 100 °C after 36 hours. If action level 3 is exceeded and there is no possibility to reduce the corresponding parameter within 12 hours, the plant has to be shut down to temperatures below 100 °C.

Table 4: Monitoring parameters, values and Action Levels for BWR-plants (VGBPowerTech, 2006).

Monitoring parameter	Normal operation	Action Level 1	Action Level 2	Action Level 3
Conductivity (at 25 °C / µS/cm)	< 0.15	> 0.25	> 1	> 5
Chloride / µg/kg	< 2	> 5	> 20	> 50
Sulphate / µg/kg	< 5	> 10	> 40	> 100

According to these Action Levels, three different chloride concentrations were adjusted during the test runs:

- without chloride (reference testing conditions)
- 5 ppb chloride (Action Level 1),
- 20 ppb chloride (Action Level 2) and
- 50 ppb chloride (Action Level 3).

Details regarding the applied testing procedures and performed measurements will be described in the respective chapters.

5. EFFECT OF CHLORIDE ON THE GENERAL CORROSION BEHAVIOUR[11]

In order to study potential effects of chloride on crack initiation, a total number of 28 exposure tests were performed with different chloride contamination levels, and different durations with increased chloride concentrations. During these tests, on-line electrochemical measurements, namely Electrochemical Impedance Spectroscopy (EIS) and Electrochemical Noise (EN) analysis were performed (see Chapter 3).

In-situ electrochemical measurements and potential measurements were conducted during all tests. After the end of the HTW-condition tests, macroscopic and microscopic examinations were performed on the tested specimens.

These techniques were applied to study the effect of increased chloride levels on the oxide properties. Therefore, a number of microscopic examinations, including Stereomicroscopy, Scanning Electron Microscoy (SEM) and determination of the oxide layer thickness, were performed. The oxide layer thickness was quantified using the Focused Ion Beam (FIB) technique, chemical analyses of the oxide layer composition were performed applying Auger Electron Spectroscopy (AES) and Time of Flight – Secondary Ion Mass Spectroscopy (ToF-SIMS)

5.1 Experimental Set-up and Testing Techniques

Two types of tests were performed to study the effect of increased chloride concentrations. These were tests on the effect of permanently increased chloride concentrations over long time periods (100, 200, 500 and 1000 hours), and tests on the effect of a 24 hour chloride transient

[11] **Parts of this chapter have previously been published elsewhere:**
M. Herbst, et al. (2011). Effect of Chloride on Environmentally Assisted Cracking of Low Alloy Steels in Oxygenated High-Temperature Water – General Corrosion, 15th International Conference on Environmental Degradation of Materials in Nuclear Power Systems – Water Reactors, August 2011, Colorado Springs, Colorado.
M. Herbst, A. Roth, (2013). Investigations on the effect of chloride on the general corrosion behaviour of low-alloy steels in oxygenated high-temperature water. Materials and Corrosion, DOI: 10.1002/maco.201206751.

followed by additional testing time (100, 200, and 500 hours) under "regular operating conditions" as specified by the water chemistry guideline (< 2 ppb chloride).

Two kinds of specimens were used in these tests, unstressed coupon specimens and pre-strained C-Ring specimens. Using these two kinds of specimens, it was possible to obtain information regarding the effect of increased chloride concentrations on the eventually increased crack initiation susceptibility for pre-strained specimens and to compare those results with the behaviour of unstressed specimens.

Thus, to reduce testing time, a testing facility that allows testing at four different water chemistry conditions (chloride levels) at the same time was developed based on an existing water conditioning facility. A picture and a schematic drawing of the developed test rig are shown in Figure 39 and Appendix 1 (Figure 99), respectively. The test rig uses the water preparation unit of an existing testing facility marked as "water conditioning" as source for the high-purity water that is used for testing (see Appendix 1, Figure 99). Appendix 1 (Figure 100) furthermore shows a schematic drawing of the high-temperature testing loop and the water preparation unit. In this facility the water chemistry parameters are adjusted according to the required testing conditions.

Figure 39: Testing facility used for exposure tests at different chloride contamination levels.

After conditioning, the water is pressurized, pre-heated and pumped into four different autoclaves that are arranged in four parallel legs. The water flow in each leg is regulated by a high temperature valve connected upstream of the autoclaves in combination with a backpressure valve connected downstream of the autoclave.

In three of the four legs High Pressure Dosing Pumps (HPDPs) are installed. During the chloride injection phases, a sodium chloride (NaCl) solution is dosed into the autoclaves using these HPDPs. This solution mixes up with the HTW flowing through the autoclaves. Thus, the chloride concentration of the HTW in the autoclaves can be adjusted by controlling the chloride concentration of the injected solution and by regulating the flow rate of the HPDPs on a volumetric basis.

By using this arrangement, it is possible to regulate both, the overall flow rate of HTW and the chloride flow through the four autoclaves individually, thus allowing tests with different levels of ionic impurities in the four stainless steel autoclaves at the same time. The water flow delivered by the water conditioning unit is approx. 8 litres per hour. Hence, the flow in the four legs is regulated to two litres per hour in each leg, resulting in an average exchange rate of the autoclave volume of 2 exchanges per hour.

As described above, the chloride concentration in the autoclaves is adjusted by controlling the chloride flow through the autoclaves delivered by the HPDPs in combination with the fluid flow delivered by the water conditioning system on a volumetric basis. The change of the electrical conductivity at the outlet of the test loop was continuously monitored during testing to evaluate the change of the electrical conductivity due to the increased chloride concentrations. Additionally, water samples were regularly taken from the outlet of the test loop and analysed by ion chromatography to verify the chloride concentration in the test solution.

The coupon specimens had a ground surface (surface roughness $R_a \sim 1.0$ µm) with a size of 10 x 20 mm and a thickness of 3 mm. The C-Ring specimen were manufactured and pre-strained according to ASTM G38-01 and EN ISO 7539-5 (ASTM G 38 - 01 (2007), EN ISO 7539-5:1995). The C-ring specimens had an outer diameter of 19 mm and an inner diameter of 15.8 mm. The maximum initial stress of the specimens was adjusted to approx. 500 MPa, which is slightly below the tensile strength (550 - 575 MPa (Devrient, 2007)) of this material at

300 °C (drawings of the coupon and C-ring specimens are attached in Appendix 2 (Figure 101 and Figure 102).

As the last manufacturing step, all surfaces of the specimens were ground to remove the transition section at the surface of the specimen from the electrical discharge machining (EDM) process and also to remove any copper contamination from the surface. Finally, the specimens were welded to a contact wire (made of 1.4541 ~ AISI 321) using arc metal welding. Furthermore, before assembling, the specimens were cleaned using ethanol to remove pollutants like hand perspiration, grease, etc. from the surface. After cleaning, the specimens were handled with extreme care, mounted into an auxiliary device and directly installed into the autoclaves.

All specimens were electrically contacted by "contact wires" to allow ECP and in-situ electrochemical measurements. The specimens, as well as all contact wires were fully electrically insulated against the autoclave and against the auxiliary device. This was achieved by using ZrO_2 spacers and PTFE tubes.

Due to the rather low conductivity of the test solution, the distance between the specimens had to be as small as possible to achieve a good quality of the electrochemical noise and EIS signals. Hence, the specimens were fixed at a distance of 5 mm using the auxiliary device and platinum electrodes were mounted between the two electrodes, acting as pseudo reference electrodes for the electrochemical measurements during the exposure to HTW (see Figure 40). The temperature at the specimens was monitored using thermocouples that were mounted adjacent to the specimens.

The electrochemical corrosion potential of the specimens and the redox potential were continuously monitored using an external high-temperature balanced Ag/AgCl HTW reference electrode. Results of the ECP, DO and EC measurements are exemplarily shown for a test run with 100 hours of continuously increased chloride concentration and another test run with a 24 hour chloride transient and subsequent 200 hours under specified water chemistry conditions (without chloride) in Appendix 3.

The electrode arrangement used for EN and EIS measurements was a so-called 3-electrode arrangement which is commonly used for this kind of measurements (see Table 5).

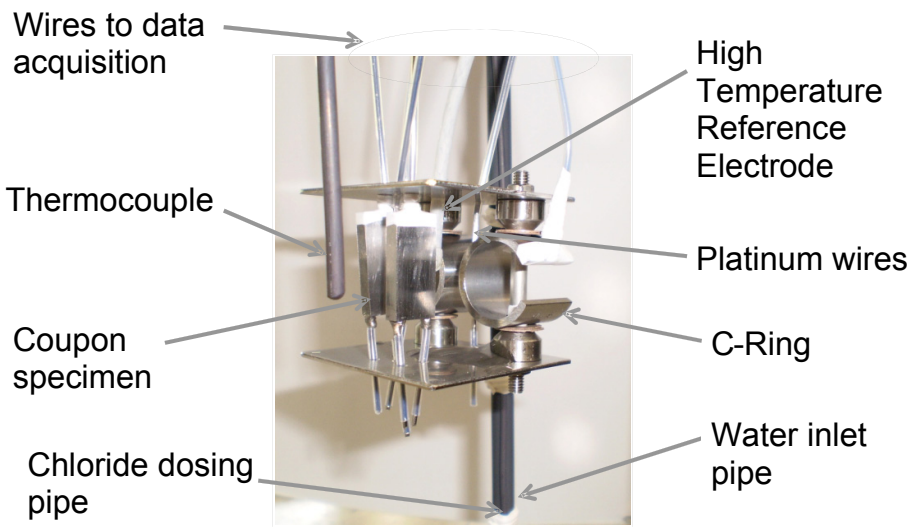

Figure 40: Specimen arrangement for the exposure tests at different chloride contamination levels.

For the EIS measurements, the excitation frequency was in the range from 0.01 Hz to 1000 kHz. The sampling rate during the EN-measurements was usually 10 Hz. In addition, further measurements were performed at higher and lower acquisition frequencies to assure high quality and accuracy of the Noise measurement as advised in (Ritter et al., 2010). The testing device was a Gamry Reference 600 Potentiostat/Galvanostat for both, EN and EIS measurements.

Table 5: Specimen set-up for EN and EIS measurements during the exposure tests

Measurements at the C-Ring specimens:		Measurements at the Coupon specimens:	
Working Electrode:	C-Ring	Working Electrode:	Coupon
Counter Electrode:	C-Ring	Counter Electrode:	Coupon
Pseudo Reference:	Pt-wire	Pseudo Reference:	Pt-wire

5.2 Experimental Procedure

Two different types of test runs were performed: Tests with continuously increased chloride concentrations and tests investigating the effect of temporary chloride transients. A simplified schematic of the testing procedure of the tests is shown in Figure 41.

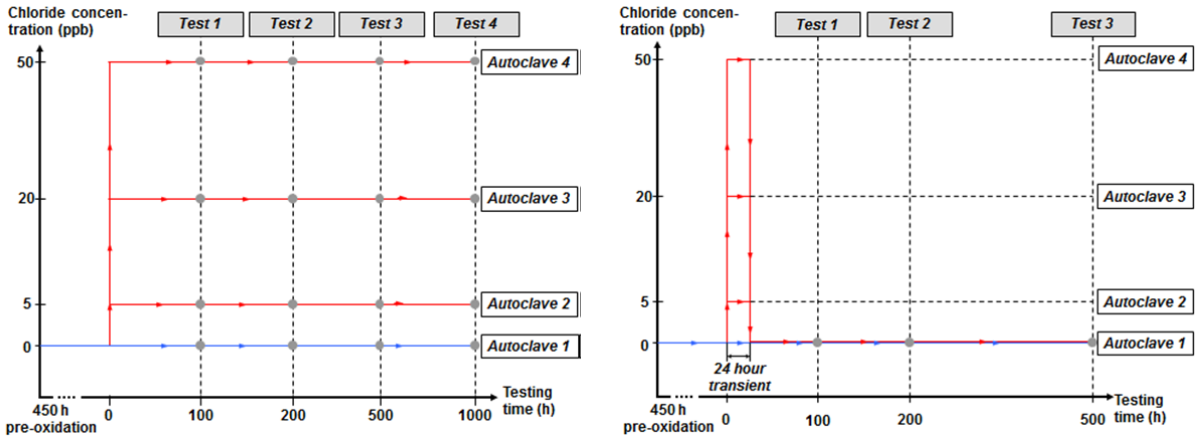

Figure 41: Simplified schematic of the testing procedure for (a) tests with permanently increased chloride contamination levels and (b) tests with temporary chloride transients and additional testing time without chloride contaminations.

i) Tests with Permanently Increased Chloride Concentrations

In the frame of these tests, the effect of permanently increased chloride concentrations was studied. After achieving the desired environmental conditions, the specimens were pre-oxidized for approx. 450 hours without chloride (see Figure 41). After this so-called pre-oxidation phase[12], the water chemistry conditions were changed as shown in Figure

[12] The pre-oxidation phase is needed in order to adjust stable environmental conditions in the test system and to ensure the development of a protective oxide layer on the surface of the investigated specimens, which is crucial for the studies on the effect of chloride on the corrosion behaviour of the investigated LAS.

41. Four separate test runs of this kind of testing, marked as Test 1 to Test 4 were performed with 100, 200, 500 and 1000 hours increased chloride concentration after the pre-oxidation phase. The adjusted chloride levels during these tests were chosen in accordance to the VGB guideline VGB-R 401 J as described in chapter 4.

ii) Tests with 24 hour Chloride Transients

These tests aimed to study the effect of chloride transients, as they may occur during plant operation, on the corrosion behaviour of the tested specimens. After achieving the desired environmental conditions and the following pre-oxidation phase of approx. 450 hours, a 24 hour chloride transient was applied. During the transient, the same chloride contamination levels as for tests with continuously increased chloride concentrations were adjusted. After the end of the transients, different additional testing times, 100 hours (Test 1), 200 hours (Test 2) and 500 hours (Test 3) (see Figure 41) under regular operating conditions without chloride were applied.

During all exposure tests, the specimens were pre-oxidised for at least 450 hours before the chloride concentration was either continuously increased or the 24 hour chloride transient was started.

During all test runs, the redox potential was in the range of 100 to 200 $mV_{SHE,T}$, and the ECP of the LAS specimens was in the range of 0 to -100 $mV_{SHE,T}$. This is in good agreement with literature values reported for 288 °C HTW with oxygen contents of approx. 400 ppb (see Figure 16). Fluctuations of the redox and corrosion potential during the tests were caused by quasi-stagnant flow conditions, which occurred during the tests due to the 4 autoclave arrangement. In these cases, the flow through one of the autoclaves decreased, causing a drop in DO and consequently leading to a decrease in corrosion and redox potential. Those short term drifts in the ECP did not change the overall results of the tests. All test runs revealed no significant change of the redox and corrosion potential due to the change of the chloride concentration, as exemplarily shown in Appendix 3.

5.3 Results of Tests with Continuously Increased Chloride Concentrations

5.3.1 Results of EN and EIS Measurements during Exposure Tests

The EN measurements that were performed on coupon specimens during pre-oxidation and exposure to different chloride concentrations clearly revealed a change of the typical appearance of the current and noise fluctuations after increasing the chloride concentration. As shown in Figure 42 for an experiment with a continuously increased chloride level of 50 ppb, both, the current and the potential noise signals changed significantly after increasing the chloride concentration. Furthermore, an increase of the noise signal after longer testing periods with increased chloride contamination levels was observed.

An increase of the recorded noise signals was measured after an incubation period of maximal 24 hours after the deliberate increase of the chloride concentration. This is exemplarily shown by noise measurements using C-ring specimens, where the chloride concentration was increased to 50 ppb after pre-oxidation of the specimens. As shown in Figure 43, a significant change of the current and potential noise signals was already observed approx. 24 hours after increasing the chloride concentration. This reveals a rather short incubation time of the chloride induced changes of the recorded noise signals.

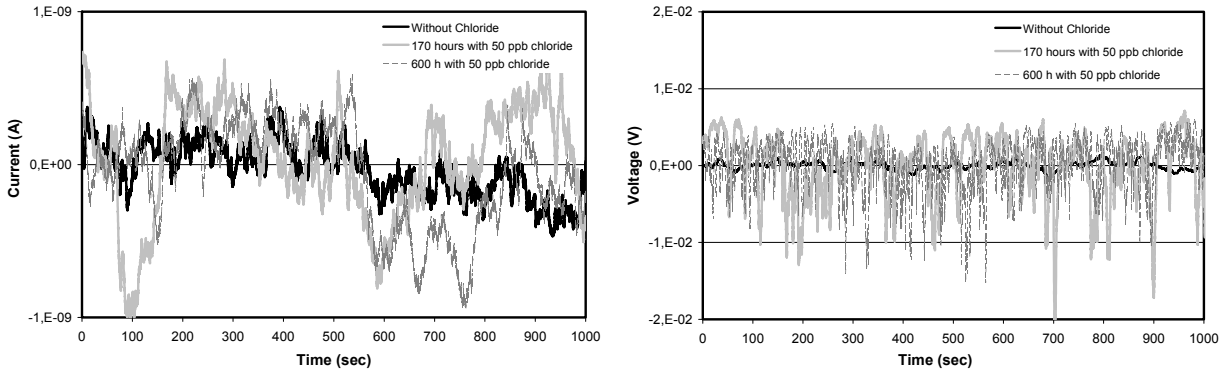

(a) **(b)**

Figure 42: **Current (a) and potential noise (b) signal acquired using coupon specimens during pre-oxidation (without chloride) and during exposure to 50 ppb chloride (Scan Rate 10 Hz).**

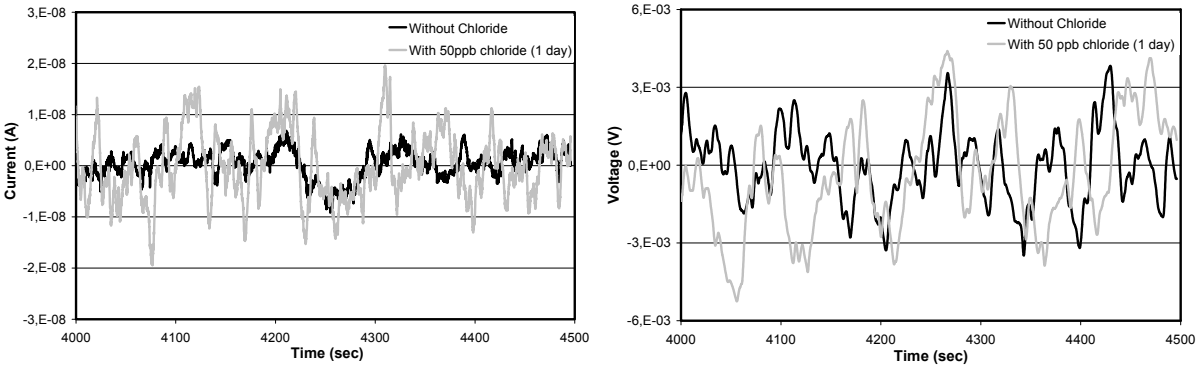

(a) **(b)**

Figure 43: **Current (a) and potential noise (b) signal acquired using C-ring specimens during pre-oxidation (without chloride) and after exposure to 50 ppb chloride for approx. 24 hours (Scan Rate 10 Hz).**

Figure 42 and Figure 43 also reveal that the fluctuations of the current and potential noise signals do not always correlate as expected. In the ideal case, transients in the noise signal and the potential signal should occur simultaneously, which was not always observed in the acquired signals. This might be attributed to the rather large specimen surface of the investigated coupon and C-ring specimens and the low conductivity of the high-purity HTW. The large specimen surface of the working and counter electrodes may lead to annihilation of acquired signals and an overlap of additional noise signals. This behavior is often observed for materials undergoing general corrosion. The relatively low electrical conductivity furthermore leads to reduced charge transfer kinetics at the specimen surface furthermore affecting the acquired noise signals.

The observed increase in the noise signal can furthermore be evaluated using the PSD (Power Spectral Density), see chapter 3.1. An increase in the PSD shows an increase in corrosion processes occurring at the investigated specimens. The assessment of the noise signals that were acquired "on-line" during testing reveals a change of the corrosion activity of the investigated specimens at increased chloride concentrations within a short incubation time. Figure 44 shows a) current and b) voltage PSDs acquired without chloride and during a continuous exposure to 50 ppb chloride. From these Figures, it clearly arises that both, the current and the voltage PSDs are increasing during exposure to increased chloride concentrations.

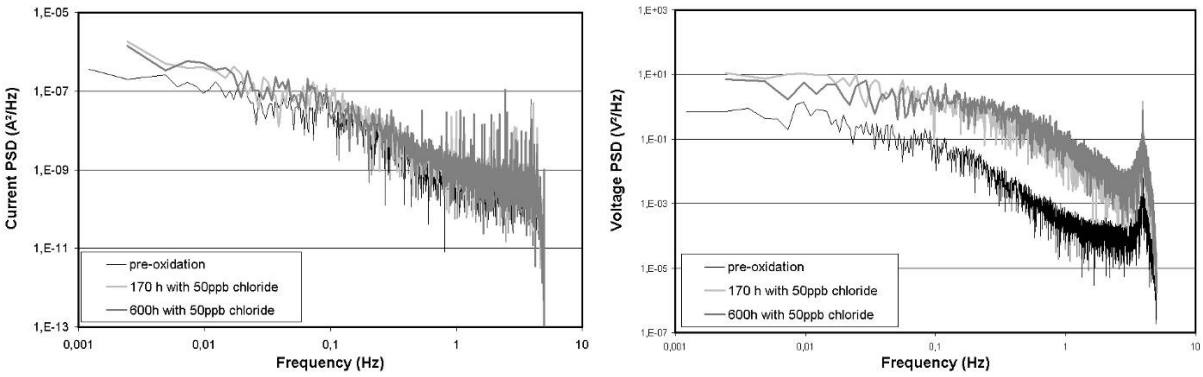

(a) **(b)**

Figure 44: **PSD of a) current and b) potential noise signal of coupon specimens during pre-oxidation and during exposure to 50 ppb chloride (Scan Rate 10 Hz).**

Derived from the PSD, the so-called Spectral Noise Impedance (R_{SN}) can be calculated (see Equation 22). Figure 45 a) and b) exhibit the spectral noise impedance calculated from EN-measurements using C-Ring specimens comparing testing conditions without chloride with conditions with a) 20 ppb chloride and b) 50 ppb chloride. From these figures it appears that the Spectral Noise Impedance is decreasing at increased chloride concentrations. This shows a change of the charge transfer resistance or the polarization resistance, respectively (Bertocci et al., 1997a, Bertocci et al., 1997b). A decrease of the R_{ct} indicates that the resistance for migration of charged species through the oxide layer is decreasing. Hence, this indicates a higher corrosion rate, in case of these tests increased anodic dissolution of iron.

Results of the EIS measurements performed on coupon specimens before and after increasing the chloride concentrations are shown in Figure 46. The results of these measurements clearly demonstrate a change in the properties of the oxide after an increase of the chloride concentration. As also observed by EN-measurements, changes in the electrochemical properties of the oxide occurred within a very short incubation time after increasing the chloride concentration (within approx. 24 h at the latest). From a comparison of the EIS measurements at different chloride concentrations (Figure 46 a to d), it arises, that the changes in the electrochemical properties of the oxides are more pronounced at higher chloride levels.

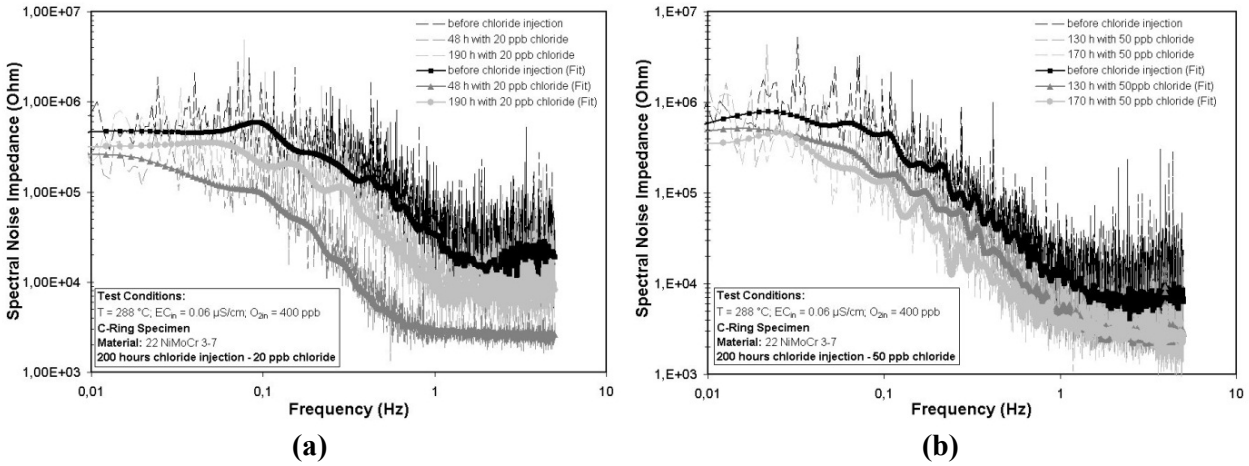

Figure 45: Spectral noise impedance plots of C-ring specimens calculated from noise data during pre-oxidation and after different exposure times to (a) 20 ppb chloride and (b) 50 ppb chloride.

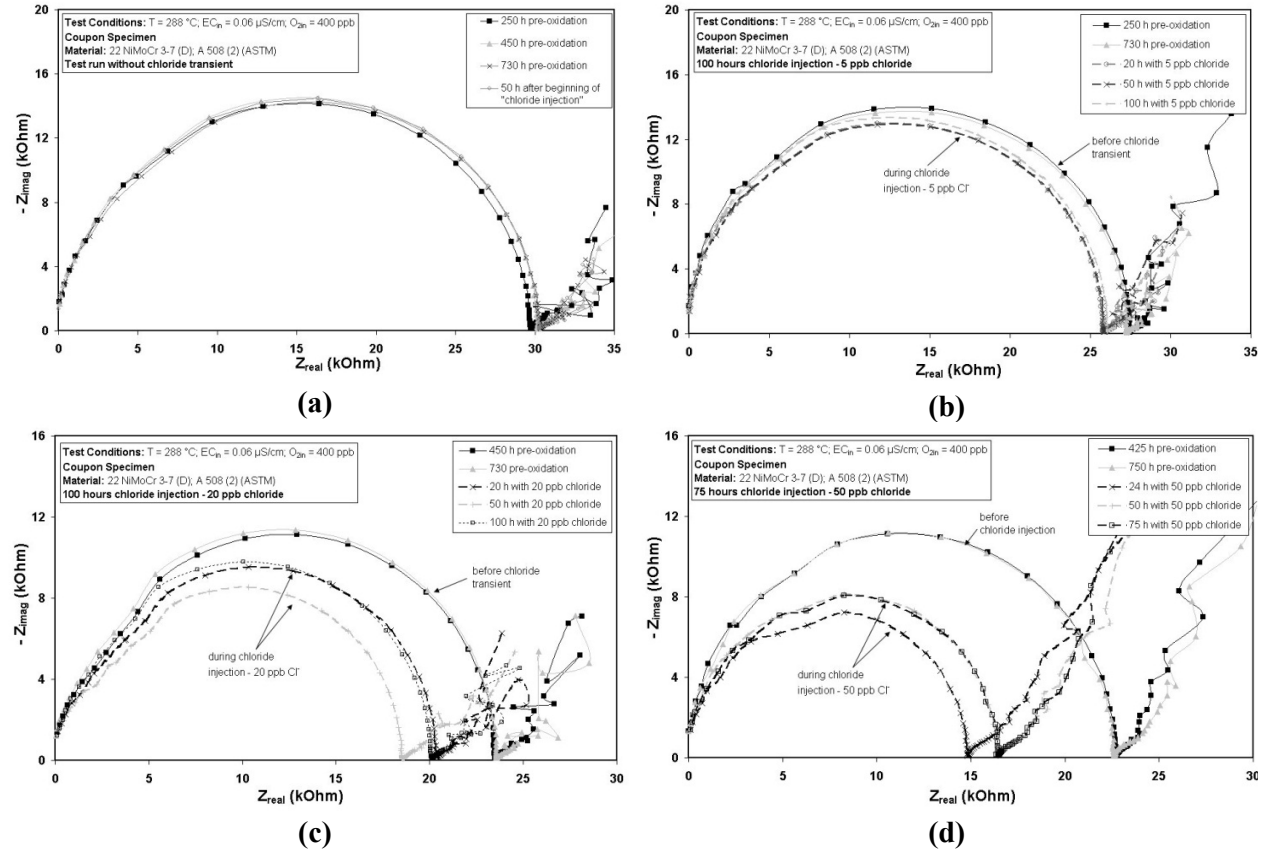

Figure 46: Nyquist plots of EIS measurements on coupon specimen during pre-oxidation and 100 hours chloride injection. Comparison of Nyquist plots from tests without and with chloride reveals a change of the oxide properties due to increased chloride concentrations. This change increases, as the chloride concentration increases.

The Nyquist plots of the EIS measurements at C-ring specimens shown in Figure 47 furthermore exhibit that the oxide layer properties further decrease at longer testing periods at increased chloride concentrations. This is derived from the continuing decrease of the diameter of the Nyquist curves after longer testing durations at continuously increased chloride contamination levels. Comparing Figure 46 and Figure 47 reveals that the change of the oxide properties occurred on both, stressed and unstressed specimens. As already described above, the observed change in the Nyquist curves can be attributed to a change of the charge transfer resistance (R_{ct}) of the oxide layer. By the change of this parameter, the EIS measurements revealed changes of the corrosion behavior of the specimens online during testing in terms of higher corrosion rates at increased chloride concentrations.

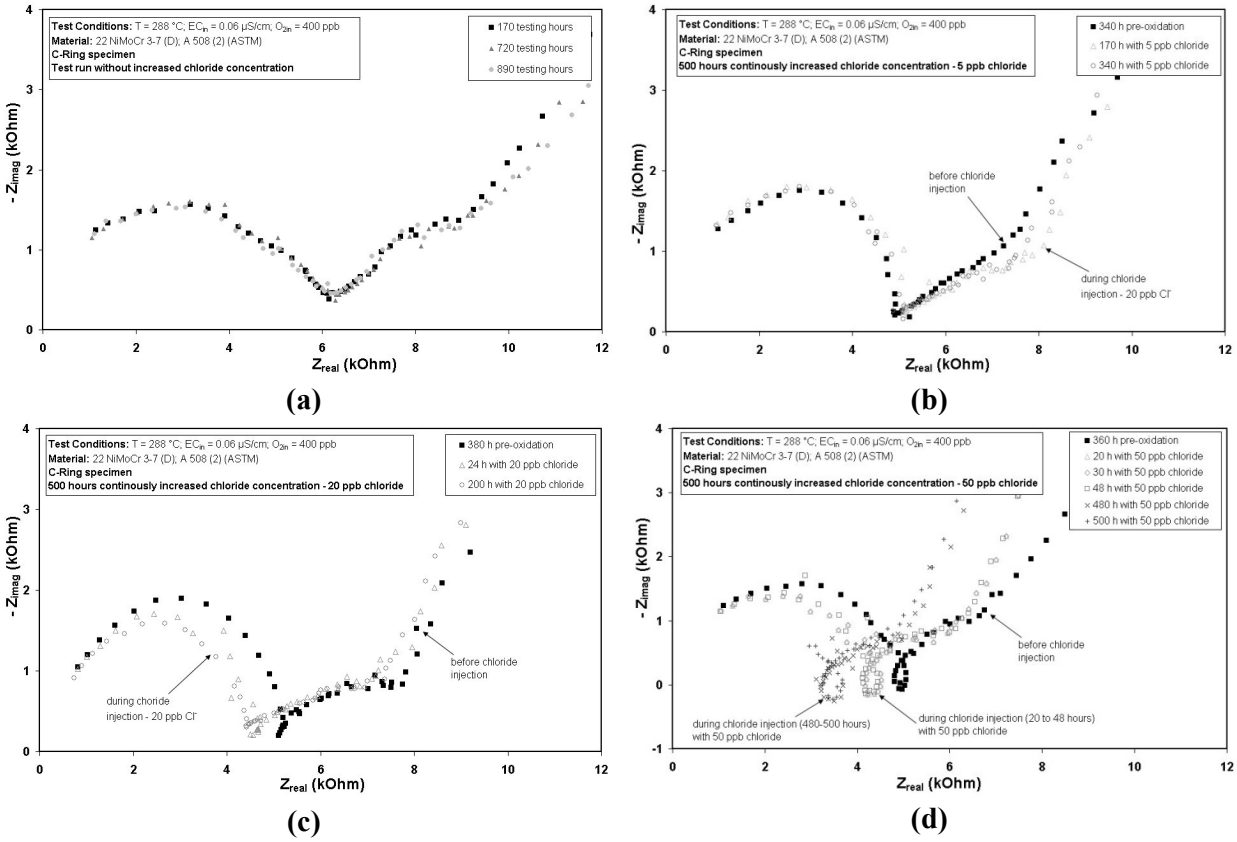

Figure 47: Nyquist plots of EIS measurements at C-ring specimens during pre-oxidation and 500 hours chloride injection. Comparison of Nyquist plots from test without chloride injection (a) and Nyquist plots of EIS measurements at increased chloride concentrations (b), (c), and (d) shows a change of the oxide properties due to increased chloride concentrations. This change increases, as the chloride concentration increases. Furthermore, the effect seems to increase at longer testing periods with increased chloride concentrations as shown in (c) and (d).

5.3.2 Results of Post-Test Investigations

After end of the exposure to HTW conditions, macro- and microscopic examinations were performed using coupon and C-ring specimens from the different test runs. During all tests with continuously increased chloride concentrations, slight pitting was observed on all specimens, which is not unlikely to be observed under the chosen testing conditions and might have occurred in particular at temperatures and testing conditions during heating up and shutdown of the tests (see Chapter 2.2.3, Figure 27) (Hickling and Blind, 1986, Videm, 1975, Vreeland et al., 1962). The macroscopic appearance of the coupon specimens shows an increase of pitting that is observed on the specimen surface tested under conditions with increasing chloride concentrations (see Figure 48). This appearance was observed in all exposure tests with increased chloride concentrations (100 to 1000 hours) for both, coupon and also C-ring specimens (see Figure 48 and Figure 49).

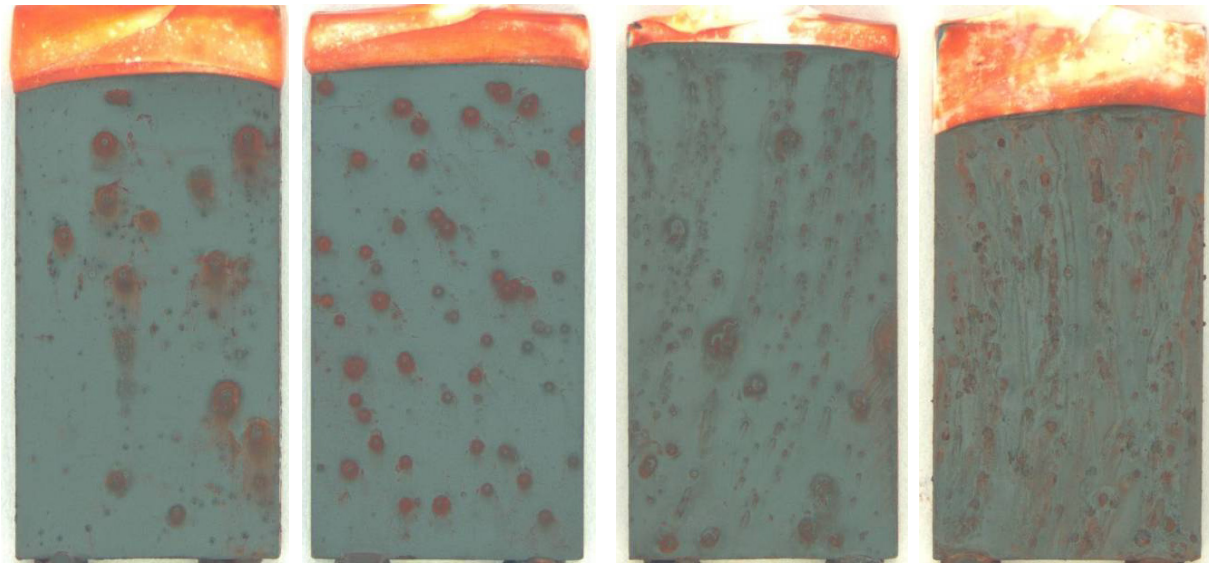

(a) **(b)** **(c)** **(d)**

Figure 48: Visual appearance of coupons specimens (specimen size: 10 x 20 mm) after 740 hours pre-oxidation and additional 1000 hours exposure to different chloride contamination levels. (a) reference specimen tested without chloride during the overall exposure test, (b) 700 hours pre-oxidation and additional 1000 hours with 5 ppb chloride, (c) same as (b) but 1000 hours with 20 ppb chloride, (d) same as (b) but 1000 hours with 50 ppb chloride. The white appearance of the upper end of the specimens is caused by a PTFE strip that is stripped around the upper end of the specimen to prevent water penetration to the connecting wire that was spot welded to the upper side of the specimen.

Figure 49 shows the visual appearance of C-ring specimens after 1000 hours with increased chloride concentrations. From this figure it appears that, as it was observed for the coupon specimens, also for the C-ring specimens the number of pits increases with increasing chloride concentrations.

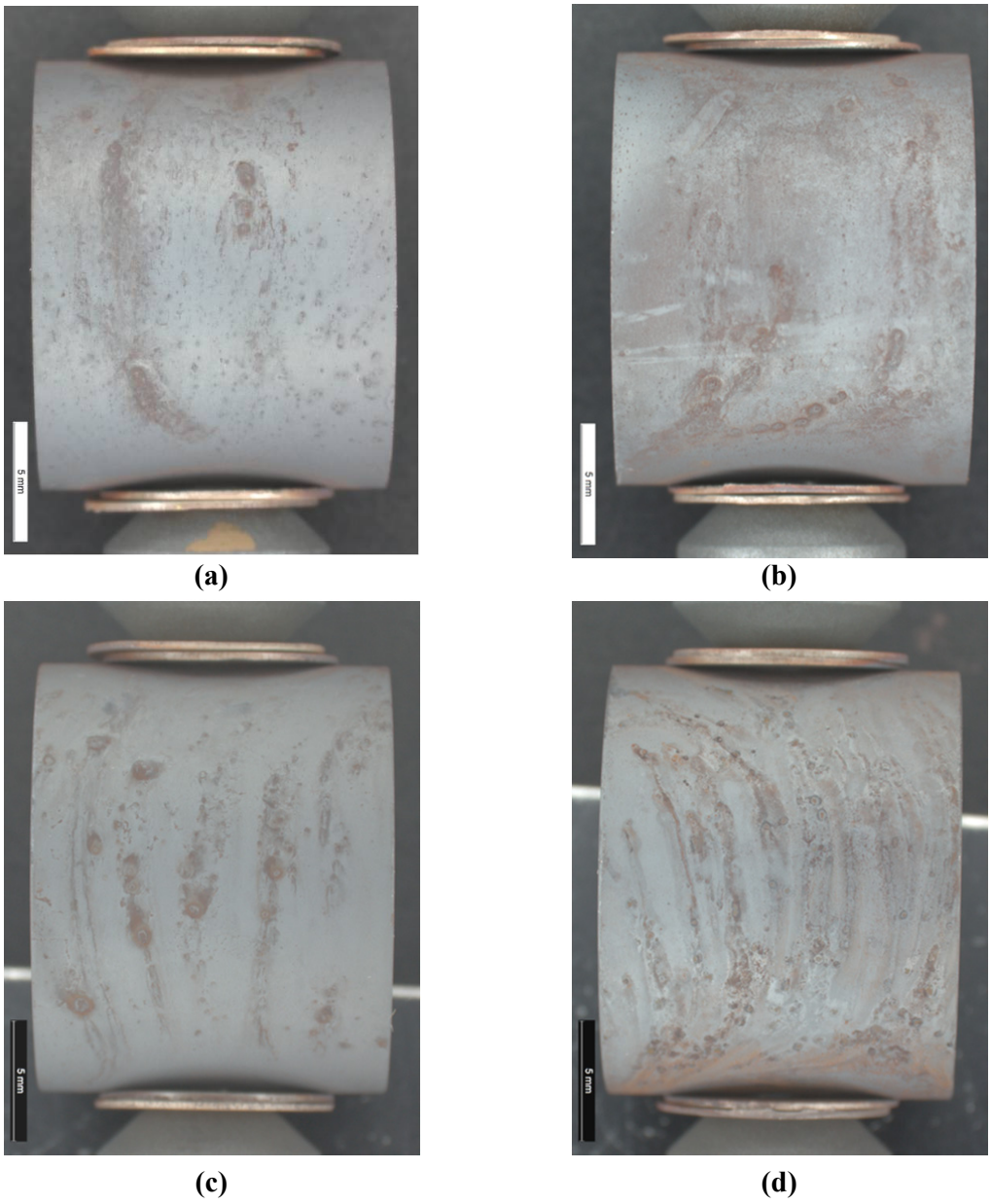

Figure 49: **Visual appearance of C-ring specimens after 740 hours pre-oxidation and additional 1000 hours exposure to different chloride contamination levels. (a) Reference specimen exposed to HTW without chloride during the overall test, (b) 700 hours pre-oxidation and additional 1000 hours with 5 ppb chloride, (c) same as (b) but 1000 hours with 20 ppb chloride, (d) same as (b) but 1000 hours with 50 ppb chloride.**

Figure 50 shows a detailed view on the surface of C-ring specimens that were exposed to a) 20 ppb chloride b) and 50 ppb chloride for 1000 testing hours. These figures reveal that some pits are active until the end of the experiment due to the shiny white colour in the middle of the pit (active area) and some are already covered by oxide.

As observed on both, pre-strained C-ring specimens and coupon specimens, pitting was more pronounced in terms of both, pit density as well as pit size at increased chloride concentrations.

Despite the more pronounced pitting, none of the pre-strained C-ring specimens revealed crack initiation in any case during all tests with a maximum chloride concentration of 50 ppb and test durations with up to 1000 hours of continuously increased chloride concentration.

Figure 51 shows "3-dimensional Scanning Electron Microscope (SEM)-Figures" (tilt angle 36 °) of coupon specimens tested at different chloride levels for 1000 hours. These SEM-figures clearly reveal that the structure and homogeneity of the oxide layer is affected by long term increased chloride concentrations. Comparing the reference specimen with the 50 ppb chloride specimens it becomes evident that the oxide structure of the oxide layer developed on the reference specimen is more homogenous.

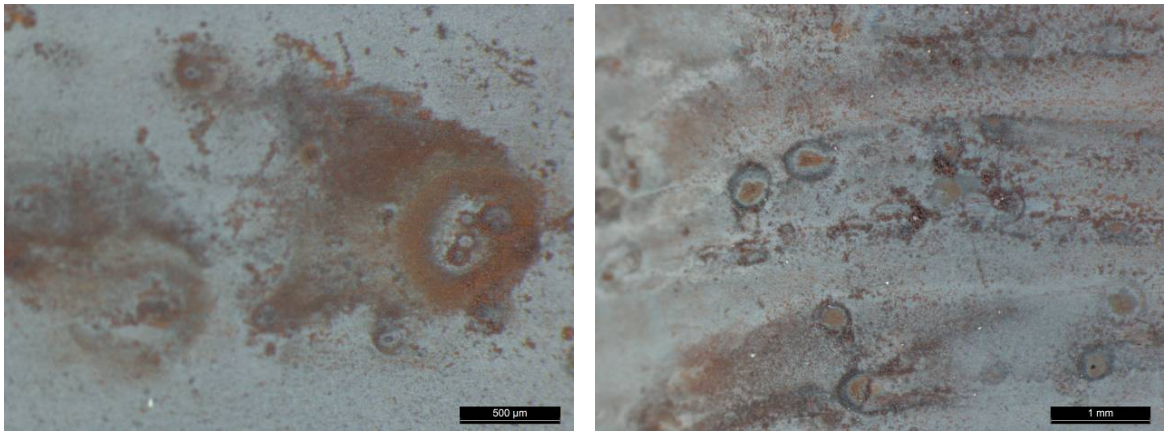

(a) **(b)**

Figure 50: **Detailed view on the surface of a C-ring specimen after 700 hours pre-oxidation and additional (a) 1000 hours with 20 ppb chloride and (b) 1000 hours with 50 ppb chloride.**

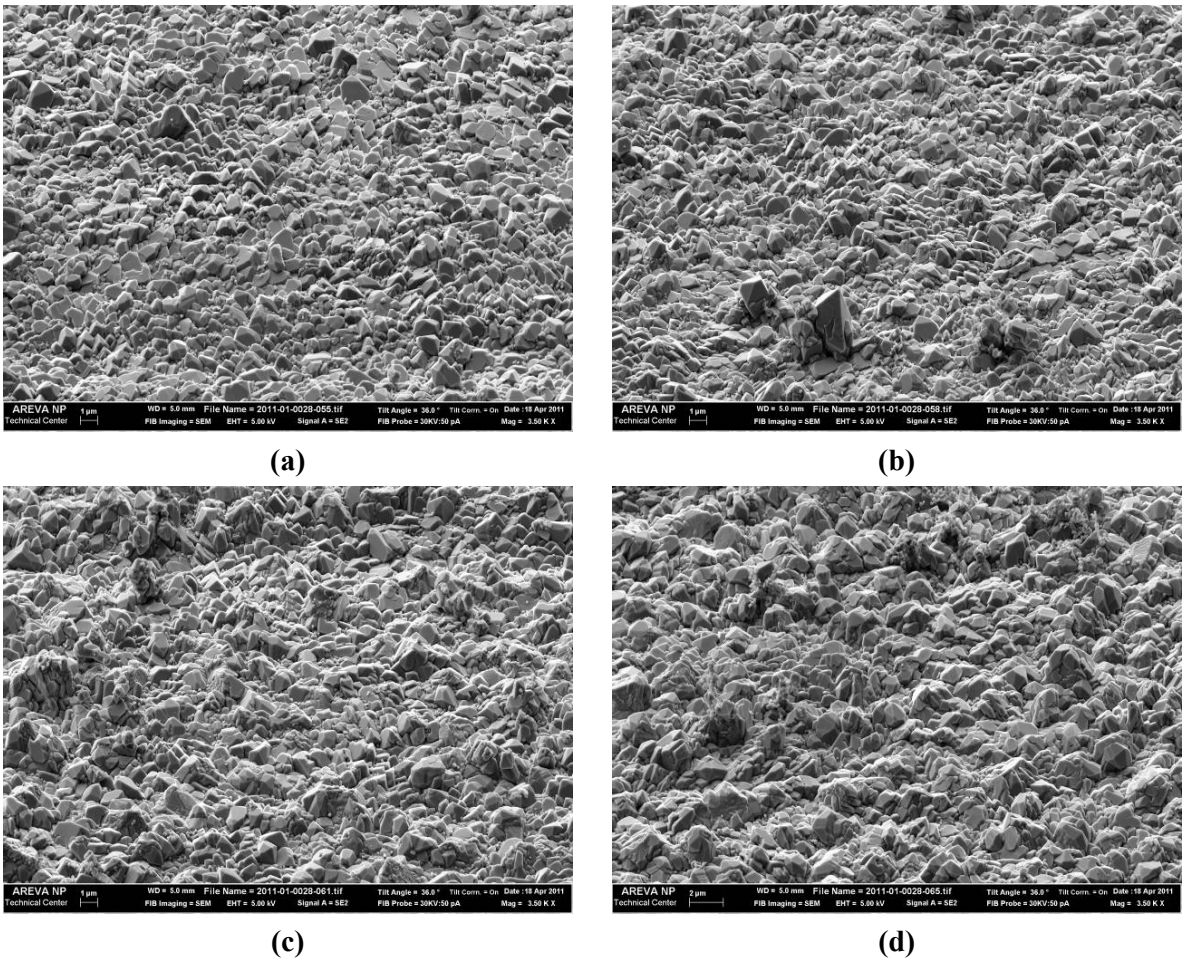

Figure 51: **SEM of coupon specimens after exposure to oxygenated HTW conditions. (a) Reference specimen, without chloride during the overall exposure test, (b) 700 hours pre-oxidation and additional 1000 hours with 5 ppb chloride, (c) 700 hours pre-oxidation and additional 1000 hours with 20 ppb chloride, (d) 700 hours pre-oxidation and additional 1000 hours with 50 ppb chloride.**

This observation is particularly true for the test with 1000 hours increased chloride concentration, where, compared to tests with shorter testing time at increased chloride concentrations, a more localized effect of chloride on both, the oxide structure and thickness was observed.

Figure 52 exemplarily shows the oxide layer thickness of coupon specimens and the characteristic appearance of pits after a test with 200 testing hours at different chloride concentrations. Figure 52 a1) to d1) show the typical appearance of pit like spots that were observed at the oxide surface. This clearly reveals an increase in both, diameter and depth of the pits with increasing chloride concentration. This shows that not only the number (see Figure 48 and Figure 49),

but also the size and depth of pits is increasing with increasing chloride concentrations during testing.

Figure 52 a2) to d2) clearly show a decrease of the oxide layer thickness with increasing chloride concentrations. This trend was observed in all test runs. The decrease of the oxide layer thickness was more pronounced for long term increased chloride concentrations and was increasing with higher chloride concentrations. The red lines in these figures indicate the interface between the inner (topotactic) and the outer (epitactic) oxide layer[13]. A decrease was observed in the thickness of both parts of the oxide layer, whereas the decrease seemed to be more pronounced in the outer part of the oxide layer.

As already mentioned above, in particular at very long testing times with increased chloride concentrations the observed appearance of the oxide layer changed. For long term increased chloride concentrations, in addition to the overall thinning of the oxide layer a more localized thinning of the oxide in combination with a less homogenous structure of the oxide layer was observed. In particular, the results from the test with 1000 hours increased chloride concentration showed a more pronounced decrease of the inner part of the oxide layer. This is of importance, since the inner part is the more protective part of the oxide layer regarding further corrosion of the LAS.

From the overall results it can be summarized, that the oxide layer decreased after continuous exposure to increased chloride contamination levels. This decrease was more pronounced, the higher the chloride contamination level was chosen during testing. Furthermore, in particular for very long exposure to chloride contaminated environments a more localized effect of increased chloride concentrations on the oxide structure was observed. In particular, a localized thinning and a more inhomogeneous structure of the oxide layer were observed after very long testing times at increased chloride concentrations.

[13] This interface was defined by the different appearance of the inner and outer part of the oxide layer in terms of size and morphology of the observed grains and crystals, respectively.

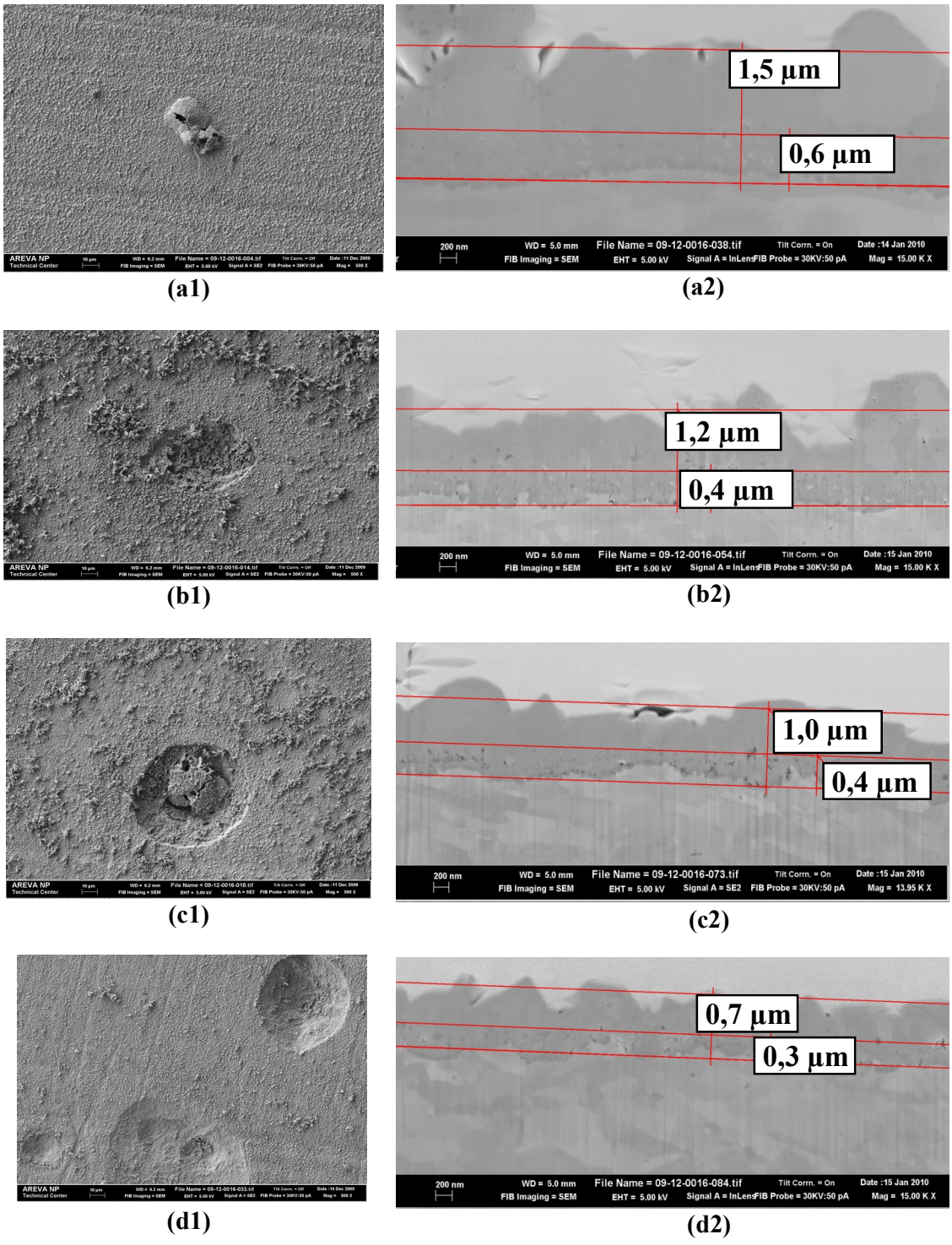

Figure 52: **SEM Figures of the oxide layer developed on coupon specimens after exposure to HTW and additional 200 hours at different chloride levels (a1) to (d1). Figures (a2) to (d2) show the oxide layer thickness that was determined after cutting the oxide layer. All specimens were pre-oxidized for approx. 450 hours. After the pre-oxidation the following chloride concentrations were adjusted, (a) < 2 ppb, (b) 5 ppb, (c) 20 ppb and (d) 50 ppb for 200 testing hours.**

5.4 Results of the Tests with 24 hour Chloride Transients

5.4.1 Results of EN and EIS Measurements during Exposure Tests

In addition to the tests with continuously increased chloride concentrations, three test runs with 24 hour chloride transients were performed. As for the tests with permanently increased chloride concentrations, EN and EIS measurements were performed during these tests.

The recorded current and potential noise data showed no significant effect of the single 24 hour chloride transients on the recorded noise signals of the specimens in the time domain. However, using the PSD (Power Spectral Density) calculated from the recorded current and potential noise data, a temporary effect of chloride transients on the corrosion behaviour of the specimen could be observed (see Figure 53). The transient causes a slight increase of the PSD, which totally recovered approx. 48 hours after the end of the transient.

Figure 54 depicts the EIS spectra obtained from tests with 200 testing hours after the end of the 24 hour chloride transients with different chloride concentrations. The impedance spectra of the coupon specimens clearly reveal a change of the oxide properties after the increase of the chloride concentration. This result is in good agreement with the results from the noise analysis. The change of the oxide properties occurs within a very short incubation time of about 5 hours after the increase of the chloride concentration.

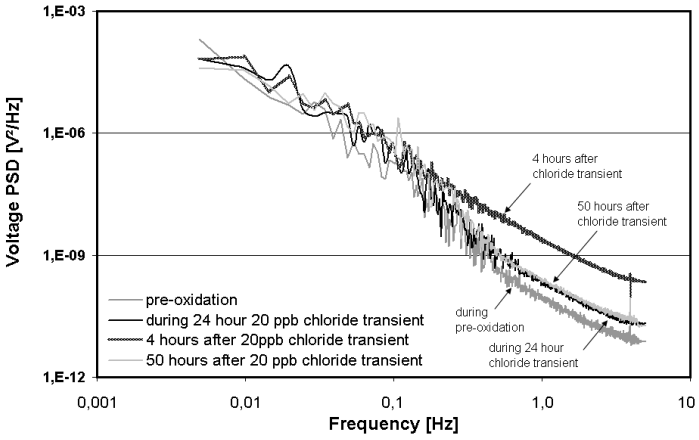

Figure 53: Power Spectral Density (PSD) of the potential noise calculated from the potential noise signal obtained from electrochemical noise measurements at coupon specimens before during and after a 24 hour 20 ppb chloride transient.

A Comparison of the effect caused by three different chloride levels with the reference specimens (tested without chloride transient) shows that a temporary effect was observed at all tested chloride concentrations. The observed change in impedance spectra was more pronounced at higher chloride levels (20 and 50 ppb chloride). After the chloride concentration was decreased to nominal operating condition levels (chloride concentration below 2 ppb) at the end of the 24 hour chloride transient, the nyquist plots indicate no long term memory effect caused by the temporarily increased chloride contamination levels.

The measured impedance curves returned to the same values as before the transients within several tens of hours after the temporary chloride transient. In the tests performed at lower chloride concentrations (5 and 20 ppb), total recovery occurred within 24 hours of the end of the chloride transient. In the tests performed at the highest chloride concentration (50 ppb), total recovery occurred approx. 48 hours after the transient occurred.

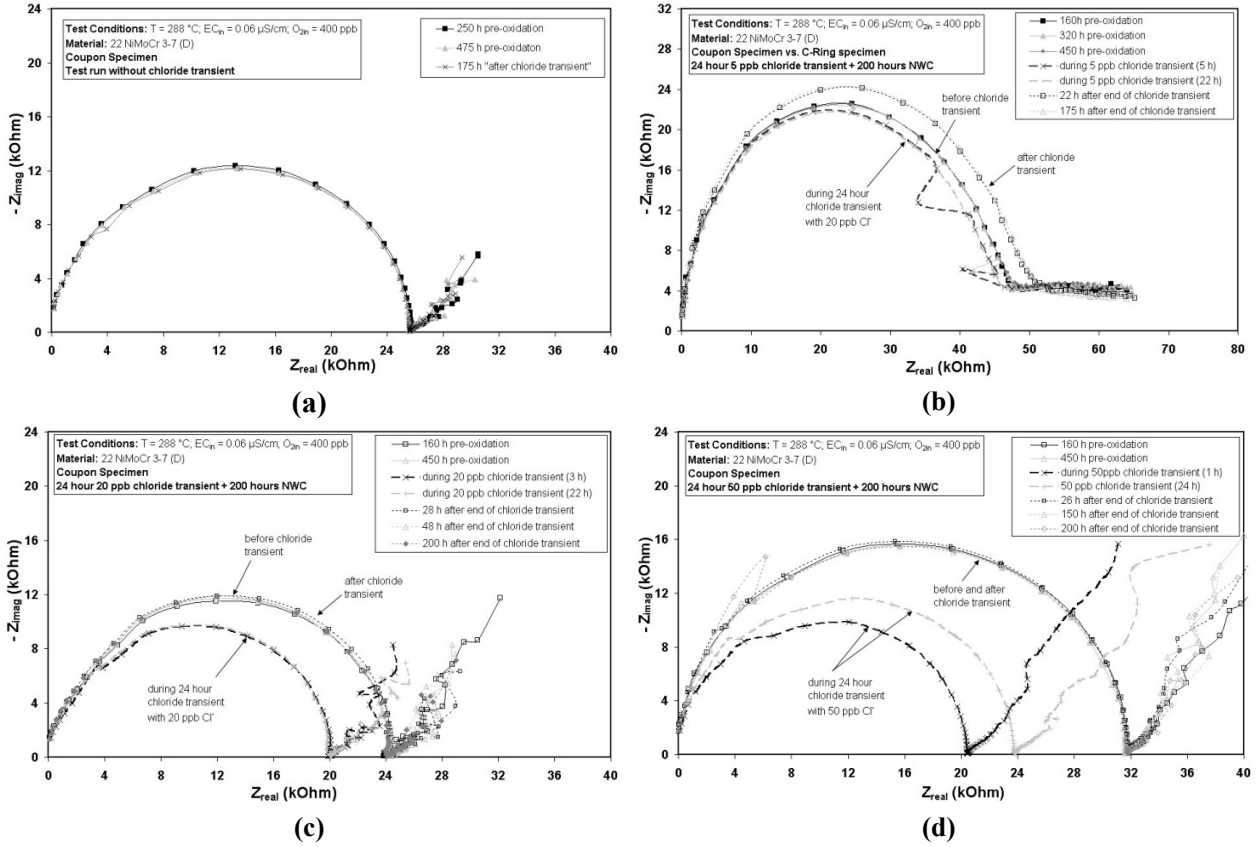

Figure 54: Nyquist plots of in-situ EIS-measurements at coupon specimens (a) without chloride transient and with 24 hour chloride transients with (b) 5 ppb, (c) 20 ppb and (d) 50 ppb chloride. After the end of the 24 hour chloride transient the water chemistry was adjusted to the same levels as before the transient.

5.4.2 Results of Post-Test Investigations

As for the tests with continuously increased chloride concentrations, all specimens of the transient test runs showed slight pitting after the end of the exposure tests, which is not unlikely to be observed under the chosen testing conditions, as described previously.

The visual appearance of both, the unstressed coupon specimens and the pre-strained C-ring specimens was analysed after the end of exposure tests in HTW by stereomicroscopy and SEM investigations.

During these investigations, no clear effect of the 24 hour chloride transients on the visual appearance of the specimen surface after the end of the tests was observed (see Figure 55).

For all investigated C-ring specimens, the single chloride transient did not cause crack initiation at any of the pre-strained C-ring specimens in any case (see Figure 55).

After the end of the 24 h chloride transients the tests were continued for different test durations from 100 up to 500 hours under nominal operating conditions without deliberate addition of chloride (chloride concentration < 2 ppb as specified in (VGBPowerTech, 2006)). Investigations on the oxide layer thickness were performed on coupon specimens from all test runs after the transient tests. These investigations showed no significant change of the oxide thickness due to the 24 hour chloride transients.

No effect of the temporary increase of the chloride concentration was seen by analyses of the oxide layer thickness already after 100 hours of operation under nominal water chemistry conditions after the end of the transient. Comparing the oxide layer thickness that was analysed on the reference specimens (tested without chloride transient during the whole test) with those obtained at all specimens exposed to different temporary chloride concentration transients, no significant difference in the oxide layer thickness was revealed in all tests (see e.g. Figure 56). The visual appearance of the specimens, as analysed by SEM, also shows no effect of the temporary increase of the chloride concentration on the number, diameter and depth of pit like spots at the oxide surface.

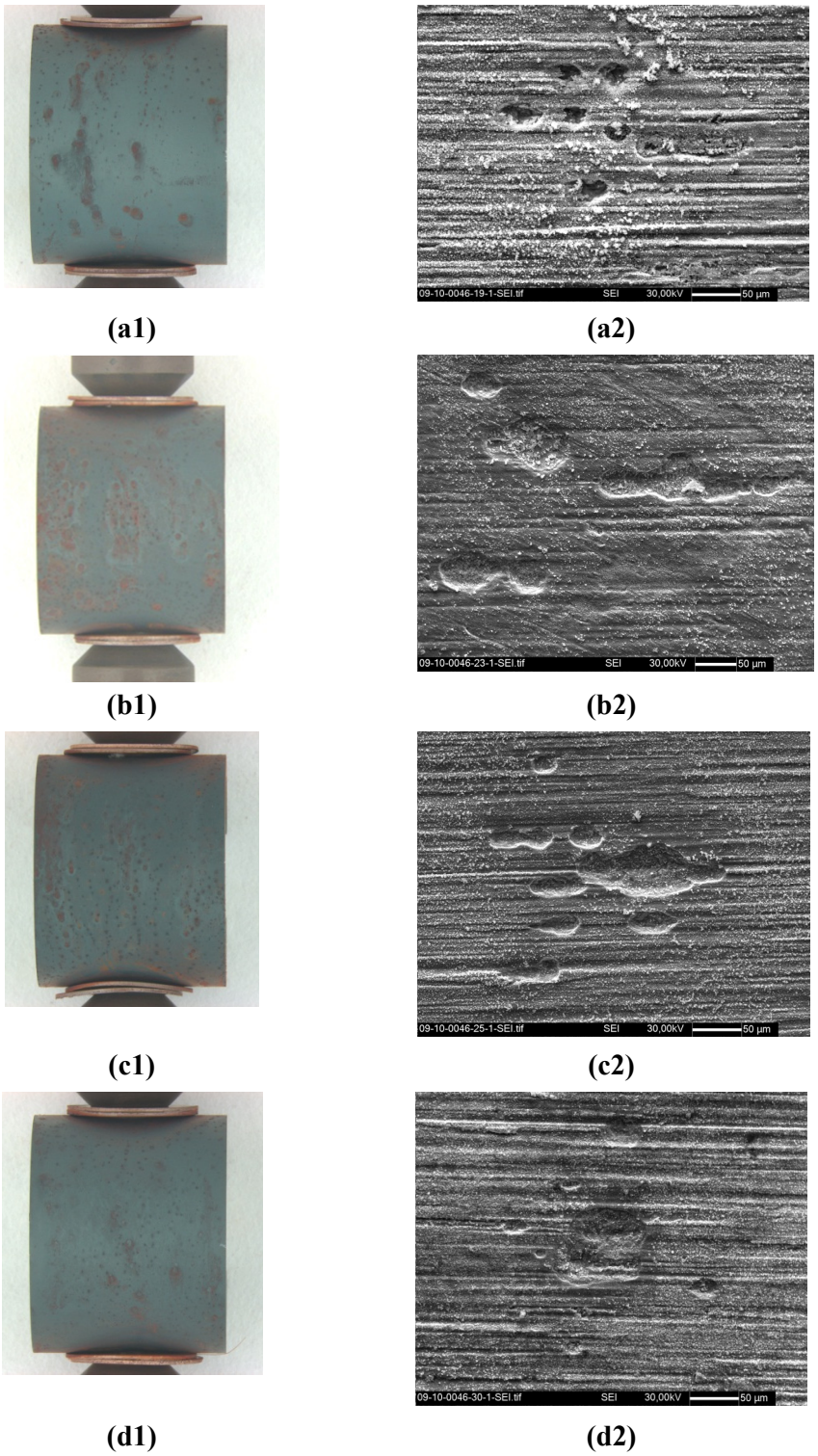

Figure 55: **Stereomicroscopy and SEM of C-ring specimens. The specimens were pre-oxidized for 400 hours, followed by a 24 hour chloride transient and additional 500 testing hours under specified HTW-conditions. The chloride levels during the 24 hour transient were adjusted to (a) without chloride (< 2 ppb), (b) 5 ppb, (c) 20 ppb and (d) 50 ppb chloride. None of the pre-strained C-ring specimens revealed crack initiation due to the chloride transients.**

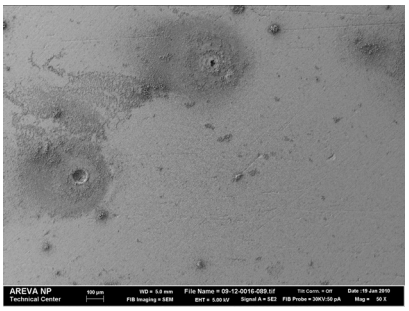

(a1)

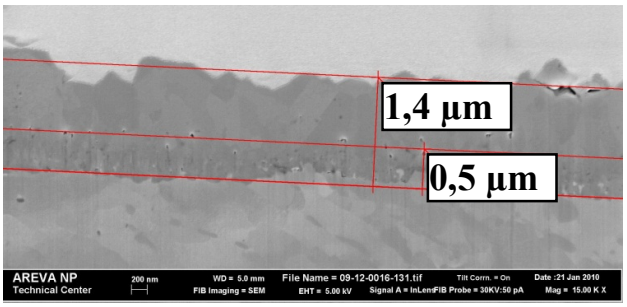

(a2)

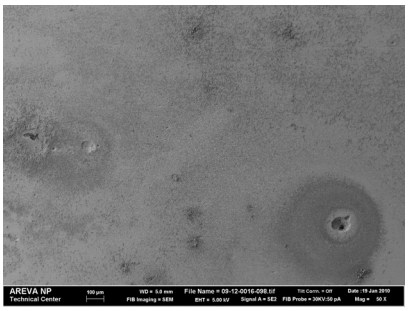

(b1)

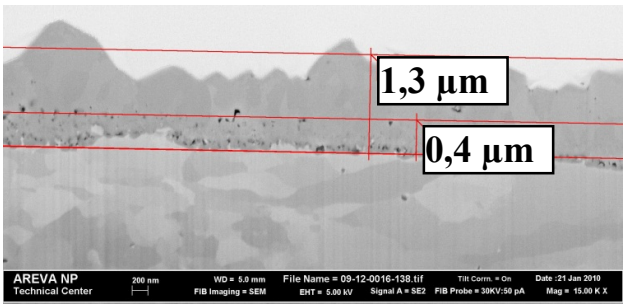

(b2)

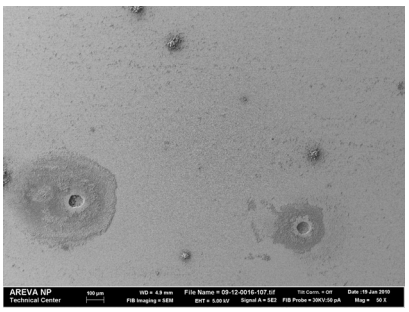

(c1)

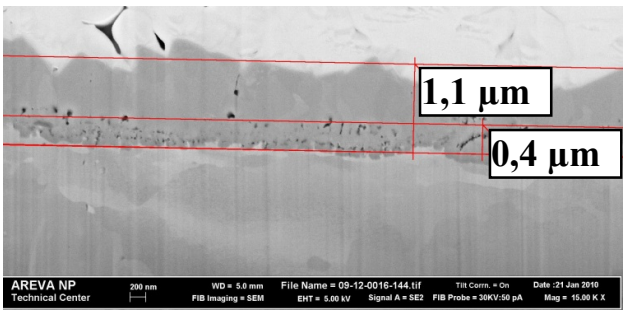

(c2)

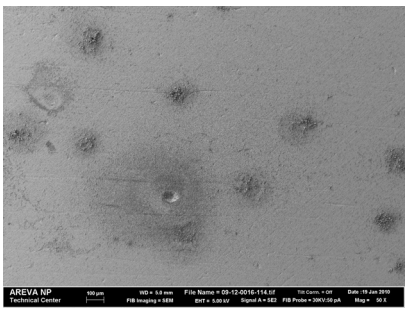

(d1)

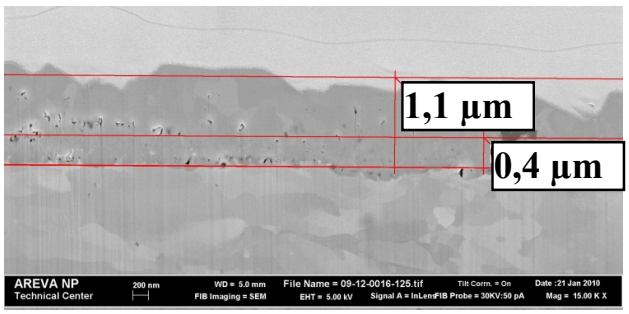

(d2)

Figure 56: SEM Figures of the oxide layer of coupon specimens after a 24 hour chloride transient and additional 500 hours under specified water chemistry conditions. The chloride levels during the 24 hour transient were adjusted to (a) without chloride (< 2 ppb), (b) 5 ppb, (c) 20 ppb and (d) 50 ppb chloride. Figures (a2) to (d2) exhibit the oxide layer thickness after cutting of the oxide layer. Prior to the chloride transients all specimens were pre-oxidized for approx. 450 hours.

5.5 Studies of the Oxide Layer Composition[14]

In order to study the effect of increased chloride concentrations on the oxide layer properties in detail, investigations on the chemical composition of the oxide layer were performed. Initially performed EDX analyses did not reveal any deeper insight to the chemical properties and, in particular, possibly increased chloride concentrations due to the detection limit of the method (approx. 0.1 wt.-%). Hence, additional investigations were performed using Auger-Electron Spectroscopy (AES). This method is much more sensitive to increased chloride concentrations. In order to perform a scan across the oxide layer thickness using this method, firstly a cut across the oxide layer was performed using the FIB-technique, as schematically shown in Figure 57. Since this method is a qualitative analysis method, two specimens from the same test run were compared. The chosen specimens were a reference specimen, tested without increased chloride concentration during the whole exposure test, and a specimen from the test run with 200 hours 50 ppb chloride concentration.

The visual appearance of the two specimens after the FIB-cut of the oxide layer is shown in Figure 58. This Figure illustrates the thinner oxide layer after testing at 50 ppb chloride for 200 hours compared to the reference specimen.

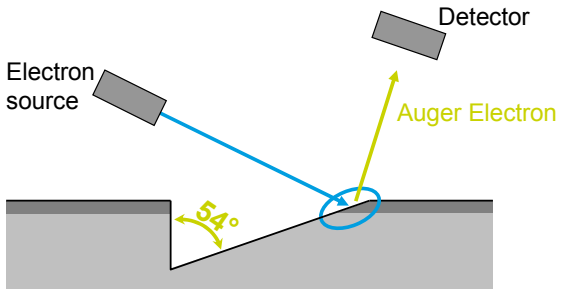

Figure 57: Simplified principle sketch of the preparation of the oxide layer prior to AES investigations.

[14] The studies of the oxide layer composition were performed in co-operation with University of Erlangen, Institute for Surface Analysis. Helga Hildebrand, who performed the experimental work using Auger Electron Microscopy and ToF-SIMS, is gratefully acknowledged.

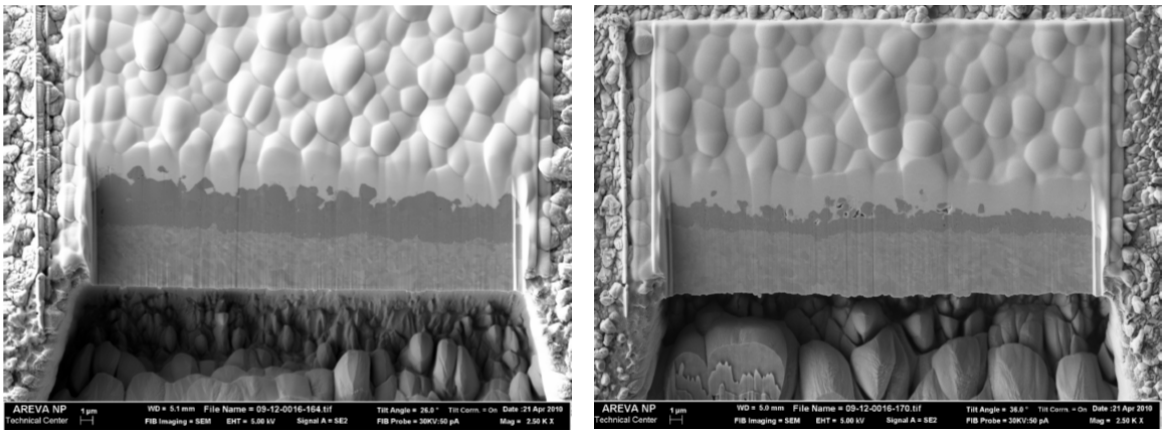

(a) **(b)**

Figure 58: (a) Cut across the oxide layer of the references specimen that was exposed to HTW for 740 hour without increasing the chloride concentration (specimen tilt 0°, angle correction 26°). (b) Cut across the oxide layer of coupon specimen that was pre-oxidized for 350 hours and additional 200 hours at a chloride concentration of 50 ppb (specimen tilt -10°, angle correction 36°).

Figure 59 a) depicts the oxide layer of the reference specimen together with the performed line scan. The white layer on the top of the oxide represents the platinum layer that was sputtered to the surface prior to cutting of the oxide using the FIB-technique. Beneath this layer the oxide is clearly visible. The analysis of the composition of the oxide layer was performed from position 1 towards position 2.

Beginning from position 1, the chemical analysis clearly reveals that the oxygen concentration in the oxide layer is increased compared to the base metal (position 2). The iron concentration in this line scan is increasing in the base metal compared to the oxide layer. Within the whole element analysis of the oxide layer composition, no increase in the chlorine concentration was observed, as expected.

In order to study the effect of increased chloride concentrations on the oxide composition after testing in HTW, a second specimen from the same test run that was exposed to a chloride concentration of 50 ppb for 200 hours was investigated using the same technique.

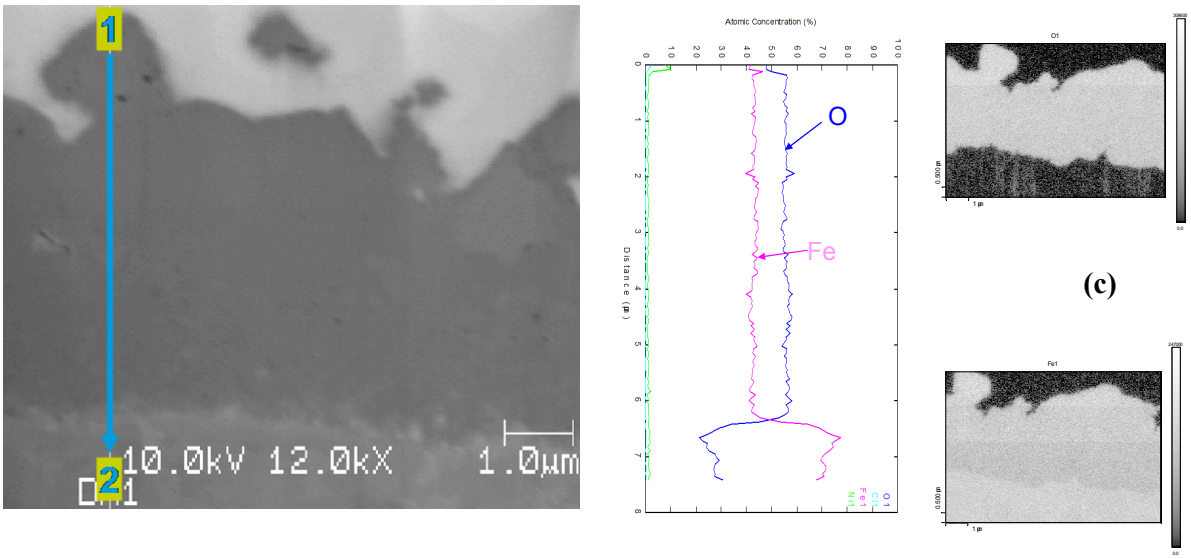

Figure 59: Results of AES using a reference coupon specimen that was exposed to HTW for 740 hours without increased chloride concentration.
(a) Position of the line-scans across the overall oxide layer, (b) representation of the concentration of different elements (O, Fe, C and N) across the oxide layer in atom-%, (c) visual representation of the oxygen and (d) iron concentration in the analysed area.

The investigated area of this specimen is shown in Figure 60. The chemical composition of the oxide layer is shown for the whole line scan in Figure 60 b). As for the reference specimen, the difference between the oxide layer and the base metal is very clear in terms of concentrations of the analysed elements, in particular oxygen and iron. The chlorine concentration was below the detection limit of the method for the whole line scan. This is also shown in Figure 60 c) to e) where the concentration of different elements is plotted for the whole scanned area. Again, no increased chlorine concentration was observed in the oxide layer.

Since neither EDX nor AES were capable of detecting any traces of increased chlorine concentrations in the area of the oxide layer, further analyses were performed using ToF-SIMS (Time of Flight – Secondary Ion Mass Spectroscopy). This method is much more sensitive to small concentrations of elements. It has already been demonstrated in the past that SIMS is capable of characterising the molecular composition of oxide layers on metals and remarkable investigations have already been performed in this field (Adriaens et al., 2001).

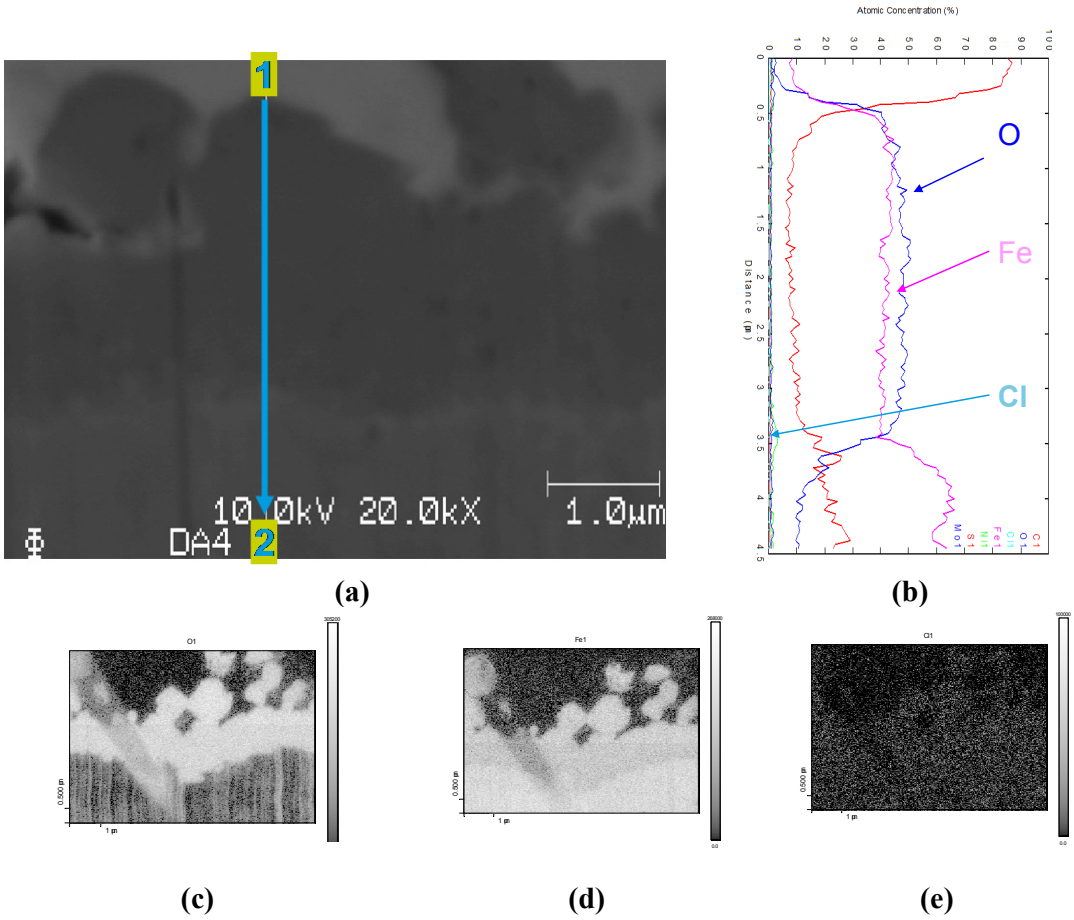

Figure 60: Results of AES performed on a coupon specimen after 350 hours pre-oxidation and additional 200 hours of exposure at a chloride concentration of 50 ppb chloride.
a) Position of the line-scan across the oxide layer, b) representation of the concentration of different elements across the oxide layer in atom-%, c) visual representation of the oxygen, d) iron, and e) chloride concentration in the analysed area.

In order to allow in-depth analysis of the chemical composition of the oxide layer, the so-called dual beam depth profiling was applied. Using the "dual beam mode", an intense, high-energy pulsed analysis gun (Bi-beam) and a low-energy sputter gun (Cs-beam) are combined. The in-depth analysis of the surface area is achieved by an ion bombardment applied with the primary beam, causing a controlled sputtering of the sample surface, in the case of this work a caesium beam. After this controlled erosion, the freshly exposed surface is analysed using the analysis beam (in this work a bismuth beam). The bismuth beam causes the extraction of secondary ions that are accelerated to a detector where these secondary ions are analysed and hence, an analysis of the composition of the oxide layer is possible. By applying this method, a crater shaped pit is formed in the surface of the specimen as schematically shown in Figure 61 and an in-

depth analysis of the chemical composition of the oxide layer is possible (Niehuis and Grehl, 2001, Vickerman, 2001).

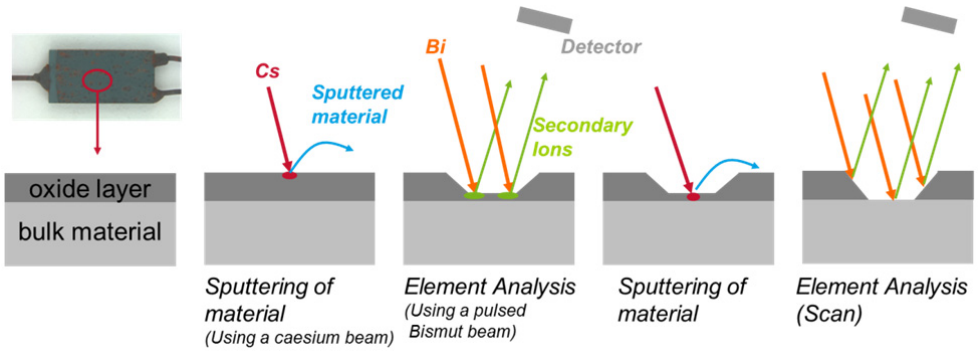

Figure 61: Simplified schematic visualization of the applied dual beam depth profiling using ToF-SIMS in the so-called dual beam mode. In order to apply a depth profile of the chloride distribution the so-called dual beam depth profiling was applied.

For the TOF-SIMS investigations, the same specimens as for the auger electron microscopy were used. The crater shaped pit in the surface that is caused by the applied analysis method (schematically shown in Figure 61) is also clearly visible in the analysis results summarized in Figure 62. In this Figure, the results obtained at the reference specimen (a – d) are directly compared to those from the specimen that was exposed to 50 ppb for 200 hours (e – h). Comparison of the presence of iron oxides clearly reveals that the oxide layer thickness at the reference specimen is thicker compared to the specimen from the 50 ppb test. For the reference specimen, iron oxides are clearly detectable for the whole scan, whereas at the 50 ppb specimen the whole oxide layer was removed by the eroding primary beam after the analysis. In Figure 62 f) the difference between oxide layer and base metal is clearly distinguishable due to the partial presence of iron oxides, whereas in Figure 62 b) iron oxides are clearly detectable for the whole analysed area.

Regarding the chloride concentration, the results from the reference specimen show some chloride signals distributed over the whole analyzed area and a slightly increased chloride concentration in the outer parts of the oxide layer, which may be designated as the acquired “chloride noise” due to pollutions from the environment and sample handling.

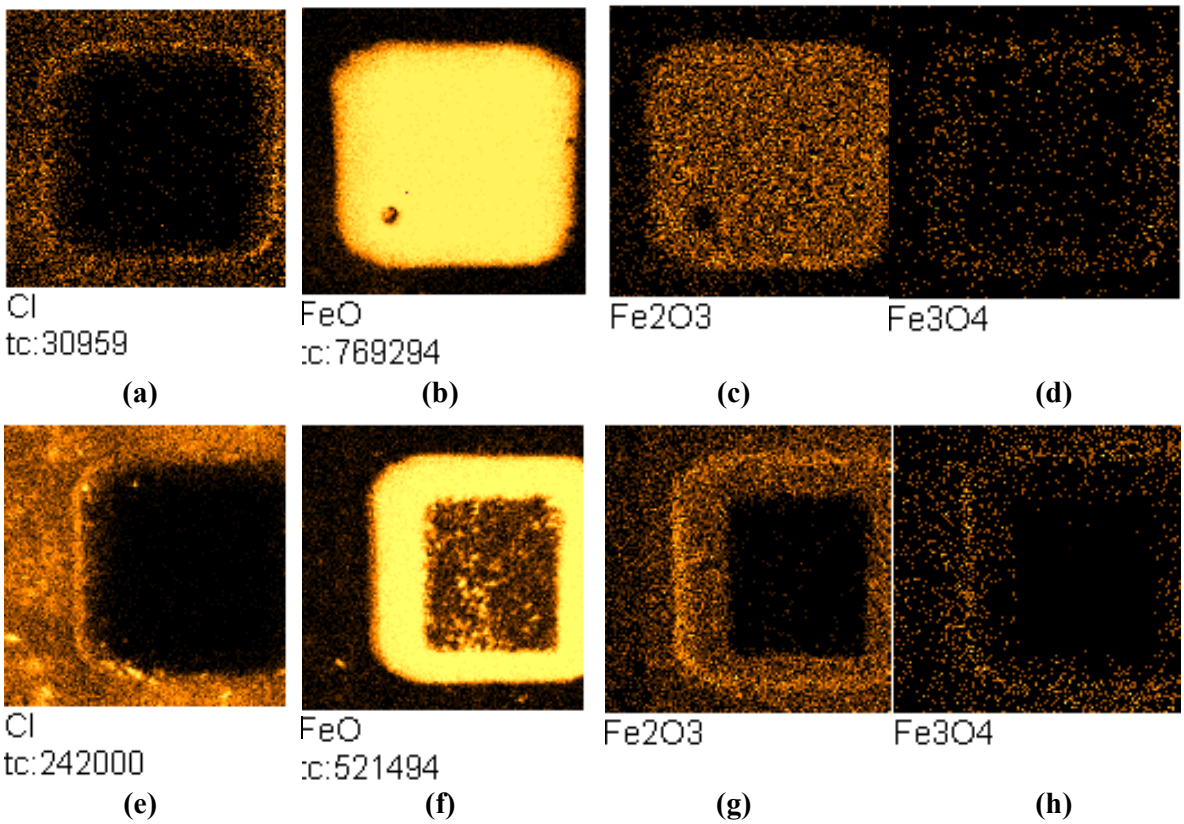

Figure 62: Results of TOF-SIMS investigations on a reference specimen (a-d) that was exposed to HTW for 740 hours without increased chloride concentration and a coupon specimen that was exposed to 50 ppb chloride for 200 hours after 350 hours pre-oxidation (e-f).

Comparing these results with those obtained from the 50 ppb chloride test clearly indicates a much higher chloride concentration in the oxide layer of the specimen from the test at increased chloride concentration (Figure 62 a and e). At this specimen, the chloride concentration is clearly increased in the outer parts of the oxide layer and some local spots with remarkably increased chloride concentrations are observed. This gets even clearer when Figure 63 is taken into account. In this Figure, a top view and depth profiles of a) the reference specimen and b) the specimen from the 50 ppb test are shown. These Figures clearly reveal that the chloride concentration is much higher in the oxide of the 50 ppb specimen and, in particular, some localized areas with locally increased chloride concentrations are detected. Depth profiles that were performed to analyze the in depth penetration of chloride into the oxide layer are also shown in this Figure for the depth profile A-A and B-B, respectively.

From the depth profiles it is obvious that no chloride penetration into the oxide layer occurs at the reference specimen. At the 50 ppb specimen, penetration of chloride into the oxide layer occurs. The penetration is in particular pronounced at spots where the chloride concentration is locally increased (chloride islands), as observed in the top view. Hence, it can be concluded that at such chloride islands, where the chloride concentration is locally increased, penetration of chloride into the oxide layer towards the interface between the oxide layer and the base metal occurs.

In addition to the analyses performed on specimens from tests with permanently increased chloride concentrations, also specimens from the transient tests were investigated to study the effect of chloride transients on the oxide layer structure. The emphasis of these investigations was to study possible long term memory effects of a single chloride transient on the chemical composition of the oxide layer.

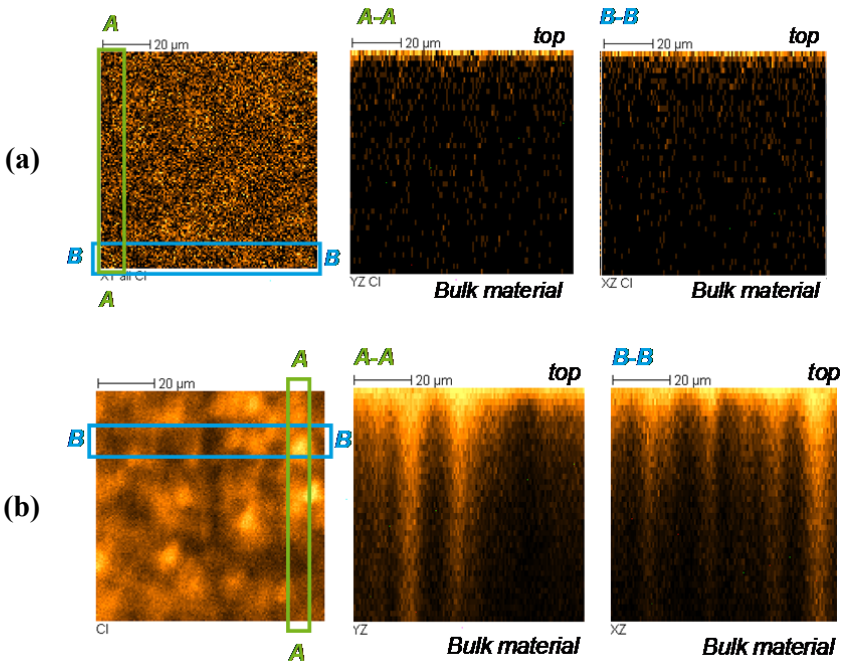

Figure 63: Top view and depth profiles of the chloride signal derived from TOF-SIMS analyses that were obtained using (a) a reference specimen that was exposed to HTW for 740 hours without increased chloride concentration and (b) a coupon specimen that was exposed to 50 ppb chloride for 200 hours after 350 hours pre-oxidation.

The specimens that were chosen for the analyses are specimens from the test run with a 24 hour chloride transient and additional 100 testing hours without increased chloride concentration. This test was chosen since the testing time after the transient was the shortest and hence, if memory effects are present, some effect of the single chloride transient should still be detectable. The reference specimen, tested without chloride transient during the overall test, and a second specimen tested with a 24 hour 50 ppb chloride transient were chosen to compare the results.

Figure 64 shows the results obtained at the reference specimen (a-d) and at the specimen with the 24 hour 50 ppb chloride transient (e-h). As it is obvious from the presence of the iron oxides (b and f) in these analyses, the oxide layer was somewhat thicker in these test runs, since using the same sputtering procedure and time, the oxide layer was not fully penetrated by the method for both investigated specimens. Hence, the overall analyzed area is positioned in the oxide layer in both specimens.

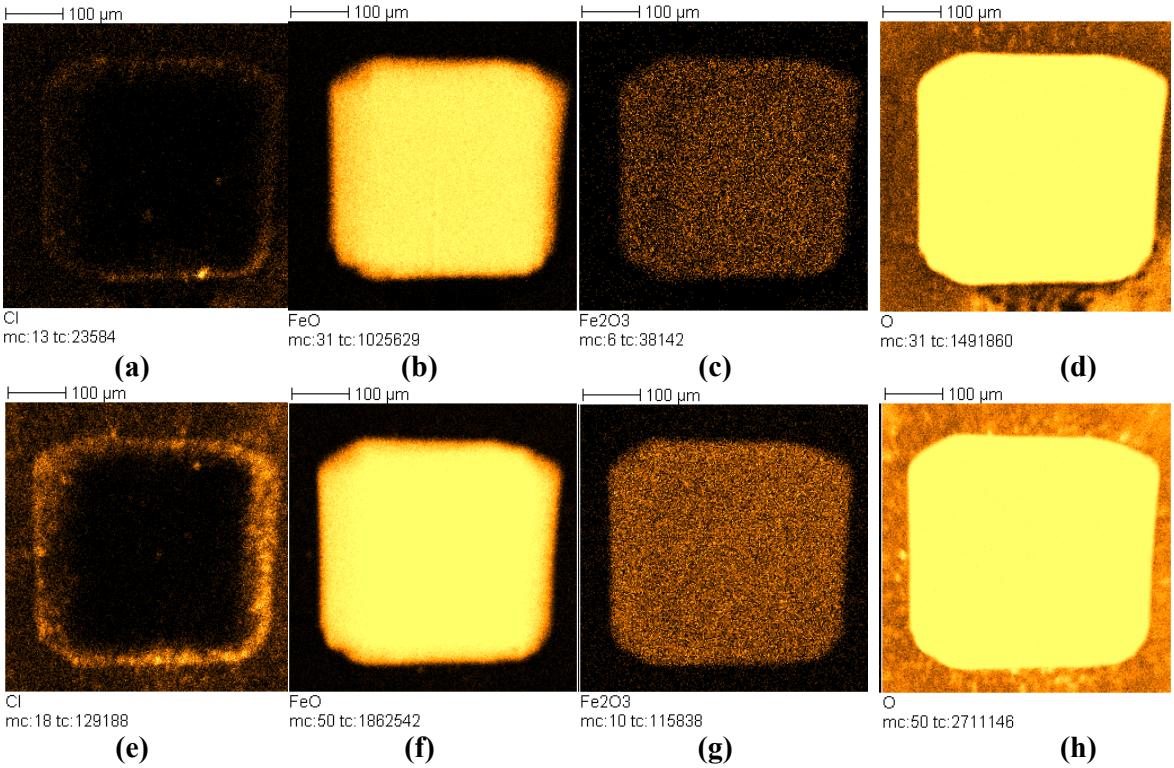

Figure 64: Results of TOF-SIMS analyses using a reference specimen tested without chloride for 850 hours of exposure to HTW (a-d) and a specimen that was exposed to HTW for 560 hours prior to a 24 hour 50 ppb chloride transient followed by 100 hours of exposure to high-purity HTW (e-f).

A comparison of the results from the chloride scan reveals that the chloride concentration on the specimen with the chloride transient is slightly increased compared to the reference specimen. In particular the area directly below the surface of the oxide shows some increased chloride concentration, whereas the concentration directly at the surface seems to be relatively low, but still higher as compared to the reference specimen.

The results shown in Figure 65 reveal that some spots with localized, high chloride concentrations occur even after additional testing time without chloride. The depth profile depicted in Figure 65 b) shows that even at spots with locally high chloride concentration nearly no penetration of chloride into the oxide layer is present.

As shown in Figure 64, the chloride concentration directly at the specimen surface is very low, whereas in the area directly underneath the surface of the oxide layer still some increased chloride concentration was observed. Comparing these results with the results from the test with permanently increased chloride concentration shows that chloride that is in a first step adsorbed on and consequently absorbed in the oxide layer seems to desorb again during immersion in pure HTW after the end of the chloride transients.

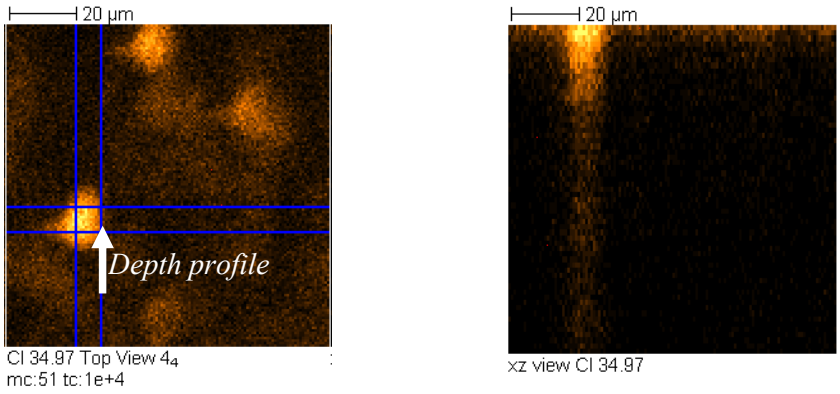

Figure 65: Results of TOF-SIMS investigations showing (a) a top view of the chloride concentration that was analysed on the surface of the specimen from the test run with the 50 ppb chloride transient and (b) a depth profile showing the in depth distribution of chloride in the cutting area that is illustrated with an arrow in (a).

It can be summarized that already 100 hours after a 50 ppb chloride transient nearly no increase of the chloride concentration was observed in the analyzed surface area. Hence, it may be concluded that desorption of chloride occurs relatively fast after the end of the transient. The results furthermore indicate that the processes that have been observed for the long term increased chloride concentrations (increased chloride concentration in the outer part of the oxide layer and localized penetration of chloride into the oxide layer) do not occur during short term transients, or are fully reversible within a short time period after the transient. Hence, no strong memory effect of the single chloride transient could be observed regarding the chemical composition of the oxide layer after the end of the exposure test.

This result is in good agreement with results from the in-situ electrochemical measurements which showed no measurable memory effect of the single chloride transient after approx. 48 hours after the end of the transient. In addition, also the post-test macroscopic and microscopic investigations revealed no significant memory effect due to the temporary chloride transients.

5.6 Summary and Discussion

5.6.1 Overall Summary

A change in electrochemical properties of the oxide layers on both, coupon specimens and pre-strained C-ring specimens due to deliberately increased chloride contamination levels was observed online during testing through electrochemical measurements. Using electrochemical noise analysis and electrochemical impedance spectroscopy, a decrease of the charge transfer resistance (R_{ct}), a controlling parameter for the kinetics of electrochemical corrosion processes, was observed due to the deliberate increase in the chloride concentration in the HTW. This change occurred after an incubation period of approx. 5 hours after increasing the chloride concentration furthermore depending on the actual chloride concentration.

The tests revealed that the change of the electrochemical properties of oxide layers depends on the chloride concentration to which the LAS is exposed. The presence of higher chloride levels results in a more pronounced change in oxide layer properties.

The decrease in R_{ct} therefore indicates higher corrosion rates of the investigated LAS after an increase in the chloride concentration, which results in a new stationary condition with increased corrosion activity of the LAS after a certain time period of testing at increased chloride concentrations. This was observed for all investigated chloride contamination levels.

Furthermore, longer testing periods at increased chloride concentrations seem to have an increasingly detrimental effect on protective oxide layer properties, since the R_{ct} further decreases during longer time periods at increased chloride concentrations, until a steady state is reached, where no more change is observed. This indicates that a new stationary condition is established after a certain time period of exposure to increased chloride concentrations.

The post-test examinations by stereo microscope and SEM at specimens from tests with permanently increased chloride contamination levels revealed that pitting and film-thinning is more pronounced at higher chloride concentrations. This result is in accordance with the results of the electrochemical measurements performed during testing which denoted a change of the oxide layer properties due to the continuously increased chloride concentration on-line during testing.

Measurements of the oxide layer thickness showed that the oxide layer thickness following tests with 50 ppb chloride for 200 h decreased to nearly 50 % of the value of a reference specimen, tested under specified pure water chemistry conditions (without chloride). The comparison of test results from specimens tested at different chloride concentrations showed that the oxide layer thickness decreased with exposure to increased chloride concentrations for all investigated chloride contamination levels. From the results of the oxide layer thickness, it can be derived that after initial thinning of the oxide layer due to the increased chloride contamination level, a new stationary condition establishes after longer exposure times to chloride containing environments. This is indicated by both, results from electrochemical methods (EN and EIS) as well as by the decrease in the oxide layer thickness (sees Figure 66).

After longer test durations with increased chloride concentrations, a new balance between the increased oxide solubility due to the increased chloride concentration and the re-development of the oxide layer seems to establish and therefore no sustained thinning of the oxide layer has been observed for long testing durations at increased chloride contamination levels (see Figure 66).

Testing at increased chloride concentrations for long testing durations resulted in a more localized thinning of the oxide layer, and, in particular, a locally pronounced thinning of the inner (topotactic) oxide layer was observed. In addition, the results after 1000 hours of testing at increased chloride concentrations indicate that the oxide layers develop a more inhomogeneous structure after long term exposure to increased chloride concentrations than a sustained overall thinning as it has been observed in tests with up to 500 hours increased chloride concentrations.

The ToF-SIMS investigations revealed that i) chloride is generally absorbed in the outer part of the oxide layer and ii) chloride islands with locally high chloride concentration develop at which significant penetration of chloride into the oxide layer occurs.

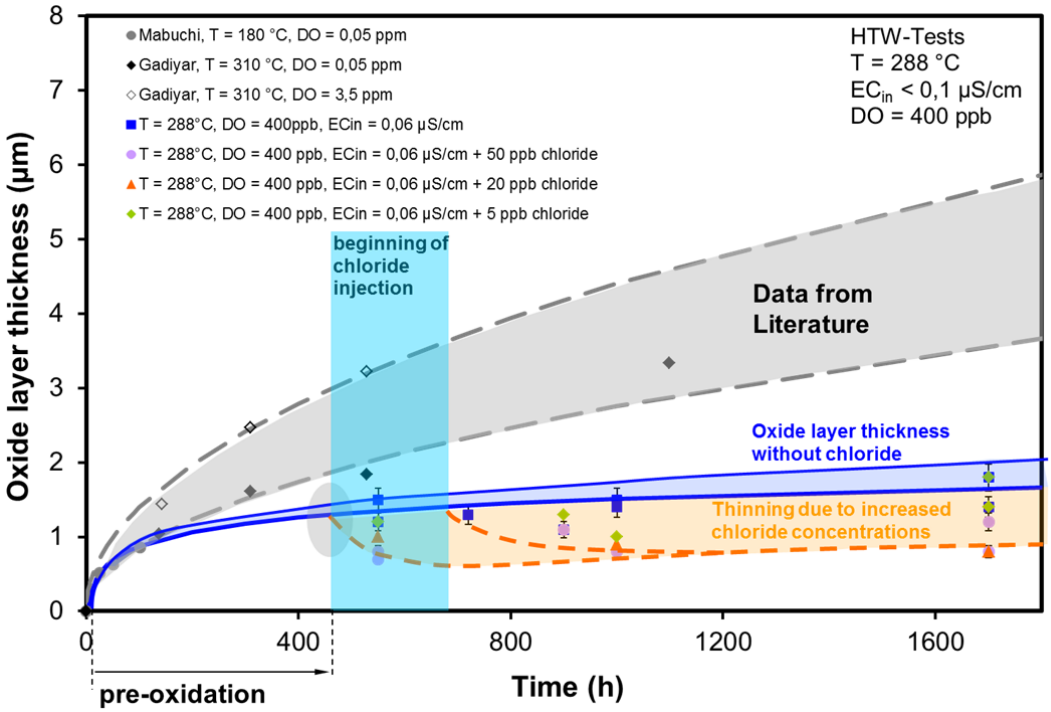

Figure 66: Comparison of oxide layer thickness proposed by literature data (Gadiyar and Elayathu, 1980) (Mabuchi et al., 1991) and the oxide layer thickness values from this investigations. The data taken from literature were obtained by weighting the specimens before and after exposure to HTW and calculation the corresponding oxide layer thickness, whereas, the data of this investigation were directly measured. The thickness of the oxide layer, as proposed by this figure, decreases due to the increased chloride concentration compared to specimens tested without chloride.

From the results of the 24-hour chloride transient tests, it appears that the detrimental effect of increased chloride concentrations on the protective oxide layer properties recovers within at the latest 48 hours after the end of the chloride transient, i.e. after the complete disappearance of dissolved chloride in the aqueous environment.

Hence, it can be concluded that there seems to be no long-term memory effect of temporarily increased chloride concentrations on the general corrosion behaviour of LAS with smooth surfaces. Total recovery of the chloride-induced effects was observed approx. 24 hours after the small chloride transient ceased (chloride concentration 5 ppb) and approx. at the latest 48 hours after the highest chloride transient (chloride concentration 50 ppb). EN and EIS measurements showed a temporary change of the corrosion activity during the transients, but no sustained effect after the end of the transient. In fact, any change due to single chloride transients van-

ished already some tens of hours after the end of the transient. Measurement of the oxide layer thickness after testing did also not indicate any significant effect of the 24-hour chloride transients on the oxide layer thickness after the end of the exposure tests. SEM on coupon and pre-strained C-ring specimens did also not indicate a significant effect of the chloride transients on the structure and appearance of the oxide layer. These results were also confirmed by the applied ToF-SIMS investigations, where no significant difference between chloride concentrations in the oxide layer of a specimen after a 24 hour 50 ppb chloride transient compared to a reference specimen were observed. As shown by chloride depth profiles, no penetration of chloride into the oxide layer was observed after the transient test. In addition, nearly no chloride was detected at the surface of the oxide layer.

From this observation it arises, that chloride, which is adsorbed on the surface of the oxide layer, respectively absorbed in the oxide layer desorbs from the oxide layer into the bulk solution immediately after the end of the chloride transient. As indicated by the results of the applied on-line monitoring techniques, this process initiates directly after the end of the transient. From the ToF-SIMS analyses that were performed 100 hours after the end of the transient no drastic residual effect of the single chloride transient was detected on the chemical composition of the oxide layer.

Taking these results into consideration it follows, that the effect of chloride transients on the corrosion behaviour of the tested specimens appears to recover completely in specimens with smooth surfaces with additional testing time under pure water chemistry conditions.

None of the tested C-Ring specimens indicated any crack initiation due to permanently increased chloride contaminations with up to 1000 hours and a maximum chloride concentration of 50 ppb or temporary chloride transients. Therefore, it can be concluded that there seems to be no immediate and drastic increase in crack initiation susceptibility for pre-strained specimens, at least for smooth surfaces and small chloride concentrations up to 50 ppb within the tested time frame. This will be discussed in more detail in chapter 6.5 which is focussing on the effects of chloride on crack initiation.

5.6.2 Mechanistic Aspects on the Effect of Chloride on General Corrosion

As it has been observed by the ToF-SIMS investigations, chloride is absorbed in the outer part of the oxide layer during testing at permanently increased chloride concentrations. The absorbed chloride seems to cause an increased solubility of the iron oxide resulting in an overall thinning of the oxide layer.

The oxide layers that develop in oxygenated HTW exhibit a thickness of few µm and have many common features in terms of morphology and constituents with rust layers formed during aqueous and atmospheric corrosion of carbon and low-alloy steels. Hence, this justifies the application of the existing knowledge on oxygen reduction and corrosion processes at ambient temperature to the HTW aqueous corrosion system that is of concern in this thesis (Stellwag et al., 1998).

STRATMANN and MÜLLER studied the mechanism of oxygen reduction on rust-covered metal substrates and came to the conclusion, that oxygen reduction mainly occurs directly at the oxide/electrolyte interface and within the rust scale (Stratmann and Müller, 1994). Furthermore, oxygen diffusion occurs along pores that are present in the oxide layers. This indicates that corrosion reactions between species from the bulk and the oxide layer occur at the oxide/electrolyte interface and within the outer part of the oxide layer, and not at the metal/oxide interface.

This behaviour is also indicated for chloride induced reactions in the oxide layer by the results obtained from TOF-SIMS. These investigations revealed that increased chloride concentrations are present directly at the oxide surface (oxide/electrolyte interface) and penetration of chloride towards the oxide/metal interface occurs only at local spots with locally increased chloride concentrations (chloride islands).

It has furthermore been reported in the literature, that the corrosion of carbon and low-alloy steels in sulphate or chloride containing electrolytes can be associated with the presence of so-called green rust phases at ambient temperatures. Several forms of green rust are known, whereas the so-called green rust 1 (GR1) is formed in chloride containing solutions (Ernst, 1984). Green rust is developed by oxidation of $Fe(OH)_2$ to GR1 and finally to lepidocrocite (γ-FeO(OH)). During this oxidation the local pH was observed to drop from approx. 8 below 4 at

ambient temperatures, whereas the ECP increased from -0.5 V_{SHE} to +0.4 V_{SHE} (Schwertmann and Fechter, 1994). Hence, the development of GR1 may cause a local acidification as well as a local increase of the corrosion potential thereby causing increased solubility of iron oxides. Therefore, the GR1 formation may play an important role in terms of the observed, chloride induced effects on the oxide layer structure, composition, and, in particular, its thickness after long-term increased chloride concentrations. However, it has to be noted that up to date there is no clear experimental evidence for the presence of GR1 at high temperatures.

Tests performed by JOVANCICEVIC et al. who studied the adsorption and absorption of chloride on passive iron systems indicate that the adsorption and absorption of chloride on passive layers are two distinct processes, where the time constant for adsorption is approx. 1 min and for absorption is about 1 h (Jovancicevic et al., 1986). These time constants are comparable to the incubation times observed in this work. By application of electrochemical methods it was observed that a change of the corrosion behaviour occurred rather immediately after an increase in the chloride concentration, which is also indicated by the time constants reported by JOVANCICEVIC. RICHTER, proposed the following reaction for the adsorption of chloride $FeOOH - Cl^- \rightleftarrows FeOCl + OH^-$ (Richter and Walter, 1988).

Similar results to those obtained in the tests of this work have been reported by HEUSLER and FISCHER which described a thinning of the oxide layer by the catalytical action of halides in tests performed at ambient temperatures (Heusler and Fischer, 1976c, Heusler and Fischer, 1976b, Heusler and Fischer, 1976a). According to their results, in the presence of chloride in the solution, Fe-Cl (e.g. Fe(OH)Cl) complexes evolve, which are much more mobile compared to iron oxides and increased dissolution of iron into the electrolyte is established. This causes a new stationary situation with a higher electric field strength and an increased (local) thinning of the oxide layer/passive film due to the increased dissolution rate (Strehblow, 2003, Murphy et al., 1983).

YANG et al., MISCHLER et al. and HUBSCHMID also studied the effect of increased bulk chloride concentrations on the composition of passive layers on austenitic stainless steel at ambient temperatures (up to 65 °C) (Mischler et al., 1991, Yang et al., 1992, Hubschmid and Landolt, 1993). They showed that chloride is only incorporated into the outer part of the oxide layer and no significant penetration into the passive layer occurs in low temperature tests.

It has furthermore been proposed that Cl^- ions induce porosity by adsorbing on oxide surfaces and thereby reduce the oxide-solution interface energy by inhibiting intergranular cohesion (Robertson and Forrest, 1991). The dissolution of inclusions in chloride containing environments has been studied by SRIVASTA and IVES. They reported that anions have a large influence on the dissolution mechanism. If chloride ions are present in the electrolyte, they will adsorb on the iron surface and displace the OH^- ions and thereby modify the dissolution mechanism. This process is particularly enhanced for low pH values (Srivasta and Ives, 1987).

MARCUS et al. also reported localized thinning of the oxide layer due to the presence of chloride in the bulk solution (Marcus et al., 2008). Their results show that, if chloride is present in the electrolyte, chloride ions will compete with OH^- for adsorption at the oxide/electrolyte interface and thereby cause a thinning of the oxide layer. Furthermore, localized penetration of chloride into the oxide may occur leading to the formation of chloride containing particles in the oxide, which may even cause stress-induced fracture of the oxide layer. In case of local breakdown of the oxide, chloride will also compete for adsorption on the metal surface and thereby hinder repassivation if the chloride concentration is sufficiently high enough to prevent sufficient OH^- supply.

Based on the results obtained from the tests performed in the frame of this work and the reported literature data, the following hypothesis on the effect of chloride on general corrosion of LAS in oxygenated HTW is proposed:

Under testing conditions without chloride, the corrosions processes as described in detail in chapter 2.4.2 and schematically shown in Figure 67 a) occur, causing the development of a protective oxide layer on the LAS.

If chloride is present in oxygenated HTW, it is adsorbed on the oxide surface of the LAS immediately, thereby decreasing the OH^- supply from the electrolyte to the oxide/electrolyte interface. After a rather short time (few hours) chloride is absorbed in the outer part of the oxide layer, causing the development of iron oxide complexes that are less strongly bound to the oxide matrix and more easily soluble. This higher solubility, in addition to the reduced OH^- supply from the electrolyte seems to cause the observed overall thinning of the oxide layer. The

dissolved iron-chloride-oxide complexes may deposit again to the material surface but have no protective properties to further corrosion processes.

As long as chloride ions are present in the electrolyte, Cl^- and OH^- are competing for adsorption on the metal surface and repassivation will be declined since the supply of OH^- is declined due to the presence of Cl^-. This may cause the development of chloride islands in the oxide layer. Hence, at spots with locally high chloride concentration, or at spots with locally less corrosion resistance (e.g. surface flaws, MnS-inclusions), pitting may initiate due to the higher solubitlity of the Fe-Cl compounds and the declined repassivation kinetics (see Figure 67 b). Such pits have been observed to be surrounded by rings of deposits, most likely iron oxides and probably also Fe-Cl compounds, which deposit around the active corrosion pit (see e.g. Figure 54).

Due to the above described processes, a local acidification due to hydrolysis of corrosion products may also occur at those spots. This acidification may also play an important role in terms of pitting, and further stabilization of localized pitting.

Even so only a small shift in the "global" corrosion potential of at the maximum approximately 20 mV_{SHE} was observed due to an increase in the chloride concentration in the experiments of this work for both, coupon and C-ring specimens (as exemplarily shown in Appendix 3, Figure 110 to Figure 113), a more pronounced localized shift in the corrosion potential and the local pH may occur.

In particular after long test durations at increased chloride concentrations a more localized thinning accompanied by a roughening of the oxide layer due to a more inhomogeneous epitactic layer was observed. This observation may be explained by the possible, localized acidic shift in pH and corrosion potentials due to formation of chloride islands and pronounced pitting.

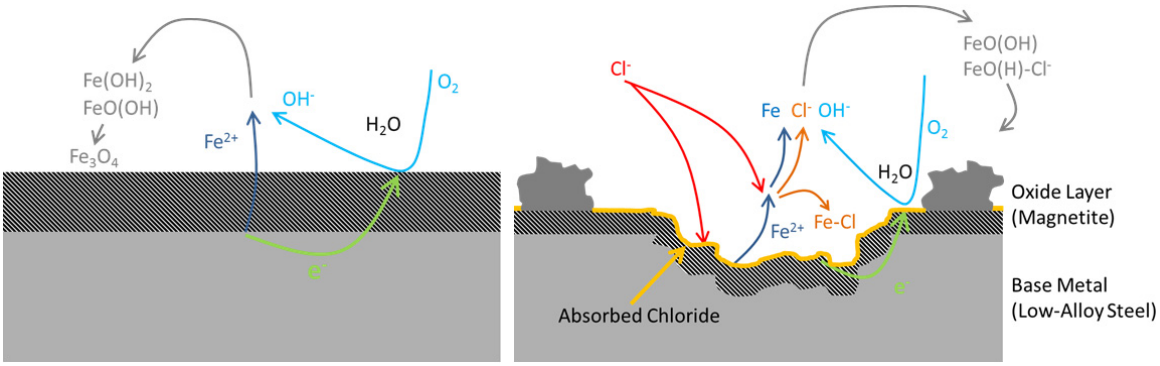

(a) (b)

Figure 67: Model of the effect of increased chloride concentrations on the general corrosion behaviour of LAS in oxygenated HTW.
(a) Conditions without chloride (see also Figure 25).
(b) Thinning of the oxide layer and increased pitting at increased chloride concentrations due to the increased solubility of Fe at increased chloride concentrations and the competition between Cl^- and OH- for adsorption on surface sites.

6. EFFECT OF CHLORIDE ON CRACK FORMATION[15]

In order to systematically study chloride induced effects on crack initiation[16], a series of crack initiation tests have been performed:

i) at different, permanently increased chloride concentrations,

ii) at different testing times after transients in the chloride concentration, and

iii) applying a special loading pattern to study the effect of different chloride contamination levels on the crack initiation and, in particular, repassivation behaviour.

6.1 Experimental Set-Up and Testing Procedure

All crack initiation tests have been performed in 18 l stainless steel autoclaves connected to an INSTRON type screw driven electromechanical tensile test machine (see Figure 68).

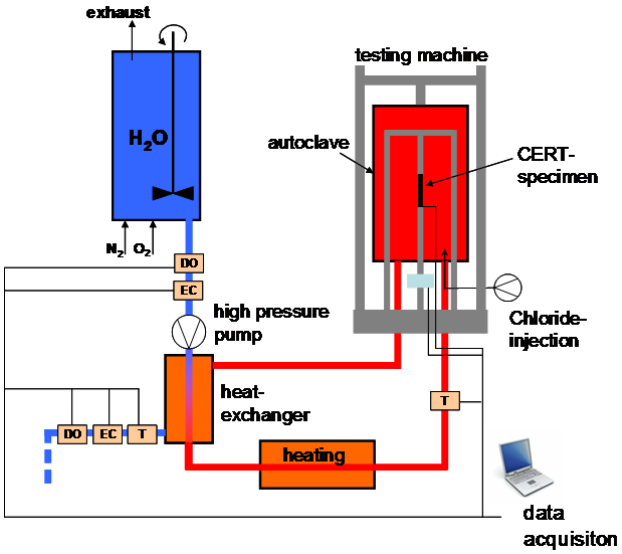

Figure 68: Schematic drawing of the high-temperature test loop that was used for CERT testing.

[15] **Parts of this chapter have previously been published:**
M. Herbst, et al. (2011). Effect of Chloride on Environmentally Assisted Cracking of Low Alloy Steels in Oxygenated High-Temperature Water – General Corrosion, 15th International Conference on Environmental Degradation of Materials in Nuclear Power Systems – Water Reactors, August 2011, Colorado Springs, Colorado. **M. Herbst, et al. (2012).** The Effect of Chloride on General Corrosion and Crack Initiation of Low-Alloy Steels in Oxygenated High-Temperature Water, 38th MPA Seminar, October 1 and 2, 2012, Stuttgart.

[16] For clarification it has to be noted that whenever it is referred to crack initiation this corresponds to crack formation during CERT testing and hence the total number of cracks that have been observed after CERT testing.

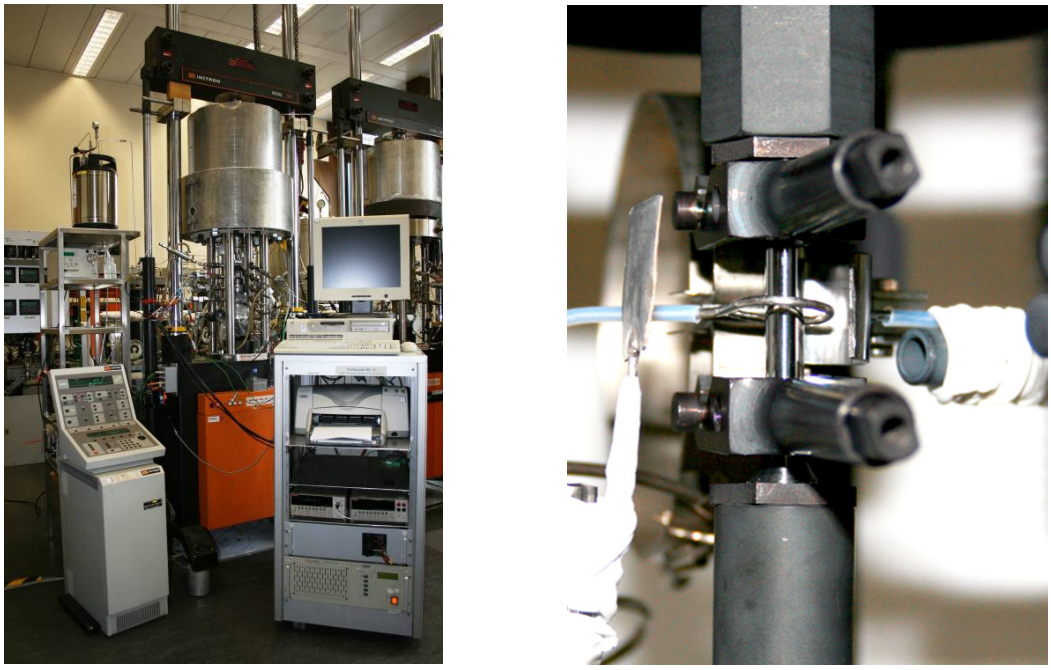

(a) (b)

Figure 69: (a) Picture of the used tensile testing machine (Type INSTRON) with high-temperature autoclave and water preparation unit in the back of the picture. (b) Tensile testing specimen after assembly in the autoclave with high-temperature extensometer for strain measurement and additional electrodes for electrochemical noise measurement.

Similar to the exposure tests described in chapter 5, all tests were performed in a once through refreshing loop with full environmental control. The flow rate was adjusted to approx. 8 l/h resulting in an average exchange rate of approx. 0.5 exchanges per hour. The testing facility as well as the specimen set-up are depicted in Figure 69 a) and b), respectively. A schematic drawing of the used test loop is shown in Figure 68.

To systematically study the effect of different amounts of continuously increased chloride concentrations on the crack initiation behaviour, a series of crack initiation tests was performed. Therefore, the testing procedure as schematically shown in Figure 70 was applied. During testing, the chloride concentration was increased to the target chloride concentration after the specimens were pre-oxidized in chloride free HTW at 288 °C for more than 450 hours. Straining of the CERT specimens was started 24 hours after the increase of the chloride concentration using an initial strain rate of 10^{-6} s^{-1}.

All investigated CERT specimens (technical drawing see Appendix 4) were polished using a 1 µm diamond paste as a final manufacturing step prior to CERT testing, which resulted in an average surface roughness of $R_a \approx 0.05$ µm.

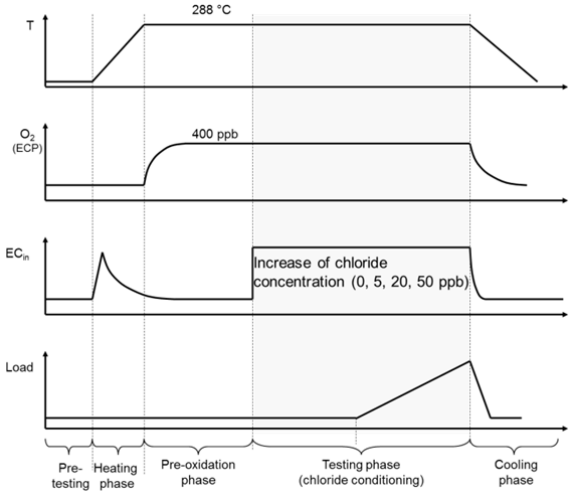

Figure 70: Schematic representation of the testing procedure applied for CERT testing at different chloride concentrations

In addition to tests at increased chloride concentrations, further CERT tests were designated to study the potential memory effect of a temporary chloride transient which was proposed by other authors earlier (Ritter and Seifert, 2003, Ritter and Seifert, 2004b). In these tests, straining of the specimens was started either directly after the end of a chloride transient or following additional testing time without chloride after the chloride transient (see Figure 71).

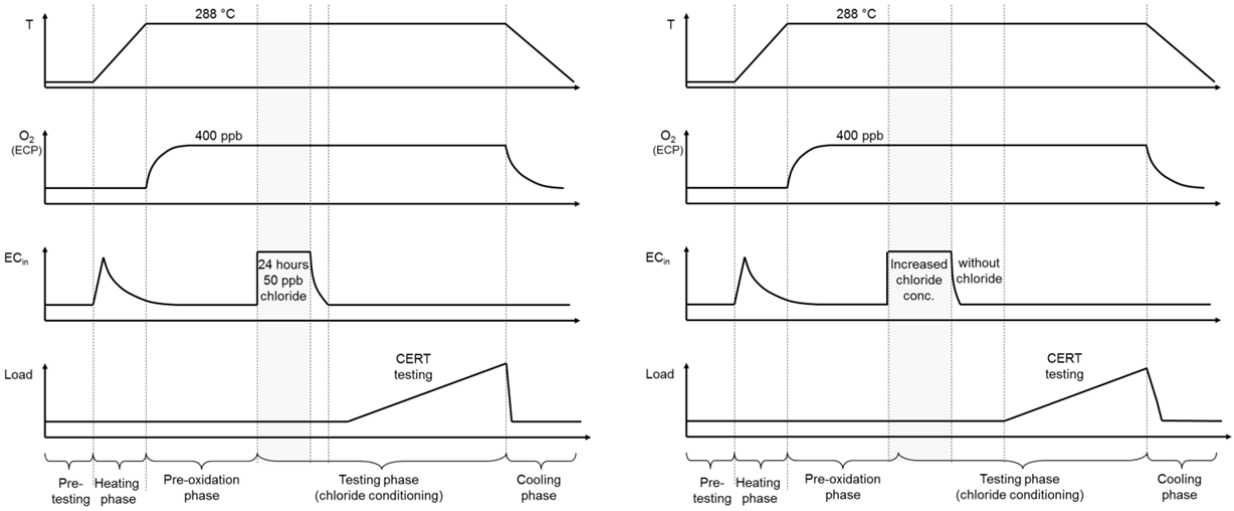

Figure 71: (a) Transient tests with beginning of straining directly after the end of a 24 hour 50 ppb chloride transient, (b) transient tests with beginning of straining 300 hours after the end of a 52 hour 50 ppb chloride transient.

To study the effect of chloride on EAC initiation behavior of LAS and possible repassivation processes, tensile tests with a modified testing procedure were performed. It is known from literature data, that the fracture strain of the protective oxide film is in the range of 0.05 to 0.20 % (Harrison, 1967, Hickling and Blind, 1986, Huiijbregts and Snel, 1972, Ford, 1982b, Field et al., 1963, Diegle and Vermiliyea, 1976, Ford and Combrade, 1985, Deimel and Läpple, 1991, Kussmaul and Navab-Motlagh, 1983). As shown in Figure 72, CERT specimens were cyclically loaded with a maximum strain above the range of the oxide fracture strain level in these tests.

This procedure was used to generate a continuous, repeated rupture of the oxide layer causing exposure of bare metal to the environment. The chosen positive strain rate was 10^{-6} s^{-1} with a maximum strain of 0.50 % and R = 0.9 (rise time approx. 30 min fall time approx. 3 min, see b). While this loading pattern was applied, the chloride concentration was stepwise increased up to a maximum chloride concentration of 50 ppb. The actual strain was measured outside the autoclave by the movement of the crosshead of the testing machine and directly at the gauge length of the specimen. In order to achieve the target strain of approx. 0.50 % at the specimens gauge length, a total strain of approximately 1 % had to be applied using the movement of the INSTRON testing device due to the system stiffness.

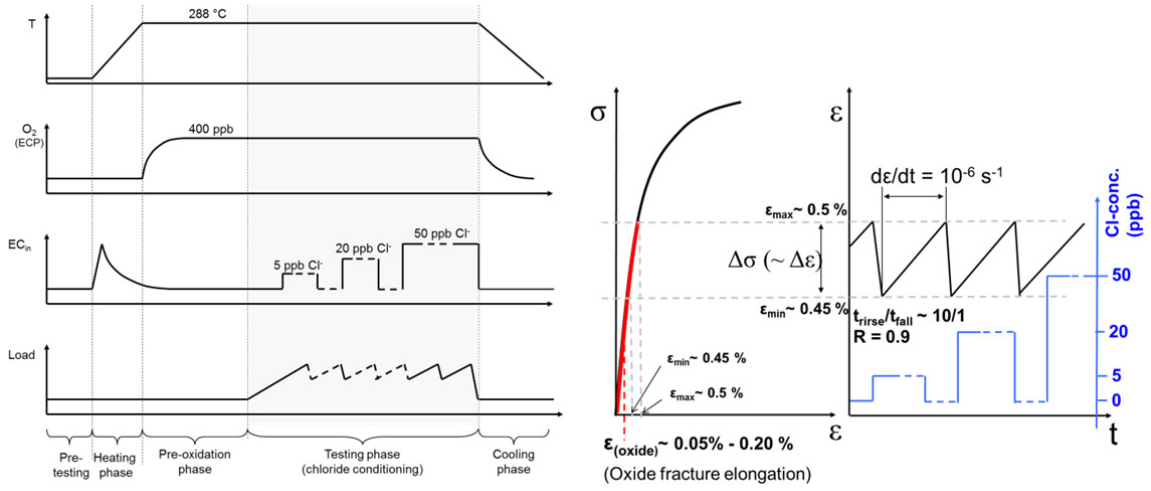

(a) **(b)**

Figure 72: (a) Schematic representation of the testing procedure applied during repeated straining using loading pattern schematically shown in (b).

6.2 Results from Crack Initiation Testing at Different Chloride Concentrations

Using the CERT technique, it is possible to study the effect of changes in distinct parameters on the crack initiation susceptibility of a corrosion system, which is known to be vulnerable to strain induced corrosion cracking (SICC). Crack initiation during testing is facilitated by application of continuously increasing strain using a constant strain rate. Hence, the effect of different amounts of deliberately increased chloride concentrations was systematically studied, while all other test parameters remained unchanged. All tests were conducted either until failure of the specimen occurred or a minimum stress limit was undershot.

Figure 73 shows stress-strain-curves[17] obtained from testing at increased chloride concentrations compared to a reference test (without chloride). The test results showed that in chloride containing environments crack initiation occurred at smaller stress and strain levels, thereby causing lower maximum strain and stress levels during testing.

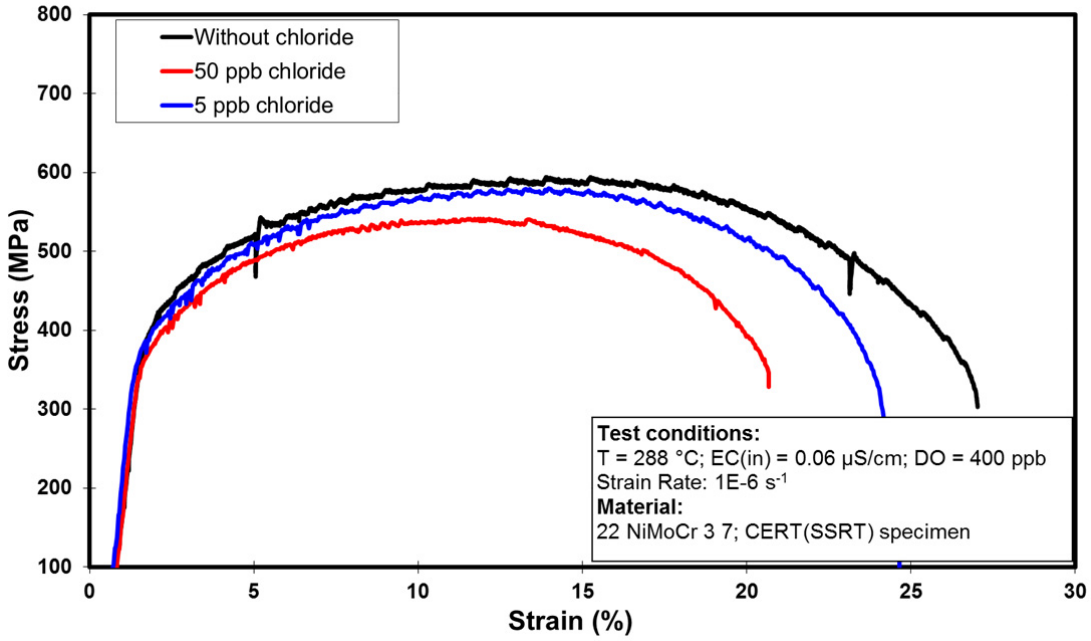

Figure 73: Effect of 50 ppb and 5 ppb chloride on the crack initiation in oxygenated HTW as compared to results obtained from a reference test run without chloride.

[17] If not otherwise stated, stress corresponds to the technical stress applied to the specimen measured using an external load cell. Strain was calculated using the movement of the crosshead. Hence, the stiffness of the test system has to be considered in particular in the low strain and stress region. Since exactly the same test assembly has been used for all tests, all test results can be directly compared, as any possible deviation is of systematic nature.

The results summarized in Figure 73 clearly illustrate a trend towards lower maximum stress and strain levels with increasing chloride concentrations. Hence, increased crack initiation susceptibility with increasing chloride concentrations is clearly highlighted by these results.

Figure 74 shows the effect of 20 ppb chloride on the crack initiation behaviour. Since the test (1) at 20 ppb chloride did not fit into the observed trend, this test was repeated to double check the effect of chloride in the middle region of the investigated chloride concentration range. The results of these two tests, that were conducted using the same testing procedure, are marked as (1) and (2) in Figure 74. As revealed by the results of the test marked with (2), there is some sensitivity of LAS for chloride induced effects on the crack initiation susceptibility in this chloride concentration region This result clearly highlights that a variety of additional parameters are influencing the investigated corrosion system, which all have to be conjointly considered. It is most likely that the surface condition of the specimen from test (1) was somewhat superior to the surface from test (2), e.g. in terms of the statistical distribution of number and location of surface breaking MnS-inclusions. This observation was made by post-test investigations, which revealed distinct differences regarding the surface conditions of specimen (1) and (2) in terms of the surface morphology as well as pit and crack initiation locations (see chapter 6.3).

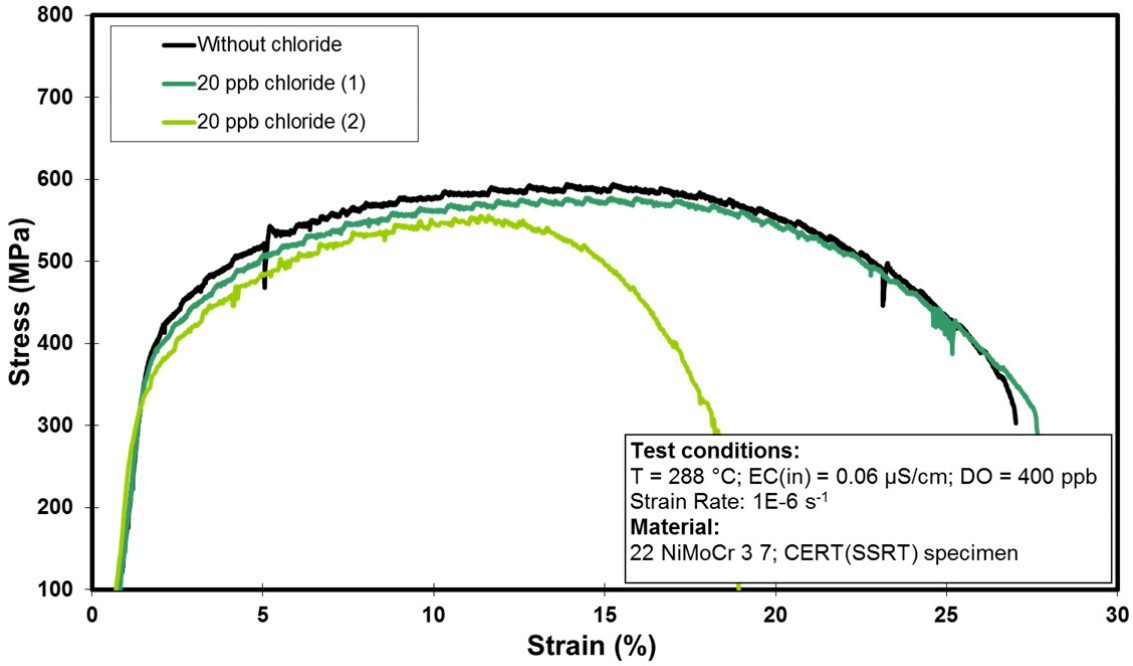

Figure 74: Comparison of the effect of 20 ppb chloride on crack initiation in oxygenated HTW as compared to results obtained from a reference test run without chloride.

Despite the observed scatter in the region of 20 ppb chloride, there seems to be a systematic trend towards lower maximum strain and stress levels with increasing chloride concentrations during straining of the specimens. However, it has to be noted that the observed changes are rather small. The change of the measured strains is within approx. 5 to 10 % and the change of the maximum stress lies in the range of approx. 70 MPa.

In addition to the tests at continuously increased chloride concentrations, the effect of chloride transients was studied in two CERT tests. The results of these tests are compiled in Figure 75. This comparison shows that the crack initiation susceptibility following chloride transients with 50 ppb chloride and up to 52 hours duration does not drastically increase. The maximum stress is in the region of the test performed at 5 ppb chloride, which shows a fast recovery after the end of the chloride transients. Similar observations have already been made in the studies on the effect of chloride transients on the general corrosion behaviour, where no significant memory effect was observed following chloride transients with up to 24 hours 50 ppb chloride and total recovery of the observed effects occurred within 48 hours after the end of the transient at the latest.

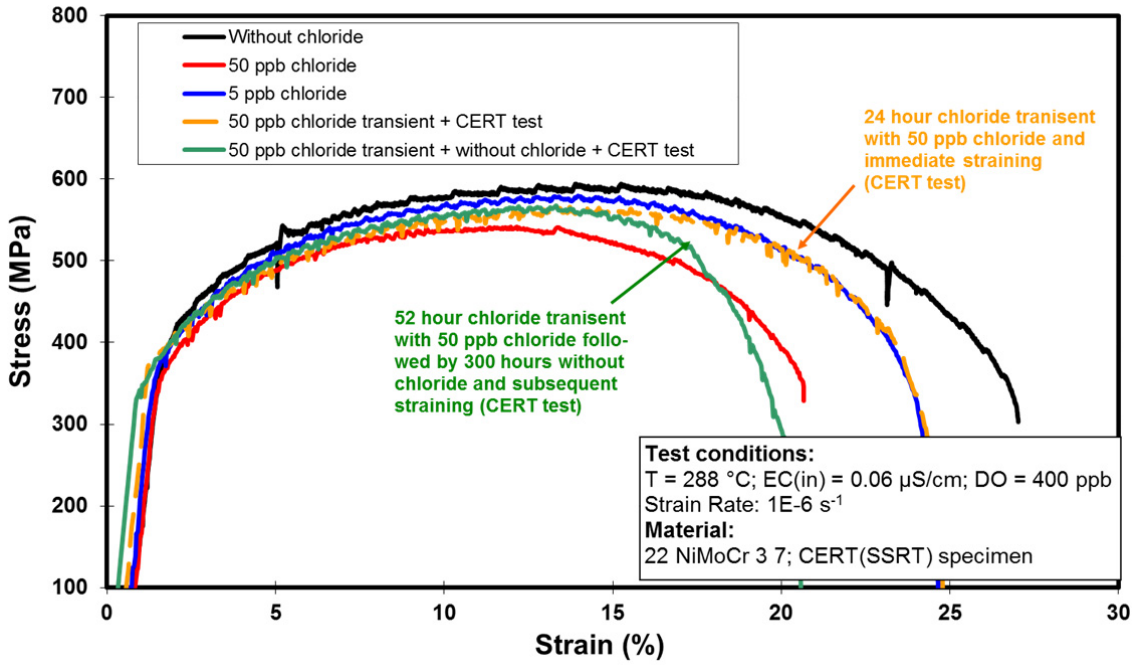

Figure 75: Comparison of stress-strain curves from tests performed during continuously increased chloride concentrations and tests performed after chloride transients.

Regarding the decrease in the maximum strain that was observed for the test following a 52 hour 50 ppb chloride transient and additional 300 hours without chloride it has to be noted that this specimen did not crack in the middle region of the gauge length. The crack initiation location in this case was a large, surface breaking MnS-inclusion. Hence, this effect is superimposed to any chloride induced effects and is thereby most likely causing the observed decrease in the maximum measured strain.

6.3 Results of Post-Test Investigations

As described in the preceding chapter, the oxide layer, which develops under HTW-conditions, has a rather low fracture elongation compared to the metallic LAS phase. Hence, applying a continuously increasing strain (with a constant strain rate), repeated fracture of the oxide occurs and the effect of different chloride concentrations on the visual appearance of the specimens after the CERT tests reveal detailed insights to the effect of chloride on crack initiation processes.

Regarding the analysis of the visual appearance after testing, special emphasis was therefore laid on studying the effect of different chloride concentrations on:

i) the number, size and location of crack initiation locations,
ii) analysis of the reduction of area, and
iii) the fracture surface.

Comparison of the tests performed at the different chloride concentrations clearly reveals an increase of pitting and crack initiation locations with increasing chloride concentrations. Similar observations have already been made during exposure tests (see chapter 5).

The investigations into the visual appearance of the tested specimens thereby again illustrate the chloride induced effects on pitting and crack initiation (see Figure 76). Significantly more crack initiation locations were observed on the specimen tested at a chloride concentration of 50 ppb in comparison to e.g. the reference specimen tested without chloride. The observed cracks typically initiated from corrosion pits on all CERT specimens. The surface condition of the specimens tested at 5 ppb chloride and 20 ppb chloride is in between the conditions that were observed without or with 50 ppb chloride.

Figure 77 shows a comparison between tests (1) and (2), both performed at a bulk chloride concentration of 20 ppb. The scatter that has been observed in the stress-strain curves is also reflected in the visual appearance of the specimens after testing. The total amount of crack initiation locations over the whole specimen surface drastically differs between these two specimens. As observed by the difference in the surface conditions, there seems to be a large scatter in the chloride induced effects in the region of 20 ppb chloride. This scatter seems to depend in particular on the actual surface condition of the specimen.

Typical fracture areas, showing the typical transgranular crack morphology, which is caused by strain induced corrosion cracking, are depicted in Figure 78. The strain induced corrosion cracking typically initiated from pitting at the surface of the specimens, in particular at MnS-inclusions. Multiaxial stresses, caused by MnS-inclusions or in the necking area therefore obviously increase the crack initiation susceptibility regardless of the actual chloride concentration during testing.

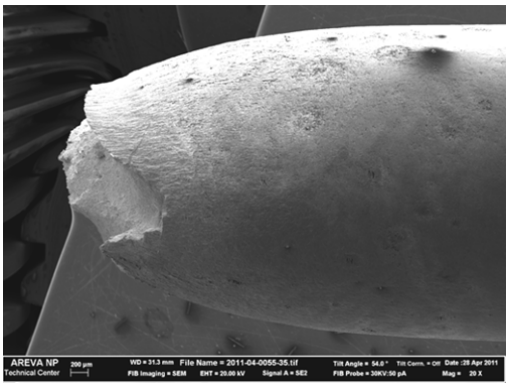

(a) without chloride – necking

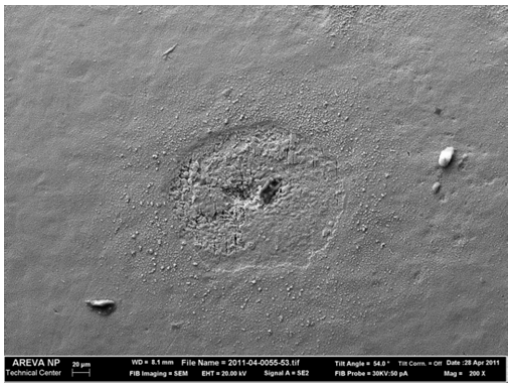

(b) without – area of uniform elongation

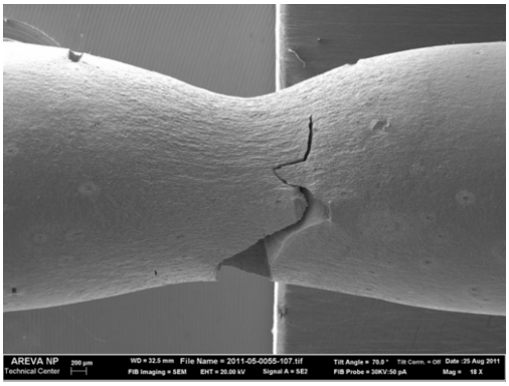

(c) 5 ppb chloride - necking

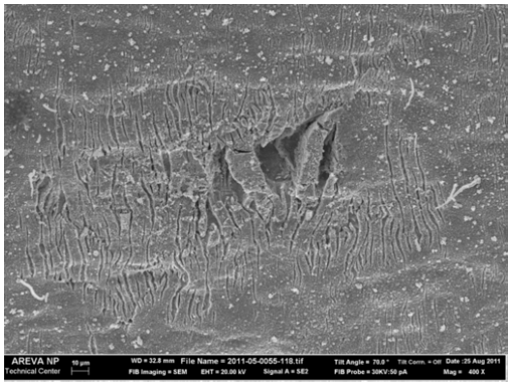

(d) 5 ppb – area of uniform elongation

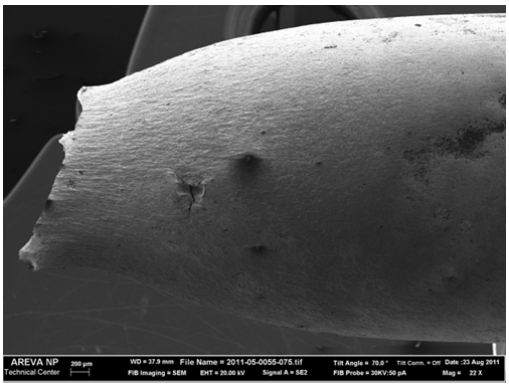

(e) 20 ppb chloride – necking (Test 1)

(f) 20 ppb - area of uniform elongation

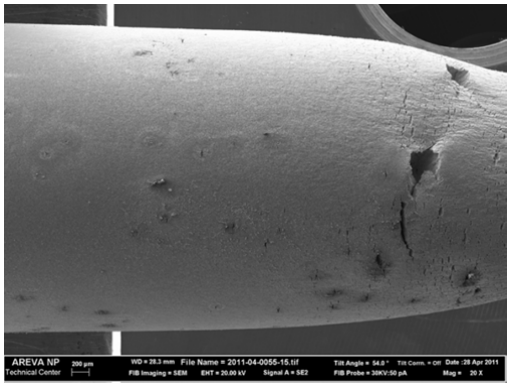

(g) 50 ppb chloride - necking

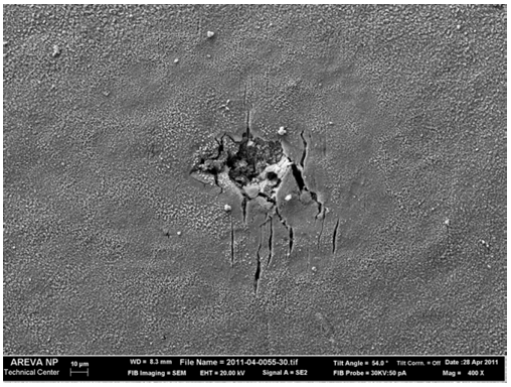

(h) 50 ppb – necking area

Figure 76: SEM figures of specimens after CERT testing at different chloride concentrations.

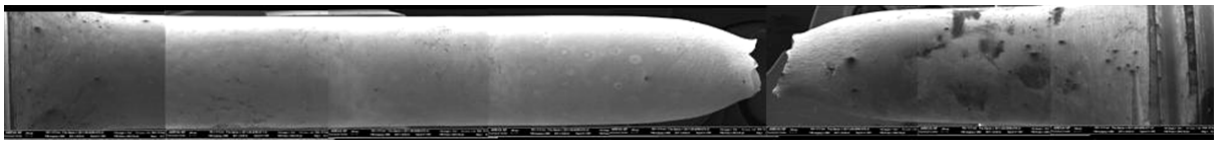

(a) Test (1)

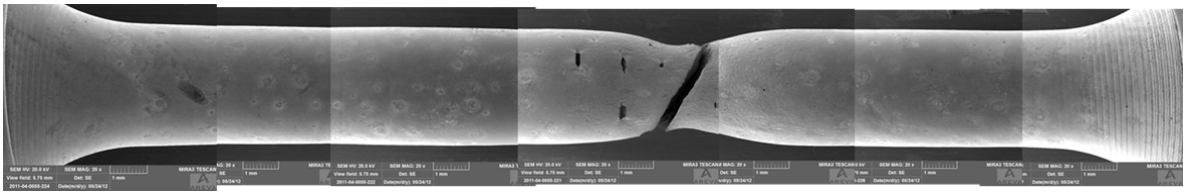

(b) Test (2)

Figure 77: Comparison of SEM Figures from two specimens tested at a chloride concentration of 20 ppb during straining.

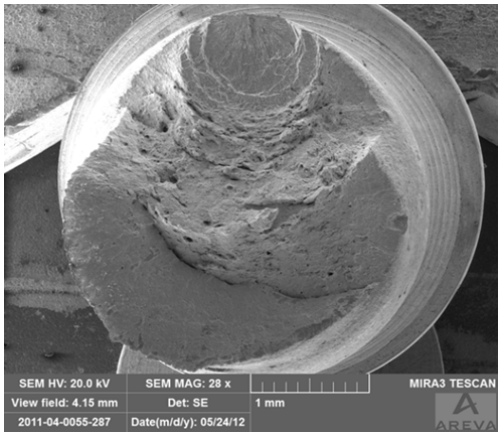

(a) 20 ppb chloride (2)

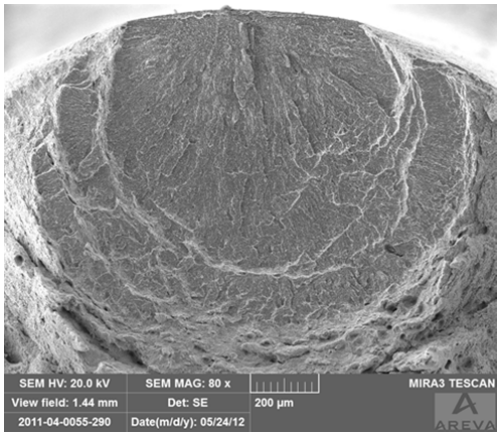

(b) Detailed view on crack initiation location from (a)

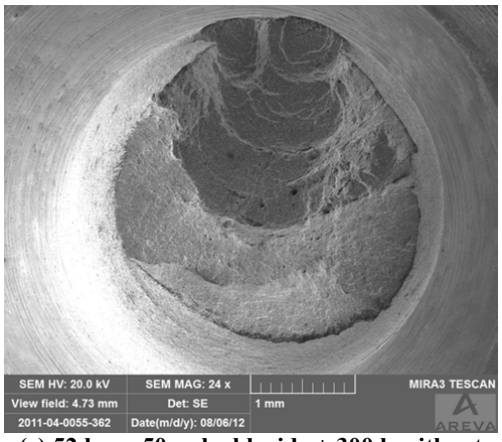

(c) 52 hour 50 ppb chloride + 300 h without

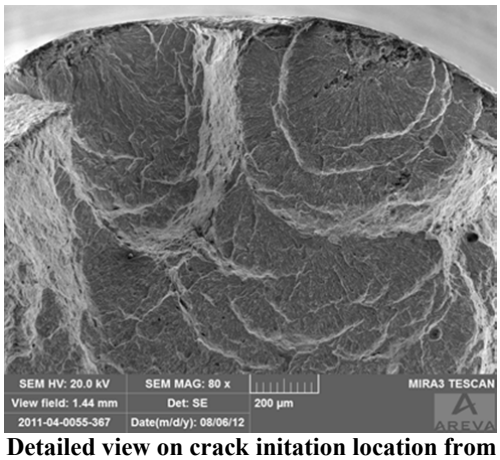

(d) Detailed view on crack initation location from (c)

Figure 78: Fracture surfaces from exemplarily chosen tests showing crack initiation locations being preferentially located at surface breaking MnS-inclusions.

Due to these observations, the microscopic examinations were extended, which resulted in a counting of crack initiation locations (designated as “cracks”) and potential crack starting locations (designated as “Possible Initiation Side”), see Figure 79. For this evaluation the “Crack” and “Initiation” features as depicted in Figure 79 were counted all over one half of the specimen (full length of the specimen and 180° of the circumference). This evaluation clearly reveals an increase of both, “Crack” locations and “Potential Initiation Sides” with increasing chloride concentrations during straining and thereby clearly illustrates an increased susceptibility for crack initiation with increasing chloride concentration during straining.

In addition to the surface analysis, further assessment was done by evaluating the reduction in area after CERT testing at different chloride concentrations, see Table 6 and Figure 80. This evaluation shows a trend towards lower reduction in area with increasing chloride concentrations which is in accordance with the results obtained from the stress-strain curves that also revealed a trend towards lower stress and strain levels with increasing chloride concentrations.

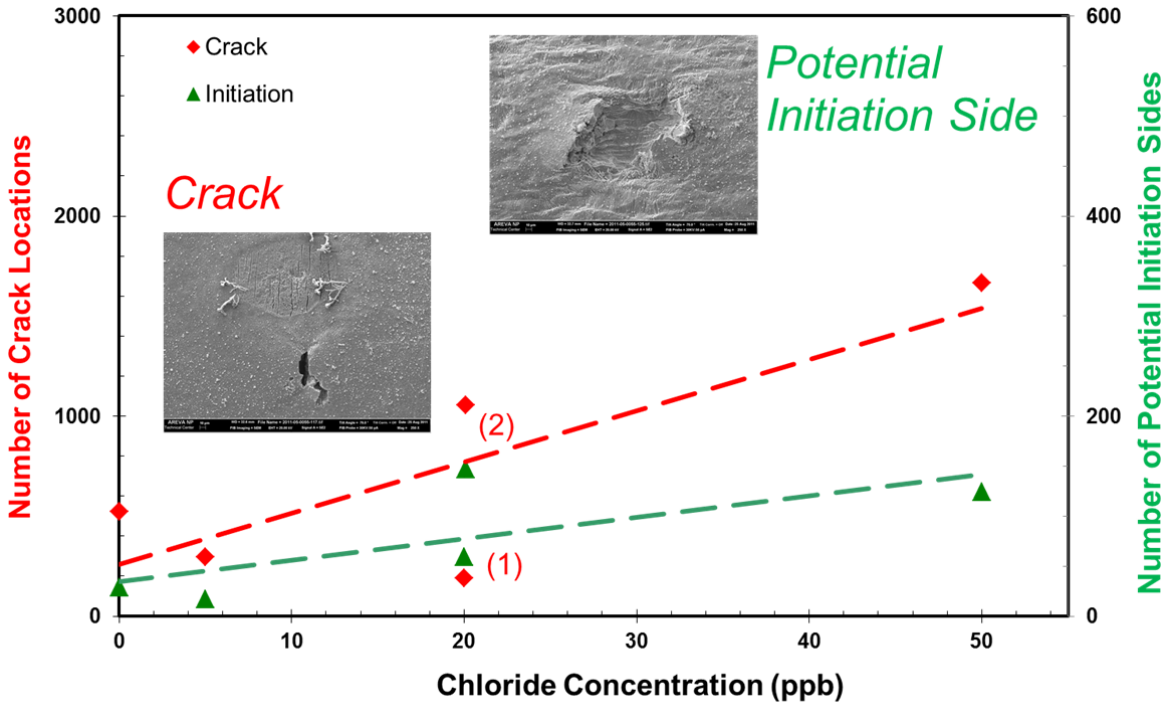

Figure 79: Effect of chloride on the number of crack initiation locations and potential initiation sides as observed on specimens from CERT tests at different chloride concentrations.

Table 6: Summary of the reduction in area and diameter of the fracture area depending on the chloride concentration during CERT testing.

Chloride Concentration (ppb)	Diameter of Fracture Area (µm)	Reduction in Area (%)
Without Chloride	1961	51
5 ppb Chloride*	2380	41
20 ppb Chloride (1)	2000	50
20 ppb Chloride (2)	2484	38
50 ppb Chloride*	2493	37

* Testing interrupted before finale failure of the specimen

In Figure 80, the reduction in area that was observed using the specimens from transient tests is plotted in addition to the results obtained from tests performed at different increased chloride concentration levels. From this comparison it becomes apparent that the reduction in area is again increasing if straining was applied after the end of chloride transients. Nearly no decrease was observed during testing directly after the end of a short term transient. Even after a long-term increased chloride concentration no drastic change was observed.

In summary both, the crack counting and the evaluation of the reduction in area reveal an increase in the crack initiation susceptibility with increasing chloride concentrations during straining of the specimen. The investigations furthermore showed that in addition to the effect of chloride a number of further parameters play a vital role regarding crack initiation, amongst which the surface condition and, in particular, the size, shape and position of MnS-inclusions seem to play the most important role.

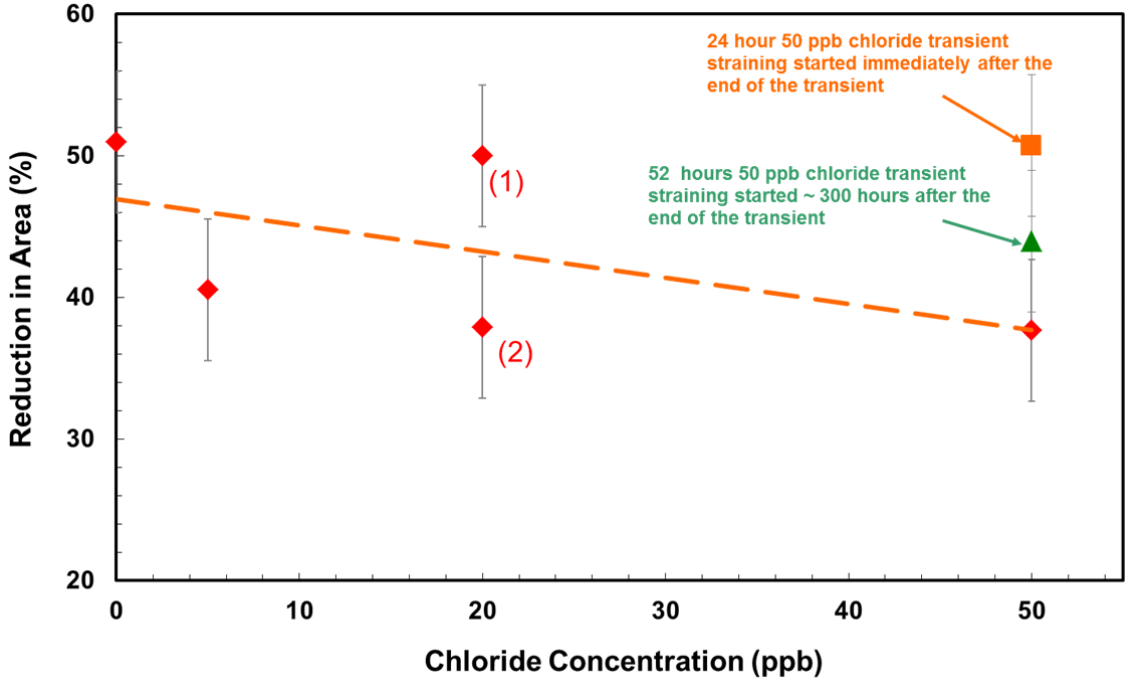

Figure 80: Effect of chloride on the reduction in area as revealed on specimens from CERT tests performed at different levels of continuously increased chloride concentrations and tests performed after chloride transients.

6.4 Results from Modified CERT Tests

In addition to testing at different, continuously increased chloride concentrations and after temporary chloride transients, this test focused on studying the repassivation and crack initiation behaviour at different chloride concentrations. Special emphasis has been laid on studying the effect of different chloride concentrations on the repassivation behaviour of LAS in oxygenated HTW. This was achieved by applying EN monitoring and measurement of the real specimen strain during testing.

During the tensile tests with modified testing procedure, the external strain (measured at the electromechanical tensile test machine) and the actual strain of the CERT specimen (measured directly at the specimen in the HTW) were monitored to study possible crack initiation processes due to the applied loading pattern and the stepwise increased chloride concentration. In addition, EN measurement, which is a very sensitive technique to study crack initiation in laboratory tests, was applied.

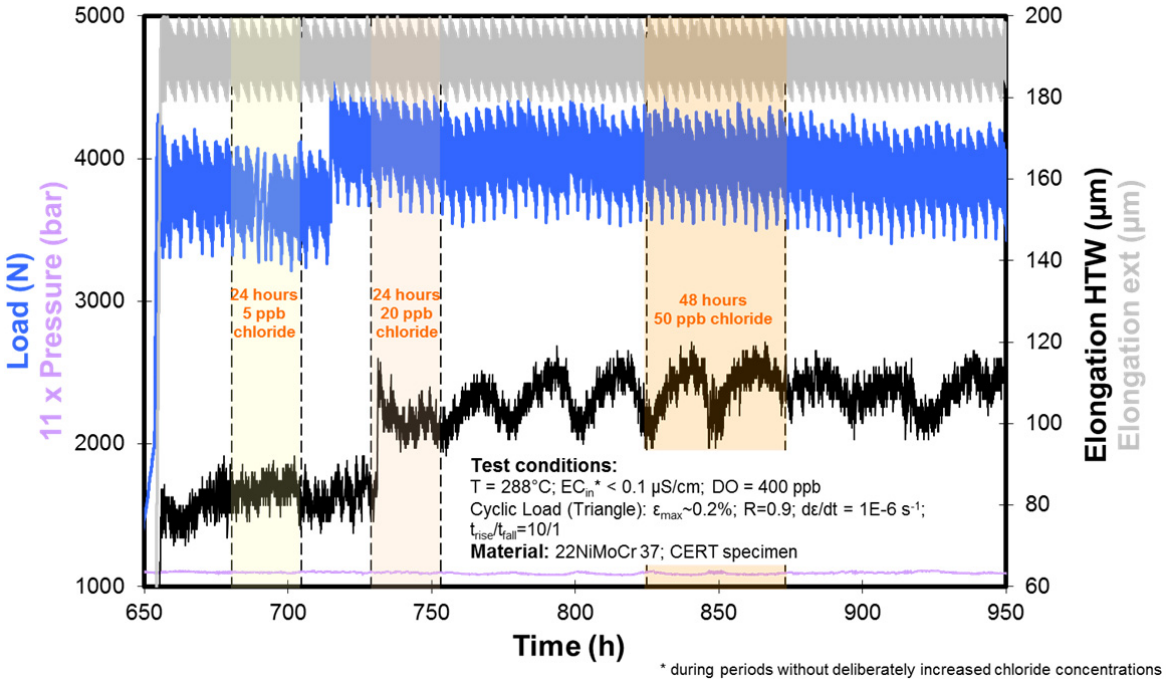

Figure 81: Load and strain signal during repeated straining of the specimen. The elongation that was calculated using the movement of the crosshead is designated as "Elongation ext", the elongation measured directly at the gauge length of the specimen is designated as "Elongation HTW".

After pre-oxidation of the specimen, the loading pattern described in chapter 6.1 was applied to the specimen under HTW testing conditions without chloride in order to generate a "reference" result. After this reference signal was acquired, the chloride concentration was step-wise increased to different chloride concentrations. During testing at different chloride concentrations, the strain of the specimen and EN were continuously monitored and evaluated. The results of the strain and load measurement are compiled in Figure 81. Some selected results of the electrochemical noise measurement are depicted in Figure 82.

During testing at 5 ppb chloride, no change of the acquired signals was observed, whereas after the chloride concentration was increased to 20 ppb, a sudden increase in the elongation that correlates to a sudden potential transient was observed (see Figure 81 and Figure 82 b). This observation should indicate initiation of pitting or even a crack at this testing time. However, after this single transient no further transients have been observed. Hence, testing was continued with testing phases without and with 50 ppb chloride. In contrast to the single transient that has been observed during testing at 20 ppb chloride no more transients were observed during the remaining test.

It was therefore concluded that the single transient that was observed after increasing the chloride concentration to 20 ppb may most likely be attributed to either a localized pit initiation or pronounced cracking of the oxide layer since no more crack initiation indications have been observed during the whole remainder of the test. Another, even more likely explanation may be sliding of the clamps of the internal extensometer that was mounted to the CERT-specimen. This would result in an offset of the measured elongation and would also explain the single potential transient that was observed in the EN-signal.

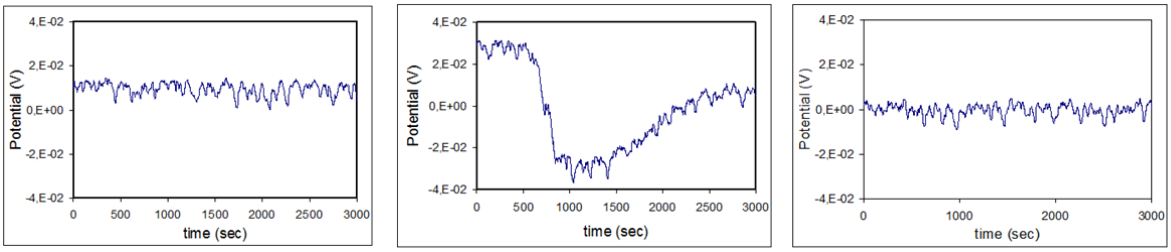

(a) **(b)** **(c)**

Figure 82: Results from EPN-measurements performed during repeated.
(a) Before increasing the chloride concentration (670 h).
(b) Potential transient during exposure to 20 ppb chloride. The potential transient correlates with the strain transient at 730 h in Figure 81.
(c) EPN during exposure to 50 ppb chloride.

This conclusion was confirmed by post-test investigations, where no sustained cracking was observed on the whole surface area of the specimen.

The SEM investigations revealed some local, very tiny crack like features which were caused by the continuously repeated fracture of the oxide layer (see Figure 83 a). In order to validate, that no cracking initiated from those local spots, a cross section was performed through one of these crack like features using the FIB technique. This cut confirmed that no cracks initiated from those features (see Figure 83 b).

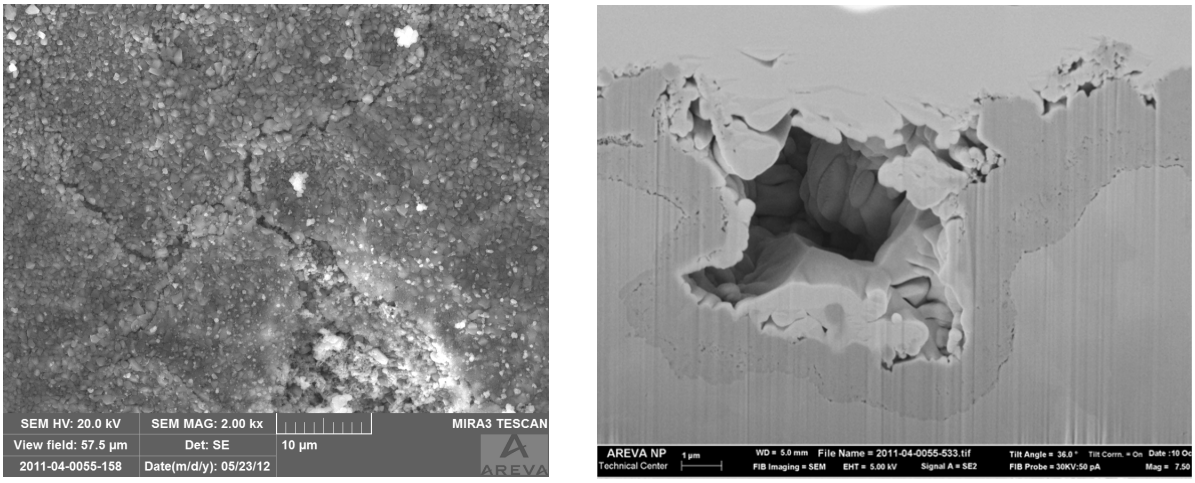

(a) **(b)**

Figure 83: (a) SEM figure of a crack like feature on the specimen surface after testing. (b) Cross section through the crack like feature depicted in (a), showing that no crack growth initiated from these locations and the crack like feature is fully covered with oxide.

6.5 Summary and Discussion

6.5.1 Overall Summary

Stress-strain curves derived from CERT tests using actively strained round bar tensile specimens showed that the total strain and tensile strength of specimens tested at different, continuously increased chloride concentrations decreased compared to the values obtained without chloride. These results were confirmed by evaluation of the reduction in area at fracture point and by counting of crack locations. Since the observed change of both, the yield strength (approximately 70 MPa) and the total strain (approximately 5 to 10%) are very low, these results have to be evaluated and assessed very carefully.

In addition, some of the tests showed a rather large scatter in the results, in particular tests conducted at a chloride concentration of 20 ppb. The reduction in area at fracture and the evaluation by counting of crack locations indicate a trend towards increased crack initiation susceptibility with increased chloride concentrations. However, it has to be noted that remarkable effects have only been observed at 50 ppb chloride.

The post-test investigations clearly highlighted that cracking predominantly initiates at surface flaws, junctions of gross slip planes, MnS-inclusions, and from pitting. This observation is often made in CERT testing and is well known from literature data and former investigations using the CERT technique (Indig, 1982, Ford, 1982a, Gladen and Kaesche, 1994, Rippstein and Kaesche, 1989).

Regarding chloride induced effects, the microscopic investigations showed that the number and extend of pitting that was observed at the specimens after testing increased with increasing chloride concentrations during straining of the specimens. Similar observations were also made for coupon and C-ring specimens from exposure tests at different chloride concentrations (see chapter 5).

No crack initiation was observed using CERT specimens that were cyclically loaded above the oxide fracture elongation. The results obtained from these tests show that the applied loading pattern was not sufficient to cause crack initiation at all investigated chloride concentrations (up to 50 ppb).

The obtained results therefore indicate that crack formation is not significant below the yield strength and a continuously rising strain above the yield strength of the base metal (at testing temperature) is needed to cause crack initiation even at increased chloride concentrations. This result corresponds to literature data reported by RIPPSTEIN and KAESCHE (Rippstein and Kaesche, 1989) who performed interrupted CERT tests to study the crack initiation time in pure HTW and results from RITTER and SEIFERT who conducted CERT tests with additional application of the EN technique. Their tests showed that crack initiation occurs above the yield strength, and slightly below the tensile strength even for increased chloride concentrations (Ritter and Seifert, 2011).

The above described results are also in good correlation with results from exposure tests using pre-strained C-ring specimens. The C-ring specimens were pre-strained to an initial maximum stress of 500 MPa. Despite this high stress level, none of the tested specimens revealed any crack initiation even so they were exposed to HTW containing up to 50 ppb chloride for up to 1000 testing hours. This again underlines the important role of active straining in the plastic strain region in order to generate crack initiation even at increased chloride concentrations.

From these results, it can therefore be concluded that even up to 50 ppb there is no immediate, significant effect of increased chloride concentrations on the EAC susceptibility of low-alloy steel under constant loading and even under cyclic load at low strain (and stress) levels.

Testing either directly after chloride concentration transients or after additional testing time in pure HTW, following a chloride transient, showed that the chloride induced effects recovered after a rather short exposure to HTW of high purity (without chloride). The stress-strain curves, as well as the reduction in area at fracture point increased if testing was continued in HTW of high purity after the end of chloride transients compared to the results from tests performed at continuously increased chloride concentrations. This confirms that no significant memory effect on the crack initiation behaviour is caused by short term chloride transients and recovery of the chloride induced effects occurs rather fast after the transient. Similar results have already been obtained from the exposure tests described in chapter 5.4. In these tests, total recovery of the chloride induced effects on the general corrosion behaviour, that was monitored using EN and EIS, was observed approx. 24 to 48 hours after the end of the chloride transient, at the latest.

All tests showed that crack initiation predominantly occurred in the necked area for all applied chloride contamination levels. Furthermore, surface breaking inclusions and localized pitting were observed to be the preferred crack initiation locations. These observations highlight that a multiaxial stress state is an important parameter regarding crack initiation even at increased chloride concentrations. As indicated by crack counting, the importance of multiaxial stress seems to decrease at higher chloride concentrations (50 ppb), where crack initiation clearly occurred over the whole specimen length, virtually independent of necking and surface flaws.

6.5.2 Mechanistic Aspects on the Effect of Chloride on Crack Initiation

According to the slip-step dissolution, also designated as FRAD (Film rupture anodic dissolution) model (see chapter 2.3.2.2), which is a broadly accepted model for SCC of LAS under HTW conditions, crack initiation and growth occurs due to a local rupture of the oxide layer developed on the surface or at crack tips of LAS under HTW conditions (Andresen and Ford, 1988, Ford, 1989). Continued straining during rising load tests, such as e.g. during CERT testing, leads to a local rupture of the otherwise protective oxide layer. Bare metal, which is thereby temporarily exposed to HTW, will dissolve by anodic dissolution ($Fe \rightarrow Fe^{2+} + 2e^-$) until this freshly exposed area is repassivated again by recovery of the oxide layer due to the formation of iron oxides (see Figure 84).

The time to crack initiation and the crack growth rate therefore depend on:

a) the strain level and local strain rate,
b) local plastification,
c) multiaxial stress/strain conditions, as crack initiation predominantly occurs in the necked region of the specimens which were loaded close to UTS and at pits,
d) the oxidation rate occurring at the strained surfaces or crack tips, and
e) the repassivation rate under given electrochemical conditions determined by local ECP and anionic activity.

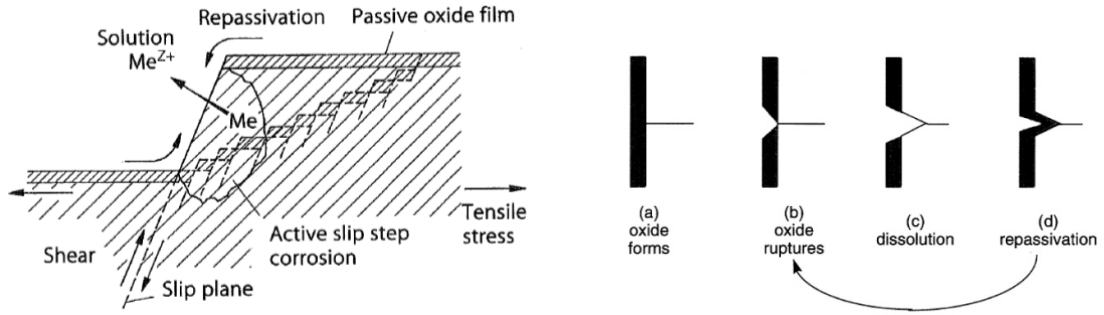

Figure 84: (a) Slip-step dissolution model for discontinuous crack initiation and crack advance under HTW-conditions according to (Kaesche, 2003, Ford, 1982b, Ford, 1989). b) Simplified scheme of the slip-step oxidation process for crack advance: (a) protective oxide film forms on the bare metal surface, (b) the oxide film ruptures near a slip plane, (c) dissolution the bare metal surface occurs, (d) metal oxidises again and is again ruptured due to local straining (Aaltonen et al., 2002).

As local breakdown of the oxide layer occurs due to local sliding along gross slip planes (according to the slip-step dissolution mechanism), the thickness of the protective oxide layer and the height of the slip steps are vital parameters regarding the crack initiation susceptibility of LAS in HTW (Kaesche, 2003). The exposure tests performed at different deliberately increased chloride concentrations (see chapter 5) revealed a change in the thickness of the oxide layer after testing periods with continuously increased chloride concentrations. Furthermore, pronounced pitting was observed in all tests after prolonged exposure to HTW with different chloride levels, whereas, pitting was more pronounced at higher chloride concentrations.

In the case of a decrease in the oxide layer thickness, smaller slip step heights are sufficient to cause local breakdown of the oxide layers which develop at increased chloride concentrations (see Figure 85). In addition, local areas where pitting like attack of the specimens has been observed may further localize the deformation and thereby act as crack initiation points. Conjoint effects of MnS inclusions, which are known to act as crack initiation locations, and localized thinning of the oxide layer due to chloride induced effects, may further promote crack initiation at those locations. Finally, a local acidification, changing the equilibrium conditions in the interface between oxide layer and HTW is possible as described in chapter 5.6. This local acidification may be caused by the formation of different Fe-Cl compounds by which the pH can be locally shifted to more acidic values. Local shifts in pH cause a change of the local equilibrium conditions causing locally increased corrosion rates. The absorption of chloride in the oxide layer, further retards the repassivation kinetics after local breakdown of the protective oxide layer and thereby prevents fast repassivation (see Figure 85).

It is proposed that the presence of chloride contaminations in HTW can cause both, accelerated crack initiation by the observed thinning of the oxide layer and enhanced crack growth due to declined repassivation kinetics at higher chloride levels, even a change in the mechanical properties of the oxide in terms of reduced plasticity seems possible but has not been investigated in the frame of this thesis. The repassivation kinetics, especially at pre-existing cracks in LAS or in crevices, can therefore be significantly retarded due to the locally variable anionic activity by accumulation of chloride.

Consequently, based on the assumption of the acting slip-step dissolution mechanism, the experimentally observed effects caused by increased chloride concentrations in HTW, clearly explain the enhancement of crack initiation and crack growth (see also chapter 7) of LAS in oxygenated HTW.

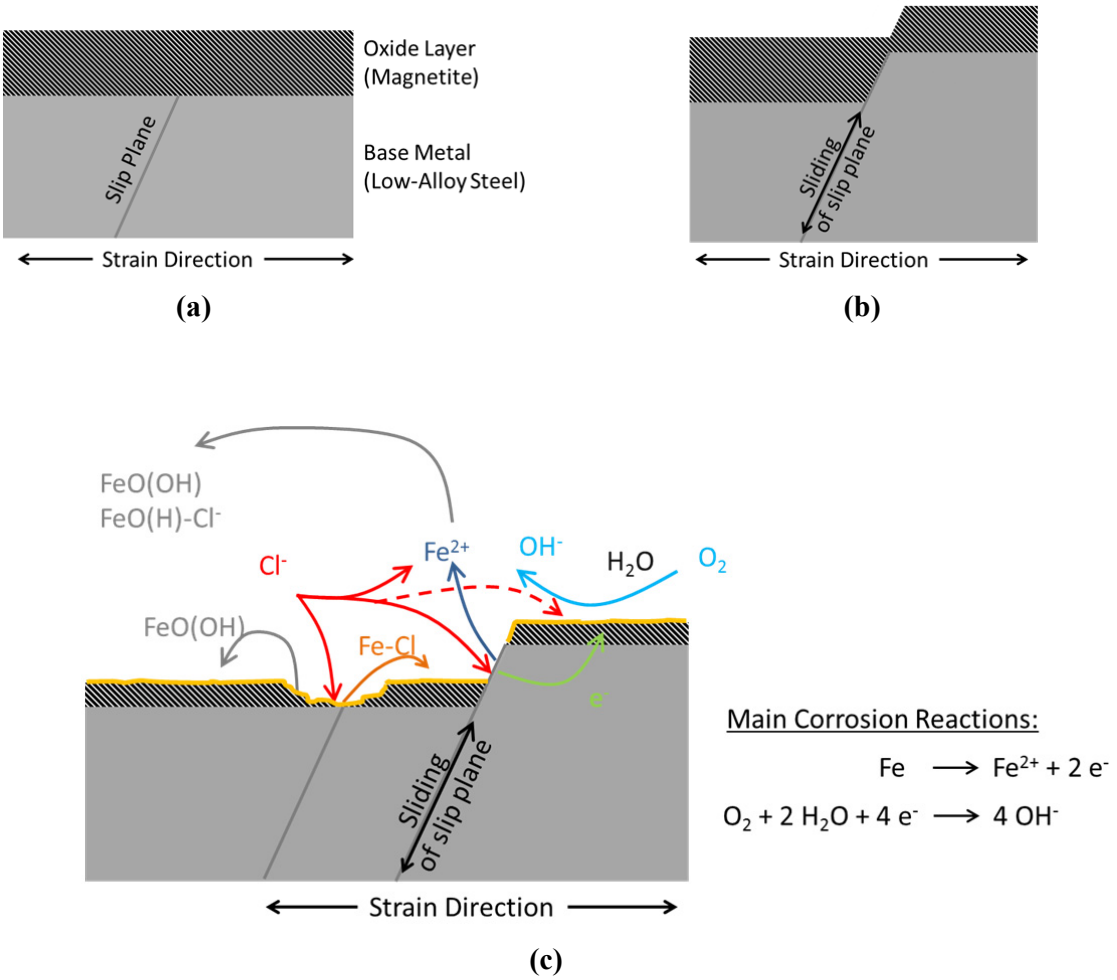

Figure 85: Schematic illustration of the effect of chloride on crack initiation of LAS in oxygenated HTW.
(a) Schematic drawing of the LAS surface prior to straining without chloride.
(b) Effect of local slip plane sliding without chloride. Due to the rather thick oxide layer no local breakdown of the oxide layer, and hence, no crack initiation occurs.
(c) After exposure to increased chloride concentrations, the overall oxide layer thickness is decreasing and increased pitting occurs. Hence, the same slip step height as in b) (without chloride) is now sufficient to cause local breakdown of the oxide layer and thereby crack initiation. Furthermore, the local pits may also act as crack initiation locations.

7. EFFECT OF CHLORIDE ON CRACK GROWTH[18]

This chapter summarizes the results from crack growth rate tests using 1T-CT specimens. The aim of these experiments was to study the effect of increased chloride concentrations on both,

(i) the crack growth rate, and
(ii) the change of the chemical composition of the crack electrolyte due to increased chloride concentrations in the bulk environment (by crack tip micro sampling).

7.1 Experimental Set-Up and Testing Procedure

Crack growth rate testing was performed in a once-through refreshing autoclave with full environmental control. The 1T-CT (CT 25) specimens were fatigue pre-cracked prior to testing in high-temperature water to an a/W value of 0.45 (see Appendix 6). After pre-cracking in air, the specimens were assembled to an 18 l stainless steel autoclave that is connected to an INSTRON type screw-driven electromechanical tensile test machine (see Figure 86).

The flow rate during testing was adjusted to approximately 8 l/h resulting in an average exchange rate of ~ 0.5 exchanges per hour. This exchange rate is sufficient to maintain the desired chemistry conditions at the specimens under so-called quasi-stagnant flow conditions.

During the experiments, all important environmental testing parameters were monitored and recorded at the inlet and outlet of the test loop (see Figure 86). The target chloride concentrations were adjusted by injection of a sodium chloride solution into the stainless steel autoclave by High Pressure Dosing Pumps (HPDPs). The injected chloride flow and the flow of the high purity water were calculated on a volumetric basis, to meet the target chloride level in the autoclaves. The amount of ionic impurities in the water was monitored online during testing by the change of the electrical conductivity. Results from on-line monitoring were verified by ion chromatography analyses of water samples that were regularly taken from the outlet of the test loop.

[18] **Parts of this chapter have previously been published:**
M. Herbst, et al. 2013. Effects of Chloride on the EAC-Behaviour of Low-Alloy Steels under simulated BWR-Conditions. 16th International Conference on Environmental Degradation of Materials in Nuclear Power Systems – Water Reactors, August 2013, Asheville, North Carolina.

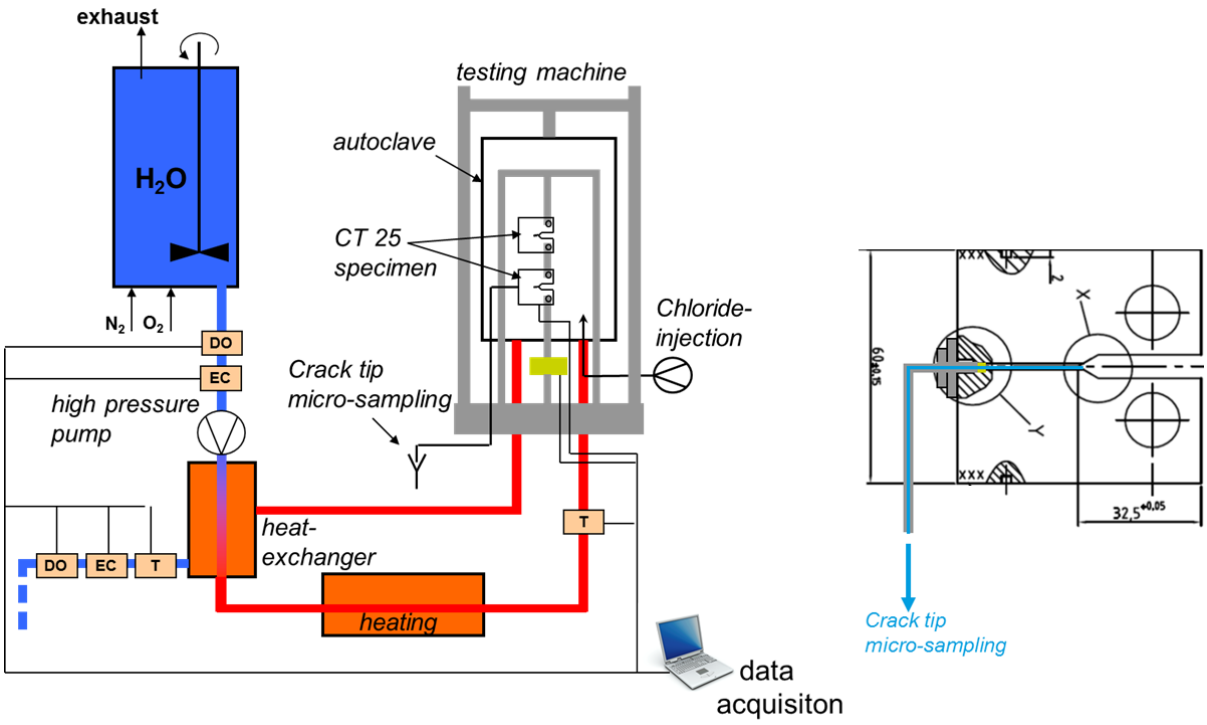

Figure 86: (a) Schematic drawing of the test set-up and (b) schematic drawing of the 1 T-CT specimen with back bore for crack tip micro sampling.

The crack advance was continuously monitored during testing using the reversed direct current potential drop (DCPD) method. The 1 T-CT specimens and the micro sampling device were electrically insulated from the autoclave using PTFE and zirconia spacers und tubing. The DCPD crack growth results were linearly corrected with the average SCC crack increments that were obtained in post-test fractography.

The nominal test environment was oxygenated HTW relevant for BWR steady state normal water chemistry operating conditions with a slightly increased oxygen concentration (see chapter 4).

For crack growth rate testing, 1 T-CT specimens with TS orientation were manufactured from the same material as used for exposure and crack initiation tests (chemical composition see Table 3).

Two specimens were assembled in the autoclave in a daisy chain arrangement. The upper specimen was used for crack growth rate measurement, the lower specimen was equipped with a back bore to allow crack tip micro sampling (see Figure 86).

For calculation of crack growth rates, only the specimen without back bore was considered. The second specimen was also equipped with DCPD monitoring and the crack advance during testing was measured, but these results have to be evaluated carefully due to the change in the K-value caused by the hole in the 1 T-CT specimen and the dilution of the crack tip by continuous soaking of the crack tip electrolyte.

In order to allow micro sampling during crack growth rate testing, a suitable test arrangement was developed within the frame of this work. The geometry of a standard 1 T-CT specimen was slightly modified to allow micro sampling. A hole was drilled to the standard 1 T-CT specimen in the crack growth plane from the back face of the specimen (see Figure 86 b and Appendix 5) and a 1/16´´ stainless steel piping with an inner diameter of approx. 0.7 mm was mounted to the specimen.

The piping has to be fully electrically isolated from the 1 T-CT specimen, in order to allow ECP and DCPD measurement. This was achieved using a pre-oxidized zirconia pipe fitting that was mounted to the back face of the 1 T-CT specimen, connecting piping and 1 T-CT specimen. The zirconia fitting electrically isolated the stainless steel piping from the 1 T-CT specimen and at the same time was leak tight to the environment. Hence, only solution from the crack tip was soaked into the stainless steel piping and “pollution” by bulk medium was prevented by the leak tight design of the micro sampling assembly. The stainless steel piping was routed out of the autoclave and connected to a microcapillary which reduced the flow to the target flow of approx. 0.13 ml/h. The end of this microcapillary was connected to a hypodermic needle that was directly injected into sampling vials.

The sampling vials were vented using hypodermic needles in order to minimize any contamination of the samples. All analyses were performed using ion chromatography.

As already mentioned above, the micro sampling rate during testing was adjusted to 0.13 ml/h. As shown by ANDRESEN and others (Andresen and Young, 1995b, Lee and Shoji, 1999, Young and Andresen, 1995) earlier, a sampling rate in the chosen flow-rate region does not

drastically influence the crack growth rate and delivers reasonable results regarding the concentration of anionic impurities at the crack tip. As also shown in some prior experiments, flushing of the crack may still occur even at the rather low sampling rate that was chosen in this work (Andresen and Young, 1995b). This has to be considered in the evaluation of the test results, since the actual concentrations of anionic impurities at the crack tip might even be higher as indicated by crack tip micro sampling.

In order to measure the actual concentration of anionic impurities at the crack tip, the following facts were considered.

After the increase of the chloride concentration during testing, the chloride concentration is the same in the overall testing system within 2 hours at the latest[19]. The bulk chloride concentration was monitored on-line by the change of the electrical conductivity at the outlet of the test loop and by water samples that were analysed using ion chromatography. If a chloride accumulation at the crack tip occurs, the overall micro sampling device has to be flushed (i.e. the total volume inside the piping of the micro sampling unit has at least to be exchanged once) before the analysis of the actual chloride concentration occurring at the crack tip may be analysed. Hence, it was conservatively assumed that both, the volume inside the notch of the 1 T-CT specimen, and also all piping routed out of the autoclave has to be flushed before the actual sampling could be started.

The volume inside the notch of the 1 T-CT specimen can be calculated to be ~ 2380 mm³ corresponding to a volume of ~ 2380 µl. Taking the piping into account that is routed out of the autoclave, the overall length of this pipe is ~ 1300 mm with an inner diameter of the pipe of ~ 0.7 mm this results in a pipe volume of approx. 500 mm³ corresponding to ~ 500 µl. Hence, the total "dead volume" of the micro sampling device is about 3000 µl. With the flow rate of

[19] The electrical conductivity measured at the outlet of the test loop is reaching a constant level 2 hours after increasing the chloride concentration. It is assumed that the chloride concentration inside the autoclave reaches the target concentration after 1 complete exchange of the solution inside the autoclave. Since the exchange rate of the autoclave is approx. 0.5 exchanges per hour, the actual chloride concentration at the specimen should reach the target level within 2 hours as indicated by the change of the electrical conductivity measured at the outlet of the test loop.

0.13 ml/h or 130 µl/h total flushing of the sampling unit occurs within approx. 24 hours at the latest. Hence, micro sampling was only started 24 hours after the chloride concentration was increased to receive sound and reliable results of the chloride concentration at the crack tip.

7.2 Results from Crack Growth Rate Testing

After fatigue pre-cracking, the specimens were assembled into the autoclave and testing was started with a pre-oxidation phase of ~ 800 hours. During the pre-oxidation phase, the micro sampling device was tested and adjusted. Following pre-oxidation, sequences of cyclic and constant loading at different maximum stress intensities ($K_{I,max}$) were applied. After a reasonable crack growth was achieved by cyclic loading with $K_{I,max}$ = 30 MPa√m (R=0.7; t_{rise} = 1000 s; t_{fall} = 200 s) the loading was changed to constant load at a K_I of 30 MPa√m (see Figure 87). After switching to constant load, the crack growth rate ceased to values below the detection limit of the DCPD method.

The chloride concentration was increased to 50 ppb chloride in the bulk solution 260 hours after the load signal was changed to constant loading.

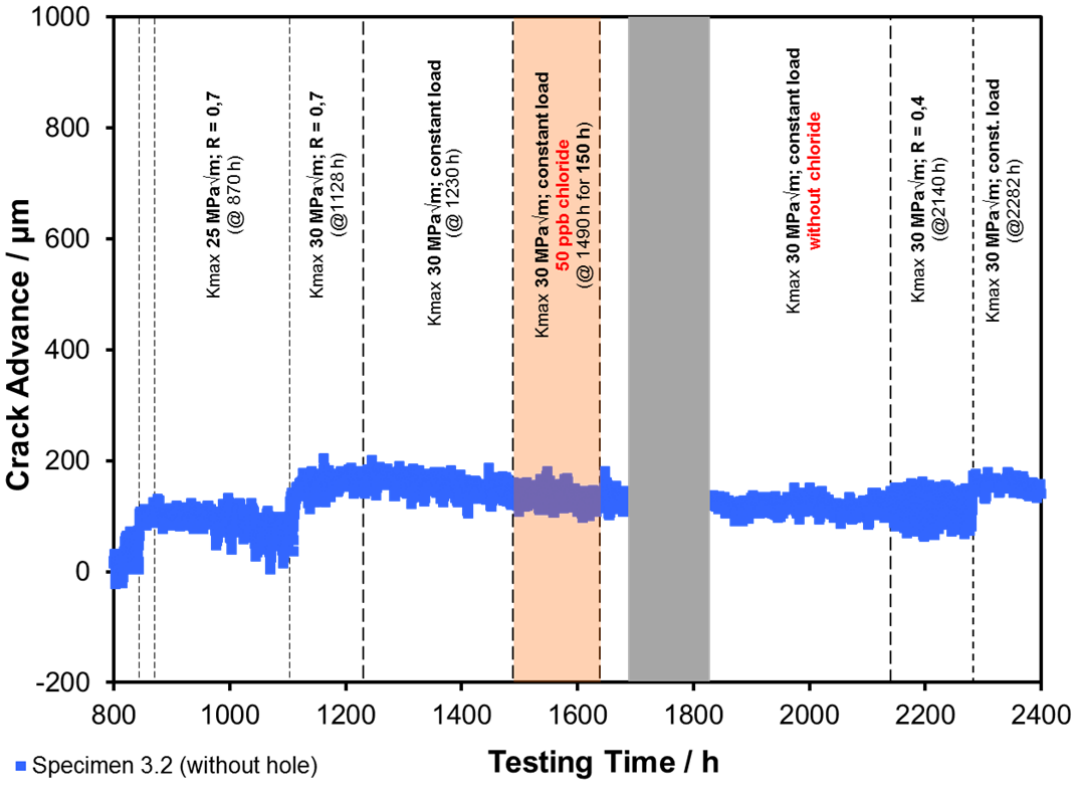

Figure 87: Crack advance from 0 to 2000 testing hours. At approx. 1700 testing hours a blackout caused a short shutdown of the test-loop and DCPD monitoring system (grey box).

After this deliberate increase of the chloride concentration, no effect on the crack growth rate was observed. Also during the following testing period of 150 hours at increased chloride concentration, no onset of crack growth occurred under pure constant loading (see Figure 87).

Since no crack growth occurred during ~ 150 testing hours at a bulk chloride concentration of 50 ppb, the chloride injection was stopped and testing conditions without chloride were applied beginning with 1640 testing hours. Shortly after this, the test, in particular DCPD monitoring, had to be temporarily interrupted due to a blackout[20] in the local electric supply system, which had no effect on the crack advance after testing was restarted (see Figure 87).

During the loading phase that was applied after the first deliberate increase in chloride concentration, the crack did not start growing again, even after severe cyclic loading was applied at a $K_{I,max}$ of 30 MPa√m (R=0.4; t_{rise} = 1000 s; t_{fall} = 200 s). From this observed behavior it seems that the crack tip blunted due to the temporary increase of the chloride concentration. Crack growth could only be re-activated by an increase of the $K_{I,max}$ to 40 MPa√m. Hence, cyclic loading at $K_{I,max}$ = 40 MPa√m (R=0.7; t_{rise} = 1000 s; t_{fall} = 200 s) was applied beginning with 2690 testing hours (see Figure 88).

After reasonable crack advance was observed, the loading mode was changed to constant load, where no further crack advance occurred for 120 testing hours (see Figure 89). The chloride concentration was again increased to 50 ppb at 3168 testing hours and an onset of crack growth under pure constant loading was observed approx. 5 hours after the deliberate change of the chloride concentration (see Figure 89 and Figure 90). As described in the previous chapter, the chloride concentration reached its target level in the bulk environment at the specimen approx. 2 hours after the increase in the chloride concentration. Hence, the incubation time between the increase of the chloride concentration at the specimen and the increase of the crack growth rate is approx. 3 hours.

---

[20] The loading that was applied to the specimen during the blackout was held at a constant strain during the temporary blackout, hence no loading exceeding the target $K_{I,max}$ during constant loading was applied. Due to the blackout, the temperature slightly decreased temporarily, which has no effect on the overall crack growth rate experiment.

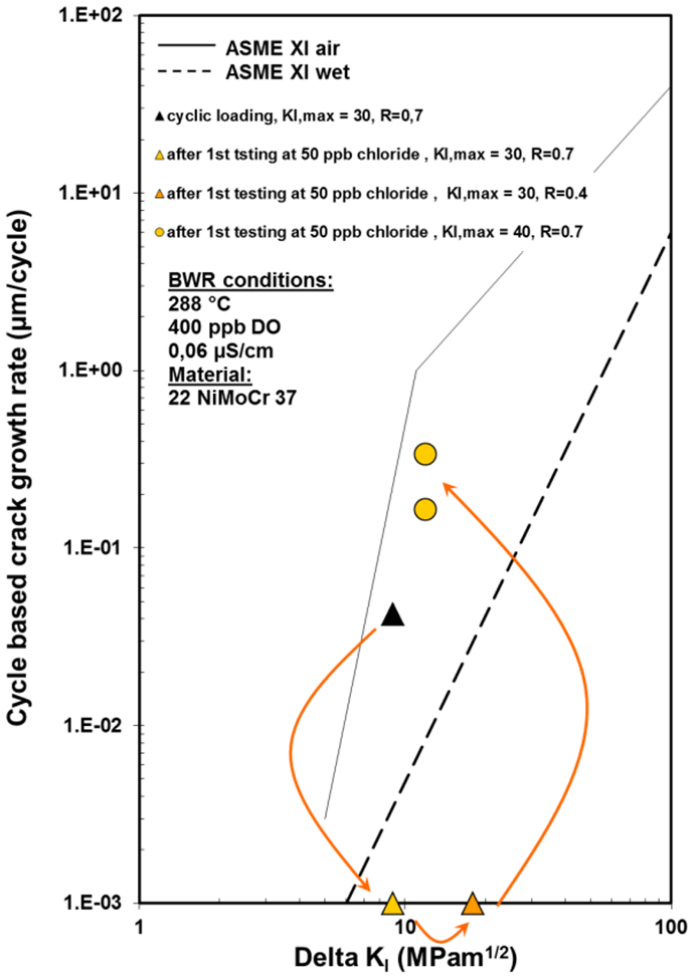

Figure 88: Cycle based crack growth rate before and after testing at increased chloride concentration.

After switching back to conditions without chloride (at 3390 testing hours), the crack growth rate decreased to approx. 1.9 x 10^{-11} m/s which is slightly above the crack growth rate that was observed before the chloride concentration was increased (see Figure 89). A decrease of the crack growth rate occurred at the latest 2 hours after chloride injection was stopped, which is approx. the time needed to flush the autoclave. This indicates that no considerable memory effect is present with regard to the chloride induced change in the crack growth rate.

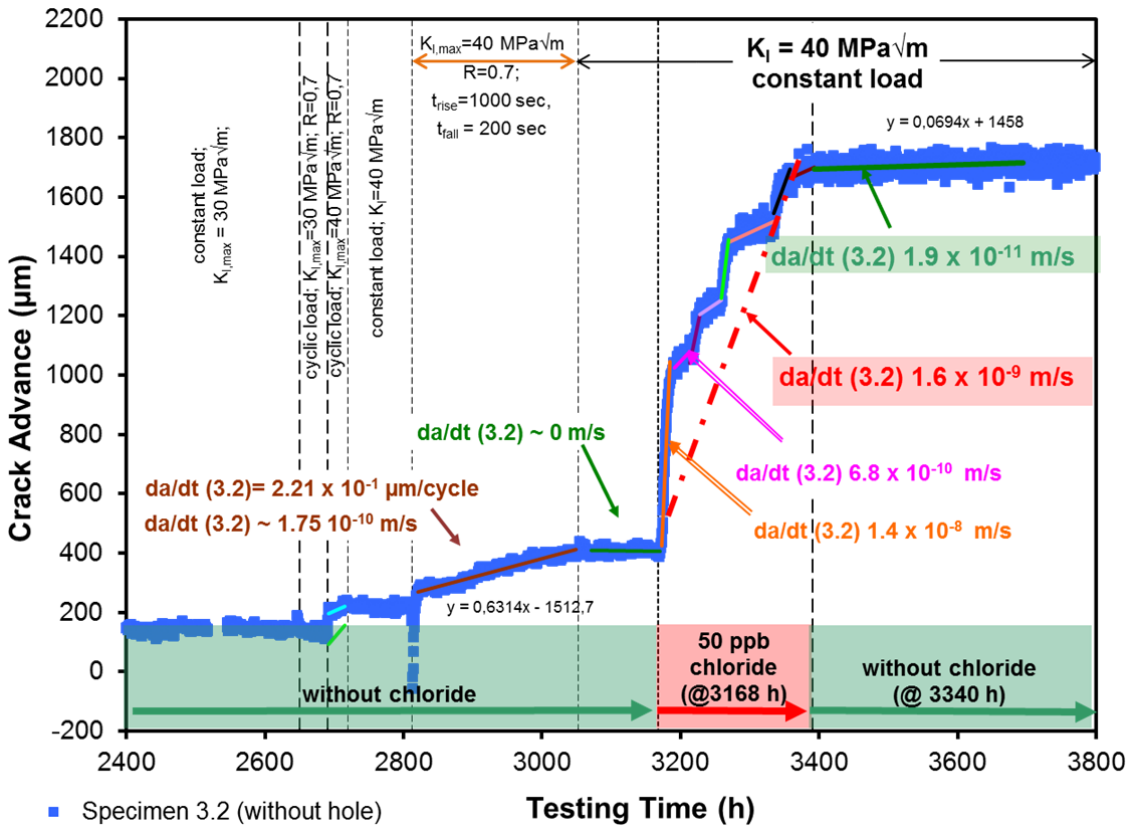

Figure 89: Crack advance between 2400 and 3800 testing hours.

After a rather long testing time under pure constant loading in high-purity water chemistry (approx. 500 h), the chloride concentration was temporarily increased to 20 ppb chloride beginning with 3838 testing hours, simulating a short term chloride transient. This 24 hour chloride transient did not result in any change of the observed crack growth rate. The same observation was made for a 50 ppb chloride transient that was applied after the 24 hour 20 ppb transient beginning with 3964 testing hours (see Figure 91).

This observation clearly shows that such chloride transients do not cause an immediate onset of crack growth if the crack was not actively growing, e.g. due to cyclic loading, prior to the increase in the chloride concentration.

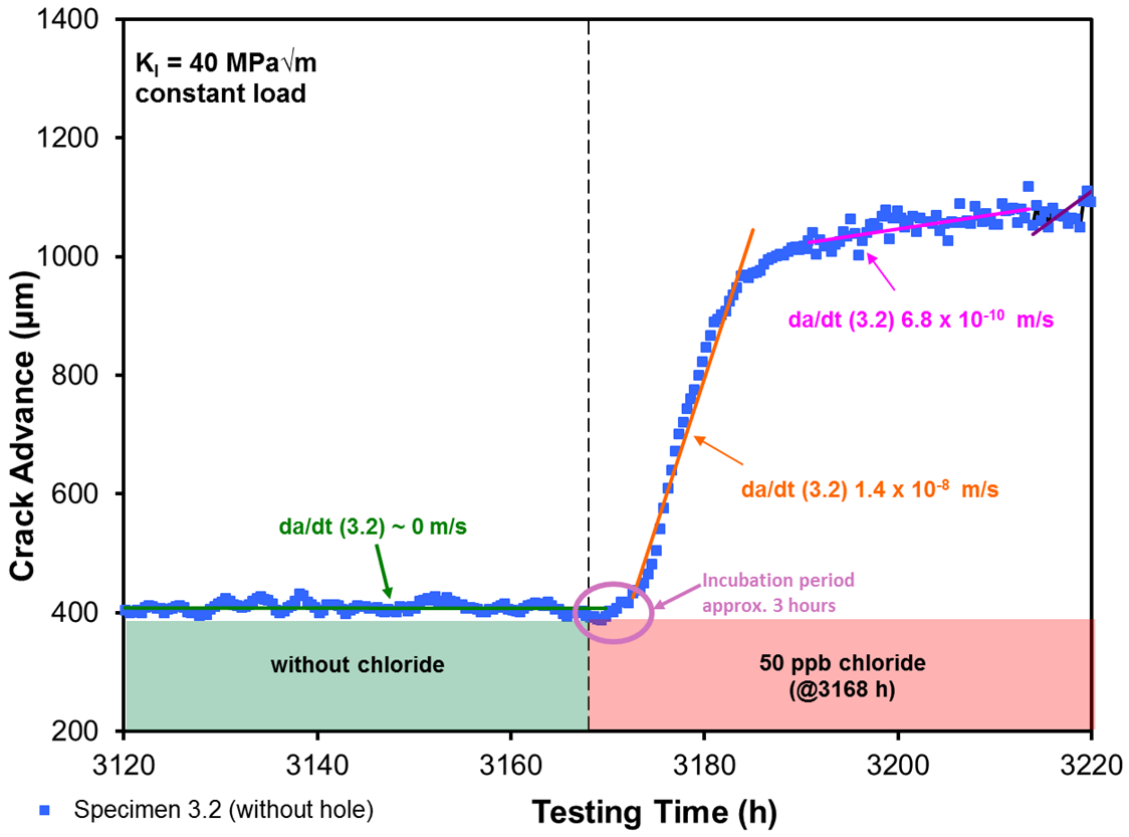

Figure 90: Detailed view on the crack advance between 3120 and 3220 hours after chloride concentration was increased to 50 ppb. In the incubation period of approx. 3 hours the 2 hours that are needed to establish the target chloride concentration have already been considered.

The next testing phase at increased chloride concentration started with 4130 testing hours. During this period, a mechanical transient (R = 0.7, t_{fall} = 200 sec, t_{rise} = 1000 sec) was applied during testing at increased chloride concentration at 4155 testing hours. This single un- and reloading caused an increase of the observed CGR during straining of the crack tip. However, after this single transient, no more crack advance was observed (see Figure 91).

Since no crack growth was observed during testing at different temporarily increased chloride concentrations, the crack was re-activated using cyclic loading ($K_{I,max}$ = 40 MPa√m, R = 0.7; t_{rise} = 1000 s; t_{fall} = 200 s) beginning with 4230 testing hours which resulted in a reasonable crack advance (see Figure 91).

Directly after switching to constant loading, the chloride concentration was again increased to 50 ppb chloride, which resulted in a rather immediate increase of the crack growth rate after an incubation period of about 3 hours (see Figure 91). The crack growth rates during this testing period were in the range between 2.2 x 10^{-8} m/s and 4.7 x 10^{-11} m/s thus resulting in a mean crack growth rate of approx. 5.5 x 10^{-10} m/s.

When the water chemistry was again changed to high-purity water chemistry conditions, the crack growth rate decreased to 2.8 x 10^{-11} m/s (see Figure 91). After additional 300 testing hours at these conditions, chloride was again injected to the test solution and resulted in the same change of the crack growth rate that was previously observed (see Figure 92).

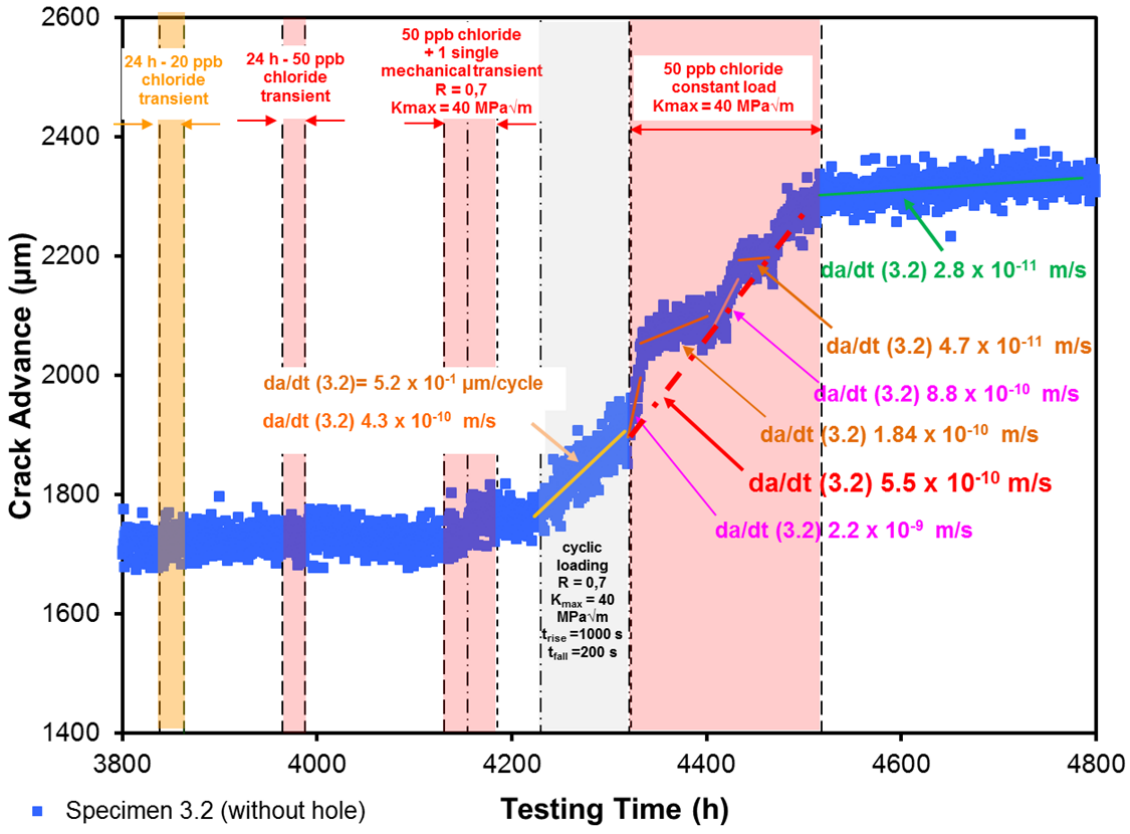

Figure 91: Crack advance between 3800 and 4800 testing hours.

During this final testing phase, the loading was temporarily increased to a maximum stress intensity of 50 MPa√m. This load sequence caused significant crack advance during straining of the specimen. However, after the single mechanical transient no change of the crack growth rate was observed compared to the CGRs obtained prior to the mechanical transient. Hence, even if a pre-existing crack is actively strained during periods with increased chloride concentrations, no crack growth rates above the levels that have been observed during various testing periods at increased chloride concentrations may occur.

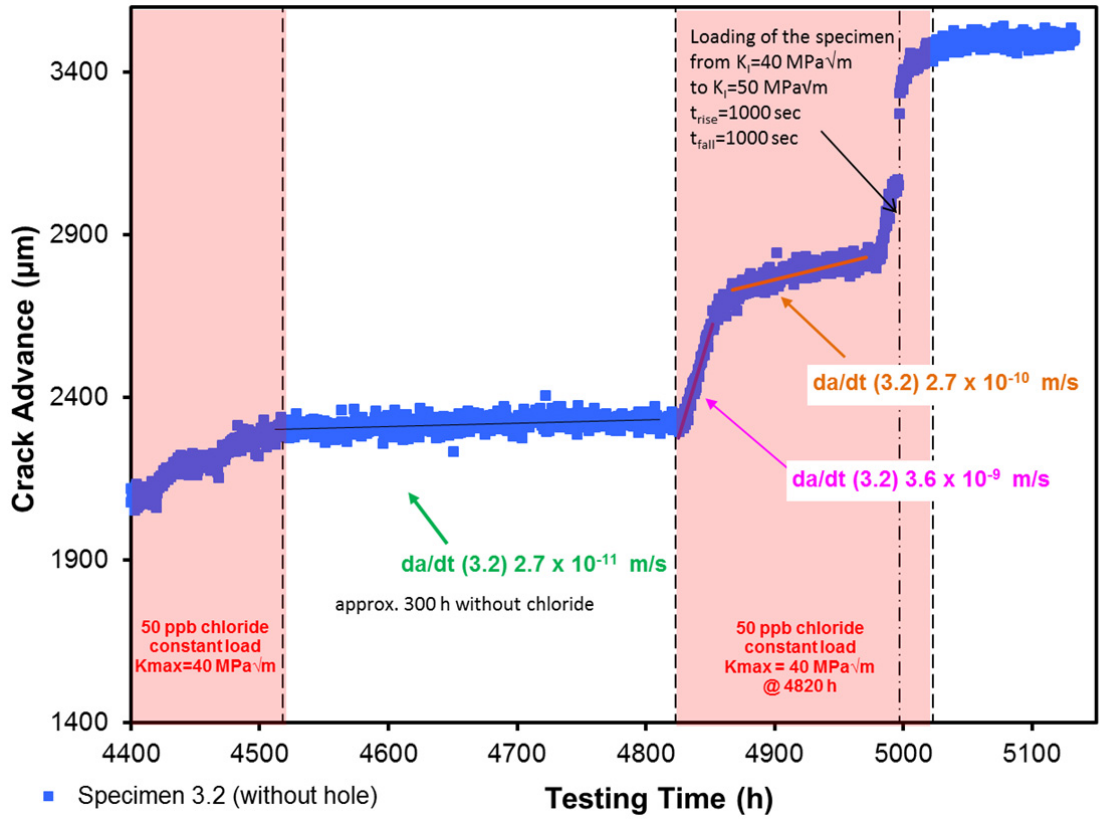

Figure 92: Crack advance between 4400 and 5200 testing hours.

7.3 Results from Crack Tip Micro Sampling

During testing under high-purity water conditions and during several testing periods with increased bulk chloride concentrations, various water samples have been analysed from both, the outlet of the test loop as well as the crack tip using crack tip micro sampling.

Prior to the increase in the chloride concentration, the micro sampling technique was verified. This included the verification of a constant flow velocity of 0.13 ml/ h during sampling and the analysis of a number of blind samples from the crack tip. These samples showed no increase in both, chloride as well as sulphate concentration.

After the bulk chloride concentration was firstly increased to 50 ppb at approx. 1490 hours of testing, the chloride concentration obtained from both, the bulk solution and crack tip samples was analysed several times. As revealed by comparison of water samples taken at the outlet of the test loop and micro sampling samples, the chloride concentration at the crack tip was around 7 to 10 times higher compared to the bulk chloride concentration. The actual chloride concentration that was observed using the micro sampling technique was in the range of 350 to 590 ppb (see Figure 93). Even these chloride concentrations at the crack tip obviously caused no onset of crack growth under purely constant loading.

Micro sampling, that was performed after the chloride concentration in the bulk was increased to 50 ppb at approx. 3170 testing hours again revealed a strongly increased chloride concentration at the crack tip (see Figure 93). The crack tip chloride concentration in fact increased to 610 ppb and 860 ppb, respectively (about 12 to 20 times the bulk concentration).

In addition to the samples taken during testing at increased chloride concentrations, some analyses were also performed during testing periods without chloride in the bulk. These analyses showed that the bulk chloride concentration was below the detection limit of the analysis method (< 0.005 ppm) and the concentration in the crack tip samples was only slightly increased to 17 ppb at the maximum (compared to 610 to 860 ppb during testing at 50 ppb chloride bulk concentration) during phases without deliberately increased chloride concentrations in the bulk medium.

Additional tests at a bulk chloride concentration of 20 ppb (not shown in Figure 93) revealed a crack tip chloride concentration of approx. 170 ppb.

From the results of crack tip micro sampling it can thus be concluded that the chloride concentration at the crack tip is at least 10 to 20 times higher as compared to the bulk concentration.

The actual chloride concentration that is established at the crack tip without micro sampling should even be higher as the obtained concentrations, since crack tip micro sampling causes flushing of the crack tip electrolyte due to soaking crack tip electrolyte out of the crack. Hence, the reported analysis results most likely underestimate the actual concentrations at the crack tip.

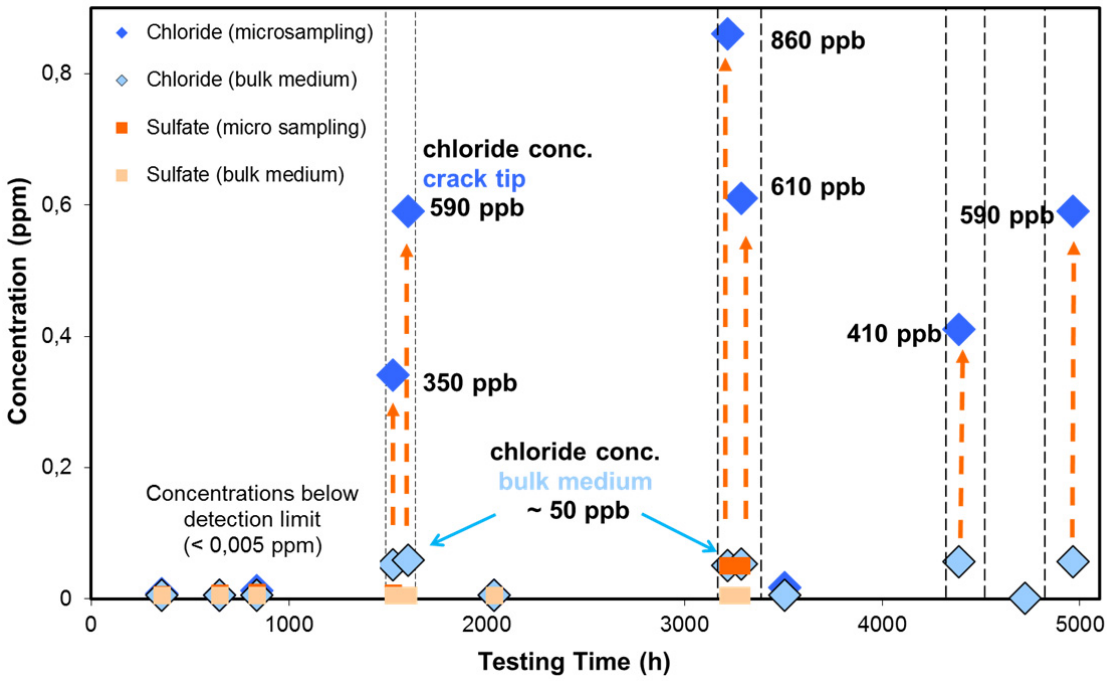

Figure 93: Overview on the amount of anionic impurities in the bulk and at the crack tip as analyzed by ion chromatography.

7.4 Results from Fractography

Some results of post-test fractography are summarized in Figure 94 and Figure 95. These Figures show that cracking was well developed over the whole width of the specimens and that crack propagation in the specimen without crack tip sampling is higher compared to the specimen without back bore.

This observation is on the first sight somewhat confusing since the actual K at the specimen with back bore is supposed to be higher as compared to the regular 1 T-CT specimen. A possible explanation for this observation is the fact that the crack tip electrolyte of the micro sampling specimen could not develop in the same way as compared to the specimen without micro sampling, since the crack tip electrolyte was continuously removed. Hence, crack growth seems to be more dominated by maintaining a critical crack tip electrolyte than by the difference in the stress intensity factor.

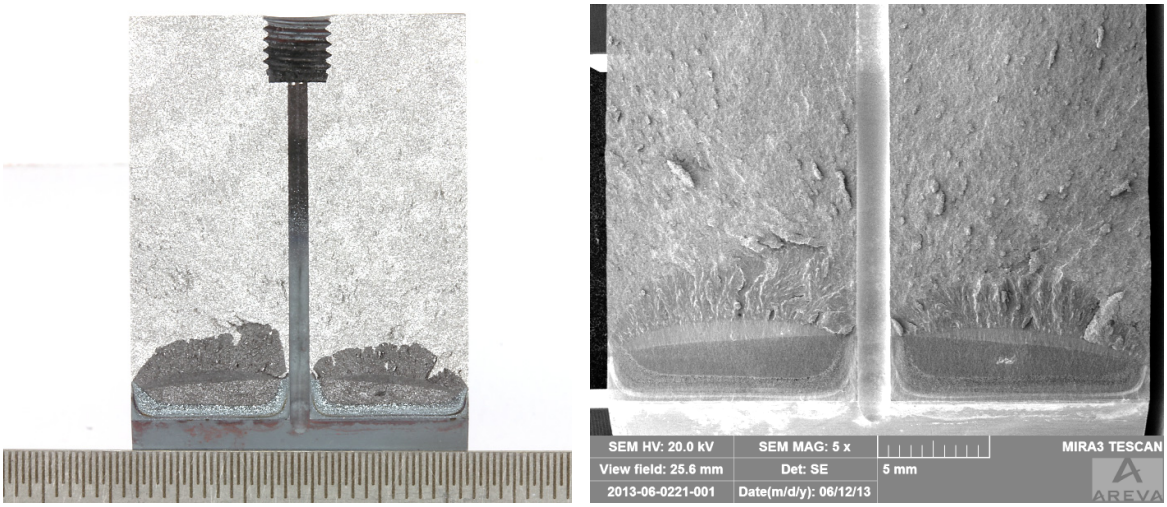

(a) **(b)**

Figure 94: (a) Macrograph of the fracture surface from the modified 1 T-CT specimen that was used for crack tip microsampling showing the backbore that was used for microsampling. Regions with environmentally assisted crack growth appear dark due to the high-temperature oxide, post-test crack appears lighter.
(b) SEM image of the of the fracture surface.

This is also indicated by the shape of the crack front that developed at the micro sampling specimen. The crack front obtained during pre-cracking developed the typical finger nail shape over the whole specimen width. In contrast to that, the SCC crack front developed during SCC-testing changed in a way that the crack growth developed a finger nail shape on both sides of the hole for micro sampling (see Figure 94). This indicates the importance of the critical crack tip electrolyte for SCC crack growth.

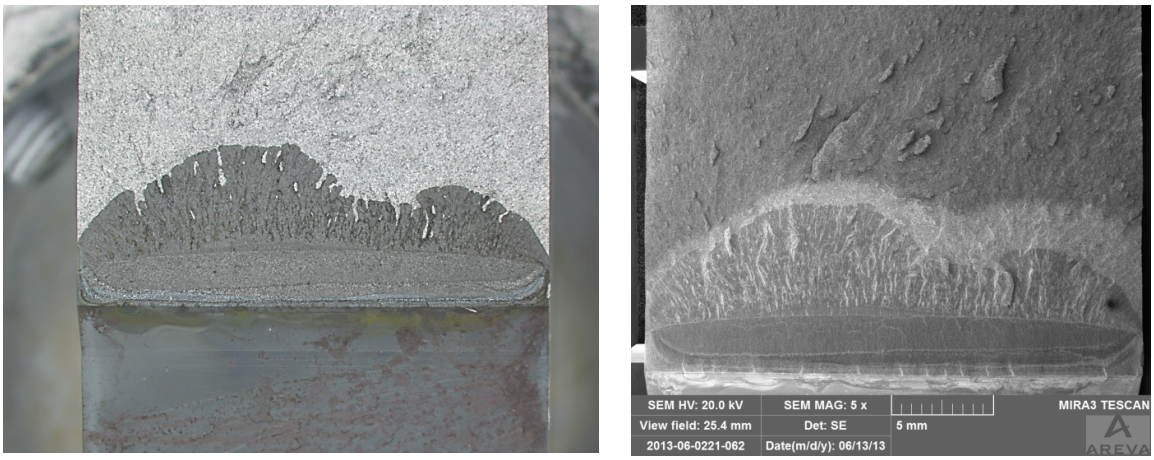

(a) **(b)**

Figure 95: (a) Macrograph of the fracture surface from the 1 T-CT specimen that was used for acquisition of the crack length during testing under simulated BWR-conditions. Regions with environmentally assisted crack growth appear dark due to the high-temperature oxide, post-test crack appears lighter.
(b) SEM image showing a detailed view on the fracture surface.

7.5 Summary and Discussion

7.5.1 Overall Summary

The effect of deliberately increased chloride concentrations on the crack growth rate of LAS under simulated BWR conditions, and its effects on the chemical composition of the crack tip electrolyte have been studied in these investigations.

On-line DCPD monitoring that was performed during testing revealed no onset of crack growth when the crack has not actively grown within a few hundred hours prior to the increase in the chloride concentration. After testing at increased chloride concentrations, it has even been observed that re-activation of the crack is somewhat difficult even under severe mechanical loading, which may be attributed to crack tip blunting caused by the increased chloride concentrations (see Figure 88).

Hence, it can be summarized that, in contrast to some experiments that have been previously published at higher K_I values, the results of this work show that an increase of the chloride concentration under purely constant loading does not necessarily cause an increase of the crack growth rate without prior activation of the crack tip.

In contrast to this observation, an increase in the measured crack growth rates was observed under pure constant loading exclusively due to an increase in the chloride concentration after prior activation of the crack by mechanical loading.

The incubation period after the increase of the chloride concentration was approx. 3 hours taking into consideration that it takes about 2 hours until a homogeneous chloride concentration in the bulk solution of the autoclave was established.

Based on the crack growth responses observed during testing, it is concluded that enhancement of crack growth by either initiating arrested cracks or by acceleration of growing cracks is depending on the condition within the crack, in particular at the crack tip.

It is therefore proposed to define the term i) "active crack", and in contrast to that ii) "passive crack":

i) A "passive crack" is expected to be blunted at the crack tip and partly or fully filled with oxide, which separates the crack tip from the bulk environment.

ii) An "active crack" is either dormant, but ready to be re-started, or actively growing with a certain rate. Such cracks are expected to have sharp crack tips and are more or less still open to the bulk environment.

Figure 96 shows a summary of the crack growth rates that were obtained during testing at different K_I-levels and chloride concentrations using one specimen together with some literature data. This shows that for K_I of 30 MPa√m, no effect of increased chloride concentrations was observed up to 50 ppb chloride. For a K_I of 40 MPa√m, an increase in the crack growth rate at 50 ppb chloride was observed for cracks that were assumed to be "active". During testing at 50 ppb chloride, phases with high and low CGR´s have been observed, as indicated in Figure 96. From the observed CGRs, a mean CGR in the range of 10^{-9} m/s can be calculated for a K_I of 40 MPa√m and a chloride concentration of 50 ppb. This rate fits well to the literature data that is also summarized in Figure 96.

Results from crack tip micro sampling indicate a crack tip chloride concentration that is strongly increased as compared to the bulk chloride concentration. The crack tip chloride concentration was about 9 to 20 times higher compared to the bulk concentration. In addition, it is important to mention that the actual crack tip chloride concentration may even be underestimated by the results obtained from crack tip micro sampling since flushing of the crack tip continuously occurs during micro sampling and may cause a dilution effect. Hence, the actual chloride concentration at the crack tip may even be higher as indicated by micro sampling. This has also been indicated in earlier published literature data which report a 20 to 30 x higher sulphate and chloride concentration at the crack tip as compared to the bulk chloride concentration (Andresen and Young, 1995a, Psaila-Dombrowski, 1990, Ford et al., 1987).

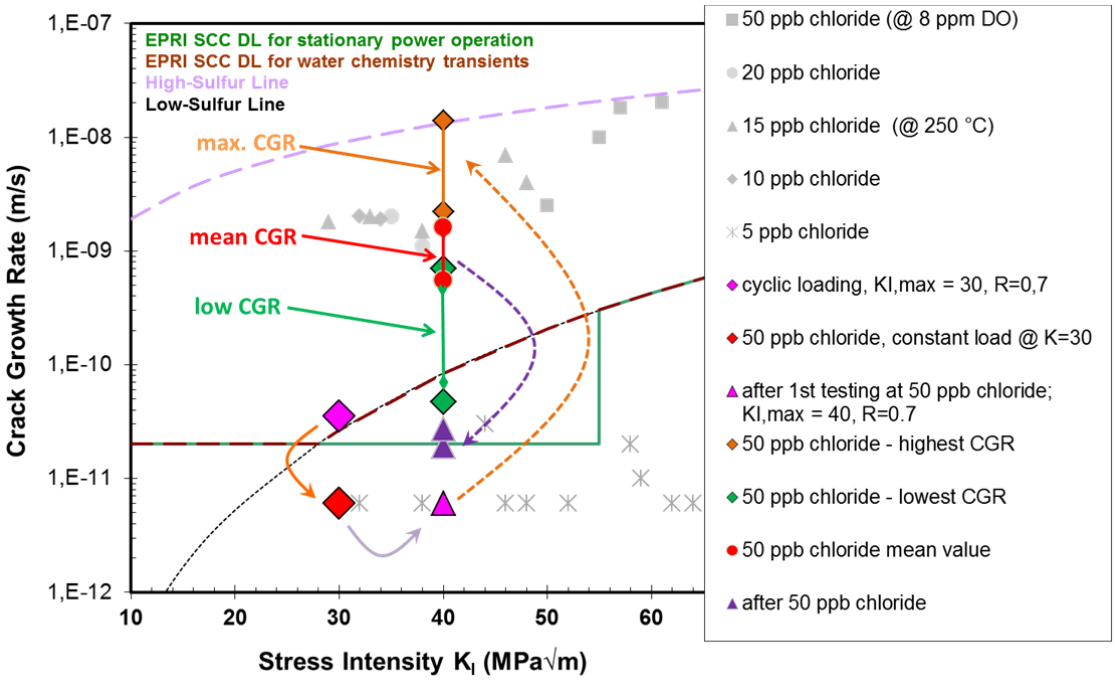

Figure 96: Crack growth rate versus stress intensity for testing conditions with- and without chloride. Grey symbols are taken from publications by RITTER and SEIFERT (Ritter and Seifert, 2009).

As indicated by crack tip micro sampling, even strongly increased chloride concentrations at the crack tip (up to 590 ppb) do not necessarily cause crack initiation at "passive cracks" without prior activation of the crack. Under such conditions, the increased chloride concentration at the crack tip seems to cause increased solubility of iron and iron oxides. This increased solubility may lead to blunting at the crack tip. Accordingly, the blunted crack, eventually partially or completely filled with oxide, could not be re-activated by the cyclic loading in pure HTW (without chloride) when the same K_I was applied as before the increase of the chloride concentration (see Figure 88).

Crack activation due to the increase in the chloride concentration was only observed for "active cracks", which are cracks that have actively grown (e.g. due to mechanical loading) within a certain time period prior to the increase in the chloride concentration. For such cracks, an increase in the crack growth rate was observed after an incubation period of approx. 3 hours after the chloride concentration was increased.

Conservatively assuming that diffusion is the leading mechanism for chloride transportation within the crack (neglecting the overlap of other driving forces, e.g. in particular migration due to potential gradients), the time needed for chloride to reach the crack tip purely by diffusion may be estimated using $x = \sqrt{D\ t}$ (Stellwag et al., 1998, Cussler, 1984), where x is the length of the diffusion path, D the diffusivity and t the time. At approx. 300 °C the diffusivity of chloride (Cl^-) in water is about 3.8 x 10^{-4} cm²/s (Psaila-Dombrowski, 1990, Engelhardt et al., 1999). With a crack depth of the 1 T-CT specimen of about 2.5 cm, the estimated time for chloride to reach the crack tip purely by diffusion is about 5 h. As observed during testing, the actual incubation period until an increase of the crack growth rate occurred was about 3 h, taking into account that it takes approx. 2 hours until the target chloride concentration is established in the autoclave.

This shows that another driving force for chloride accumulation plays an additional or even a more significant role. As chloride ions are electrically, negatively charged particles, migration in the electric field due to the potential gradient of the electrochemical potential within the crack is therefore assumed to be the leading mechanism regarding chloride accumulation at the crack tip under the chosen testing conditions (see chapter 7.5.2).

After the chloride concentration was decreased to levels < 2 ppb chloride, the crack growth rate slowed down to values in the range of 10^{-11} m/s within approx. 2 hours at the latest. This indicates that a critical crack tip chloride concentration can only be maintained if chloride is present in the bulk solution, which can be explained by the fact that chloride accumulation at the crack tip occurs due to the so-called “anion pump” which is only active as long as chloride is present in the bulk solution (see Figure 97). These results also clearly show that no memory effect is to be expected from temporarily increased chloride concentrations, since even growing cracks will slow down to irrelevant crack growth rates under high-purity water conditions.

During testing at increased chloride concentrations, time periods with higher and lower crack growth rates were observed. This behaviour may be attributed to the rupture of uncracked ligaments, which causes the observed stepwise changes in the acquired DCPD signal.

Another possible explanation for this behaviour may be the fact that a critical crack tip electrolyte (in particular in terms of critical chloride concentration) may not be maintained after onset

of fast crack growth. As shown by crack tip micro sampling, the chloride concentration at the crack tip is strongly increased as compared to the bulk chloride concentration (approx. 9 to 20 times higher). Hence, a transport of chloride from the bulk solution to the crack tip and its importance regarding the observed crack growth rates is confirmed.

The incubation time that was observed between the increase of the chloride concentration and the crack growth rate was approx. 3 hours, indicating that the transport of chloride from the bulk to the crack tip occurs not immediately and a critical crack tip electrolyte causing onset of crack growth may only develop after a critical crack tip electrolyte was established due to migration of chloride towards the crack tip. Furthermore, crack growth was only observed as long as the chloride concentration in the bulk solution was increased. This also indicates the importance of chloride supply from the bulk solution to the crack tip. Similar results in terms of maintaining a critical crack tip sulphur concentration due to the presence of a critical crack growth rate have been reported by LIN and WIRE (Wire, 2000, Yin Li, 2000).

When the crack is advancing into the LAS, new bare metal is exposed at the crack tip, which causes also a change of the crack tip electrolyte since chloride from the crack tip is absorbed in the oxide layers that develop on the new side surfaces of the crack. Without sufficient chloride supply from the bulk solution, the critical crack tip electrolyte may not be maintained. Hence, crack advance may only be re-activated after a critical crack tip electrolyte has re-established which may be the reason for periods with higher and lower crack growth rates (see Figure 89 and Figure 91).

7.5.2 Mechanistic Aspects on the Effect of Chloride on Crack Growth and Crack Tip Electrolyte

The local mechanical, metallurgical and environmental conditions, and in particular the chemistry conditions at the crack tip are essential parameters regarding crack initiation and environmentally assisted crack growth.

The impurity concentration at the crack tip depends on the impurity concentration in the bulk, the production or depletion rate (in particular regarding sulphur from MnS inclusions in the LAS) and the transport of impurities into and out of the crack. The most important transport mechanisms are:

- **Convection** (of neutral and charged species) which is mainly relevant for high flow rates.
- **Diffusion** (of neutral and charged species) which is relevant mainly for PWR-conditions were no or just a small potential gradient between crack mouth and crack tip is present.
- **Migration** (only charged species) which is driven by the potential difference between the crack mouth and the crack tip and is therefore mainly relevant for BWR-conditions.

For BWR-conditions with normal water chemistry (oxygenated HTW), a differential aeration cell between crack tip and crack mouth develops since oxygen reduction alongside the narrow crack occurs faster as oxygen diffusion inside the crack. Therefore, almost all oxygen is consumed over a short distance from the crack mouth causing a decrease in both, the DO and ECP inside the crack (Gabetta, 1991, Gabetta, 1982). In addition to the oxygen depletion inside the crack, iron is exposed at the crack tip due to anodic dissolution after straining of the crack tip furthermore depleting oxygen near the crack tip.

The low conductivity of the solution furthermore avoids direct electric coupling between crack tip and crack mouth which are therefore only coupled by mass transfer alongside the crack. Hence, the anodic dissolution current is balanced by reduction of hydrogen or reduction of water at the crack walls near the crack tip (Gabetta, 1991, Gabetta, 1982, Andresen, 1987, Andresen and Young, 1995a).

These processes cause a very low ECP of around -550 mV_{SHE} at the crack tip, whereas the ECP at the crack mouth is around 0 to +100 mV_{SHE}. This potential drop of about 500 to 700 mV_{SHE} is acting as a pump, the so-called "anion pump", for anionic impurities towards the crack tip (Andresen and Young, 1995a).

The effect of steel sulphur concentration, ECP, and hydrogen or oxygen concentration on EAC of LAS have been investigated in the past (Atkinson et al., 1996, James and Moshier, 1999, Moshier and James, 1999) and the importance of maintaining a critical crack tip sulphide concentration could be experimentally underlined (Wire, 2000, Yin Li, 2000).
As chloride ions are electrically negatively charged particles, migration in the electric field due to the potential gradient of the electrochemical potential within the crack is the most important driving force in oxygenated HTW, causing the high chloride concentrations at the crack tip that have been observed in this work (see Figure 97).

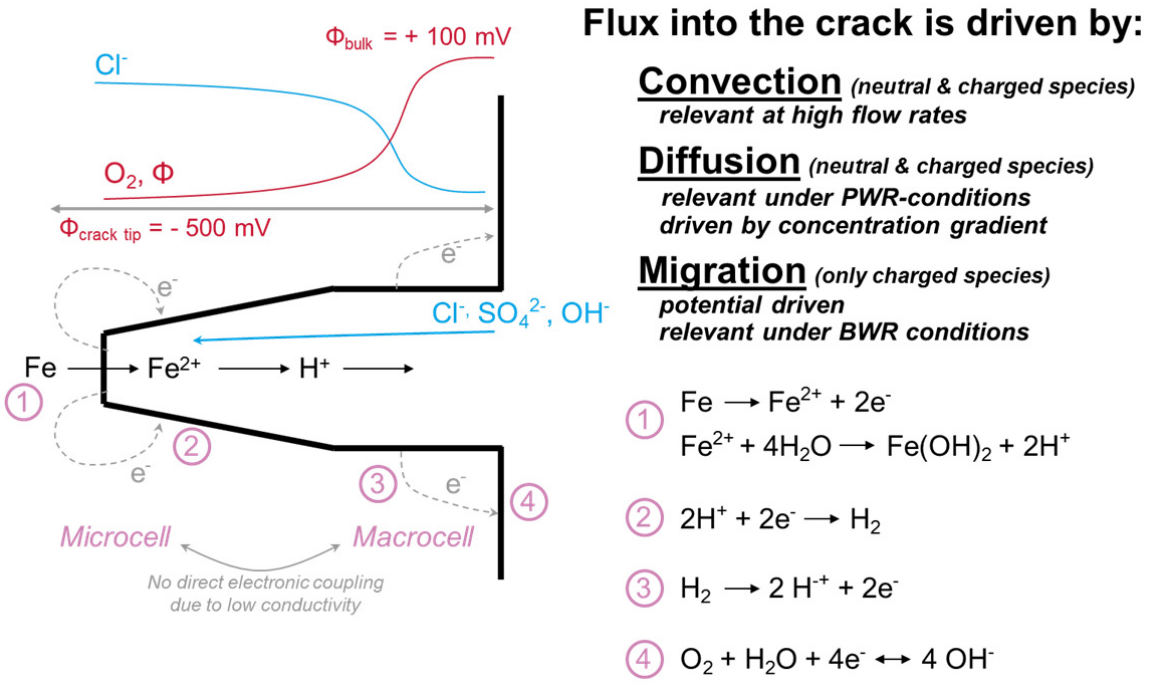

Figure 97: Schematic of the crack electro and water chemistry. The figure shows the differential aeration cell at the crack-mouth (reaction 3 and 4) that establishes the crack-tip chemistry and the local microcell (reaction 1 (metal oxidation and hydrolysis reaction) and reaction 2 (reduction of hydrogen)) associated with metal dissolution at the crack tip (Andresen and Young, 1995a).

The metal dissolution and hydrolysis ($Fe \rightarrow Fe^{2+} + 2e^-$; $Fe^{2+} + 2\ H_2O \rightarrow Fe(OH)_2 + 2\ H^+$) cause an acidification of the crack tip. In addition, the migration of charged particles (e.g. Cl^-, F^-, S^{2-}, SO_4^{2-}, HS^-) results in compensation of the positive charge of the H+ ions at the crack tip and therby further enhances the acidification at the crack tip, which has been observed to be in the range of Δ pH 1 to 2 (Andresen and Young, 1995b, Andresen and Young, 1995a, Young and Andresen, 1995, Lee and Shoji, 1999, Ford and Combrade, 1985, Ford, 1986, Maeng et al., 2005, Aaltonen et al., 2002, Ford et al., 1987).

Increasing dissolution of the protective oxide layer in crevices with increasing bulk chloride concentration in combination with an acidification within the crevice has also been reported by HOFFMEISTER (Hoffmeister, 2009, Hoffmeister and Klein, 2011). According to their results, the restricted chloride solubility in the aqueous crevice solution acidifies more than often assumed by pure metal hydrolysis (by precipitation of oxides only).

Another factor that has been discussed to influence the CGR is the conductivity within the crack. The solubility of corrosion products in near neutral pH is rather low and the crack tip conductivity is approx. 100 to 1000 x higher as compared to the bulk conductivity. However, the conductivity has only little effect on the CGR, since it is mainly the concentration of anionic impurities which influence crack-tip repassivation kinetics and pH (Andresen, 1996, Andresen and Young, 1995a).

The profile of the chloride concentration along cracks has been calculated by MACDONALD and ENGELHARDT (Macdonald and Urquidi-Macdonald, 1991, Engelhardt et al., 1999). Their calculations showed that chloride accumulates within the crack and the chloride concentration reaches a plateau at rather short depth inside the crack. The concentration factor that is predicted in the literature is ranging from 20 to 30 (as revealed by crack tip micro sampling) (Andresen and Young, 1995b, Andresen and Young, 1995a) up to 300 (Balachov et al., 2000) or 10^3 to 10^6 (Macdonald and Urquidi-Macdonald, 1991), which is much higher as compared to the results obtained in this work.

Regarding changes in pH, calculations by MACDONALD (Macdonald and Urquidi-Macdonald, 1991) showed only a slight acidification of $\Delta pH \sim -0.48$ at the crack tip for an oxygen concentration of 100 ppb in the bulk solution in pure HTW. The bulk chloride (NaCl)

concentration, however, seems to strongly affect the crack tip pH (Hoffmeister, 2009, Hoffmeister and Klein, 2011). Increasing the bulk NaCl concentration to approx. 60 ppb causes an acidification of $\Delta pH \sim -2.03$ (Macdonald and Urquidi-Macdonald, 1991). A pH shift of approx. 2 has also been proposed by ANDRESEN et al. (Ford et al., 1987). Hence, an acidification within this range is to be expected to have occurred in the experiments performed in the frame of this work.

Based on the results obtained during crack growth rate testing, two cases have to be considered regarding the effect of increased chloride concentrations on crack growth of LAS in oxygenated HTW:

i) conditions, where the crack has not been active prior to the increase of the chloride concentration (long-term arrest after growth), such cracks are designated as **"passive crack"**, and
ii) conditions, where the crack is dormant and has been recently active prior to the increase of the chloride concentration (short-term arrest after growth), such cracks are designated as **"active crack"**.

i) In case of a **passive crack** (see Figure 98 a), the crack was not growing for a long period prior to the increase of the chloride concentration. Hence, the crack tip as well as the crack flanges are assumed to be covered by oxide. Furthermore, no iron dissolution at the crack tip occurs as long as no active loading (straining of the crack tip) is applied to the specimen. If the chloride concentration in the bulk is increased, chloride is migrating and/or diffusing (depending on the environmental conditions) towards the crack tip and a high chloride concentration is established in the overall crack already after a short distance inside the crack.

The increased chloride concentration causes a higher solubility of iron oxides and thereby a thinning of the oxide layer thickness in the crack. Due to the increased solubility, the crack is then filled with iron oxides and Fe-Cl compounds. Furthermore, a slight acidification inside the crack occurs depending on the bulk chloride concentration, as discussed above. The obtained results indicate that these processes seem to cause oxide filling and/or blunting of the crack tip under such conditions (constant loading, crack not active prior to the increase of the chloride

concentration). This was indicated by the observation that the crack could only be re-activated by severe cyclic loading after testing times at increased chloride concentrations, but without onset of crack growth.

In the case of a pre-existing crack, the observed blunting due to temporarily increased chloride concentrations may be even beneficial due to the lower susceptibility of crack re-activation.

ii) In the case of an **active crack** (see Figure 98 b), the corrosion potential of the crack tip is very low and migration of anions into the crack is enhanced in oxygenated HTW. Furthermore, acidification at the crack tip occurs due to the formation of iron hydroxides.

If the crack flanks are covered by oxide, only the crack tip is actively corroding (anodic dissolution of iron) under this condition. Therefore, migration of chlorides occurs directly towards the crack tip. Due to the high chloride concentration at the crack tip, corrosion processes are accelerated and repassivation kinetics at the crack tip are declined.

The actual effects of chloride may depend on a variety of parameters such as shift of pH, a change in the conductivity, etc. The most important parameter is probably the increased solubility of iron and iron oxides due to absorption of chloride in the oxide layer and the formation of Fe-Cl compounds. In addition, a delay in the repassivation behaviour at the crack tip is caused by the presence of chlorides. These effects can cause enhanced anodic dissolution and onset of crack growth even under purely constant load.

As discussed in chapter 5.6.2, in the presence of chloride, Cl^- and OH^- are competing for adsorption on the surface of the LAS. Therefore, the formation of iron hydroxides is furthermore supressed in the presence of chloride. Due to the formation of Fe-Cl compounds, chloride is consumed inside the crack and has to migrate towards the crack tip. Since this process does not occur immediately due to the crack geometry, a delay of a few hours until a critical crack tip electrolyte is reached is to be expected. The results from crack tip micro sampling indicate a delay time of some hours. Hence, this observation may explain the observed phases with high- and low crack growth rates (see Figure 89 and Figure 91).

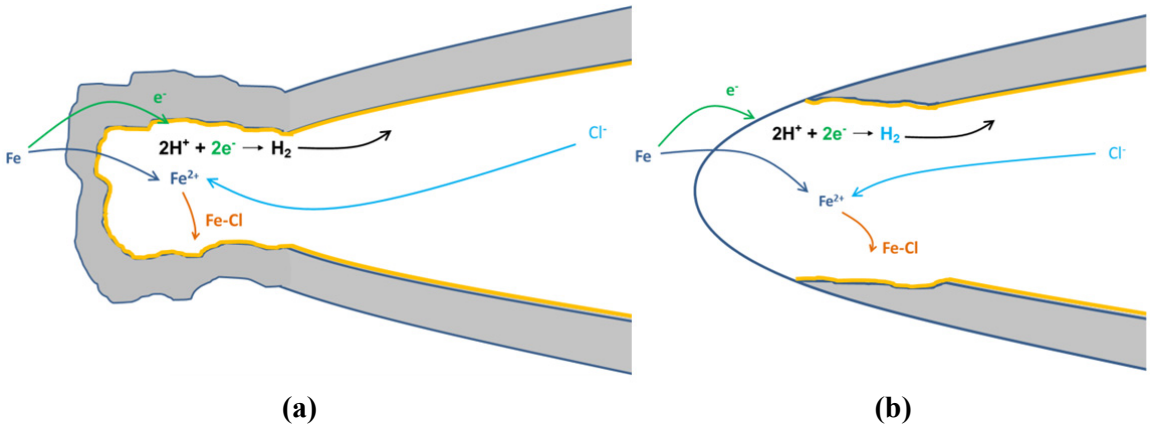

Figure 98: Effect of chloride on crack crack growth of LAS in oxygenated HTW (a) in case of a "passive crack", where no increase in the CGR was observed, and (b) in case of an "active crack", where an increase in the CGR was observed during testing at increased chloride concentration.

These results clearly indicate that maintaining a critical crack tip electrolyte is a crucial precursor for the observed high crack growth rates. The importance of the critical crack tip electrolyte is also indicated by the fact that lower crack growth rates have been observed for the specimen used for crack tip micro sampling as compared to the specimen without micro sampling which shows that flushing of the crack tip obviously decreased the crack growth rates at this specimen. Furthermore, the observed crack growth rates decreased within a few hours after the chloride concentration in the bulk was decreased to regular operating conditions (< 2 ppb). This clearly indicates that a continuous chloride supply from the bulk towards the crack tip is needed in order to maintain a critical crack tip electrolyte. In addition, these results also clearly show that no memory effect is to be expected from temporarily increased chloride concentrations, since even growing cracks will slow down to irrelevant crack growth rates under high-purity water conditions.

In addition to the observed effects of "active" or "passive" cracks, the importance of the ECP gradient on the effect of chloride on the crack growth rate has also earlier been reported by Ritter and Seifert (Ritter and Seifert, 2009). They compared results from crack growth rate testing under oxygenated and hydrogenated testing conditions, which revealed that significant effects of chloride on the crack growth rate were only observed under oxygenated conditions. Therefore, the corrosion potential, respectively the difference of the corrosion potential be-

tween the free metal surface outside the crack (crack mouth), which is in typically in the region of 0 to 150 mV_{SHE} under the chosen testing conditions (oxygenated HTW), and the corrosion potential at the crack tip, which is significantly lower (approx. -550 mV_{SHE}), plays a significant role regarding chloride induced effects in crack growth.

8. SUMMARY AND PRACTICAL RELEVANCE

8.1 Summary of the Observed Effects of Chloride on EAC of LAS

The aim of this thesis was to derive a better understanding with regard to the effects of chloride on the general corrosion behaviour of LAS in oxygenated HTW and to investigate the underlying mechanisms for crack initiation and propagation due to chloride assisted EAC. Therefore, systematic investigations on the effect of chloride on the EAC behaviour of LAS were performed to understand and elucidate the underlying mechanisms.

Studies on the effect of chloride on the general corrosion behaviour were performed using electrochemical monitoring techniques and post-test investigation methods like SEM, ToF-SIMS, and others. From the performed investigations it is concluded that if chloride is present in oxygenated HTW, chloride is adsorbed on the oxide surface of the LAS immediately (within minutes), thereby decreasing the OH^- supply from the electrolyte to the oxide/electrolyte interface. After a rather short time (few hours) chloride is absorbed in the outer part of the oxide layer, which seems to cause the development of iron oxide complexes that are less strongly bound to the oxide matrix and more easily soluble. This higher solubility, in addition with the reduced OH^- supply from the electrolyte most likely causes the observed overall thinning of the oxide layer. The dissolved iron-chloride-oxide complexes may deposit again to the material surface but have no protective properties to further corrosion processes.

If chloride is present in the electrolyte, Cl^- and OH^- are competing for adsorption on the metal surface and repassivation will be declined since the supply of OH^- is reduced due to the presence of Cl^-. Hence, at spots with locally high chloride concentration, or at spots with locally less corrosion resistance (e.g. surface flaws, MnS-inclusions, pre-existing pits), pitting may initiate or re-initiate due to the higher solubitlity of the Fe-Cl compounds and the declined repassivation kinetics. Such pits have been observed to be surrounded by rings of deposits, most likely iron oxides and probably also Fe-Cl compounds, which deposit around the active corrosion pit.

Tests on the effect of temporary chloride transients showed that the detrimental effect of increased chloride concentrations on the protective oxide layer properties (as revealed by electrochemical monitoring techniques on-line during testing and post-test investigations) recovers within at the latest 48 hours after the end of the chloride transient, i.e. after the complete disappearance of dissolved chloride in the aqueous environment. Hence, the observed effects of chloride on the corrosion behaviour appear to recover completely at LAS with smooth surfaces after exposure to pure water chemistry conditions.

As local breakdown of the oxide layer occurs due to local sliding along slip planes (according to the slip-step dissolution mechanism), the thickness of the protective oxide layer is a vital parameter regarding crack initiation susceptibility of LAS in HTW. As already discussed above, increased chloride concentrations cause a change in the thickness of the oxide layer after testing periods with continuously increased chloride concentrations. Furthermore, pronounced pitting is observed after prolonged exposure to HTW with different increased chloride levels, whereas, pitting was more pronounced at higher chloride concentrations.

In case of a decrease in the oxide layer thickness, smaller slip step heights are sufficient to cause local breakdown of the oxide layers and exposure of bare metal to the HTW. In addition, local areas, where pitting like attack of the specimens has been observed, may further localize the deformation and thereby act as crack initiation points, as it has been observed during CERT testing in particular at 50 ppb chloride. Conjoint effects of MnS inclusions, which are known to act as crack initiation locations, and localized thinning of the oxide layer or pitting due to chloride induced effects, may further promote crack initiation at those locations. Finally, a local acidification, changing the equilibrium conditions in the interface between oxide layer and HTW is possible. This local acidification is caused by the formation of different Fe-Cl compounds by which the pH is locally shifted to more acidic values. The shift in pH causes a change of the local equilibrium condition, leading to locally increased corrosion rates.

Chloride additions thereby cause both, accelerated crack initiation by the observed thinning of the oxide layer and pronounced pitting, and enhanced crack growth due to declined repassivation kinetics at higher chloride levels. Even a change in the mechanical properties of the oxide in terms of reduced plasticity seems possible, but has not been investigated in the frame of this thesis. The repassivation kinetics, especially at pre-existing cracks in LAS or in crevic-

es, can therefore be significantly retarded due to the locally variable anionic activity by accumulation of chloride.

In the case of an initiated, active crack the corrosion potential of the crack tip is very low and migration of anions into the crack is enhanced in oxygenated HTW. Furthermore, acidification at the crack tip occurs due to the formation of iron hydroxides and the presence of chloride.

If the crack flanks are covered by oxide, only the crack tip is actively corroding (anodic dissolution of iron) under this condition. Therefore, migration of chloride occurs directly towards the crack tip. Results from crack tip micro sampling revealed that the chloride concentration at the crack tip is strongly increased as compared to the bulk chloride concentration (up to ~ 20 x). Due to the high chloride concentration at the crack tip, corrosion processes are accelerated and repassivation kinetics at the crack tip are declined. This causes sustained cracking even under purely constant loading, since anodic dissolution of iron at the crack tip is not supressed by re-oxidation of the crack tip. Hence, chloride causes anodic dissolution at the crack tip and at the same time retards the repassivation kinetics in a way that no oxidation of the crack tip occurs. In case of a not fully oxidised crack tip, crack re-initiation and crack growth by anodic dissolution of iron are possible under purely constant load due to the presence of rather small amounts of chloride in oxygenated HTW (50 ppb). If the bulk chloride concentration is decreased below detectable levels (< 2 ppb), the crack growth rates decrease to insignificant values after a few hours. This again indicates that continuous chloride supply from the bulk towards the crack tip is an essential pre-cursor for the observed effects, and therefore long term memory effect of increased chloride concentrations are not to be expected.

8.2 Practical Relevance of the Observed Effects

Regarding power plant applications, in particular BWR plant operation, the results of this work deliver some important conclusions on possible effects of increased chloride contamination levels in plant applications.

Exposure tests with up to 1000 hours of testing at chloride concentrations with up to 50 ppb chloride showed that none of the pre-strained C-ring specimens with an initial stress of up to 500 MPa indicated crack initiation, due to either up to 1000 hours permanently increased chloride contaminations or temporary chloride transients. It can therefore be concluded that there seems to be no immediate and drastic increase in the crack initiation susceptibility for pre-strained specimens, at least for smooth surfaces and small chloride concentrations up to 50 ppb within the tested time frame.

Regarding the assessment of BWR LAS components during plant operation, it follows that temporarily increased chloride concentrations with up to 50 ppb should therefore not cause an immediate increase in the crack initiation susceptibility of LAS components under realistic component stress levels and steady state operating conditions, even if the presence of cracks is assumed.

The results of this work clearly indicate that chloride transients may only cause substantial cracking, if they are accompanied by severe mechanical loading. Results from CERT-testing revealed that continuously increasing straining of specimens above the yield strength is needed to cause crack initiation even with up to 50 ppb chloride. Hence, regarding plant operation it is concluded that temporarily increased chloride concentrations even in the range of the VGB action level 3 (50 ppb chloride) do not cause an immediate initiation of fast, sustained crack growth in the investigated German type low-alloy RPV-steel.

However, for actively growing cracks, rather high crack growth rates in the range of the EPRI SCC disposition line have been observed at increased chloride concentrations.

For practical applications this means that short term transients seem to be not harmful, but long term increased chloride concentrations should by prohibited since they cause increased general corrosion of LAS.

Taking crack initiation into consideration, the conjoint occurrence of increased chloride concentrations and mechanical straining at stress levels above the yield strength may cause a remarkable increase in the crack initiation susceptibility.

Regarding crack growth the obtained results clearly indicate that it is not the increased chloride concentration per se which causes an increase in the observed crack growth rates, but the conjoint occurrence of both, an “active” crack and increased bulk chloride concentrations.

8.3 Recommendations for Future Work on the Effect of Chloride on EAC of LAS

Based on the results obtained within the frame of this thesis, it is recommended that future work on the effect of chloride on the EAC behaviour of LAS in HTW should focus on:

- **Chemical interactions between LAS and chloride in HTW**
  In the presence of chloride in oxygenated HTW, complex interactions between chloride and LAS, or more precisely the developed oxide layer on LAS, occur under the chosen testing conditions. Detailed investigations into the chemical processes occurring between LAS and chloride in high-temperature water and how such processes depend on ECP and pH should therefore be performed in future research activities. Such investigations should focus on possible interactions in terms of development of Fe-Cl compounds as well as effects on the local ECP and pH. Since any chloride influenced effects seem to depend on the oxygen concentration, and thereby on ECP, additional tests should also study the effects of dissolved oxygen concentrations in HTW.

- **Mechanical properties of the oxide layer in the presence of chloride**
  The mechanical properties of the oxide layer may be influenced by the presence of chloride in terms of a embrittlement of the oxide layer. This may influence the stability of the oxide. Modified CERT-tests that have been performed in the frame of this work did not indicate a pronounced effect of increased chloride concentrations on the crack initiation susceptibility. However, the actual oxide properties may be affected by incorporation of chloride. This should be investigated in more detail.

- **Cracking in the interface region of LAS and austenitic stainless steel or Ni-base Alloys**
  In the presence of chloride, sustained crack growth from Ni-base weld materials into LAS has been observed. The actual effect of chloride on this observed effect is not well understood up to know. Further research activities should therefore focus on the chemical processes regarding chloride accumulation in the LAS region and the differences in the corrosion behaviour of dissimilar metal welds as compared LAS material.

- **pH in the crack**

  From the performed investigations and some literature data it seems that the pH inside the crack has a strong influence on the observed crack growth rates and that the crack, and in particular crack tip pH seem to be influenced by the actual bulk and crack tip chloride concentration. Hence, investigations on the crack tip pH and possible chloride effects on the pH seem to be promising.

- **Effect of ECP**

  The tests performed in this thesis have only been performed in oxygenated HTW. It is well known that hydrogen water chemistry causes a change of the observed corrosion behaviour of LAS and reduces the observed changes of CGRs in the presence of chloride. Hence, a comparison of tests in oxygenated to hydrogenated conditions should be performed in order to investigate the effect of potential gradients under both, constant and cyclic loading, on the chemical composition of the crack tip electrolyte, in particular the crack tip chloride concentration (by micro sampling).

- **Effect of chemical composition of the LAS**

  As for dissolved oxygen concentrations, all tests performed in this thesis have only been performed using one material heat. Conjoint effects by varying chemical compositions of different material grades and increased chloride concentrations in the HTW are possible and should also be taken into consideration in future tests.

9. REFERENCES

ASTM G 38 - 01 (2007). ASTM G38 - 01 (Reapproved 2007) Standard Practice for Making and Using C-Ring Stress-Corrosion Test Specimens. West Conshohocken, PA, USA: ASTM International.

EN ISO 7539-5:1995. DIN EN ISO 7539-5 Corrosion of metals and alloys - Stress corrosion testing - Part 5: Preparation and use of C-ring specimens (ISO 7539-5:1989); German version EN ISO 7539-5 : 1995. Euopean Committee for Standardization (CEN).

AALTONEN, P., BOJINOV, M., HELIN, M., KINNUNEN, P., LAITINEN, T., MUTTILAINEN, E., MÄKELÄ, K., REINVALL, A., SAARIO, T. & TOIVONEN, A. 2002. Facts and views on the role of anionic impurities, crack tip chemistry and oxide films in environmentally assisted cracking. Espoo 2002. VTT Research Notes 2148.

ADRIAENS, A., VAN HAM, R. & VAN VAECK, L. 2001. Fundamental Aspects of Inorganic SIMS. *In:* VICKERMAN, J. C. & BRIGGS, D. (eds.) *ToF-SIMS: Surface Analysis by Mass Spectrometry.* IM Publications and Surface Spectra Limited.

ANDRESEN, P. 1987. Modeling of Water and Material Chemistry Effects on Crack Tip Chemistry and the Resulting Crack Growth Kinetics. *3rd International Symposium on Environmental Degradation of Materials in Nuclear Power Systems - Water Reactors.* Traverse City: TMS.

ANDRESEN, P. 1996. Conceptual similarities and common predicitive approaches for SCC in high temperature water systems. *Corrosion 96, Paper No. 258, pp 258-1 - 258-15,.* NACE.

ANDRESEN, P., EMIGH, P. W., HICKLING, J., TAYLOR, D. F., BURGER, J. M., HORN, R. M. & PATHANIA, R. 1997. Detection of Stress-Corrosion Crack Initiation in the BWR Environment by Electrochemical Noise. *8th International Symposium on Environmental Degradation of Materials in Nuclear Power Systems - Water Reactors.* Amelia Island: ANS.

ANDRESEN, P. & FORD, F. P. 1988. Life Prediction by Mechanistic Modeling and System Monitoring of Environmental Cracking of Iron and Nickel Alloys in Aqueous Systems (Paper presented at the Workshop on the Mechanics and Physics of Crack Growth: Application to Life Prediction, Keystone, CO, USA, August 4-7, 1987). *Materials Science and Engineering, A103,* 103**,** 167-184.

ANDRESEN, P. & YOUNG, L. M. 1995a. Characterization of the Roles of Electrochemistry, Convection and Crack Chemistry in Stress Corrosion Cracking. *7th International Symposium on Environmental Degradation of Materials in Nuclear Power Systems - Water Reactors.* Breckenridge: NACE.

ANDRESEN, P. & YOUNG, L. M. 1995b. Crack Tip Microsampling and Growth Rate Measurements in Low-Alloy Steel in High-Temperature Water. *Corrosion Science,* 51**,** 223-233.

ATKINSON, J. D. & FORREST, J. E. 1985. Factors influencing the rate of growth of fatigue cracks in RPV steels exposed to a simulated PWR primary water environment. *Corrosion Science,* 25**,** 607-631.

ATKINSON, J. D. & YU, J. 1997. The role of dynamic strain-aging in the environment assisted cracking observed in pressure vessel steels. *Fatigue Fract. Engng Mater. Struct.,* 20**,** 1-12.

ATKINSON, J. D., YU, J. & CHEN, Z. Y. 1996. An analysis of the effects of sulphur content and potential on corrosion fatigue crack growth in reactor pressure vessel steels. *Corrosion Science,* 38**,** 755-765.

BALACHOV, I., BOJINOV, M., LAITINEN, T., MUTTILAINEN, E., MÄKELÄ, K., REINVALL, A., SAARIO, T., SIRKIÄ, P. & TOIVONEN, A. 2000. A Correlation between the Stability of Oxide Films in Simulated BWR Crack Conditions, SO4-enrichment and Cracking Susceptibility. *International Conference of Water Chemistry of Nuclear Reactor Systems 8, Vol. 1.* Bournemouth, UK.

BARD, A. J. & FAULKNER, L. R. 2001. *Electrochemical Methods - Fundamentals and Applications,* New York, John Wiley & Sons.

BARD, A. J. & STRATMANN, M. 2003. *Encyclopedia of Electrochemistry; Volume 3: Instrumentation and Electroanalytical Chemistry,* New York, John Wiley & Sons.

BARD, A. J., STRATMANN, M. & FRANKEL, G. S. 2003. *Encyclopedia of Electrochemistry; Vol. 4: Corrosion and Oxide Films,* New York, John Wiley & Sons.

BÄßLER, R., ANDRESEN, P., TAYLOR, D. F. & HORN, R. 2000. Development and Evaluation of Electrochemical Noise Monitoring in BWRs. EPRI, Palo Alto, CA, and ESEERCO, New York, NY: 2000. TR-114740.

BERTOCCI, U., GABRIELLI, C., HUET, F. & KEDDAM, M. 1997a. Noise Resistance Applied to Corrosion Measurements I. Theoretical Analysis. *Journal of the Electrochemical Society,* 144**,** 31-37.

BERTOCCI, U., GABRIELLI, C., HUET, F., KEDDAM, M. & ROUSSEAU, P. 1997b. Noise Resistance Applied to Corrosion Measurements II. Experimental Tests. *Journal of the Electrochemical Society,* 144**,** 37-43.

BERTOCCI, U. & HUET, F. 1997. Noise Resistance Applied to Corrosion Measurements III. Influence of the Instrumental Noise on the Measurements. *Journal of the Electrochemical Society,* 144**,** 2786-2793.

BEVERSKOG, B. & PUIGDOMENECH, I. 1996. Revised Pourbaix Diagrams for Iron at 25 - 300 °C. *Corrosion Science,* 38**,** 2121-2135.

BLIND, D., KÜSTER, K., SEIFERT, H. P., ROTH, A., EHRNSTEN, U. & KARJALAINEN-ROIKONEN, P. 1999. European Round Robin on Constant Load EAC Tests of Low Alloy Steel under BWR Conditions. *9th International Symposium on Environmental Degradation of Materials in Nuclear Power Systems - Water Reactors.* New Port Beach: TMS.

BOCKRIS, J. O. M., DRAZIC, D. & DESPIC, A. R. 1961. The electrode kinetics of the deposition and dissolution of iron. *Electrochimica Acta,* 4**,** 325-361.

BOHNSACK, G. 1971. Zum Verständnis der Schikorr-Reaktion (eine kritische Literaturstudie) - Towards understanding of the Schikorr reaction (a critical literature review). *Mitteilungen der VGB,* 51.

BORNAK, W. E. 1988. Chemistry of Iron and its Corrosion Products in Boiler Systems. *Corrosion,* 44**,** 154-158.

BOSCH, R.-W. 2005. Electrochemical impedance spectroscopy for the detection of stress corrosion cracks in aqueous corrosion systems at ambient and high temperature. *Corrosion Science,* 47**,** 125-143.

BRIGHAM, E. O. 1995. *FFT - Schnelle Fourier Transformation (German Translation of "The Fast Fourier Transformation" puplished by Pentice-Hall Inc. 1974),* München, Wien, R. Oldenbourg Verlag.

BRUSH, E. G. & PEARL, W. L. 1972. Corrosion and Corrosion Product Release in Neutral Feedwater. *Corrosion,* 28**,** 129-136.

BULLOCH, J. H. & ATKINSON, J. D. 1992. An assessment of the influence of sulphide distribution in the promotion of environmentally assisted crack growth in ferritic pressure vessel steels. *18th MPA-Seminar.* Stuttgart.

CARTER, R. 2003. BWRVIP-60-A: BWR Vessel and Internals Project, Evaluation of Stress Corrosion Crack Growth in Low Alloy Steel Vessel Materials in the BWR Environment. EPRI, Palo Alto, CA: 2003. 1008871.

CHEN, C. M., ARAL, K. & THEUS, G. J. 1983a. Computer-calculated potential pH diagrams to 300°C. Vol. 1. Computer-Calculated Potential pH-Diagrams to 300°C. Executive Summary. EPRI, Palo Alto, CA: 1983. EPRI NP-3137

CHEN, C. M., ARAL, K. & THEUS, G. J. 1983b. Computer-calculated potential pH diagrams to 300°C. Vol. 2. Handbook of diagrams. Final report. [PWR; BWR]. EPRI, Palo Alto, CA: 1983. EPRI NP-3137.

CHOI, H., BECK, F. H., SZKLARSKA-SMIALOWSKA, Z. & MACDONALD, D. D. 1982. Stress Corrosion Cracking of ASTM A 508 Cl 2 Steel in Oxygenated Water at Elevated Temperatures. *Corrosion,* 38**,** 136-144.

CHOI, H., SZKLARSKA-SMIALOWSKA, S. & MACDONALD, D. D. 1983. Stress Corrosion Cracking of ASME508-Cl2 Pressure Vessel Steel. *In:* MACDONALD, D. D., SMIALOWSKA, S. & PEDNEKAR, S. (eds.) *The General and Localized Corrosion of Carbon and Low-Alloy Steels in Oxygenated High-Temperature Water.* Palo Alto, California 94304: Electric Power Research Institute (EPRI). EPRI NP-2853, Project T115-5. Final Report.

COMBRADE, P. 1985. Prediction of Environmental Crack Growth in Nuclear Power Plant Components. EPRI TR-102797. Final Report of EPRI Contract RP2006-1 and RP2006-8, Unirec Report 1667.

COMBRADE, P., FOUCAULT, M. & SLAMA, G. 1987. Effect of Sulfur on Fatigue Crack Growth Rates of Pressure Vessel Steel Exposed to PWR Coolant. *3rd International Symposium on Environmental Degradation of Materials in Nuclear Power Systems - Water Reactors.* Traverse City: TMS.

COMBRADE, P., MARCUS, P., SLAMA, G. & FOUCAULT, M. 1989. On the role of sulfur on the dissolution of pressure vessel steels at the tip of a propagating crack in PWR environments. *4th International Symposium on Environmental Degradation of Materials in Nuclear Power Systems - Water Reactors.* Jekyll Island: NACE.

CONGLETON, J., SHOJI, T. & PARKINS, R. N. 1985. The stress corrosion cracking of reactor pressure vessel steel in high-temperature water. *Corrosion Science,* 25**,** 633-650.

COTTIS, R. A. & GEBRIL, A. 2005. The Use of Electrochemical Noise to Detect Initiation of Stress Corrosion Cracking. *Corrosion 2005. Paper No. 05366.* Houston: NACE International.

CUSSLER, E. L. 1984. *Diffusion - Mass Transfer in Fluid Systems*, Cambridge University Press. ISBN 0 521 23171 1

DAWSON, J. L. 1994. Electrochemical Noise Measurement: The Definitive In-situ Technique for Corrosion Applications? *1st International Symposium on Electrochemical Noise Measurement for Corrosion Applications.* Montreal: ASTM.

DEIMEL, P. & LÄPPLE, V. 1991. Zusammenstellung und Bewertung von Modellansätzen zur Quantifizierung des korrosionsgestüzten Risswachstums in Hochtemperaturwasser. Abschlussbericht, Forschungsvorhaben 73025/RS 788, October 1991, MPA Stuttgart, Germany.

DEVRIENT, B. 2007. *Untersuchungen zum Einfluss der dynamischen Reckalterung auf die mediumsgestützte Risskorrosion von niedriglegierten Stählen in sauerstoffhaltigem Hochtemperaturwasser.* Ph D Thesis, Universität Stuttgart.

DEVRIENT, B., ROTH, A., KÜSTER, K., ILG, U. & WIDERA, M. 2007. Effect of dynamic strain aging on the environmentally assisted cracking of low-alloy steels in oxygenated high-temperature water. *13th International Conference on Environmental Degradation*

of Materials in Nuclear Power Systems - Water Reactors. Whistler, Canada: The Canadian Nulear Society.

DEVRIENT, B., ROTH, A., KÜSTER, K., WIDERA, M. & ILG, U. 2009. Influence of Dynamic Strain Ageing on the Crack Growth Rates and Crack Tip Plasticity of Low-Alloy Steels in Oxygenated High-Temperature Water. *14th International Conference on Environmental Degradation of Materials in Nuclear Power Systems.* Virginia Beach, USA: TMS.

DIEGLE, R. B. & VERMILIYEA, D. A. 1976. Deformation of Iron Oxides Formed in Caustic Electrolyte. *Corrosion,* 32**,** 411-414.

DORSCH, T., KILIAN, R. & WENDLER-KALSCH, E. 1998. Possibility of detection of crack initiation in high temperature water. *Materials and Corrosion,* 49**,** 659-670.

EDEN, D. A. 1998. Electrochemical Noise - The First Two Octaves. *Corrosion 98. Paper No. 386, NACE, Houston, TX.*

EDEN, D. A., ROTHWELL, A. N. & DAWSON, J. L. 1991. Electrochemical Noise for Detection of Susceptibility to Stress Corrosion Cracking. *Corrosion 91. Paper No. 444, NACE, Houston, TX.*

EFFERTZ, P. H. 1972. Morphology and Composition of Magnetite Layers in Boiler Tubes Following Long Exposure. *5th International Congress on Metallic Corrosion.* Tokio.

EHRNSTEN, U., GOMEZ-BRICENO, D., LAPENA, J., ERNESTOVA, M., ZAMBOCH, M., RITTER, S., SEIFERT, H. P., ROTH, A., FÖHL, J., HÜTTNER, F. & WEISSENBERG, T. 2003. Inter-Laboratory Crack Growth Test on Pressure Vessel Steel 20 MnMoNi 5 5 in Simulated BWR Environment. *11th International Conference on Environmental Degradation of Materials in Nuclear Systems - Water Reactors.* Stevenson: ANS.

ENGELHARDT, G. R., MACDONALD, D. D. & URQUIDI-MACDONALD, M. 1999. Development of fast algorithms for estimating stress corrosion crack growth rate. *Corrosion Science,* 41**,** 2267-2302.

ENGELL, H.-J. 1971. The Role of Surface Films on Stress Corrosion Cracking of Metals. *In:* SCULLY, J. C. (ed.) *The theory of stress corrosion cracking in alloys.* Brüssel.

ENGELL, H.-J. & SPEIDEL, M. O. 1968. Ursachen und Mechanismen der Spannungsrißkorrosion. *In:* KAESCHE, H. (ed.) *Diskussionstagung 1986 der Deutschen Gesellschaft für Metallkunde 35. Veranstaltung der Europäischen Föderation Spannungsrisskorrosion.* Frankfurt/Main: Verlag Chemie.

ERNESTOVA, M., ZAMBOCH, M., DEVRIENT, B., EHRNSTEN, U., FÖHL, J., GOMEZ-BRICENO, D., LAPENA, J., RITTER, S., ROTH, A., SEIFERT, H. P. & WEISSENBERG, T. 2004. Crack Growth Behaviour of Low-Alloy Steels for Pressure Boundary Components under Transient Light Water Reactor Operating Conditions - CASTOC, Part II: VVER Conditions, Paper No. 241. *Eurocorr 2004.* Nice.

ERNST, K. 1984. *Untersuchungen über Phasenumwandlungen an reinen Eisenoxiden im Hinblick auf die atmosphärische Korrosion.* Ph D Thesis, Universität Erlangen-Nürnberg.

EVANS, U. R. 1971. Inhibition, passivity and resistance: A review of acceptable mechanisms. *Electrochimica Acta,* 16**,** 1825-1840.

FESER, R. 2003. Uniform Corrosion of Metals in Acid, Neutral and Alkaline Electrolytes. *In:* BARD, A. J. & STRATMANN, M. (eds.) *Encyclopedia of Electrochemistry; Vol. 4: Corrosion and Oxide Films.* New York: John Wiley & Sons.

FIELD, E. M., STANLEY, R. C., ADAMS, A. M. & HOLMES, D. R. 1963. The Growth, Structure and Breakdown of Magnetite Films on Mild Steel. *2nd International Congress on Metallic Corrosion.* New York.

FÖHL, J., WEISSENBERG, T., GÓMEZ-BRICENO, D., ERNESTOVA, M., ZAMBOCH, M., SEIFERT, H. P., RITTER, S., ROTH, A., DEVRIENT, B. & EHRNSTEN, U. 2004. Crack Growth Behaviour of Low Alloy Steels for Pressure Boundary Components under Transient Light Water Reactor Operating Conditions (CASTOC), Final Summary Report. Contract No. FIKS-CT-2000-00048. Project funded by the European Community under the 5th Framework Programme (1998-2002).

FORD, F. P. 1982a. Effect of oxygen / temperature combinations on the stress corrosion susceptibility of SA 333-Gr6 carbon steel in BWR quality water, in: BWR Environmental Cracking Margins for Carbon Steel Piping. *Report No. NP-2406.* Palo Alto, CA (May 1982): EPRI (Electric Power Research Institute).

FORD, F. P. 1982b. Mechanisms of environmental cracking in systems peculiar to the power generation industry. *Report No. NP-2589.* EPRI NP-2589, 1982.

FORD, F. P. 1986. Overview of collaborative research into mechanisms of environmentally controlled cracking in the low-alloy pressure vessel steel/water system. *Proceedings of the 2nd International IAEA Specialists Meeting on Sub-critical Crack Growth, NUREG/CP-0067, Vol. 2.* Sendai, Japan.

FORD, F. P. 1989. 3 Mechanisms of environmentally-assisted cracking. *International Journal of Pressure Vessels and Piping,* 40**,** 343-362.

FORD, F. P. 1992. Environmentally Assisted Cracking of Low-Alloy Steels. *NP-7473-L, Final Report, January 1992.* Electric Power Research Institute.

FORD, F. P. 1993. Prediction of Corrosion-Fatigue Initiation in Low-Alloy Steel and Carbon-Steel/Water Systems at 288 °C. *6th International Symposium on Evironmental Degradation of Materials in Nuclear Power Systems - Water Reactors.* San Diego: TMS.

FORD, F. P. 2006. Repair and Replacement Applications Center: Stress Corrosion Cracking in Closed Cooling Water Systems: Damage Mechanism Evaluation and Proposed Research. *EPRI, Palo Alto, CA: 2006 1013563.* EPRI, Palo Alto, CA: 2006 1013563.

FORD, F. P. & ANDRESEN, P. 1989a. Stress Corrosion Cracking of Low Alloy Steels in 288 °C Water. *Corrosion 1989. Paper No. 498.* New Orleans, Louisiana.

FORD, F. P. & ANDRESEN, P. 1990. Corrosion Fatigue of A533B/A508 Pressure Vessel Steels in 288 °C Water. *Proceedings of the 3rd International IAEA Specialists Meeting on Sub-critical Crack Growth, Vol. 1.* Moscow, USSR: Cullen, W.

FORD, F. P., ANDRESEN, P., WEINSTEIN, D., RANGANATH, S. & PATHANIA, R. 1991. Stress Corrosion Cracking of Low-Alloy Steels in High Temperature Water. *5th International Symposion on Environmental Degradation of Material in Nuclear Power Systems - Water Reactors.* Monterey, California: ANS.

FORD, F. P. & ANDRESEN, P. L. 1989b. Stress Corrosion Cracking of Low Alloy Steels in 288°C Water, Paper No. 498. *Corrosion.* New Orleans, Louisiana: NACE.

FORD, F. P. & COMBRADE, P. 1985. Electrochemical reaction rates on bare surfaces and their use in a crack prediction model for the low-alloy steel/water system. *Proceedings of the 2nd International IAEA Specialists Meeting on Subcritical crack Growth, NUREG/CP-0067, Vol 2.* Sendai, Japan.

FORD, F. P., HORN, R. M., HICKLING, J., PATHANIA, R. & BRUEMMER, S. M. 1999. Stress Corrosion Cracking of Low Alloy steels under BWR Conditions; Assessment of Crack Growth Rate Algorithms. *9th International Symposium on Environmental Degradation on Material in Nuclear Power Systems - Water Reactors.* New Port Beach: TMS.

FORD, F. P. & SCOTT, P. 2008. Environmentally-Assisted Degradation of Carbon and Low-Alloy Steels in Water-Cooled Nuclear Reactors. *LCC4 Special Topical Report on Environmentally-Assisted Degradation of Carbon and Low-Alloy Steels in Water-Cooled Nuclear Reactors.*: Advanced Nuclear Technology International.

FORD, F. P., TAYLOR, D. F., ANDRESEN, P. & BALLINGER, R. G. 1987. Corrosion-Assisted Cracking of Stainless and Low-Alloy Steels in LWR Environments. Electric Power Research Institute (EPRI), EPRI NP 5064, Research Project 2006-6.

GABETTA, G. 1982. A method to measure electrochemical potential at the tip of a growing crack during environmental fatigue test. *Fatigue of Engineering Materials and Structures,* 5**,** 2015-220.

GABETTA, G. 1991. Measure of chemical and electrochemical parameters inside an environmentally-assisted growing crack. *In:* CULLEN, W. (ed.) *Proceedings of the 3rd International IAEA Specialist´s Meeting on Subcritical Crack Growth.* Moscow, Russia: NUREG/CP-0112, Vol.2, pp. 129-143.

GABRIELLI, C. & KEDDAM, M. 1992. Review of Applications of Impedance and Noise Analysis to Uniform and Localized Corrosion. *Corrosion,* 48**,** 794-811.

GADIYAR, H. S. & ELAYATHU, N. S. D. 1980. Corrosion and Magnetite Growth on Carbon Steels in Water at 310°C - Effect of dissolved Oxygen, pH and EDTA Addition. *Corrosion,* 36**,** 306-312.

GAMRY. 2011. GAMRY INSTRUMENTS, Gamry Application Note: Basics of Electrochemical Impedance Spectroscopy, http://www.gamry.com.

GLADEN, H. & KAESCHE, H. 1994. Stress corrosion cracking of mild steel in high pressure, high temperature water during slow strain rate testing. *Nuclear Engineering and Design,* 151**,** 463-472.

GÖLLNER, J. 2002. *Elektrochemisches Rauschen unter Korrosionsbedingungen.* Dr.-Ing. habil. habilitation treatise Otto-von-Guericke-Universtät.

GÖLLNER, J. & BURKERT, A. 1998. Examination of corrosion propensity by means of electrochemical noise Part 1: Appearance, trends and problems. *Materials and Corrosion,* 49**,** 614-622.

GÖLLNER, J., BURKERT, A., DEIMEL, P. & KLENKE, K. 1998. Electrochemical noise at crack initiation on low-alloy steel in high temperature water. *Materials and Corrosion,* 49**,** 671-676.

GUTMAN, E. M. 2007. An inconsistency in "film rupture model" of stress corrosion cracking. *Corrosion Science,* 49**,** 2289-2302.

HALL JR, M. M. 2009a. Critique of the Ford–Andresen film rupture model for aqueous stress corrosion cracking. *Corrosion Science,* 51**,** 1103-1106.

HALL JR, M. M. 2009b. Film rupture model for aqueous stress corrosion cracking under constant and variable stress intensity factor. *Corrosion Science,* 51**,** 225-233.

HAMANN, C. H. & VIELSTICH, W. 1998. *Electrochemistry,* WILEY-VCH Verlag GmbH, D-69469 Weinheim, Germany, Wiley-VCH.

HÄNNINEN, H., AHO-MANTILA, I. & TORRONEN, K. 1987. Environment sensitive cracking in pressure-boundary materials of light water reactors. CSNI Report 141.: Committee on the safety of nuclear installations, OECD Nuclear Energy Agency.

HÄNNINEN, H., KEMPAINEN, M. & TÖRRONEN, K. 1988. The role of inclusions in corrosion fatigue crack growth of pressure vessel steels in high temperature reactor water. *In:* RUNGTA, R. (ed.) *Proceedings of a Symposium held in confunction with the 1988 World Materials Congress.* Chicago, Illinois, USA: ASM International.

HÄNNINEN, H., TÖRÖNNEN, K. & CHULLEN, W. H. 1985. Comparison of Proposed Cyclic Crack Growth Mechanisms of Low-Alloy Steels in LWR Environments. *2nd International Atomic Energy Agency Specialists Meeting on Sub-Critical Crack Growth, NUREG/CP-0067.* Sendai, Japan.

HÄNNINEN, H., TÖRRÖNEN, K., KEMPAINEN, M. & SALONEN, S. 1983. On the mechanism of environment sensitive cyclic crack growth of nuclear reactor pressure vessel steels. *Corrosion Science,* 23**,** 663-679.

HÄNNINEN, H., YAGODZINSKY, Y., TARASENKO, O., SEIFERT, H. P., EHRNSTEN, U. & AALTONEN, P. 2001. Effects of Dynamic Strain Aging on Environment-Assisted Cracking of Low Alloy Pressure Vessel and Piping Steels. *10th International Conference on Environmental Degradation of Materials in Nuclear Power Systems - Water Reactors.* Lake Tahoe: NACE.

HARRISON, P. L. 1967. Tensile fracture of magnetite films. *Corrosion Science,* 7**,** 789-794.

HERBST, M. & ROTH, A. 2013. Investigations on the effect of chloride on the general corrosion behavior of low-alloy steels in oxygenated high-temperature water. *Materials and Corrosion,* 64**,** 691-699.

HERBST, M., ROTH, A., NOWAK, E. & ILG, U. 2011. Effect of Chloride on Environmentally Assisted Cracking of Low-Alloy Steels in Oxygenated High-Temperature Water - Gerneral Corrosion. *15th International Conference on Environmental Degradation of Materials in Nuclear Power Systems - Water Reactors.* Colorado Springs, Colorado: ANS.

HERBST, M., ROTH, A., WIDERA, M., KÜSTER, K., HÜTTNER, F. & NOWAK, E. 2012. The effect of chloride on general corrosion and crack initiation of low-alloy steels in oxygenated high-temperature water. *38th MPA-Seminar, October 1 and 2.* Stuttgart, Germany.

HERBST, M., ROTH, A., WIDERA, M. & NOWAK, E. 2013. Effects of Chloride on the EAC-Behavior of Low-Alloy Steels in Oxygenated High-Temperature Water. *16th International Conference on Environmental Degradation of Materials in Nuclear Power Systems – Water Reactors.* Asheville: NACE.

HERTER, K.-H., SCHULER, X. & WEIßENBERG, T. 2012. Fatigue behaviour and crack growth of ferritic steel under environmental conditions. *38th MPA Seminar, October 1 and 2.* Stuttgart.

HERTER, K.-H., SCHULER, X. & WEISSENBERG, T. 2013. Crack Growth Behaviour of Ferritic Pressure Vessel Steels in Oxygenated High Temperature Water under Transient Loading. *Proceedings of the ASME 2013 Pressure Vessel and Piping Conference, PVP2013-97370.* Paris, France.

HEUSLER, K. E. 1982. Iron. *In:* BARD, A. J. (ed.) *Electrochemistry of the Elements.* New York: Marcel Dekker.

HEUSLER, K. E. & FISCHER, L. 1976a. Film Growth and Dissolution of Iron Ions at Passive Iron in Neutral Solutions Containing Chloride. *Werkstoffe und Korrosion,* 27**,** 697-701.

HEUSLER, K. E. & FISCHER, L. 1976b. Kinetics of Pit Initiation at Passive Iron. *Werkstoffe und Korrosion,* 27**,** 551-556.

HEUSLER, K. E. & FISCHER, L. 1976c. Kinetics of Pit Initiation at the Alloy Fe5Cr. *Werkstoffe und Korrosion,* 27**,** 788-791.

HICKLING, J. 1994. Evaluation of acceptance criteria for data on environmentally assisted cracking in Light Water Reactors. SKI Report 94:14, September 1994.

HICKLING, J. & BLIND, D. 1986. Strain-induced corrosion cracking of low-alloy steels in LWR systems - case histories and identification of conditions leading to susceptibility. *Nuclear Engineering and Design,* 91**,** 305-330.

HICKLING, J., SEIFERT, H. P. & RITTER, S. 2005. Research and Service Experience with Environmentally Assisted Cracking of Low-Alloy Steel. *Power Plant Chemistry,* 7**,** 4-14.

HICKLING, J., TAYLOR, D. F. & ANDRESEN, P. 1998. Use of electrochemical noise to detect stress corrosion crack initiation in simulated BWR environments. *Materials and Corrosion,* 49**,** 651-658.

HLADKY, K. & DAWSON, J. L. 1981. The measurement of localized corrosion using electrochemical noise. *Corrosion Science,* 21**,** 317-322.

HLADKY, K. & DAWSON, J. L. 1982. The measurement of corrosion using electrochemical 1/f noise. *Corrosion Science,* 22**,** 231-237.

HOARE, J. P. 1970. Oxide Film Studies on Iron in Electrochemical Machining Electrolytes. *Journal of the Electrochemical Society,* 117**,** 142-145.

HOFFMEISTER, H. 2009. Modeling the effects of nuclear environments on crevice corrosion of pure nickel by coupling of phase and polarization behavior. *Nuclear Engineering and Design,* 239**,** 1795-1803.

HOFFMEISTER, H. & KLEIN, O. 2011. Modeling of SCC initiation and propagation mechanisms in BWR environments. *Nuclear Engineering and Design,* 241**,** 4893-4902.

HUBSCHMID, C. & LANDOLT, D. 1993. Formation Conditions, Chloride Content, and Stability of Passive Films on an Iron-Chromium Alloy. *Journal of the Electrochemical Society,* 140**,** 1898 - 1902.

HUET, F., BAUTISTA, A. & BERTOCCI, U. 2001. Listening to Corrosion. *The Electrochemical Society, Interface, Winter 2001*.

HUIIJBREGTS, W. M. M. & SNEL, A. 1972. The protection effectiveness of magnetite layer in relation to boiler corrosion. *5th International Congress on Metallic Corrosion.* Tokio.

INDIG, M. E. 1982. Environmental aspects of carbon steel stress corrosion, in: BWR Environmental Cracking Margins for Carbon Steel Piping. *Report No. NP-2406.* Palo Alto, CA: EPRI (Electric Power Research Institute).

IVERSON, W. P. 1968. Transient Voltage Changes Produced in Corroding Metals and Alloys. *Journal of the Electrochemical Society,* 115.

JAMES, L. A. & MOSHIER, W. C. 1999. The effect of potential upon the high-temperature fatigue crack growth response of low-alloy steels, part 1: crack growth results. *Corrosion Science,* 41**,** 373-399.

JOVANCICEVIC, V., BOCKRIS, J. O. M., CARBAJAL, J. L., ZELENAY, P. & MIZUNO, T. 1986. Adsorption and Absorption of Chloride Ions on Passive Iron Systems. *Journal of the Electrochemical Society,* 133**,** 2219 - 2226.

JÜTTNER, K., LORENZ, W. J., PAATSCH, W., KENDING, M. & MANSFELD, F. 1985. Importance of the dynamic system analysis for corrosion testing in research and practice. *Werkstoffe und Korrosion,* 36**,** 120-130.

KAESCHE, H. 2003. *Corrosion of Metals: Physicochemical principles and current problems*, Springer-Verlag, Berlin, Heidelberg.

KHALIL, W., HAUPT, S. & STREHBLOW, H. H. 1985. The thinning of the passive layer of iron by halides. *Werkstoffe und Korrosion,* 36**,** 16-21.

KUMAGAI, K., MORRA, M., ANDRESEN, P. L., CATLIN, G. N., L., SUZUKI, S., TAKAGI, Y. & HORN, R. 2009. Effects of K and Anion Impurity Concentration on Crack Growth Kinetics Near Alloy 182/A533B Weld Overlay Boundaries in BWRs. *14th International Conference on Environmental Degradation of Materials in Nuclear Power Systems - Water Reactors.* Virginia Beach, USA: TMS.

KUNIYA, J., MASAOKA, I., SASAKI, R., ITOH, H. & OKAZAKI, T. 1985. Stress Corrosion Cracking Susceptibility of Low Alloy Steels Used for Reactor Pressure Vessel in High Temperature Oxygenated Water. *Journal of Pressure Vessel Technology,* 107**,** 430-435.

KUSSMAUL, K., BLIND, D. & LÄPPLE, V. 1997. New observations on the crack growth rate of low alloy nuclear grade ferritic steels under constant active load in oxygenated high-temperature water. *Nuclear Engineering and Design,* 168**,** 53-75.

KUSSMAUL, K., BLIND, D., STEINMILL, H., BILGER, H., ECKERT, G., BIESELT, R., LÖHLBERG, R. & SCHNELLHAMMER, W. 1986. Experience in the replacement of safety related piping in German boiling water reactors. *International Journal of Pressure Vessels and Piping,* 25**,** 111-138.

KUSSMAUL, K. & NAVAB-MOTLAGH, M. 1983. Verhalten der Magnetitschutzschicht unter Kesselbedingungen (Abschlussbericht zum VGB-Forschungsvorhaben 24). *VGB Kraftwerkstechnik,* 63**,** 153-162.

LÄPPLE, V. 1996. Untersuchungen zum korrosionsgetützten Rißwachstum ferritischer Stähle in sauerstoffhaltigem Hochtemperaturwasser. *Technisch-wissenschaftliche Berichte der Staatlichen Materialprüfanstalt Universität Stuttgart. Heft 96/02. ISSN 0721-4529.* Staatliche Materialprüfanstalt (MPA) Stuttgart.

LÄPPLE, V. & DEIMEL, P. 1994. Influence of corrosion and mechanical loading on the crack growth of low-alloyed ferritic steels in oxygenated high temperature water. *Werkstoffe und Korrosion,* 45**,** 583-592.

LEE, Y. J. & SHOJI, T. 1999. Evaluation of Crack Tip Solution Chemistry of Low Alloy Steel in Oxygenated High Temperature Water. *9th International Symposium on Environmental Degradation in Nuclear Power Systems - Water Reactors.* New Port Beach: TMS.

LEGAT, A. & DOLECEK, V. 1995. Corrosion Monitoring System Based on Measurement and Analysis of Electrochemical Noise. *Corrosion Science,* 51**,** 295-300.

LEGAT, A. & ZEVNIK, C. 1993. The Electrochemical Noise of Mild and Stainless Steel in Various Water Solutions. *Corrosion Science,* 35**,** 1661-1666.

LENZ, E. & WIELING, N. 1986a. Mediumseitige Einflußgrößen bei der dehnungsinduzierten Rißkorrosion und Beispiele für anwendungsbezogene Fälle. *VGB Kraftwerkstechnik,* 66**,** 481-485.

LENZ, E. & WIELING, N. 1986b. Strain-induced corrosion cracking of low-alloy steels in LWR systems - interpretation of susceptibility by means of a three dimensional (T, ε, dissolved oxygen) diagram. *Nuclear Engineering and Design,* 91**,** 331-344.

LENZ, E., WIELING, N. & MÜNSTER, H. 1988. Influence of Variation of Flow Rates and Temperature on the Cyclic Crack Growth Rate under BWR Conditions. *3rd International Symposium on Environmental Degradation of Materials in Nuclear Power Systems - Water Reactors.* Traverse City: TMS.

LÖCHEL, B. P. & STREHBLOW, H. H. 1983. Breakdown of Passivity of iron by fluoride. *Electrochimica Acta,* 28**,** 565-571.

LÖCHEL, B. P., STREHBLOW, H. H. & SAKASHITA, M. 1984. Breakdown of Passivity of Nickel by Fluoride. *Journal of the Electrochemical Society,* 131**,** 522-529.

LOWE, A. M. 2002. *Estimation of Electrochemical Noise Impedance and Corrosion Rates from Electrochemical Noise Measurements.* Doctor of Philisophy, Curtin University of Technology.

MABUCHI, K., HORII, Y., TAKAHASHI, H. & NAGAYAMA, M. 1991. Effect of Temperature and Dissolved Oxygen on the Corrosion Behavior of Carbon Steel in High Temperature Water. *Corrosion,* 47**,** 500 - 508.

MACÁK, J., SAJDL, P., KUCERA, P., NOVOTNÝ, R. & VOSTA, J. 2006. In situ electrochemical impedance and noise measurements of corroding stainless steel in high temperature water. *Electrochimica Acta,* 51**,** 3566-3577.

MACDONALD, D. D. 1990. Review of Mechanistic Analysis by Electrochemical Impedance Spectroscopy. *Electrochimica Acta,* 35**,** 1509-1525.

MACDONALD, D. D. 2006. Reflections on the history of electrochemical impedance spectroscopy. *Electrochimica Acta,* 51**,** 1376-1388.

MACDONALD, D. D. & URQUIDI-MACDONALD, M. 1991. A Coupled Environment Model for Stress Corrosion Cracking in Sensitized Type 304 Stainless Steel in LWR Environments. *Corrosion Science,* 32**,** 51-81.

MAENG, W. Y., LEE, J. H. & KIM, U. C. 2005. Environmental effects on the stress corrosion cracking susceptibility of 3.5 NiCrMoV steels in high temperature water. *Corrosion Science,* 47**,** 1876-1895.

MAGDOWSKI, R., KRAUS, A. & SPEIDEL, M. O. 1994. Stress Corrosion Cracking of Reactor Pressure Vessel Steel in 288°C Water: The Effect of Oxygen, Electrochemical Potential, and Steel Composition, Paper No. 133. *Corrosion 1994, NACE Conference.*

MAGDOWSKI, R., KRAUS, A. & SPEIDEL, M. O. 1995. Stress Corrosion Cracking of Carbon and Low Alloy Steels in High Temperature Water, Paper No. 402. *Corrosion 1995, NACE Conference.*

MARCUS, P., MAURICE, V. & STREHBLOW, H. H. 2008. Localized corrosion (pitting): A model of passivity breakdown including the role of the oxide layer nanostructure. *Corrosion Science,* 50**,** 2698-2704.

MARCUS, P., TESSIER, A. & OUDAR, J. 1984. The influence of sulphur on the dissolution and the passivation of a nickel-iron alloy - I. Electrochemical and radiotracer measurements. *Corrosion Science,* 24**,** 259-268.

MISCHLER, S., VOGEL, A., MATHIEU, H. J. & LANDOLT, D. 1991. The chemical composition of the passive film on Fe24Cr and Fe24Cr11Mo studied by AES, XPS and SIMS. *Corrosion Science,* 32**,** 925-944.

MIZUNO, T., MACDONALD, D. D., SMIALOWSKA, S., PEDNEKAR, T. & CHOI, H. J. 1983a. The General and Localized Corrosion of Carbon and Low-Alloy Steels in Oxygenated High-Temperature Water, EPRI NP-2853 (Research Project T115-5, Final Report, February 1983). Palo Alto, CA: EPRI (Electric Power Research Institute).

MIZUNO, T., PEDNEKAR, T., SZKLARSKA-SMIALOWSKA, S. & MACDONALD, D. D. 1983b. Corrosion and Stress Corrosion Cracking of Carbon Steel in Oxygenated, High-Purity Water at Elevated Temperatures. *1st International Symposium on Environmental Degradation in Nuclear Power Systems - Water Reactors.* Myrtle Beach: NACE.

MOSHIER, W. C. & JAMES, L. A. 1999. The effect of potential on the high-temperature fatigue crack growth response of low alloy steels, part 2: sulfide–potential interaction. *Corrosion Science,* 41**,** 401-415.

MURPHY, O. J., BOCKRIS, J. O. M., POU, T. E., TONGSON, L. L. & MONKOWSKI, D. 1983. Chloride Ion Penetration of Passive Films on Iron. *Journal of the Electrochemical Society,* 130**,** 1792-1794.

NIEHUIS, E. & GREHL, T. 2001. Dual Beam Depth Profiling. *ToF-SIMS: Surface Analysis by Mass Spectrometry.* IM Publications and Surface Spectra Limited.

PARK, J. H. & MACDONALD, D. D. 1989. The Fast-Growth Mechanism of Magnetite on Carbon Steel in Oxidizing High-Temperature Aqueous Solutions. *Corrosion,* 45**,** 563-567.

PARK, J. R. & MACDONALD, D. D. 1983. Impedance Studies of the Growth of Porous Magnetite Films on Carbon Steel in High Temperature Aqueous Systems. *Corrosion Science,* 23**,** 295-315.

PEARL, W. L. & WOZADLO, G. P. 1965. Corrosion of Carbon Steel in Simulated Boiling Water and Superheat Reactor Environments. *Corrosion,* 21**,** 260-267.

PENG, Q., SHOJI, T., RITTER, S. & SEIFERT, H. P. 2005. SCC Behaviour in the Transition Region of an Alloy 182-SA508 Cl.2 Dissimilar Weld Joint under Simulated BWR-NWC Conditions. *12th International Conference on Environmental Degradation of Materials in Nuclear Power Systems - Water Reactors.* Salt Lake City, USA: TMS.

PISTORIUS, P. C. 1997. Design Aspects of Electrochemical Noise Measurements for Uncoated Metals: Electrode Size and Sampling Rate. *Corrosion,* 53**,** 273-283.

POTTER, E. C. & MANN, G. M. W. 1963. Mechanism of Magnetite Growth on Low-Carbon Steel in Steam an Aqueous Solutions up to 550°C. *2nd International Congress on Metallic Corrosion.* NACE, Houston (Texas).

PSAILA-DOMBROWSKI, M. J. 1990. *Modeling of Crack and Crevice Chemistry in Light Water Reactor Environments.* PhD, Massachusetts Institue of Technology.

RICHTER, M. & WALTER, A. 1988. The adsorption of chloride on austenitic Cr-Ni-steel at high temperatures. *Werkstoffe und Korrosion,* 39**,** 355-364.

RIPPSTEIN, K. & KAESCHE, H. 1989. The stress corrosion cracking of a reactor pressure vessel steel in high-temperature water at high flow rates. *Corrosion Science,* 29**,** 517-534.

RITTER, S., HUET, F. & COTTIS, R. A. 2010. Guideline for an assessment of electrochemical noise measurement devices. *Materials and Corrosion,* doi: 10.1002/maco.201005839

RITTER, S. & SEIFERT, H. P. 2003. The Effect of Chloride and Sulphate Transients on the Environmentally-Assisted Cracking Behaviour of Low-Alloy RPV Steels under Simulated BWR Conditions. *Eurocorr 2003.* Budapest, Hungary.

RITTER, S. & SEIFERT, H. P. 2004a. Corrosion Fatigue Crack Growth Behaviour of Low-Alloy RPV Steels at Different Temperatures and Loading Frequencies under BWR/NWC Environment, Paper No. 276. *Eurocorr 2004.* Nice.

RITTER, S. & SEIFERT, H. P. 2004b. The Effect of Chloride and Sulphate Transients on the Stress Corrosion Cracking Behavior of Low-Alloy RPV Steels under Simulated BWR Environment. *Corrosion NACE.* Paper No. 04680.

RITTER, S. & SEIFERT, H. P. 2008a. Detection of stress corrosion cracking in a simulated BWR environment by combined electrochemical potential noise and direct current potential drop measurements. *Energy Materials: Materials Science and Engineering for Energy Systems,* 3**,** 72-80.

RITTER, S. & SEIFERT, H. P. 2008b. Effect of corrosion potential on the corrosion fatigue crack growth behavior of low-alloy steels in high-temperature water. *Journal of Nuclear Materials,* 375**,** 72-79.

RITTER, S. & SEIFERT, H. P. 2009. The Influence of Chloride Impurities on the SCC Crack Growth Behavior of Low-Alloy Reactor Pressure Vessel Steels under Simulated BWR Conditions. *12th International Conference on Fracture, ICF12, Paper 01226.*

RITTER, S. & SEIFERT, H. P. 2011. Environmentally-Assisted Crack Initiation Behaviour of Low-Alloy Steel in Simulated BWR Environment - Effect of Chloride, Paper 429. *18th International Corrosion Congress.* Perth, Australia: Curran Associates, Inc.

RITTER, S. & SEIFERT, H. P. 2012. Effect of chloride on EAC initiation in low-alloy steels. *In:* SEIFERT, H. P., RITTER, S. & LEBER, H. J. (eds.) *Environmentally-Assisted Cracking in Austenitic Light Water Reactor Structural Materials - Final Report of the KORA-II Project, PSI Bericht Nr. 12-02, June 2012, ISSN 1019-0643.* Paul Scherrer Institut.

ROBERTSON, J. & FORREST, J. E. 1991. Corrosion of Carbon Steels in High Temperature Acid Chloride Solutions. *Corrosion Science,* 32**,** 521-540.

ROTH, A. 2005. Spannungsrisskorrosion niedriglegierter Druckbehälterstähle in sauerstoffhaltigem Hochtemperaturwasser und ihre Bedeutung für den sicheren Betrieb von Siedewasserreaktoren. *Jahrestagung Kerntechnik 2005.* Paper 1211.

ROTH, A., DEVRIENT, B., GÓMEZ-BRICENO, D., LAPENA, J., ERNESTOVA, M., ZAMBOCH, M., EHRNSTEN, U., FÖHL, J., WEIßENBERG, T., SEIFERT, H. P. & RITTER, S. 2005. The Effect of Transients on the Crack Growth Behaviour of Low Alloy Steels for Pressure Boundary Components under Light Water Reactor Operating Conditions. *12th International Conference on Environmental Degradation of Materials in Nuclear Power Systems - Water Reactors.* Salt Lake City, USA: TMS.

ROTH, A., HÄNNINEN, H., BRÜMMER, G., WACHTER, O., ILG, U., WIDERA, M. & HOFFMANN, H. 2003. Investigations of dynamic strain aging effects of low alloy steels and their possible relevance for environmentally-assisted cracking in oxygenated high-temperature water. *11th International Conference on Environmental Degradation of Materials in Nuclear Power Systems - Water Reactors.* Stevenson: ANS.

SCHULTZE, J. W. & HASSEL, A. W. 2003. Passivity of Metals, Alloys, and Semiconductors. *In:* BARD, A. J. & STRATMANN, M. (eds.) *Encyclopedia of Electrochemistry; Vol. 4: Corrosion and Oxide Films.* New York: John Wiley & Sons.

SCHULTZE, J. W. & LOHRENGEL, M. M. 2000. Stability, reactivity and breakdown of passive films. Problems of recent and future research. *Electrochimica Acta,* 45**,** 2499-2513.

SCHWERTMANN, U. & FECHTER, H. 1994. The formation of green rust and its transformation to lepidocrocite. *Clay Minerals,* 29**,** 87-92.

SCOTT, P. 1985. A Review of Environment-Sensitive Fracture in Water Reactor Materials. *Corrosion Science,* 25**,** 583-606.

SCOTT, P., COMBRADE, P., KILIAN, R., ROTH, A., ANDRESEN, P. & KIM, Y. 2005. Status Review of Initiation of Environmentally Assisted Cracking and Short Crack Growth. EPRI, Palo Alto, CA: 2005. 1011788.

SCOTT, P. M. & TICE, D. R. 1990. Stress corrosion in low alloy steels. *Nuclear Engineering and Design,* 119**,** 399-413.

SEIFERT, H. P. 2002. Literature Survey on the Stress Corrosion Cracking of Low-Alloy Steels in High-Temperature Water. PSI-Report 02-06. Paul Scherrer Institute, Nuclear Energy and Safety Division - Laboratory for Materials Behaviour, Structural Integrity Group.

SEIFERT, H. P. & RITTER, S. 2003. New observations about the SCC crack growth behavior of low-alloy RPV steels under BWR/NWC conditions. *11th International Conference on Environmental Degradation of Materials in Nuclear Systems - Water Reactors.* Stevenson: ANS.

SEIFERT, H. P. & RITTER, S. 2005a. Research and Service Experience with Environmentally-Assisted Cracking Behaviour of Low-Alloy Steels in High-Temperature Water. *SKI Report 2005:60.*

SEIFERT, H. P. & RITTER, S. 2005b. Review and Assessment of SCC Experiments with RPV Steels in Oskarshamn 2 and 3 (ABB Report SBR 99-020). SKI Report 2005:61.

SEIFERT, H. P. & RITTER, S. 2008a. Strain-Induced corrosion cracking behaviour of low-alloy steels under boiling water reactor conditions. *Journal of Nuclear Materials,* 378**,** 312-326.

SEIFERT, H. P. & RITTER, S. 2008b. Stress corrosion cracking of low-alloy reactor pressure vessel steels under boiling water reactor conditions. *Journal of Nuclear Materials,* 372**,** 114-131.

SEIFERT, H. P., RITTER, S. & HICKLING, J. 2003. Environmentally Assisted Cracking of Low-Alloy RPV and Piping Steels under LWR Conditions. *11th International Conference on Environmental Degradation of Materials in Nuclear Power Systems - Water Reactors.* Stevenson: ANS.

SEIFERT, H. P., RITTER, S. & HICKLING, J. 2004. Research and Service Experience with Environmentally Assisted Cracking of Low-Alloy Steel Pressure-Boundary Components under LWR Conditions. *Power Plant Chemistry,* 6**,** 111-123.

SEIFERT, H. P., RITTER, S., LEBER, H. J. & ROYCHOWDHURY, S. 2013. SCC Behavior in the Transition Region of Alloy 182 / Low-Alloy Reactor Pressure Vessel Steel Dissimilar Metal Weld Joints in Light Water Reactor Environments. *16th International Conference on Environmental Degradation of Materials in Nuclear Power Systems - Water Reactors.* Asheville: NACE.

SEIFERT, H. P., RITTER, S., SHOJI, T., PENG, Q., YAKEDA, Y. & LU, Z. P. 2008. Environmentally-Assisted Cracking Behaviour in the Transition Region of an Alloy 182/SA508 Cl.2 Dissimilar Metal Weld Joint in Simulated Boiling Water Reactor Normal Water Chemistry Environment. *Journal of Nuclear Materials,* 378**,** 197-210.

SHOJI, T., TAKAHASHI, H., AIZAWA, S. & SAITO, M. 1988. Effects of sulphate contamination, sulphur in steel and strain-rate on critical cracking potential for SCC of pressure vessel steels in pressurized high-temperature waters. *3rd International Symposium on Environmental Degradation of Materials in Nuclear Power Systems - Water Reactors.* Traverse City.

SPEIDEL, M. O. 1984. Stress Corrosion Cracking and Corrosion Fatigue Fracture Mechanics. *In:* SPEIDEL, M. O. & ATRENS, A. (eds.) *Corrosion in Power Generating Equipment.* Plenum Press NY.

SPEIDEL, M. O. & MAGDOWSKI, R. 1988. Stress Corrosion Cracking of Nuclear Reactor Pressure Vessel and Piping Steels. *International Journal of Pressure Vessels and Piping,* 34**,** 119-142.

SPEIDEL, M. O. & MAGDOWSKI, R. 1995. Stress Corrosion Crack Growth Rates and General Corrosion Rates at Crack Tips of Steels in High Temperature Water, Paper No. 179. *Corrosion 1995, NACE Conference.*

SRIVASTA, S. C. & IVES, M. B. 1987. Dissolutions of Inclusions in Low-Alloy Steel Exposed to Chloride-Containing Environments. *Corrosion,* 43**,** 687-692.

STELLWAG, B., LASCH, M. & STAUDT, U. 1998. Investigations into alternatives to hydrogen water chemistry in BWR plants. *JAIF International Conference on Water Chemistry in Nuclear Power Plants, Water Chemistry ´98.* Kashiwazaki, Japan.

STRATMANN, M. & MÜLLER, J. 1994. The Mechanism of the Oxygen Reduction on Rust-Covered Metal Substrates. *Corrosion Science,* 36**,** 327-359.

STREHBLOW, H. H. 1976. Nucleation and Repassivation of Corrosion Pits for Pitting on Iron and Nickel. *Werkstoffe und Korrosion,* 27**,** 792-799.

STREHBLOW, H. H. 2003. Pitting Corrosion. *In:* BARD, A. J., STRATMANN, M. & FRANKEL, G. S. (eds.) *Encyclopedia of Electrochemistry; Vol. 4: Corrosion and Oxide Films.* New York: John Wiley & Sons.

STREHBLOW, H. H., TITZE, B. & LÖCHEL, B. P. 1979. The Breakdown of Passivity of Iron and Nickel by Fluoride. *Corrosion Science,* 19**,** 1047-1057.

TENCKHOFF, E., ERVE, M., LENZ, E. & VAZOUKIS, G. 1990. Environmentally assisted crack growth in low alloy steels - results and their relevance to lwr components. *Nuclear Engineering and Design,* 119**,** 371-378.

TIRBONOD, B. 2000. Modelling of the Stress Corrosion Cracking Behavoiur for Low Alloy Steels in High Temperature Water. PSI-Report 00-08. 5232 Villingen PSI: Paul Scherrer Institut.

TOMLINSON, L. 1981. Mechanism of Corrosion of Carbon and Low Alloy Ferritic Steels by High Temperature Water. *Corrosion,* 37**,** 591-596.

TÖRRÖNEN, K. & KEMPAINEN, M. 1984. Fractography and Mechanisms of Environmentally Enhanced Fatigue Crack Propagation of a Reactor Pressure Vessel Steel. *Corrosion Fatigue: Mechanics, Metallurgy, Electrochemistry, and Engineering. ASTM STP 801, T.W. Crooker and B.N. Leis, Eds., American Society for Testing and Materials, 1983, pp. 287-318.*

TOWNSEND, H. E. 1970. Potential/pH Diagrams at Elevated Temperature for the System Iron-Water. *Corrosion Science,* 10**,** 343-358.

TURNBULL, A. 1993. Modelling of environment assisted cracking. *Corrosion Science,* 34**,** 921-960.

UHLIG, H. H. 1979. Passivity in Metals and Alloys. *Corrosion Science,* 19**,** 777-791.

UHLIG, H. H. & REVIE, R. 1985. *Corrosion and corrosion control,* New York, John Wiley & Sons.

VAN DER SLUYS, W. A. 1993. Evaluation of the available data on the effect of the environment on the low cycle fatigue properties in light water reactor environments. *6th International Symposium on Environmental Degradation of Materials in Nuclear Power Systems - Water Reactors.* San Diego: TMS.

VAN DER SLUYS, W. A. & PATHANIA, R. 1991. Studies of stress corrosion cracking in steels used for reactor pressure vessels. *5th International Symposium on Environmental Degradation of Materials in Nuclear Power Systems - Water Reactors.* Monterey: ANS.

VETTER, K. J. 1953. Über die Größe des Flade-Potentials der Aktivierung und Passivierung von Eisen und weitere Eigenschaften der Passivschicht. *Zeitschrift der physikalischen Chemie,* 202.

VGBPOWERTECH, E. V. 2006. Richtlinie für das Wasser in Kernkraftwerken mit Leichtwasserreaktoren. VGB-R 401.

VICKERMAN, J. C. 2001. ToF-SIMS - An Overview. *In:* VICKERMAN, J. C. & BRIGGS, D. (eds.) *ToF-SIMS: Surface Analysis by Mass Spectrometry.* IM Publications and Surface Spectra Limited.

VIDEM, K. 1975. Corrosion of Steel in High-Temperature Water - The Influence of Oxygen in the Water and of Performed Oxide Coatings. *7th Scandinavian Corrosion Conference.* Trondheim, Norway.

VREELAND, D. C., GAUL, G. G. & PEARL, W. L. 1962. Corrosion of Carbon Steel and Other Steels in Simulated Boiling-Water Reactor Environment: Phase II. *Corrosion,* 18**,** 368-377.

WAGNER, C. 1965. Passivity and inhibition during the oxidation of metals at elevated temperatues. *Corrosion Science,* 5**,** 751 - 764.

WEIL, K. G. & BONHOEFFER, K.-F. 1955. Zur Passivität des Eisens in neutralen und schwach sauren Lösungen. *Zeitschrift für Physikalische Chemie,* 4**,** 175 - 191.

WEINSTEIN, D. 1982. BWR Environmental Cracking Margins for Carbon Steel Piping. EPRI, San Jose, CA: 1982: EPRI NP-2406, Research Project 1248-1.

WIRE, G. L. 2000. Cessation of environmentally-assisted cracking in a low-alloy steel: theoretical analysis. *Nuclear Engineering and Design,* 197**,** 25-44.

YANG, W. P., COSTA, D. & MARCUS, P. 1992. Chemical Composition, Chemical Sates and Resistance to Localized Corrosion of Passive Films on a Fe-17%Cr Alloy. *In:* MACDOUGALL, ALWITT, R. S. & RAMANARAYANAN, T. A. (eds.) *PV 92-22.* Princeton, N.J.: The Electrochemical Society.

YIN LI, Y. 2000. Cessation of environmentally-assisted cracking in a low-alloy steel: experimental results. *Nuclear Engineering and Design,* 197**,** 45-60.

YOUNG, L. M. & ANDRESEN, P. 1995. Crack Tip Microsampling and Growth Rate Measurements in a 0.021%S Low Alloy Steel in High Temperature Water. *7th International Symposium on Environmental Degradation of Materials in Nuclear Power Systems - Water Reactors.* Breckenridge, Colorado: NACE.

ZHOU, X. Y., LVOV, S. N., WEI, X. J., BENNING, L. G. & MACDONALD, D. D. 2002. Quantitative evaluation of general corrosion of Type 304 stainless steel in subcritical and supercritical aqueous solutions via electrochemical noise analysis. *Corrosion Science,* 44**,** 841-860.

10. APPENDIX

Appendix 1 (Schematic Drawing of the Testing Facility for Exposure Tests)

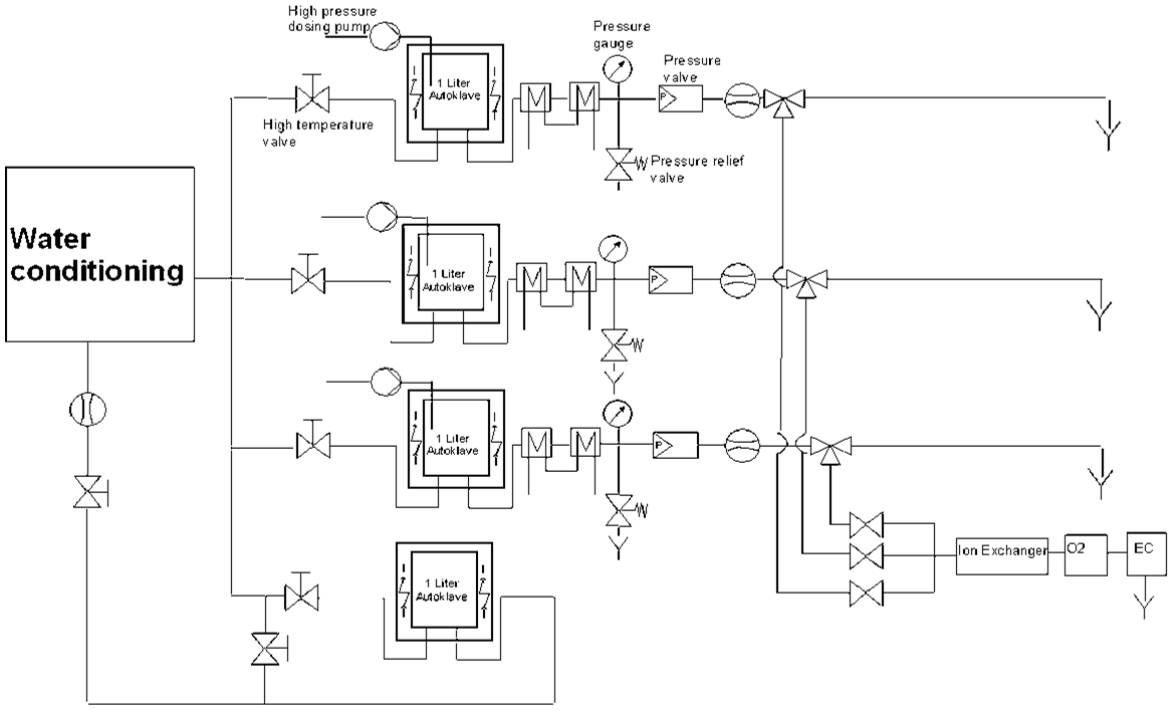

Figure 99: Schematic drawing of the 4 autoclave testing facility used for tests on the general corrosion behaviour.

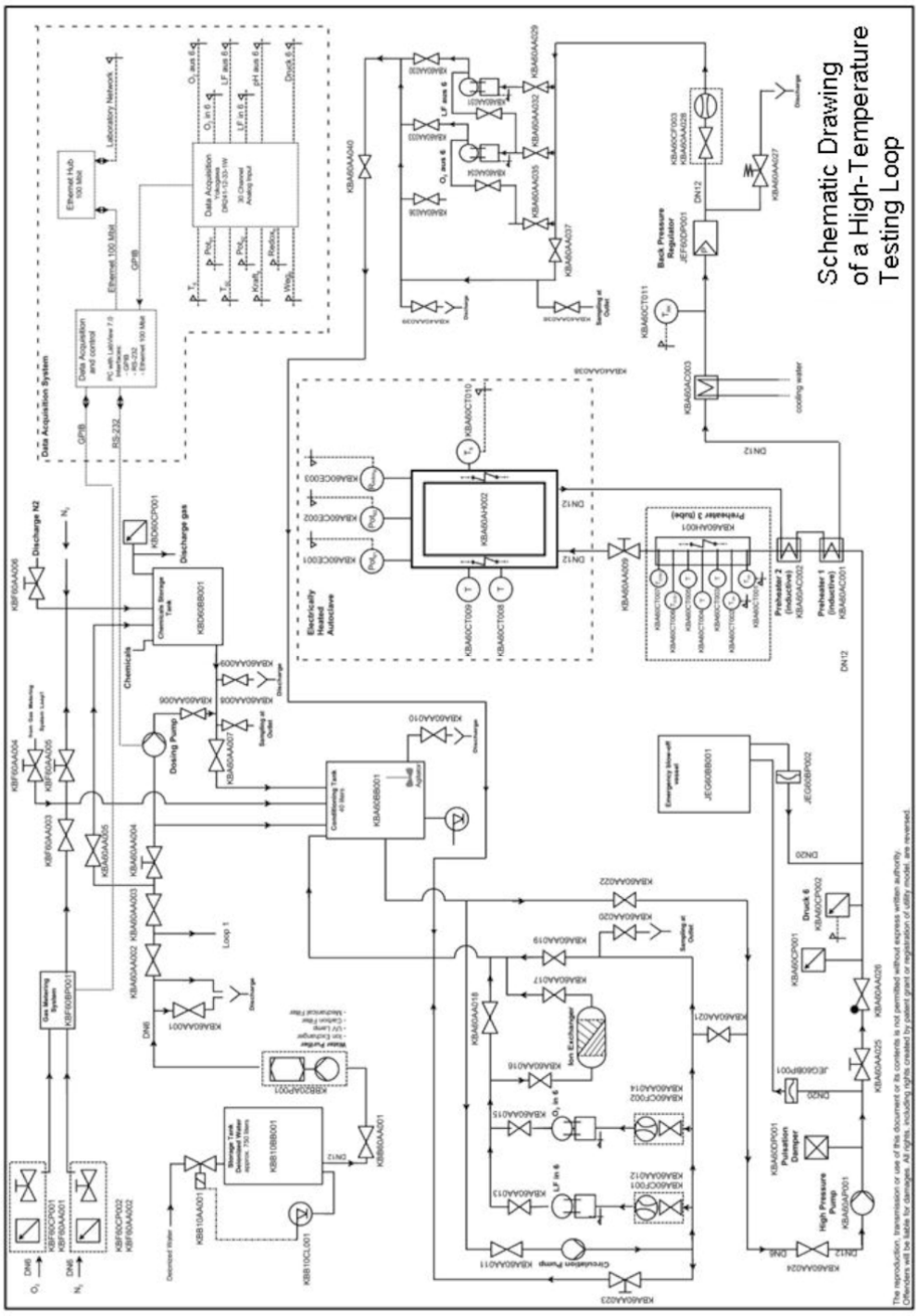

Figure 100: Schematic drawing of the test loop and the water preparation unit used for testing under HTW-conditions.

Appendix 2 (Technical Drawing of C-ring and Coupon Specimen)

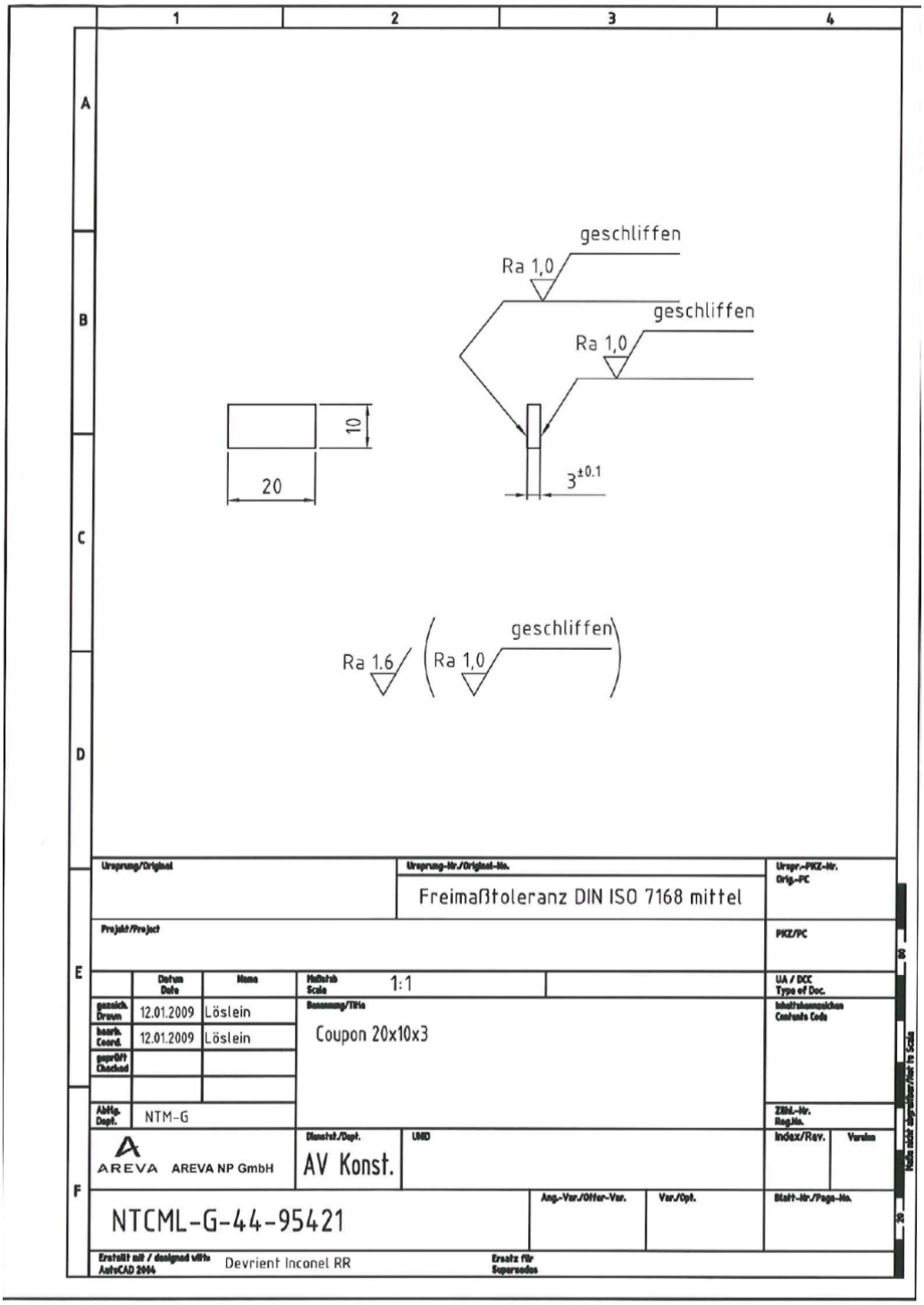

Figure 101: Technical Drawing of the coupon specimen

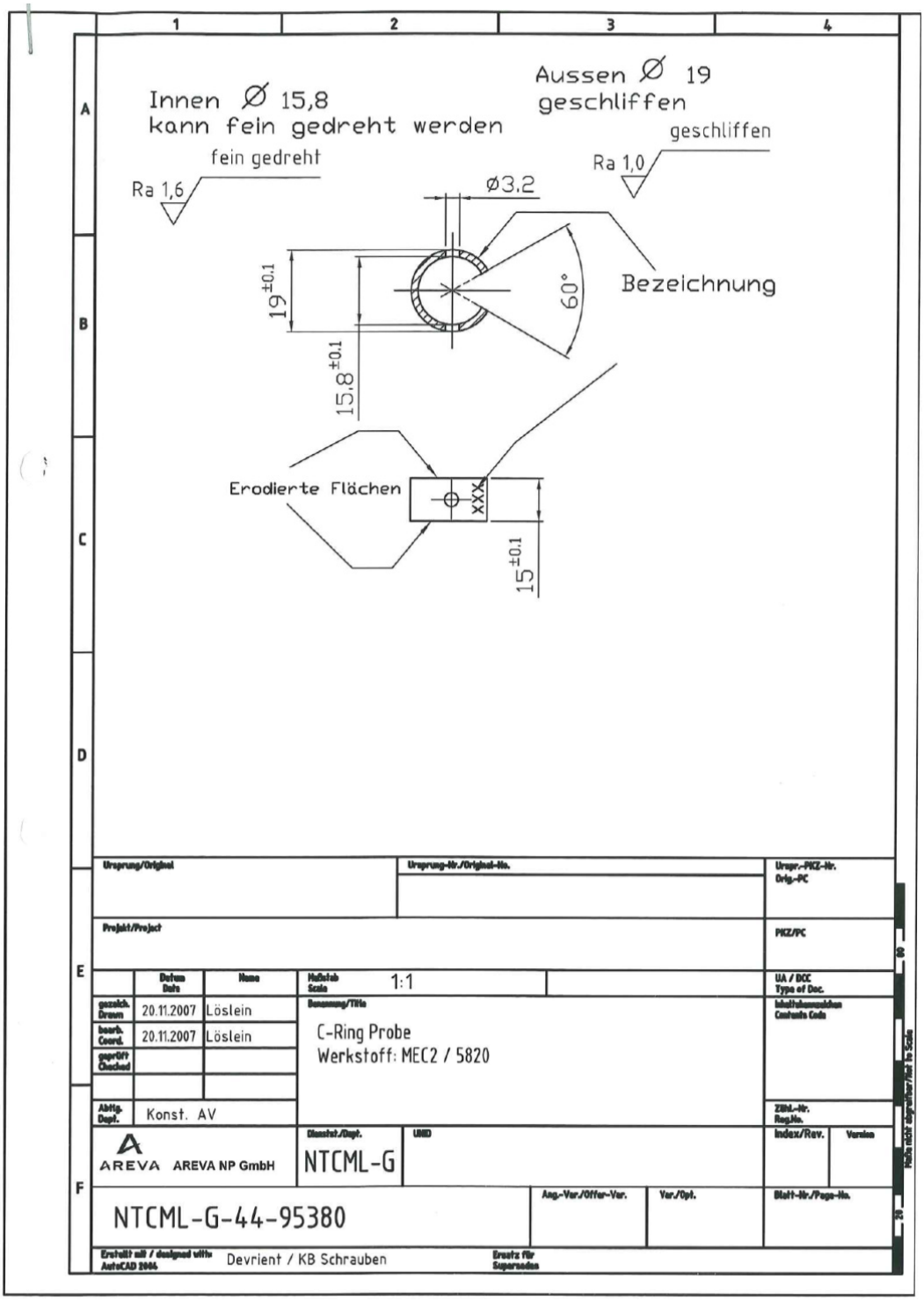

Figure 102: Technical drawing of the C-ring specimens

Appendix 3 (Exemplary Results from the Exposure Tests)

ECP and Water chemistry diagrams of a test run with 100 hours continuously increased chloride concentration

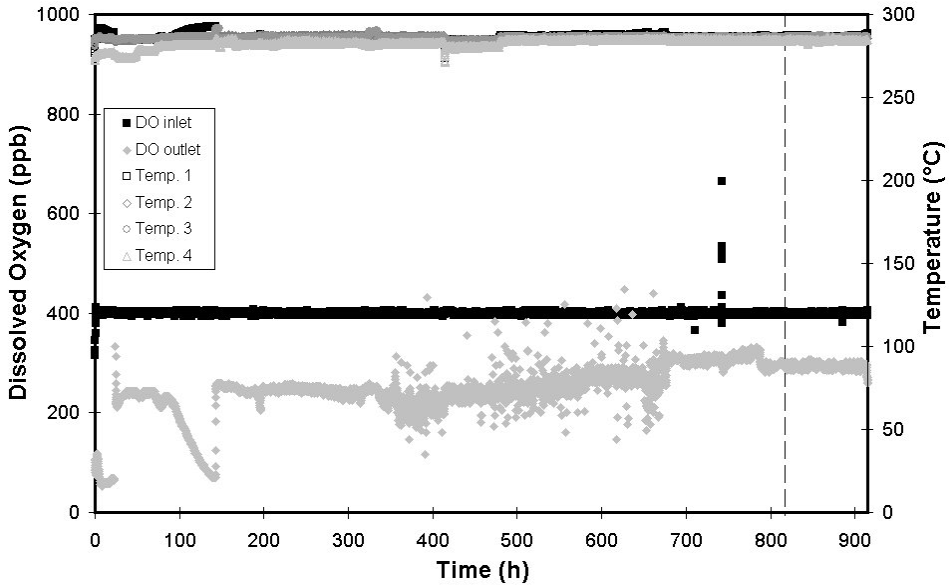

Figure 103: Dissolved Oxygen and Temperature for the test run with 100 hours permanently increased chloride concentration.

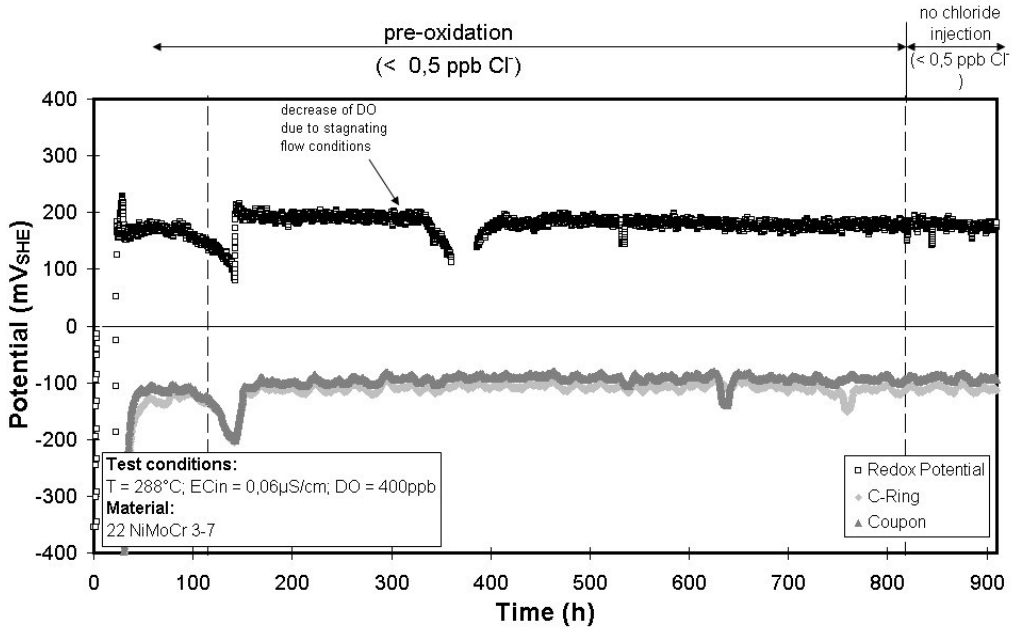

Figure 104: Redox- and Corrosion Potential of C-Ring and Coupon specimens for the test run with 100 hours permanently increased chloride concentration. This Figure shows the Potentials measured for the specimens tested without increased chloride concentration.

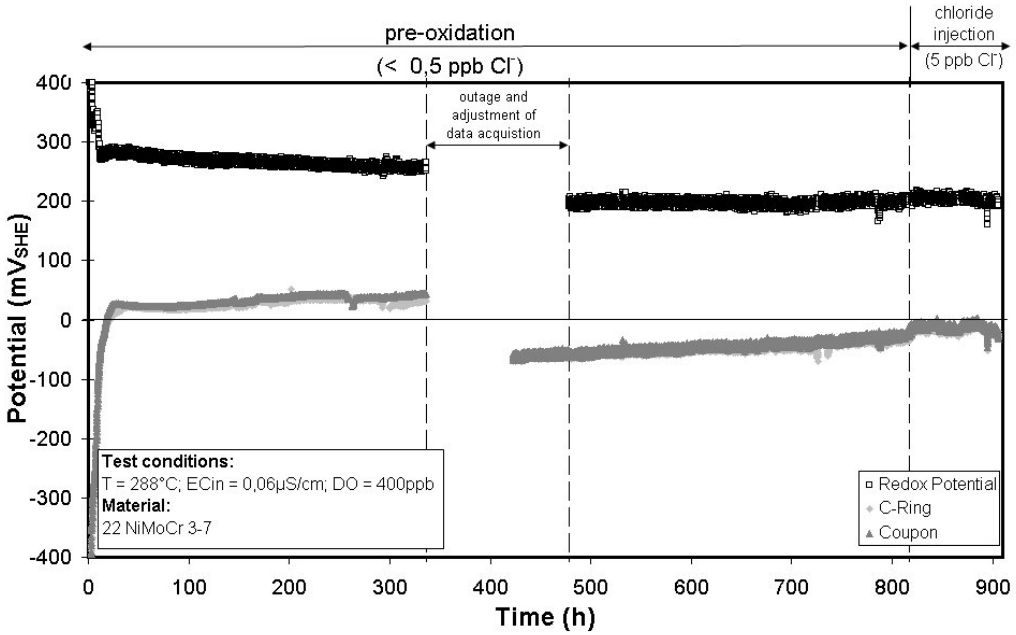

Figure 105: Redox- and Corrosion Potential of C-Ring and Coupon specimens for the test run with 100 hours permanently increased chloride concentration. This Figure shows the Potentials measured at the specimens tested at a chloride concentration of 5 ppb.

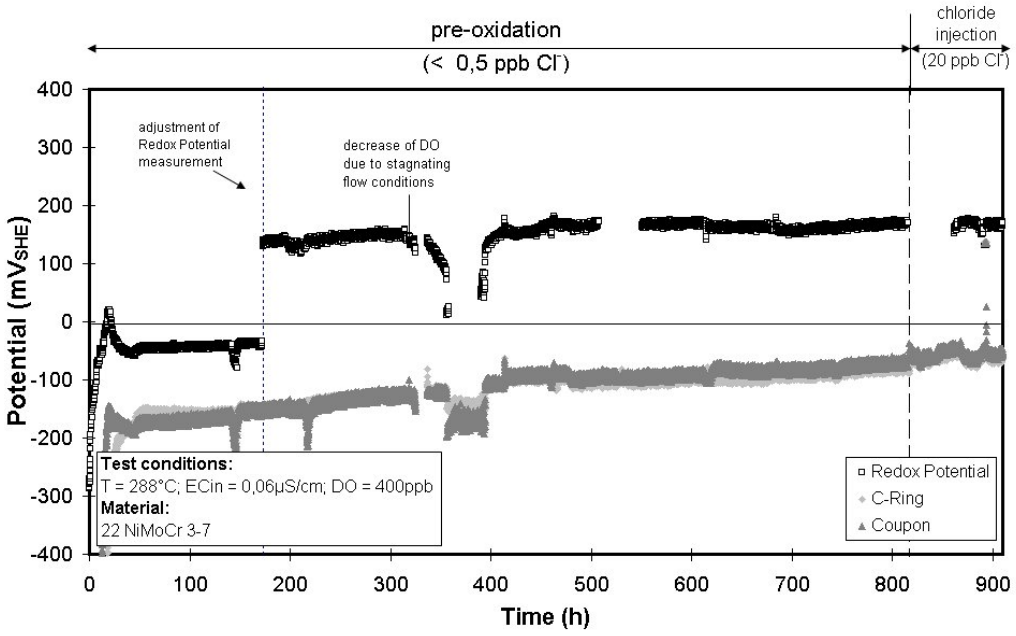

Figure 106: Redox- and Corrosion Potential of C-Ring and Coupon specimens for the test run with 100 hours permanently increased chloride concentration. This Figure shows the Potentials measured at the specimens tested at a chloride concentration of 20 ppb.

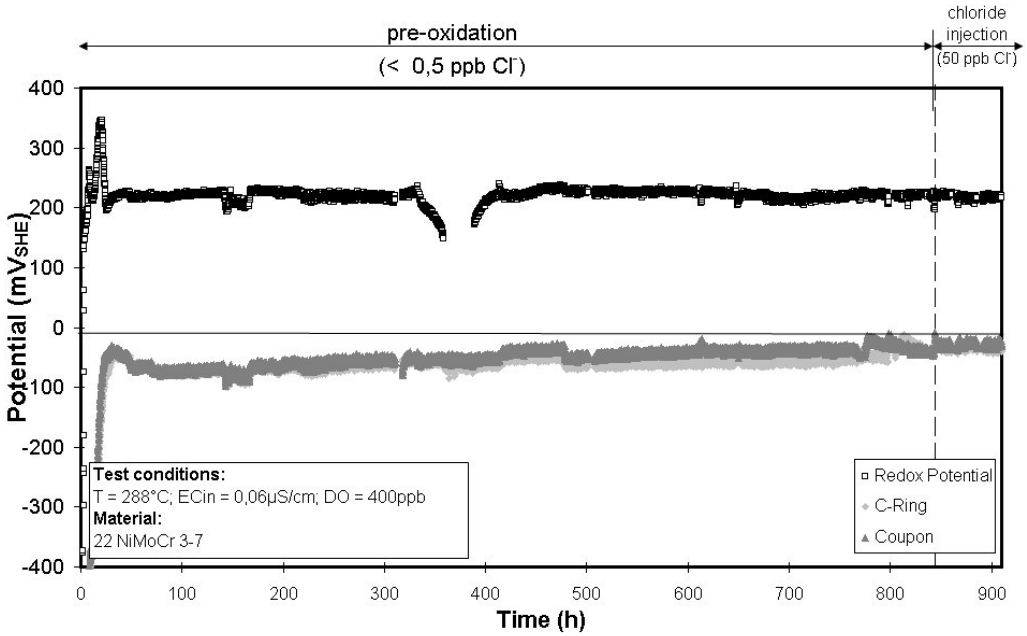

Figure 107: Redox- and Corrosion Potential of C-Ring and Coupon specimens for the test run with 100 hours permanently increased chloride concentration. This Figure shows the Potentials measured at the specimens tested at a chloride concentration of 50 ppb.

ECP and Water chemistry diagrams of a test run with a 24 hour chloride transient und subsequent 200 hours under specified water chemistry conditions (without chloride)

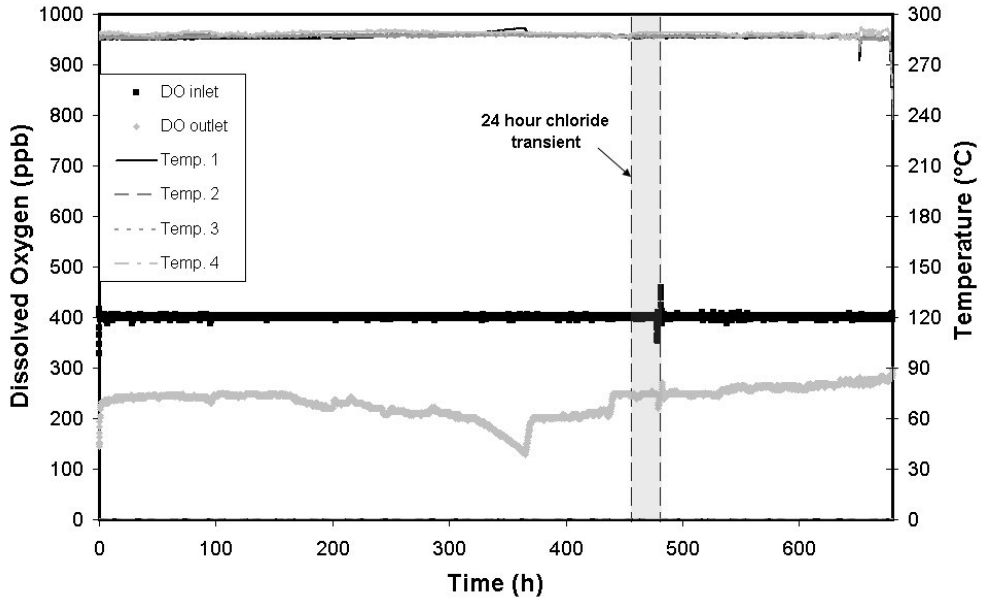

Figure 108: Dissolved Oxygen and Temperature for the test run with a 24 hour chloride chloride transient and additional 200 hours without chloride.

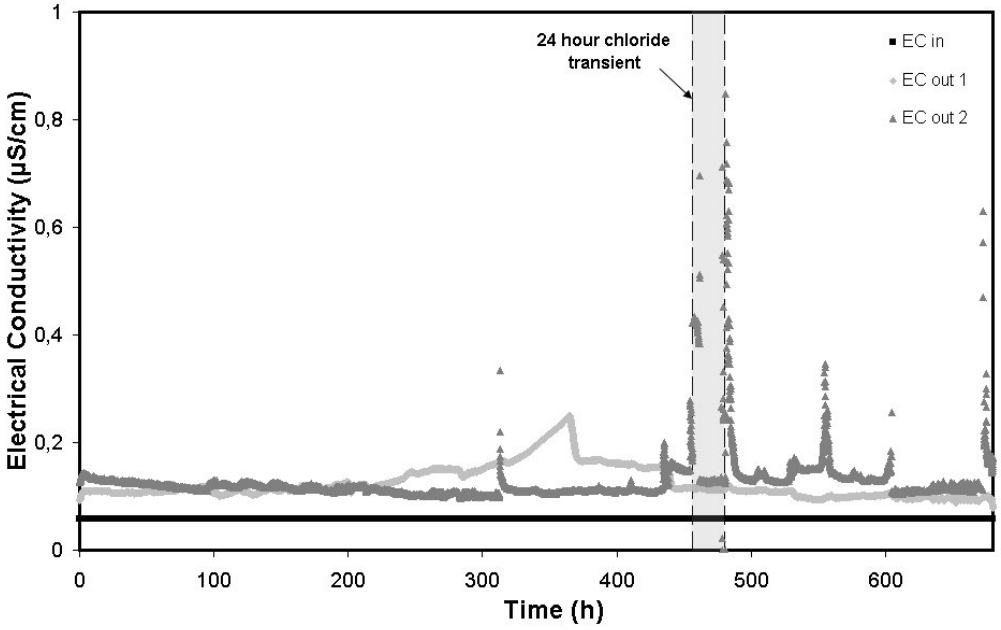

Figure 109: Electrical Conductivity at inlet and outlet for the test run with a 24 hour chloride transient and additional 200 hours without chloride.

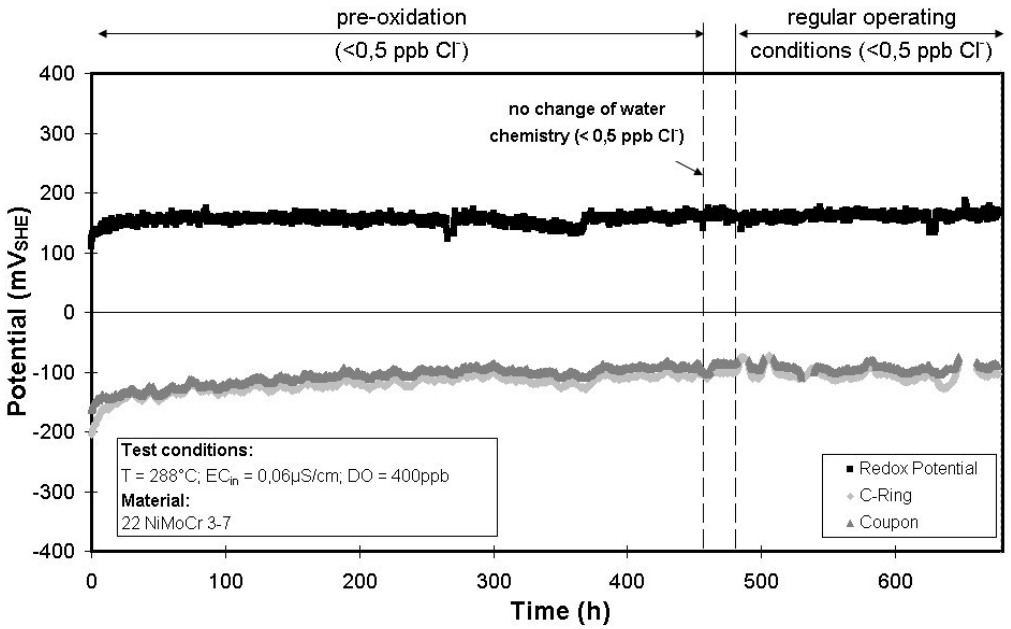

Figure 110: Redox- and Corrosion Potential of C-Ring and Coupon specimens for the test run with 24 hour chloride transient and additional 200 hours without chloride. This Figure shows the Potentials measured at the specimens tested without chloride transient.

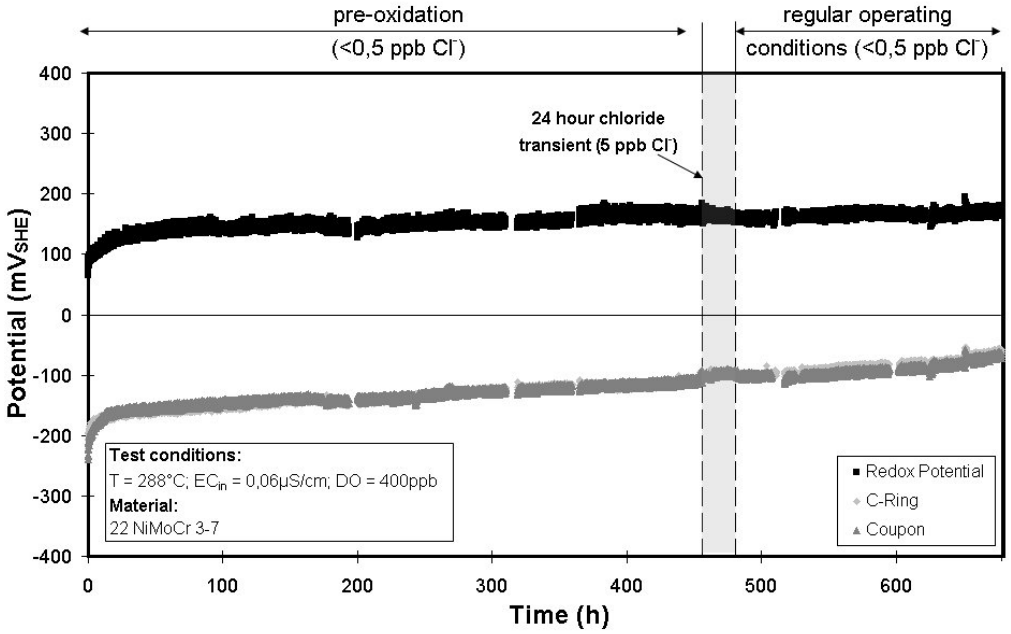

Figure 111: Redox- and Corrosion Potential of C-Ring and Coupon specimens for the test run with 24 hour chloride transient and additional 200 hours without chloride. This Figure shows the Potentials measured at the specimens tested with a chloride concentration of 5 ppb during the 24 hour transient.

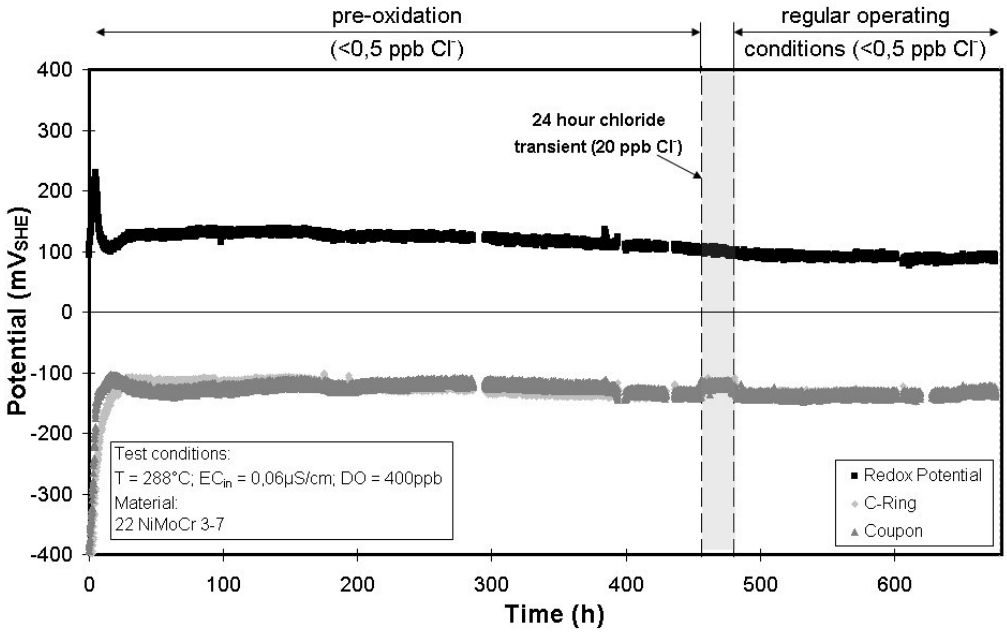

Figure 112: Redox- and Corrosion Potential of C-Ring and Coupon specimens for the test run with 24 hour chloride transient and additional 200 hours without chloride. This Figure shows the Potentials measured at the specimens tested with a chloride concentration of 20 ppb during the 24 hour transient.

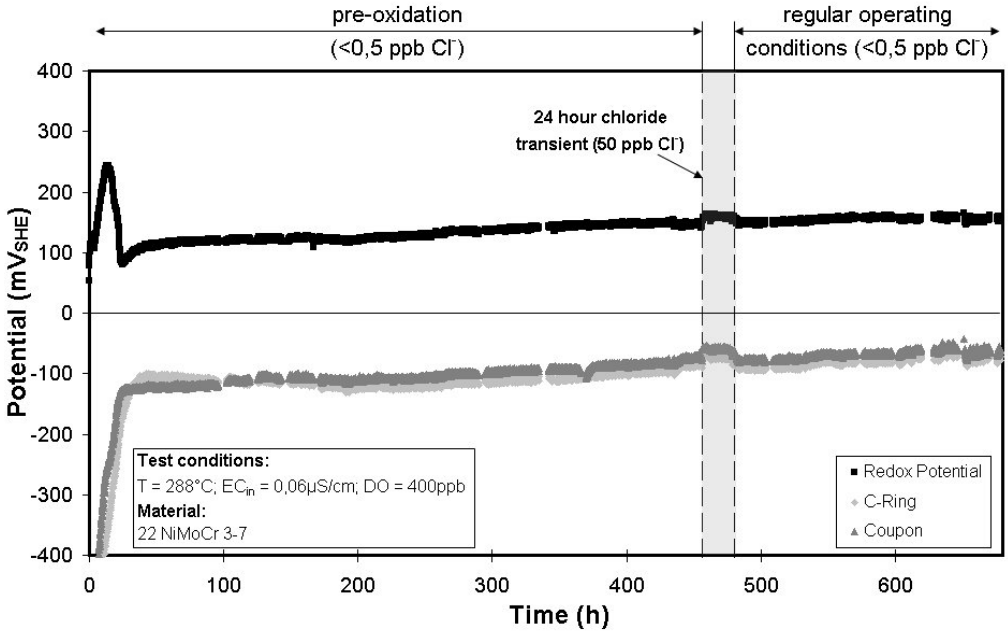

Figure 113: Redox- and Corrosion Potential of C-Ring and Coupon specimens for the test run with 24 hour chloride transient and additional 200 hours without chloride. This Figure shows the Potentials measured at the specimens tested with a chloride concentration of 50 ppb during the 24 hour transient.

Appendix 4 (Technical Drawing of the CERT Specimens)

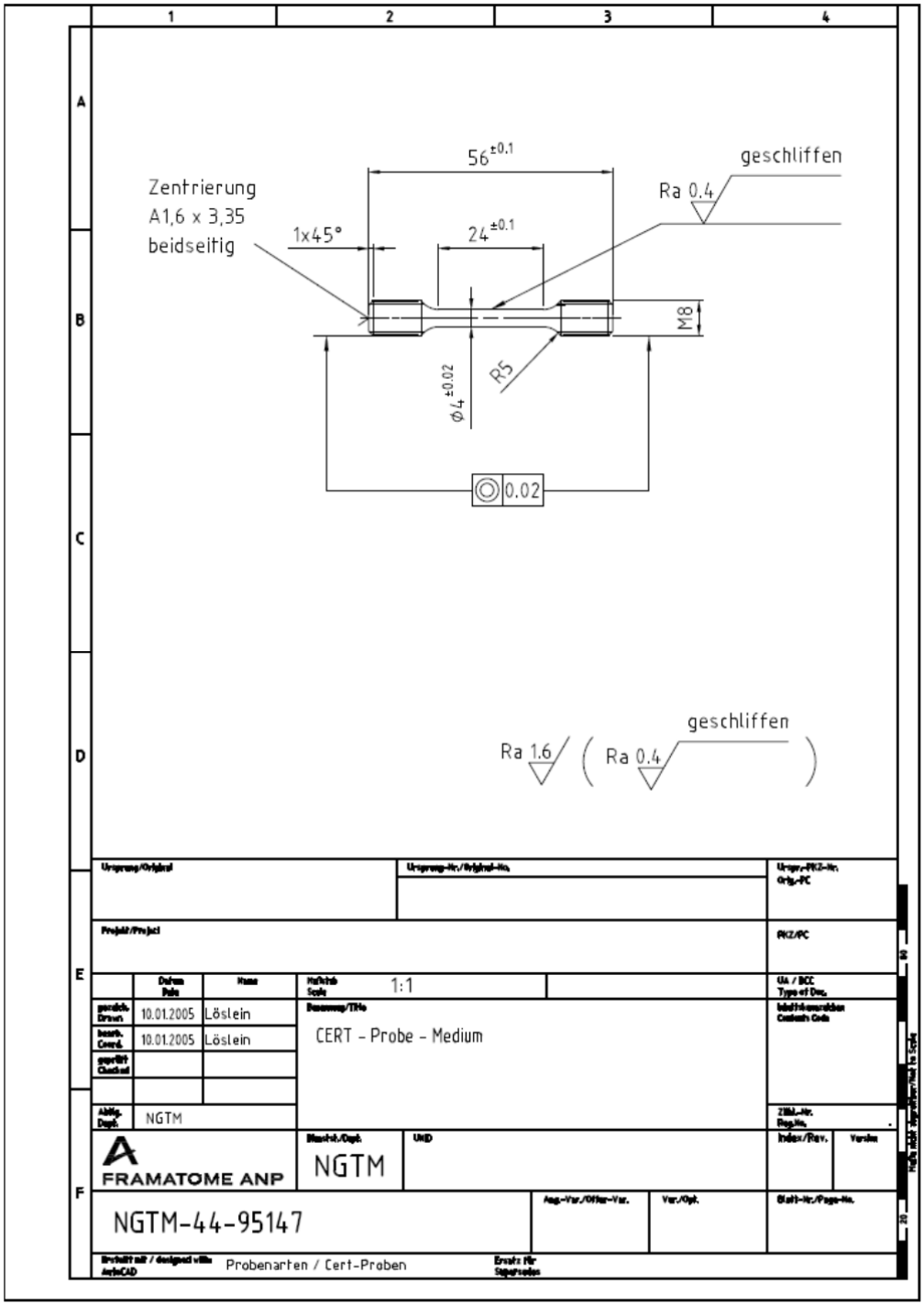

Figure 114: Technical drawing of the used CERT-specimens. Note: As a final manufacturing step, the specimens were polished to a final value of Ra ≈ 0.05 µm and cleaned using ethanol prior to testing, which is not shown in the technical drawing.

Appendix 5 (Technical Drawings of 1 T-CT specimens)

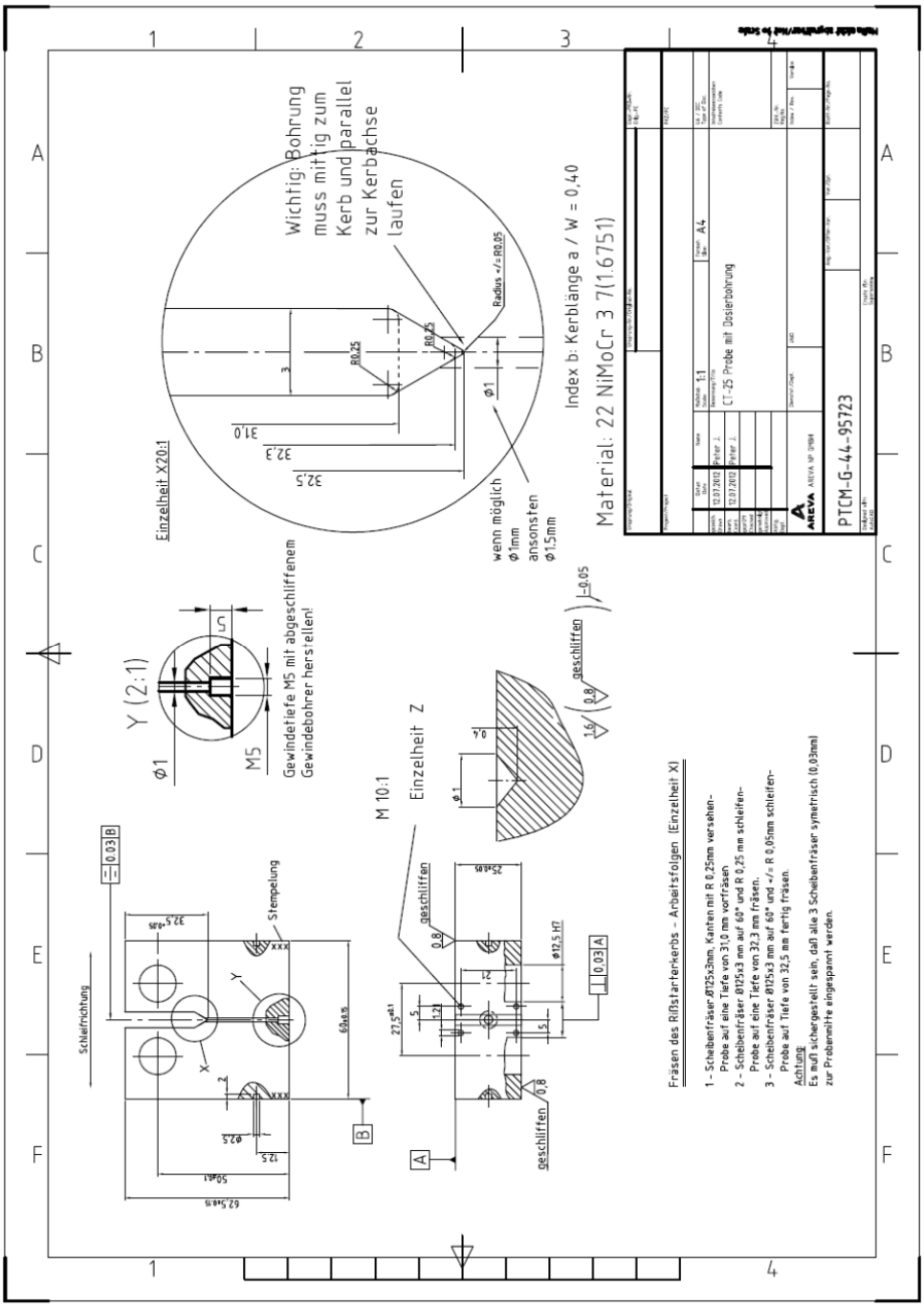

Figure 115: Technical drawing of the 1 T-CT specimen with back bore.

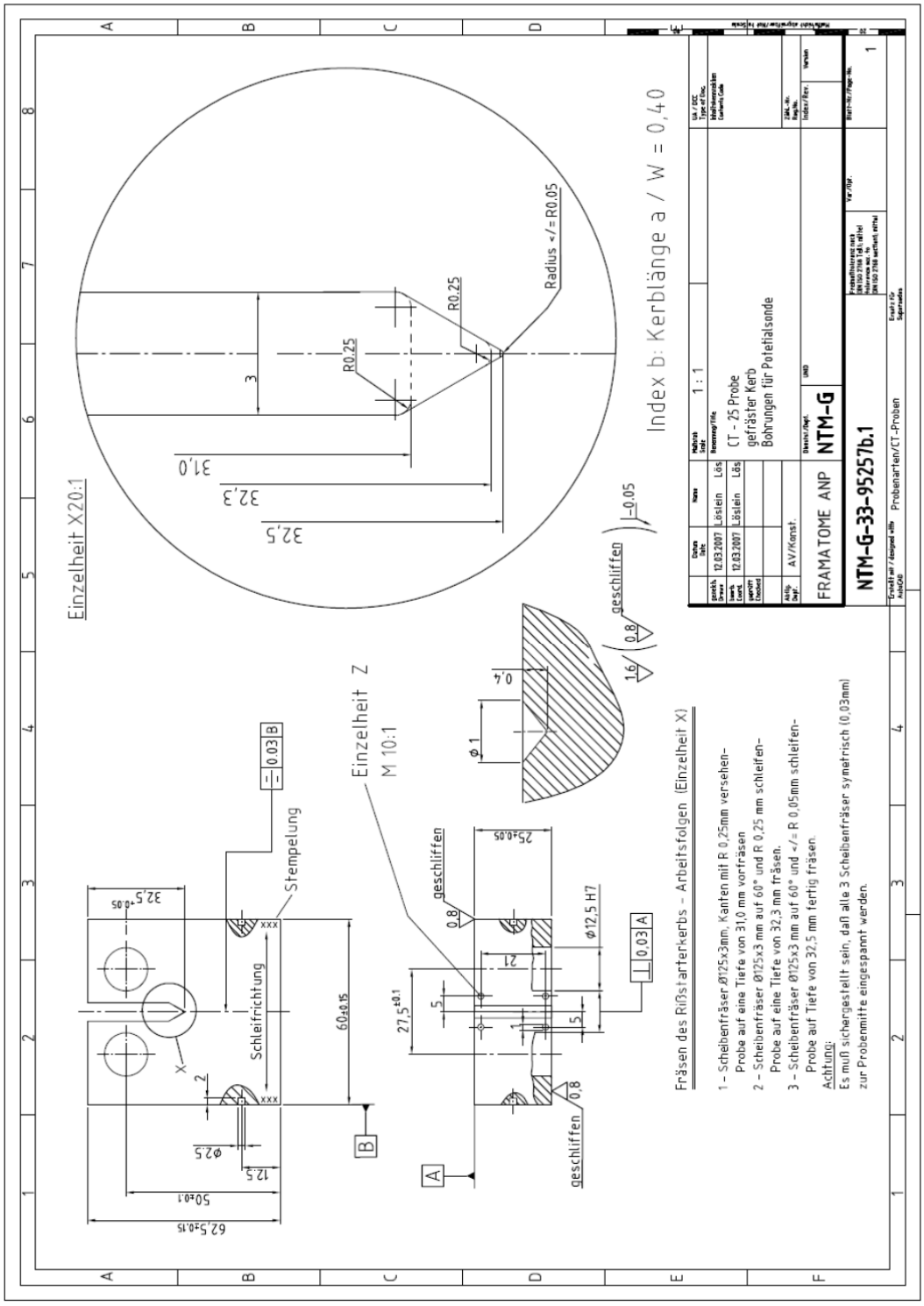

Figure 116: Technical drawing of the 1 T-CT specimen (without back bore).

Appendix 6 (Results from Pre-Cracking in Air)

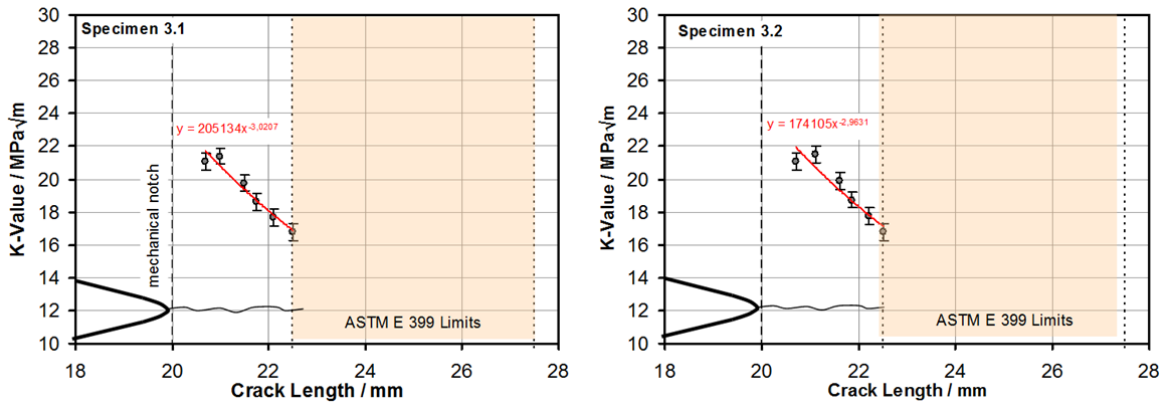

a) b)

Figure 117:

Fatigue pre-cracking of a) specimen 3.1 and b) specimen 3.2.

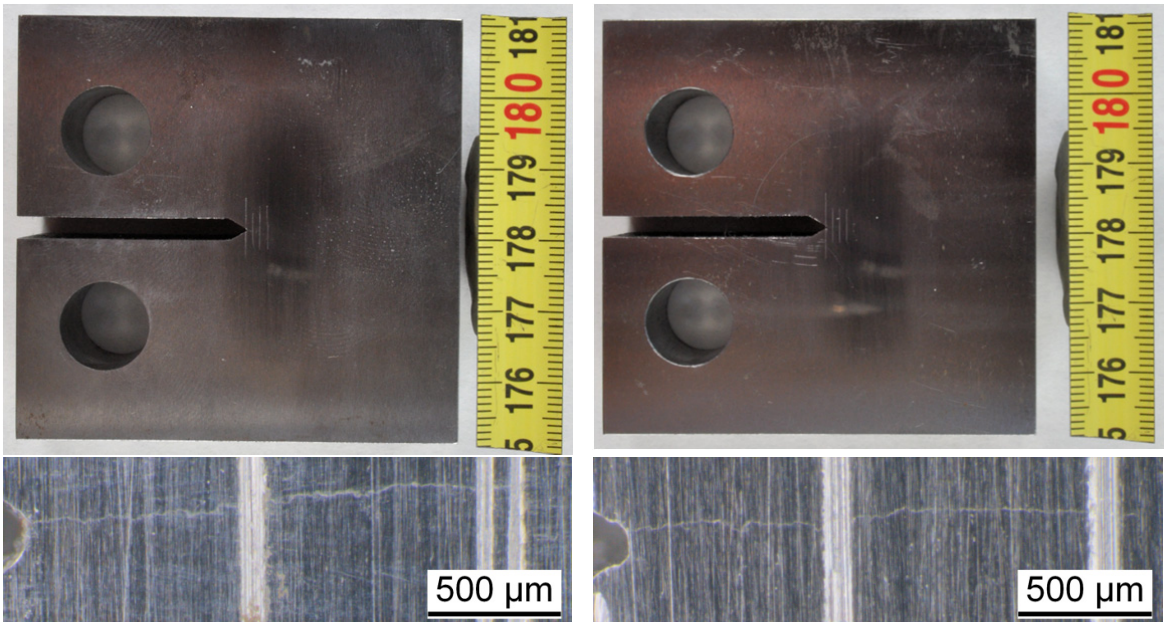

a) b)

Figure 118: Visual appearance of the 1 T-CT specimens after fatigue pre-cracking a) specimen 3.1 (used for crack tip microsampling), b) specimen 3.2 (used for acquisition of crack growth rate).